In presenting this thesis in partial fulfillment of the requirements for an advanced degree at Idaho State University, I agree that the Library shall make it freely available for inspection. I further state that permission for extensive copying of my thesis for scholarly purposes may be granted by the Dean of the Graduate School, Dean of my academic division, or by the University Librarian. It is understood that any copying or publication of this thesis for financial gain shall not be allowed without my written permission.

Signature _____

Date _____

Development of a Sample Preparation Technique for Determining the Tensile Strength of Select Layers and Layer Interfaces of TRISO Particles

by

Tanner Mauseth

A thesis

Submitted in partial fulfillment

of the requirements for the degree of

Master of Science in the Department of Nuclear Engineering

Idaho State University

Summer 2021

To the Graduate Faculty:

The members of the committee appointed to examine the thesis of Tanner Mauseth find it satisfactory and recommend that it be accepted.

_____

Mary Lou Dunzik-Gougar
Major Advisor, Committee Chair

_____

Fei Teng
Committee Member

_____

John Dudgeon
Graduate Faculty Representative

Acknowledgements

The credit of this work goes to the guidance and leadership of Dr. Mary Lou Dunzik-Gougar, Dr. Fei Teng, and Dr. LaBrier, the technical support and expertise of Dr. John Dudgeon at Idaho State University's Center for Archaeology, Materials and Applied Spectroscopy (CAMAS), the technicians from Superior Technical Services out of Portland, Oregon, the microscopy experts from Bruker Hysitrons headquarters out of Eden Prairie, Minnesota, and all my friends and family who kept pushing me to overcome any and all obstacles set before me along this journey.

This research work is financially supported through the Department of Energy's Nuclear Energy University Program (NEUP) grant for project 17251. We thank Dr. Isabella Van Rooyen for providing the surrogate TRISO particle samples in this study.

Table of Contents

List of Equations

List of Figures

List of Tables

Development of a Sample Preparation Technique for Determining the Tensile Strength of Select Layers and Layer Interfaces of TRISO Particles

Thesis Abstract--Idaho State University (2021)

This work describes the development of a capability that enables micrometer scale strength characterization of the buffer, IPyC, and buffer-IPyC interface of TRISO particles. TRISO particle based fuel is an attractive accident tolerant fuel for advanced reactors. Results are intended to fill a recognized gap in the knowledge base regarding the characteristics of individual layers and interlayer bonds of TRISO particles under development as part of the DOE's AGR Program. The capability involves the use of FIB micromachining and in-situ SEM tensile testing of TRISO particle tensile samples to achieve results. Baseline materials of copper, molybdenum, silicon, and ZrO2 fuel surrogate TRISO particles are the sole materials tested in this work. The tensile strength results obtained from the baseline materials align with the known literature and the fracture behavior of one TRISO particle sample containing the buffer-IPyC interlayer was obtained. Unirradiated and Irradiated TRISO fuel particles are the subject of future work.

Key words: buffer; inner pyrolitic carbon (IPyC); tri-structural isotropic (TRISO); focused ion beam (FIB); scanning electron microscope (SEM), PicoIndenter.

1.0 Introduction

1.1 Background

The United States Department of Energy founded the Generation IV International Forum (GIF) in the year 2000 to assess future energy needs and to improve nuclear energy technology. The GIF had four main objectives in mind in regards to nuclear power: sustainability, economic competitiveness, safety and reliability, and proliferation resistance and physical protection. The goal of sustainability aims to provide energy now that can be used indefinitely into the future. This encompasses areas such as waste management, resource utilization, transportation, and hydrogen production. The goal of economic competitiveness aims to make nuclear energy more financially attractive in comparison to other energy sources. This includes strategies such as reducing operating and capital cost through increased efficiency, design simplification, advances in fabrication and construction techniques, and standardization and modularization techniques. The goal of safety and reliability aims to remove the stigma surrounding nuclear energy and to provide safe living and operating conditions. Generation IV reactors plan on accomplishing this by the use of inherent safety features and designs. The goal of proliferation resistance and physical protection aims to make access to nuclear materials more secure in order to protect against unintentional and intentional threats to nuclear facilities. With these goals in mind, ten separate countries set out to tackle different nuclear reactor designs in order to accomplish the objectives set out by the GIF. The United States decided to focus on two priorities: develop the Next Generation Nuclear Plant (NGNP) Program in the mid-term, and develop a fast reactor to improve proliferation resistance in the long-term (Chapin et al., 2004). A subdivision of the NGNP was the Advanced Gas Reactor (AGR) Fuel Development Program. This program aimed to further advanced fabrication and

characterization technologies and conduct irradiation and safety performance testing for the licensing of TRISO particle fuel, which was meant for use in future high temperature gas reactors (HTGR) (Office of Nuclear Energy, 2009). While the NGNP no longer exists, TRISO fuel particle testing is still in continuation and is being sought after for use in future HTGRs. The HTGR design, using TRISO particles as its fuel source, is a promising solution to the United States commitments to the GIF.

1.11 HTGRs

HTGRs possess numerous qualities that differentiate them from other reactor types, including lower costs in the long run, a safer waste stream, inherent safety, proliferation resistance, and high performance characteristics that would enable nuclear to provide more energy to the future United States energy supply. These qualities are made possible by a few defining design and physical characteristics of the HTGR, such as helium coolant that has a high exit temperature, graphite moderated core, and TRISO particle fuel. The HTGR typically has a helium exit temperature in the range of 850°C to 900°C that provides a 40 to 48% thermal efficiency by the use of the recuperated Brayton cycle. HTGRs possess greater electrical generation efficiency for the same thermal power and reduced component complexity in comparison to light water reactors, reducing the large capital cost usually associated with the current nuclear plants. It should be noted, however, that the first generation of HGTRs will still be expensive and that the reduced price will only come into effect once a number of HTGRs have been built. The high temperature that leads to HTGR electric generation efficiency also maximizes burn up efficiency of the fuel, minimizing the nuclear waste stream. The HTGR is inherently safe through its graphite moderated cores characteristics, being that the graphite core conducts and absorbs away excessive core heat even if coolant is lost. This enables the HTGR to passively shut down if there is an accident. The

encapsulation of fuel in TRISO particles also makes the HTGR more proliferation resistant than other fuel forms. These performance characteristics maximize electrical generation efficiency and enable efficient thermochemical cycles for hydrogen production, providing a potential foot hold in the future United States energy grid for HTGR technology to thrive (Parma et al., 2003).

There are two main types of HTGR core design: prismatic core and pebble-bed core. In a prismatic block fuel assembly, the TRISO fuel particles are molded into cylindrical fuel compacts before being inserted into hexagonal graphite fuel elements, as seen in Fig.1 (Kallman, 2013). Isolated fuel and coolant holes are drilled into the graphite block with six fuel holes encompassing each coolant hole in a hexagonal formation. Pre-fabricated fuel compacts, around 12.5 mm-diameter by around 50 mm long contain the TRISO fuel particles in a close-packed array, mixed throughout a carbonaceous matrix. The fuel compacts are then arranged in the fuel holes (Verfondern et al., 2013).

Figure 1. From left to right: TRISO particles, fuel compacts, and graphite block matrix (IAEA, n.d.).

In a prismatic core, hexagonal moderator and fuel blocks are organized to form an inner graphite reflector, a center active fuel core, and an outer graphite reflector. In conjunction with the graphite components, the prismatic core also includes a side graphite reflector, vessel coolant channels, and a core barrel. A schematic of this set-up is shown in Fig.2. Helium and molten salts are the two most commonly used primary coolants in prismatic cores. The coolant enters the reactor core and flows up through the vessel coolant channels before flowing downward through the integral coolant channels in the fuel assemblies. This exposes the core barrel to the cooler inlet coolant, rather than the hotter outlet coolant, thereby reducing the operating temperature of the barrel material. Compared to a pebble-bed core, the integral coolant channels allow better core cooling, which in turn allows greater power density and total core power with prismatic block fuel (Kallman, 2013).

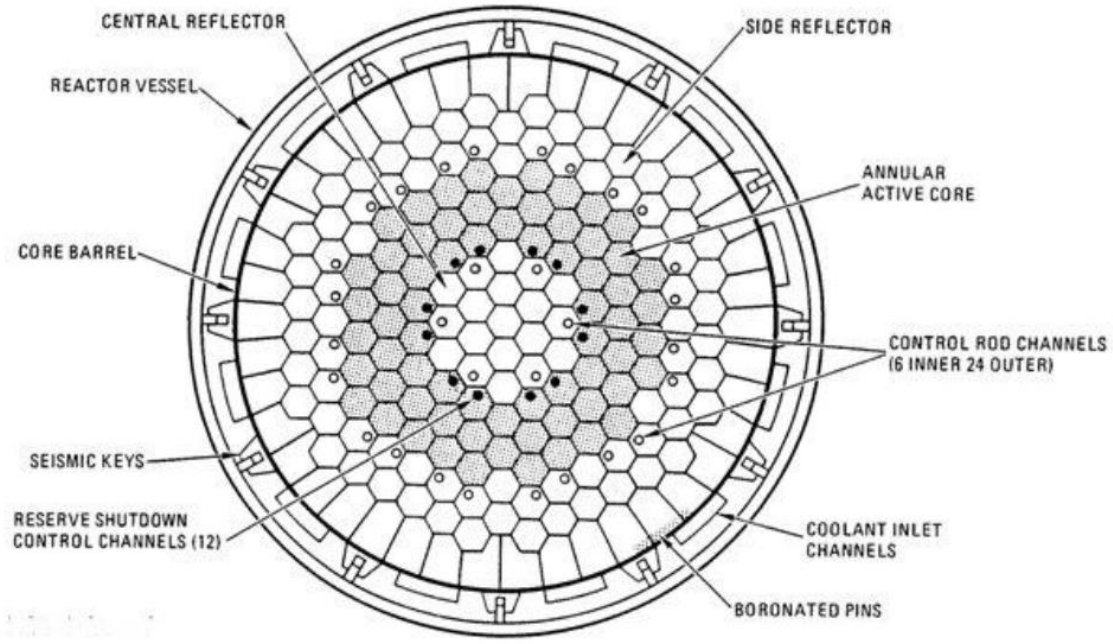

Figure 2. Diagram of prismatic reactor core assembly (IAEA, n.d.).

The prismatic core design was originally pursued in the United States of America, United Kingdom, and Japan. Today, the prismatic core continues development in the USA and Russia. Meanwhile, in Japan, the prismatic core design takes the form of a Pin-in-Block design with a different fuel configuration and coolant path (Verfondern et al., 2013). A diagram of The Gas Turbine – Modular Helium Reactor (GT-MHR), a joint project between the United States (General Atomics) and Russian Federation program, is shown in Fig.3 (Chapin et al., 2004).

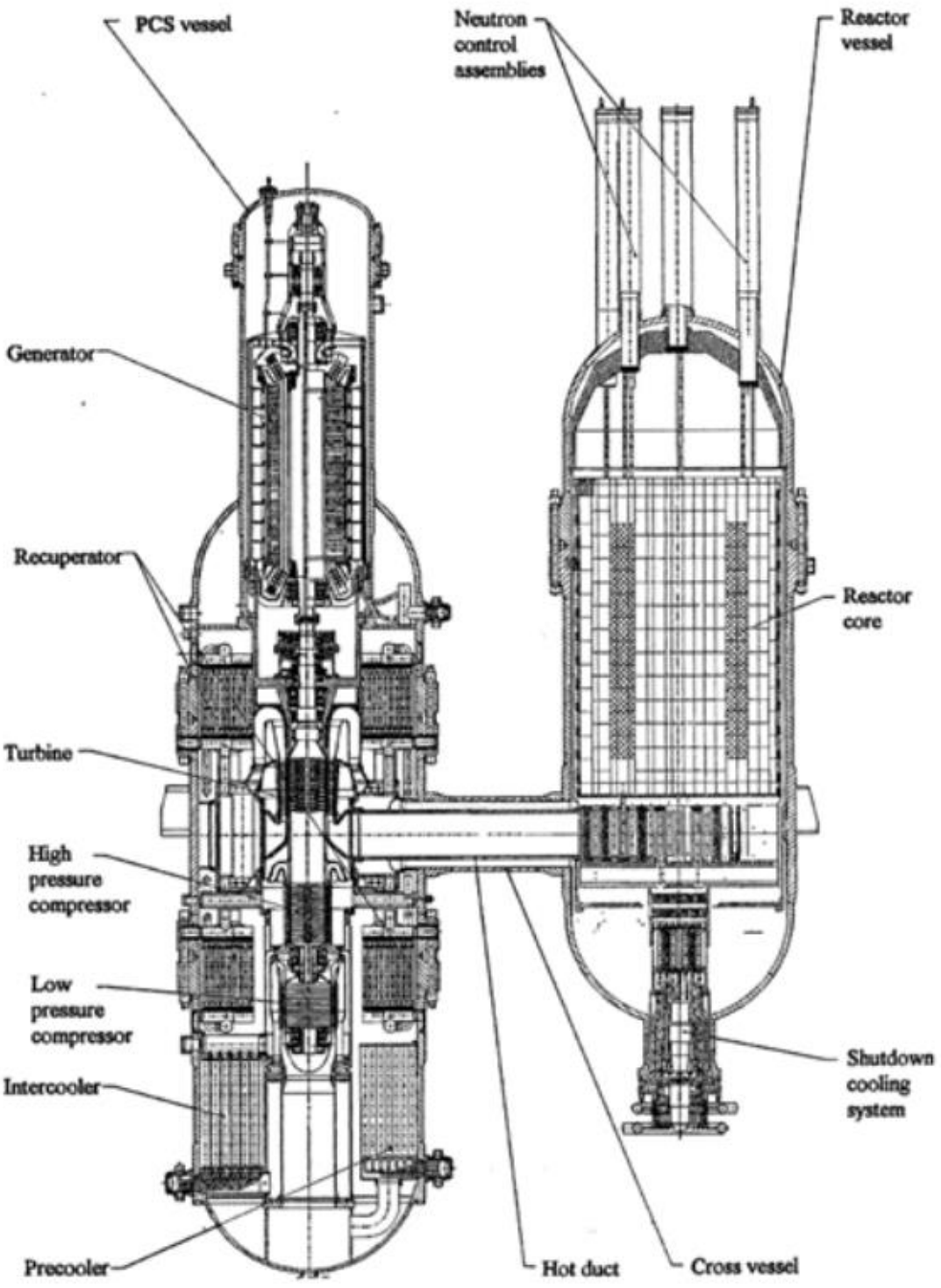

Figure 3. Schematic of The Gas Turbine – Modular Helium Reactor (GT-MHR) (Chapin et al., 2004).

In the pebble-bed reactor, spherical fuel elements approximately 60-mm in diameter are used and are referred to as fuel pebbles (as seen in Fig. 4). The pebbles are a two-part design, comprised of an inner fuel zone 50 mm in diameter encompassed by a 5 mm-thick shell of graphitized fuel matrix material. The inner fuel zone contains the TRISO particles and is homogenously dispersed within the graphitized matrix (Verfondern et al., 2013).

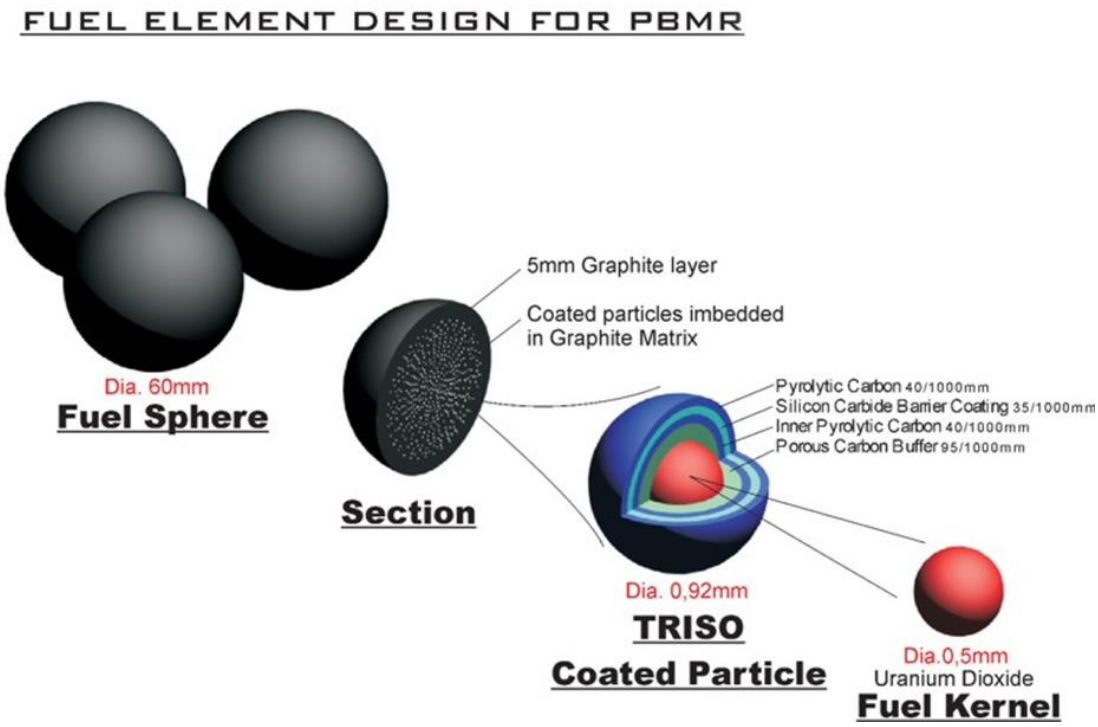

Figure 4. Components of a fuel pebble, descending in scale from left to right (PBMR, 2017).

The arrangement of the pebble-bed core is similar to the prismatic core, where prismatic fuel blocks in the active annular core region are replaced by mobile fuel pebbles. These pebbles constantly circulate downward through the core, driven by gravity (as seen in Fig. 5). The pebbles are taken from the bottom of the core, at which point their total burn-up is assessed. Active pebbles are returned to the top of the core, while spent pebbles are taken to storage/reprocessing. Much like in a prismatic core, the inner and outer reflectors in a pebble-bed core are constructed from

static moderator blocks. In the pebble design, either helium or molten salt coolant flows between the gaps of the pebbles (Kallman, 2013).

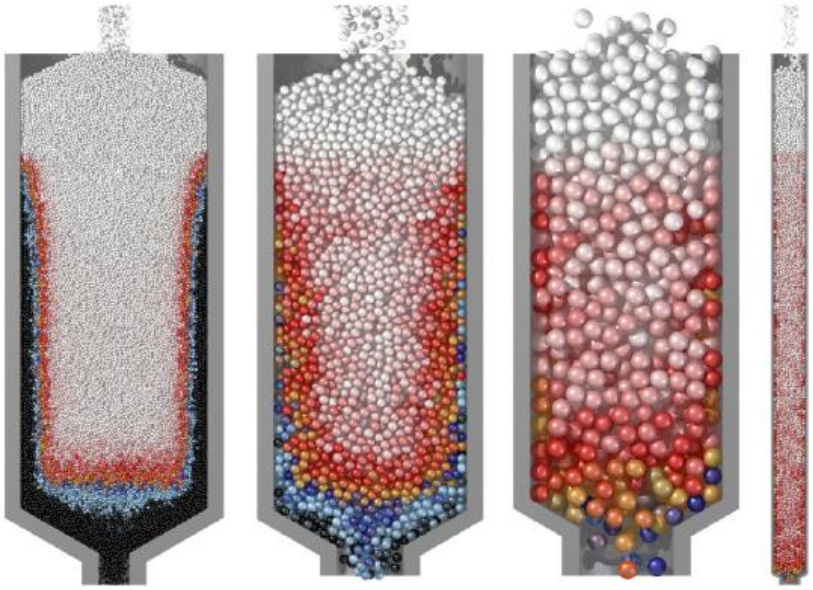

Figure 5. Visual of fuel pebbles in pebble-bed core. This particular diagram shows how varying fuel pebble sizes would arrange themselves in the core (Jiang et al., 2019).

The pebble bed concept was initially pursued in Germany, Russia, and South Africa, and today China is where the pebble-bed HTGR is being developed (Verfondern et al., 2013). A diagram of the HTR-10 reactor from Tsinghua University in China is shown in Fig. 6.

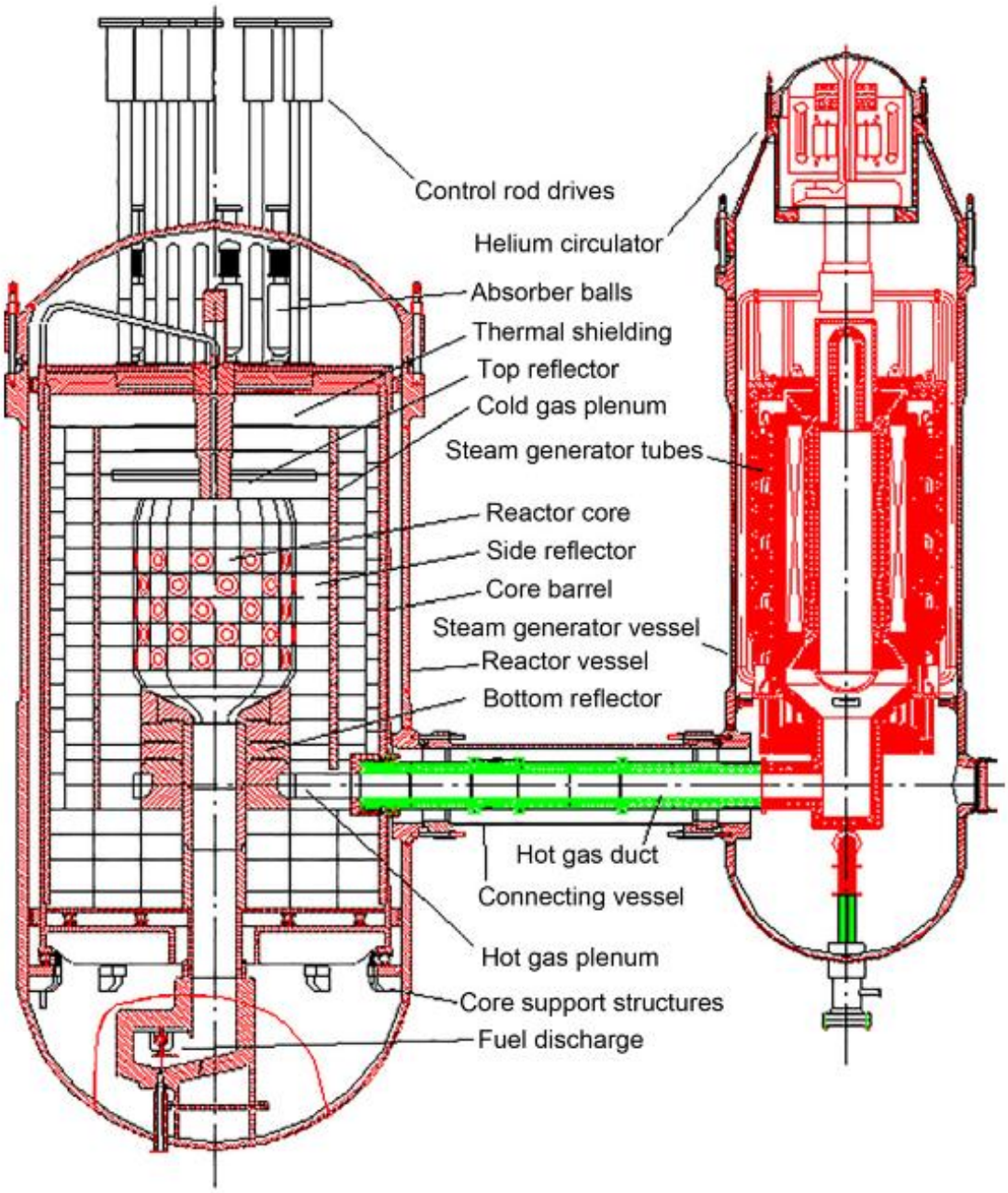

Figure 6. Schematic of the HTR-10 reactor from Tsinghua University in China (Jiang et al., 2019).

1.12 TRISO Particles

The TRISO particle is the primary fuel form used by current and future HTGR designs. The TRISO particle is ~1 mm in diameter and consists of a fuel kernel (UO_2, UCO, ThO_2, etc.)

surrounded by layers of various materials that serve to protect the TRISO particle and other layers and to contain fission products. The first layer is a low-density, porous pyrolytic carbon (PyC) layer, called the buffer, which provides void volume for the buildup of gaseous fission products freed from the fuel kernel. It also takes into account fuel kernel swelling, and serves as a sacrificial layer to mitigate fission fragments. The second layer is a high-density, isotropic PyC layer, named the inner PyC (IPyC) layer. The IPyC layer is a gas-tight layer that shields the fuel kernel from hot, gaseous chlorine compounds during the silicon carbide (SiC) layer deposition process and provides a smooth surface for SiC layer deposition. The IPyC also aids as a diffusion barrier for gaseous and metallic fission products. During irradiation it contracts, helping to reduce tensile stresses on the SiC layer. The third layer is an isotropic SiC layer which acts as the pressure bearing element of the TRISO particle and the main metallic fission product diffusion barrier (Verfondern et al., 2013). Fission products created from the fuel contain no free oxygen, which could otherwise aggravate chemical degradation of the ceramic SiC layer. The layer begins to lose its integrity above around 1600 °C, which signifies the limiting fuel temperature under accident conditions (Kallman, 2013). The fourth layer is a high density, isotropic PyC layer, called the outer PyC (OPyC) layer. This layer functions as the outermost diffusion barrier for gaseous and metallic fission products. Much like the IPyC layer, it contracts during irradiation. This property assists in reducing tensile stress on the SiC layer. The OPyC also shields the SiC layer during particle handling and pebble/compact creation, and offers a bonding surface for the over coating process (Verfondern et al., 2013). These particles are combined with graphite powder and binders before being shaped and formed into the final fuel element (Kallman, 2013). Fig. 7 and 8 depict the various layers contained within a TRISO particle.

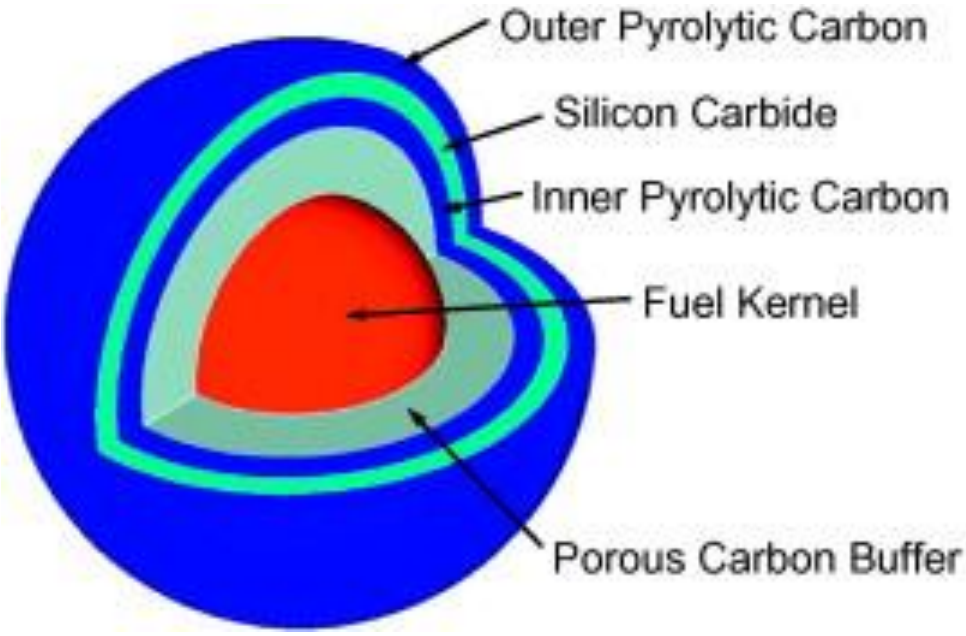

Figure 7. Illustration of the various layers of a TRISO particle (Hales et al., 2013).

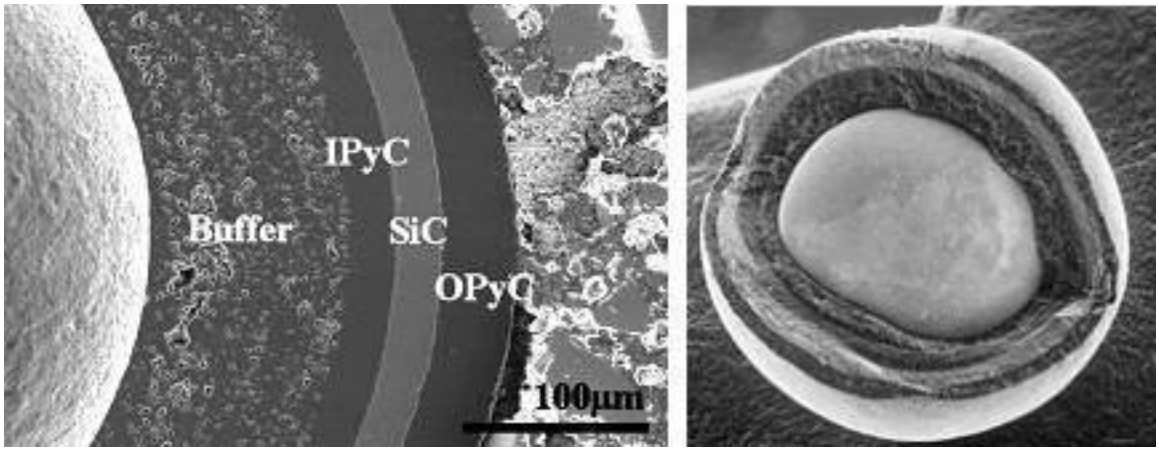

Figure 8. Scanning electron microscope (SEM) image of an exposed TRISO particle (Honorato, 2011).

According to Verfondern et al., "the conditions under which layer deposition takes place are very important as they determine the material properties of the coated particles formed. Parameters such as time, temperature, pressure, gas composition and gas ratios all play an

important role in fixing the coated particle properties." Therefore, understanding the process in which TRISO particles are formed is vital in understanding how TRISO particles will perform. TRISO particle kernels receive their four coating layers in a fluidized bed coating furnace in a procedure termed chemical vapor deposition (CVD). A flowchart for the coating process is shown in Fig. 9. The deposition gases in the furnace cause the kernels to float, where organic gases are designed to decompose and deposit at up to 1600°C. The films formed on the kernels are termed as pyrolytic, as they undergo pyrolysis of organic materials brought about by the high temperatures and form the carbonaceous layers on the TRISO particle. All the constituent layers formed in this process are deposited in an uninterrupted sequential process by the same fluidized bed coating furnace, as seen in Fig. 10 (Verfondern et al., 2013). Changing the parameters at any point in the CVD process will alter the final layer thickness for any of the four layers and will affect the final material properties of the TRISO particle.

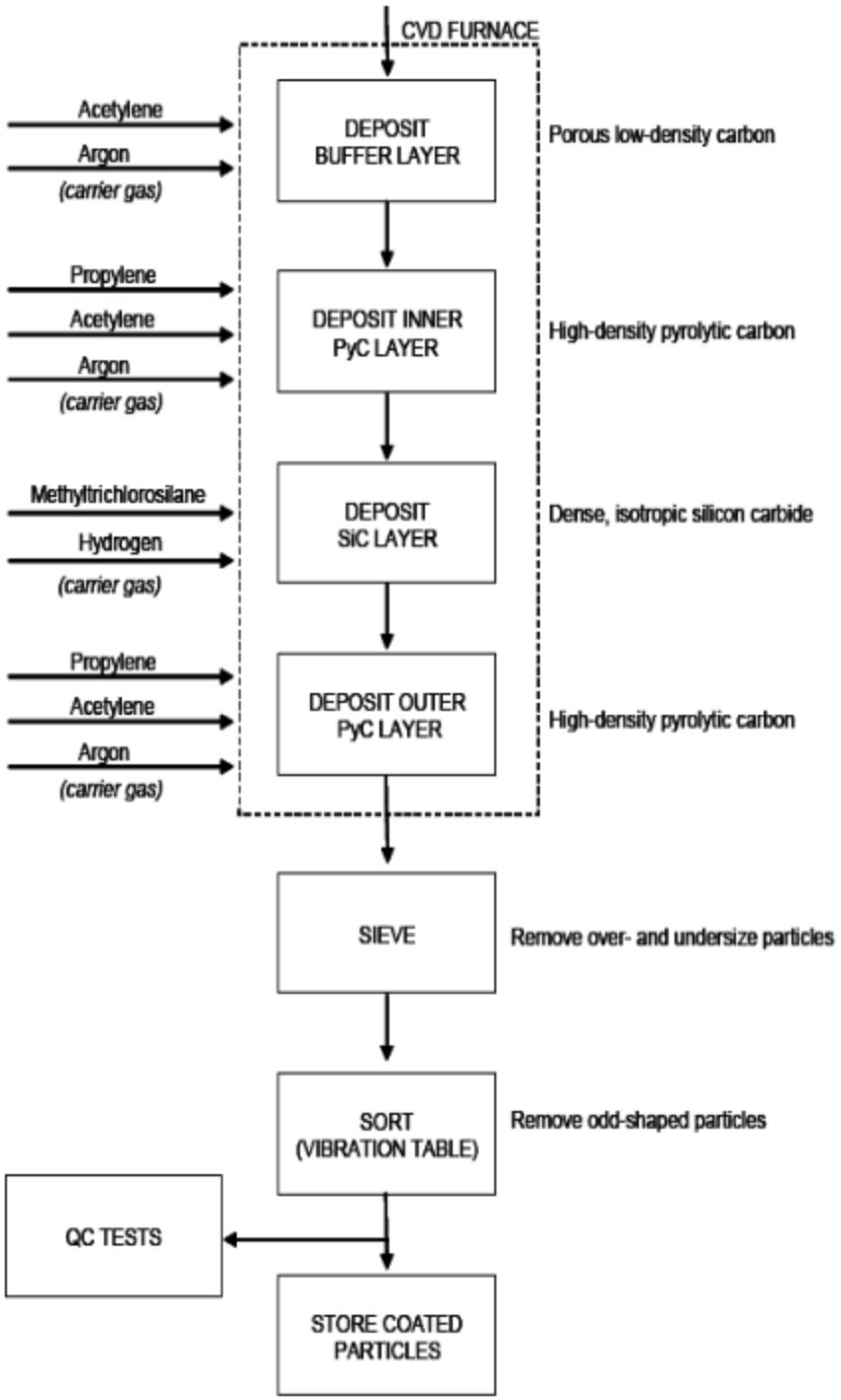

Figure 9. Various steps of the chemical vapor deposition process (Verfondern et al., 2013).

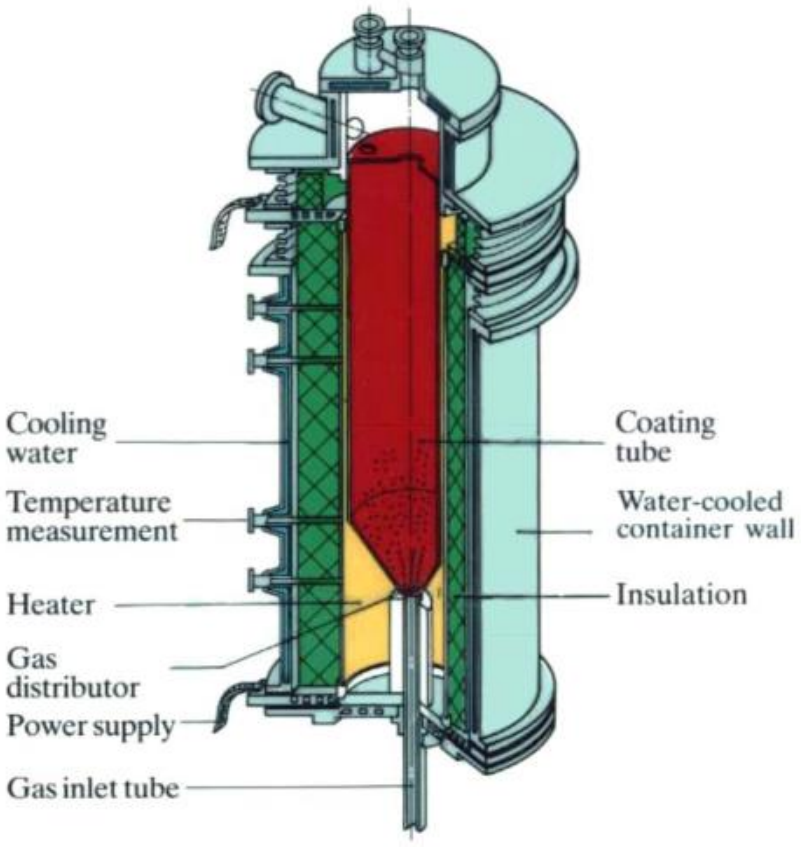

Figure 10. Illustration of a fluidized bed coating furnace (Verfondern et al., 2013).

TRISO fuel particles offer a very flexible fuel arrangement by fundamentally separating the cooling geometry and neutronic optimization of the fuel. The fuel assembly shape, core alignment, number of coolant channels, and packing fraction of fuel particles can all be changed independently for different power levels, outlet temperatures, and fuel cycles. The fuel flexibility can encompass different fuel cycles, such as a closed fuel cycle with a fast or thermal neutron spectrum. However, the current SiC layer in TRISO fuel particles has increased vulnerability to fission product release under the fast neutron conditions shown in the U-Pu closed fuel cycle. TRISO fuel particles possess other inherent advantages within reactor cores. With each fuel particle being able to retain its own fission products, it results in very little radioactive release

during operation. Furthermore, the carbide layers retain fission products even after the operational lifetime of the fuel is over. TRISO fuel particles embody an ideal final waste form, if they can be disconnected from the large amounts low-level radioactive graphite waste. Because of this, TRISO fuel may also require less overpacking than traditional LWR fuel, reducing the total amount of repository space needed (Kallman, 2013). All these characteristics demonstrated by the TRISO particle help support the HTGR in being an attractive candidate for the NGNP program.

1.13 IPyC and Buffer Carbon

The mechanical and physical properties of the IPyC and buffer carbon layers are the focus of this thesis work are very important when determining the material properties and structural integrity of TRISO particle fuel. As mentioned in the TRISO particle section, the parameters surrounding the chemical vapor deposition process can affect the performance of the IPyC layer. In particular, the deposition temperature and coating gas fraction (acetylene-propylene ratio) greatly affected the measured properties of IPyC. This was found in a study done by Hunn & Lowden, where polished cross-sections of TRISO particle layers were viewed under an ellipsometry microscope to determine the average diattenuation and thus anisotropy of the IPyC layer. A plot of this diattenuation can be viewed in Fig. 11.

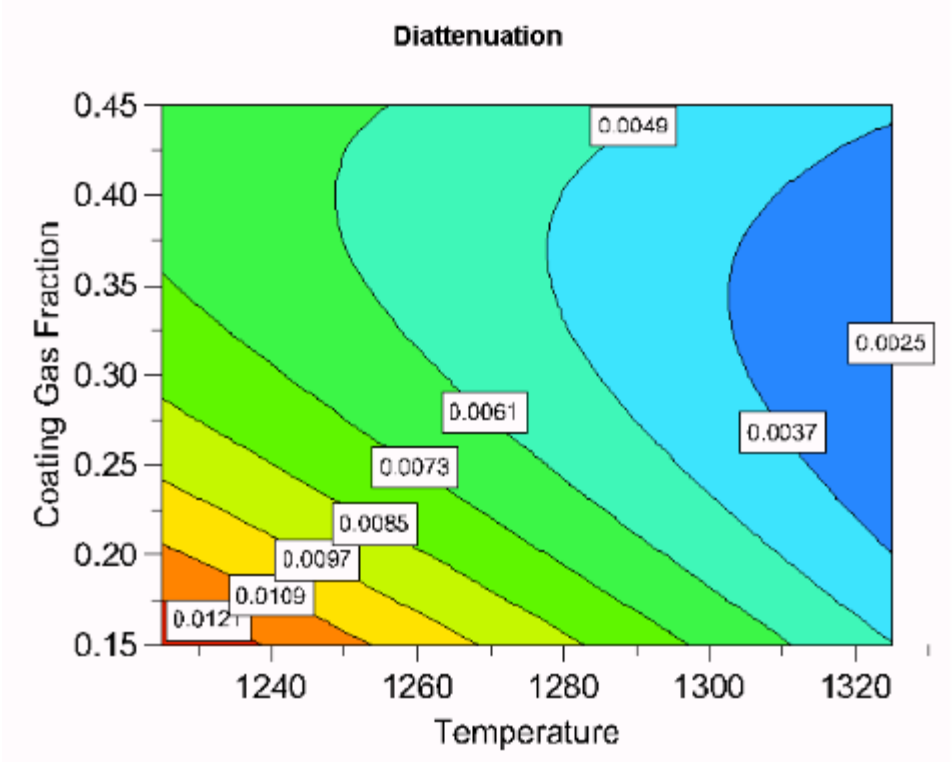

Figure 11. Plot of diattenuation that shows the dependence on both coating temperature and coating gas fraction (Hunn & Lowden, n.d.).

Variance in the diattenuation (and thus variance in isotropic configuration) of the IPyC layer can have important physical repercussions. The inner and outer pyrolytic carbon layers support and stabilize the SiC layer by introducing additional compressive force through carbon coating shrinkage during neutron irradiation. This force acts against the tensile stress imposed by internal pressure buildup from fission products. However, it has been shown that excessive contraction of the PyC layers can lead to cracking which can devolve into a failure of the whole TRISO particle layer assembly. Neutron irradiation favors contraction along graphene planes but expansion perpendicular to these planes, so TRISO particles with higher abundance of anisotropic graphene planes (single preferred orientation) will experience much higher carbon coating shrinkage than TRISO particles with primarily isotropic graphene planes (random orientation)

(López-Honorato et al., 2010). TRISO particles with the highest abundance of isotropic graphene planes will be the most structurally sound. Therefore, it is important to control the coating temperature and coating gas fraction to facilitate the production of isotropic graphene planes in the chemical vapor deposition process. A visualization of the differences between anisotropic and isotropic pyrolytic carbon can be seen in Fig. 12.

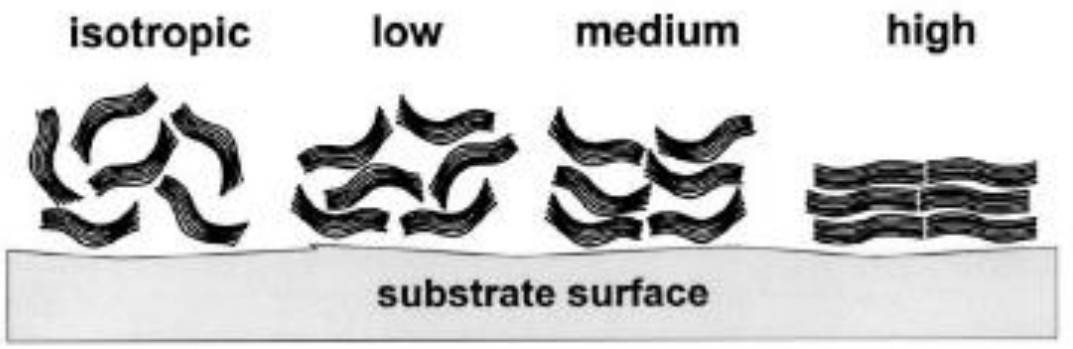

Figure 12. Differences in physical structure between isotropic and anisotropic pyrolytic carbon. Individual illustrations become more anisotropic from left to right (Reznik & Hüttinger, 2002).

The buffer carbon layer is important in the fission product transport properties of TRISO particles. The buffer layer is composed of porous pyrolytic carbon and acts as a void volume to absorb fission gases, fission recoils, and swelling of the fuel kernel. During irradiation the porosity of the buffer carbon layer can become altered and the layer can undergo densification and contraction. This can lead to tangential stresses that cause the buffer to crack. The buffer layer also has the lowest thermal conductivity of all the layers in the TRISO particle, due to its high porosity. Irradiation can cause the buffers thermal conductivity to change over time and produce a temperature gradient within the layer that can cause Soret fission product diffusion to occur (NRC, n.d.). Buffer densification can also lead to reduced buffer layer thickness, causing the buffer and IPyC layers to delaminate from each other and create a gap between the two layers (Bower et al.,

2017). Fig. 13 displays both buffer cracking due to kernel swelling and delamination of the buffer and IPyC layers.

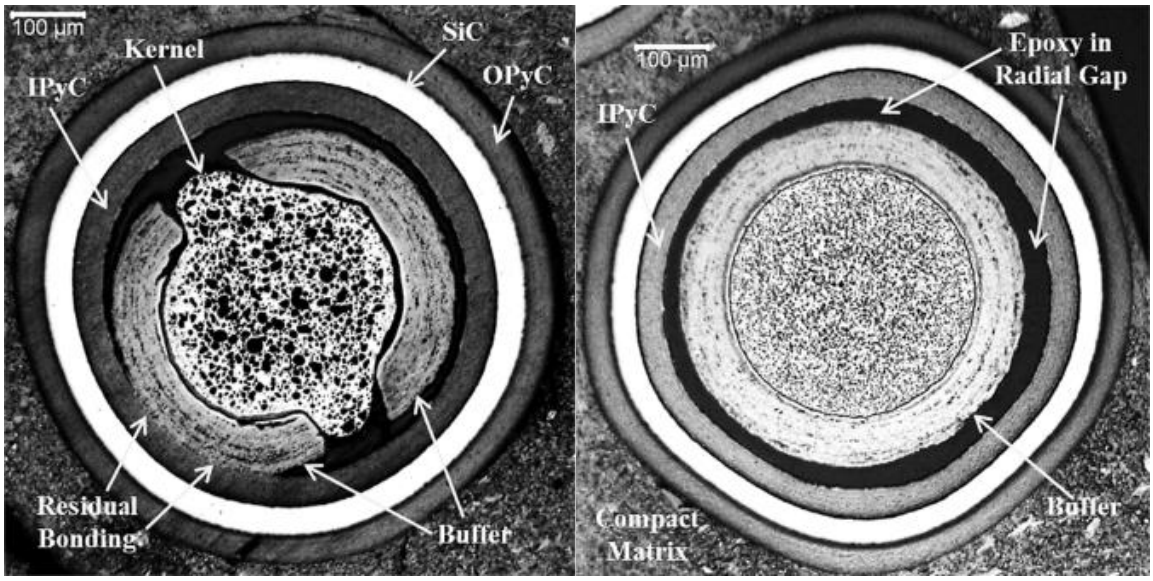

Figure 13. Left, buffer cracking due to kernel swelling. Right, delamination of IPyC and buffer layer. Buffer densification is present in both cases (Bower et al., 2017).

1.2 Objective

TRISO particle layers are currently modeled as one unit, rather than individual layers and their constituent parts. This leads to a recognized gap in the knowledge base regarding the characteristics of individual layers and interlayer bonds of TRISO particles, with special interest in the buffer, IPyC, and buffer-IPyC interface. As demonstrated in Fig. 13, buffer-IPyC interface strength is an important parameter in regards to failure prediction, failure prevention, and modeling of future TRISO particles. The objective of this thesis is to develop a new capability that enables micrometer scale strength characterization of the buffer, IPyC, and buffer-IPyC interface of

TRISO particles. The technique developed in this work can then be compared to results of other characterization techniques and made available to other researchers for future testing.

2.0 Literature Review

2.1 TRISO Particle Layer Mechanical Strength Testing

This section references the body of knowledge obtained through the work of other researchers thus far in regards to the mechanical strength of the various layers of TRISO particles. Most of the research done thus far focuses on the SiC layer rather than the buffer and IPyC layers, leaving an opportunity to explore the properties of the buffer and IPyC layers. This section is organized by characterization technique to correlate the variance in results in respect to which technique was used.

2.11 Nanoindentation

Nanoindentation is a useful materials characterizing technique and can be used to study the mechanical properties of TRISO particles. The most common use of nanoindentation is a measurement of mechanical properties such as modulus and hardness of materials in different shapes, sizes, and scales. The technique is applicable to a variety of materials differing over a large range of hardness and does not require extensive sample preparation. The two main variables of nanoindentation testing are load and depth. The load is the amount of force exerted on the nanoindentation instrument, while depth is the distance moved by the instrument. Nanoindentation probes come in a variety of shapes, such as spherical for stress-strain, Berkovich for elasticity and height, flat punch for complex modulus, wedge for three-point bending, spherical cone for scratch measurements, and cube corner for fracture toughness. The process of nanoindentation involves

multiple steps. The first step involves an actuation process to apply a load. The instrument senses the displacement and then makes adjustments accordingly. These adjustments are used to calibrate the frame stiffness, which can be used to calculate the elastic, viscoelastic, and soft material properties. This process is also rate dependent, temperature dependent, and plasticity dependent. The depth of penetration during this process helps define the area of the tip in contact during indentation, which determines hardness. When combining the stiffness obtained from displacement adjustments and the hardness obtained from the surface area of the indentation tip, the reduced modulus of the system can be calculated (Nanoscience Instruments, 2021). Fig. 14 illustrates a common load-displacement diagram, the geometry of the indentation procedure, and the equations for hardness (H) and reduced elastic modulus (E_r). Hardness is defined as the maximal indentation load (P_{max}) over the projected contact area at maximal indentation load (A_c). A_c can be deduced by multiplying the contact depth (h_c) by the indenter geometry variable (f), where f is dependent on the indenter type being used. When determining reduced elastic modulus (E_r), stiffness (S) and the indenter geometry constant β also need to be taken into consideration. Stiffness is calculated by taking the derivative of the tangent line to the unloading curve at the point of P_{max} (NanoScan, 2018).

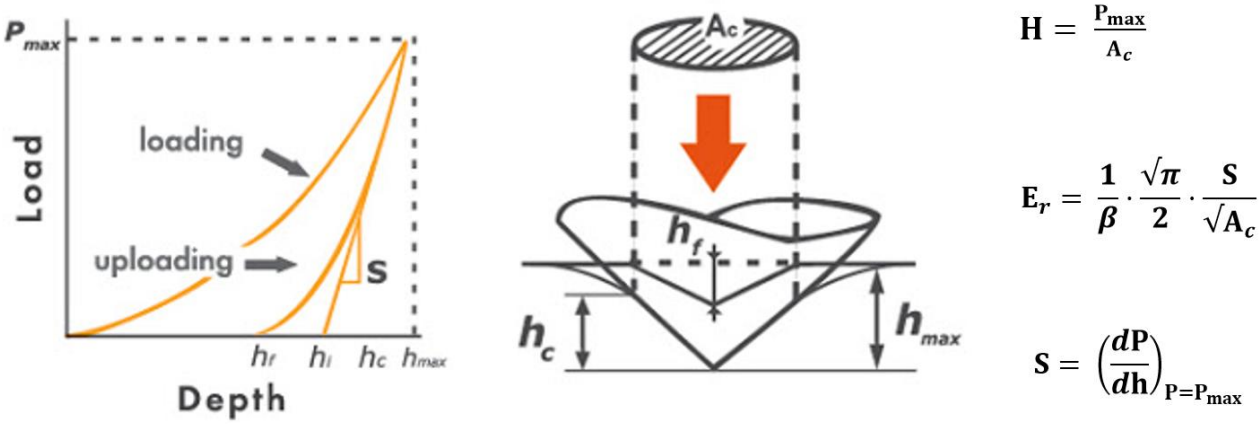

Figure 14. Illustration of the indentation procedure accompanied by the equations for hardness (H) and reduced elastic modulus (E_r) (NanoScan, 2018).

The studies done by López-Honorato et al., Van Rooyen et al., Rohbeck & Xiao, and Bellan & Dhers demonstrate good work in respect to nanoindentation for TRISO particle layers. In the study done by López-Honorato et al., nanoindentation was used to determine the Young's modulus of the IPyC layer in the given TRISO particle. The measurement proved that the Young's modulus of the IPyC layer decreased after SiC deposition. This observation was in line with other studies, which showed that a similar change occurred after SiC deposition in which the Young's modulus changed from 29 to 18 GPa (López-Honorato et al., 2010).

In the study done by Van Rooyen et al., the hardness of the SiC layer in the sample TRISO particle was measured using a CSM Nano-indentation Hardness tester. A load of 100 mN was applied to the polished cross-section pieces of the SiC equator for 15 seconds before unloading. All measurements were conducted on a single particle but at three different locations, leading to a total of 27 measurements per batch. The measured Nano-Indentation hardness for batches D and E from the experiment are shown in MPa in Fig. 15, with values ranging from around 27 to 35

GPa. While this study focused on forming relationships between grain size and hardness, the hardness values obtained in this study offer valuable information in regards to measuring the mechanical properties of TRISO particle layers (I. J. van Rooyen et al., 2012).

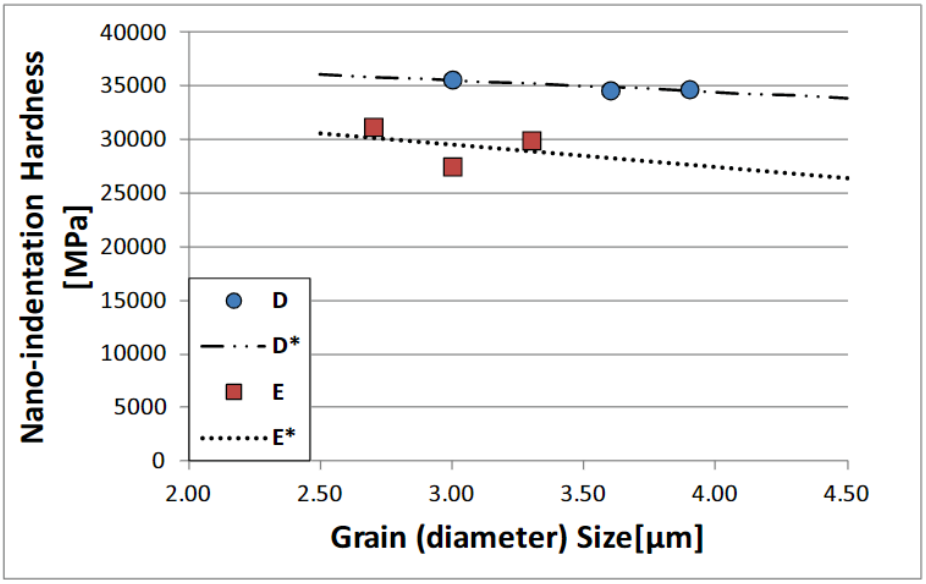

Figure 15. Measured Nano-Indentation hardness of the SiC layer for batches D and E from study done by Van Rooyen et al.

In the study done by Rohbeck & Xiao, hardness values were obtained for the SiC layer using a Nanoin-denter XP (MTS systems) and the elevated temperature measurements were performed using a MicroMaterials (UK) system. The maximum load applied to the polished cross-section of the TRISO particles was 100 mN for the MTS system or 500 nm for the UK system. The diamond indenter used was of Berkovich shape. The values obtained in this study are comparable to prior nanoindentation studies, and the hardness ranging from 30 to more than 40 GPa (see Fig. 16). With this study providing the hardness values over a large range of temperatures,

it provides comprehensive information with regards to the SiC layer in TRISO particles (Rohbeck & Xiao, 2016).

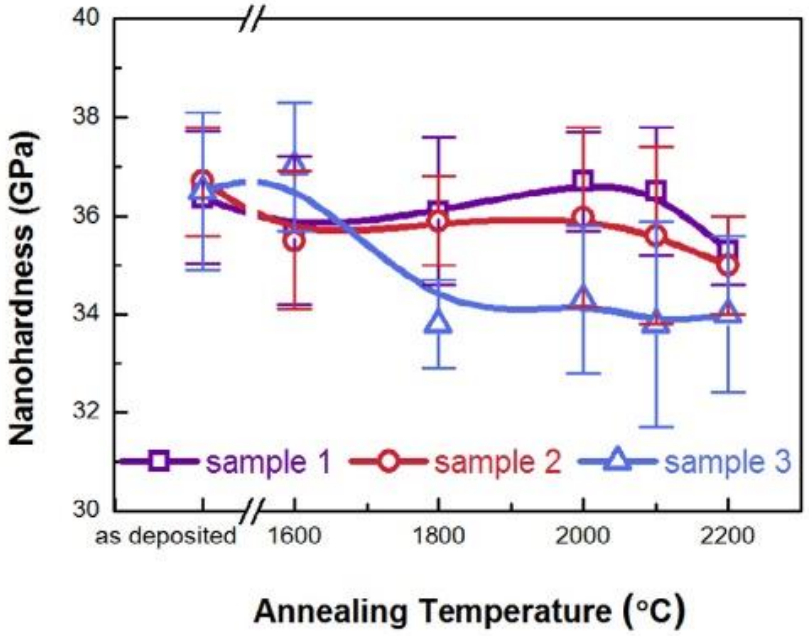

Figure 16. The nanohardness values of the SiC layer at various temperatures (Rohbeck & Xiao, 2016).

The study done by Bellan and Dhers determined the elastic modulus of SiC and PyC deposited by way of fluidized bed chemical vapor deposition (FBCVD) onto flat substrates. Nanoindentation tests done in the study unveiled an average elastic modulus of 25.5±2 GPa for the pyrocarbon substrates. This value was compared to other tests done in the same study by the impulse excitation method, which uncovered a value of between 28.9 and 30.8 GPa for the pyrocarbon substrates. The final conclusion of Bellan and Dhers was that while the nanoindentation technique is highly reproducible and simple to perform, it is not the most accurate method for determining elastic modulus (Bellan & Dhers, 2004).

2.12 Vickers Indentation Fracture Toughness

Vickers indentation tests are used to determine fracture toughness of brittle materials and have been used on TRISO particles before. In the past, methods such as Chevron notch bar, single-edge notch beam, single-edge V-notched beam, single edge pre-cracked beam, edge-loaded split, and double cantilever beam have been used for brittle material characterization. Most of these methods, however, are difficult to implement and are not practical. Vickers indentation solves this problem by evaluating small cracks created in the material by the test, thus simplifying the technical aspect. Vickers indentation was first developed by Palmqvist and has three primary techniques: the first involves Palmqvist cracks with half-ellipse sub-structure, the second is based on half-penny or median cracks, and the third is based on a curve fitting technique. A model of the first two techniques is demonstrated in Fig. 17, while the third technique involves specific curve fitting equations. In the model shown below, l is defined as the length from the center of the indentation to the end of the crack, a is radius of the indentation, and c is the sum of l and a. Typically, if $c/a \geq 2$ then the half-penny crack model will be used and if $c/a < 2$ the Palmqvist model will be used. Once these techniques are applied to a given crack on a material, the hardness of the material can be derived (Moradkhani et al., 2013).

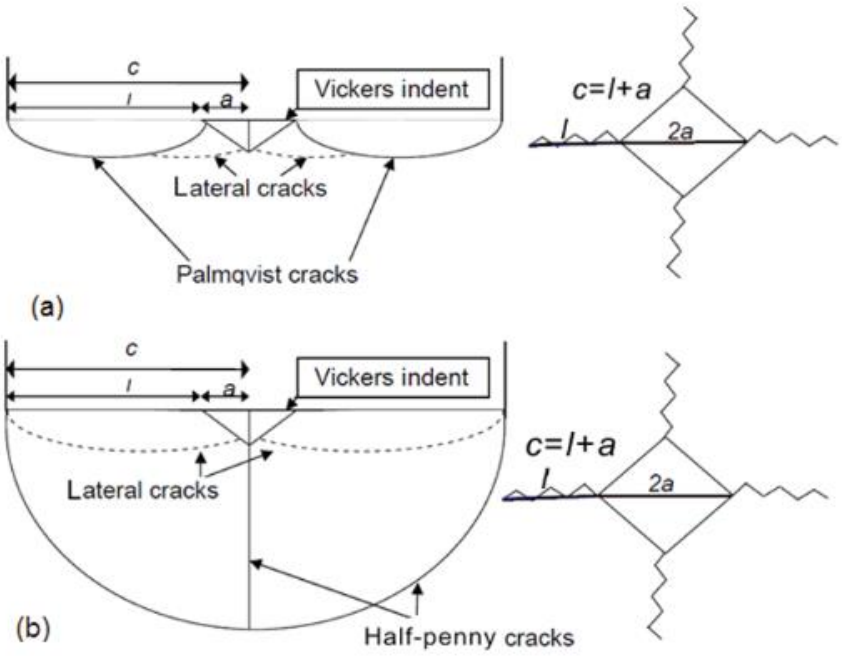

Figure 17. Model of first two Vickers indentation determination techniques pioneered by Palmqvist. The diagram in figure (a) illustrates the technique used when there are Palmqvist cracks with half-ellipse sub-structure and the diagram in figure (b) illustraties the technique used when there are half-penny or median shaped cracks (Moradkhani et al., 2013).

In the study done by Zhang et al. the Vickers indentation fracture toughness is determined for three different types of SiC coatings in TRISO particles. Fig. 18 shows the crack morphology observed in the SiC layer with an extra-Si coating applied to the sample. The Vickers indentation fracture toughness observed for the three different types of SiC coatings in this study ranged between 3.5 and 4.9 $MPa \cdot m^{1/2}$. These results have demonstrated that the Vickers indentation fracture toughness is influenced by the microstructure and non-stoichiometry of SiC coatings (Zhang et al., 2012).

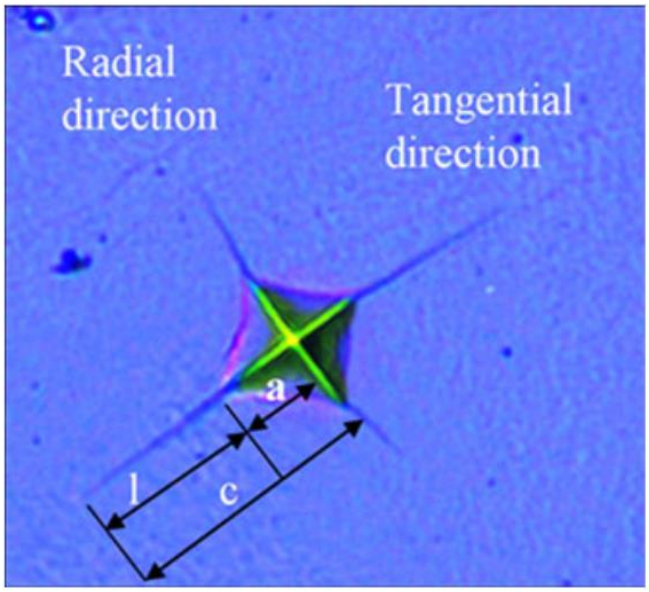

Figure 18. Visual of a Vickers indent in a SiC coated sample (Zhang et al., 2012).

2.13 Compression/Crush Testing

The studies of many research teams have uncovered valuable information in respect to compression/crush testing for TRISO particle layers. An important study to note is one done by Van Rooyen et al., which successfully conducted compression tests on full TRISO particles by crushing them in between anvils of varying materials. While the load required for fracture of the TRISO particles remained nearly the same between hard and soft anvils, the study found that hard anvils cause high local contact bending stresses at the point of contact while soft anvils cause tensile stresses to develop along the latitudinal direction of the TRISO particle. These tensile stresses lead to the development of cracks at right angles to the stress, giving insights into how much internal pressure can be applied for fracture. This led to the conclusion that soft anvils are better for crush testing than hard anvils. The final results of using this crushing technique yielded an average fracture strength of 935 MPa in batch A of the TRISO particles. This value includes all

layers of the TRISO particle, including the zirconia kernels, SiC layer, and PyC layers, so a direct comparison to individual layers is not possible (G. T. van Rooyen et al., n.d.). An illustration of the crushing apparatus is shown below in Fig. 19.

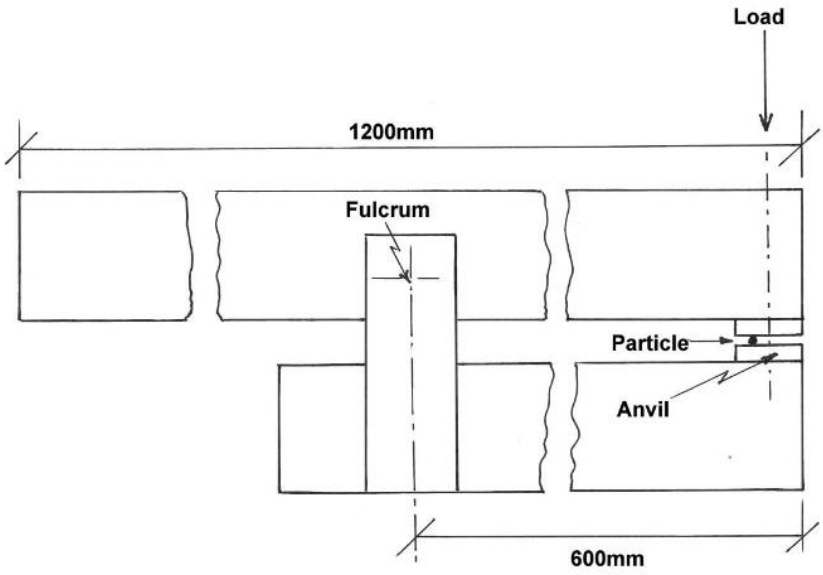

Figure 19. Illustration of crushing apparatus used by Van Rooyen et al. (G. T. van Rooyen et al., n.d.).

Another style of compression testing, the ring crush test, is similar to micro cantilever and nanoindentation testing and involves creating a ring shape out of the desired material and pressing until fracture. Fig. 20 illustrates a sample preparation technique developed by Frazer et al. for creating a ring style TRISO particle specimen for crush testing, while Fig. 21 demonstrates how samples of this type are loaded into the crushing anvil (Byun et al., 2008). While this technique has only been used to assess the SiC layer, it still provides valuable insight that can be used for future testing of the PyC layers.

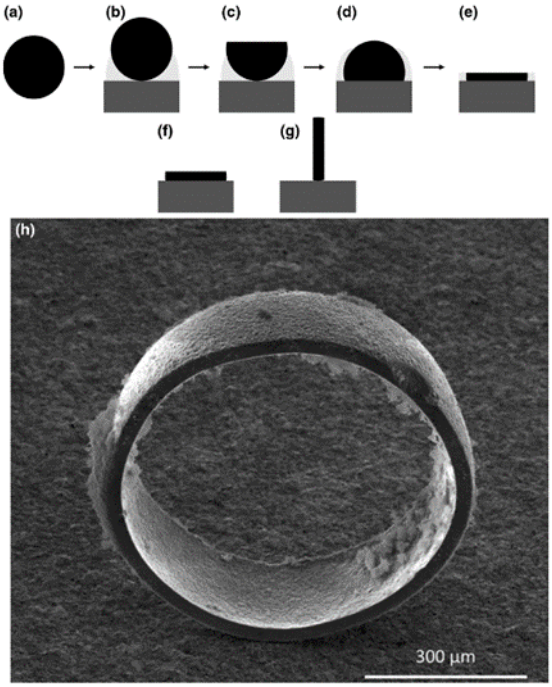

Figure 20. Diagram of ring style TRISO particle sample preparation for ring crush test (Frazer et al., 2017).

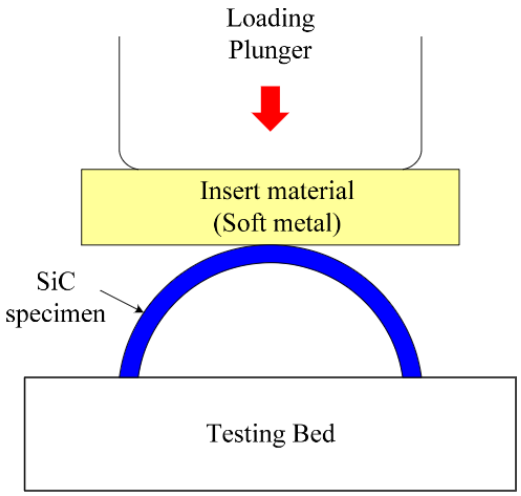

Figure 21. Crushing anvil set-up (Byun et al., 2008).

In the study done by Frazer et al. nanoindentation measurements are compared to ring crush tests of the SiC layer in TRISO particles. The study found the two technique styles may be correlated to each other, as seen in Fig. 22. The values derived from this study ranged from around 350 GPa to over 500 GPa for the SiC layer, which is in agreement with other studies of this sort (Frazer et al., 2017).

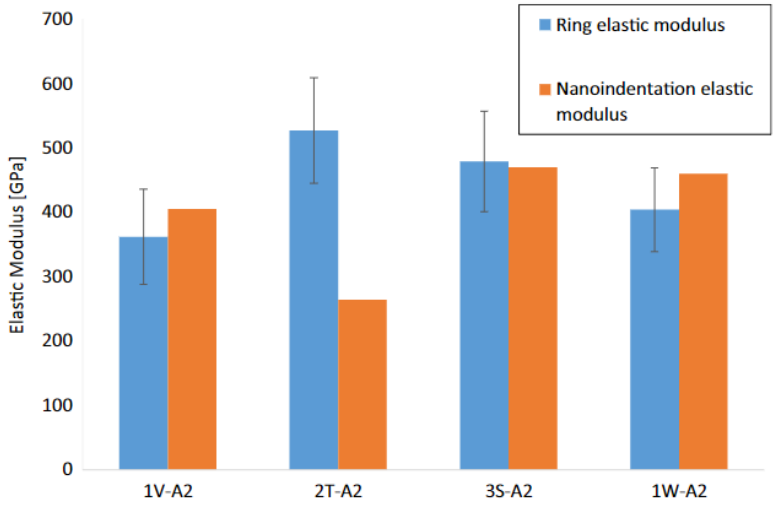

Figure 22. Test results from Frazer et al. that may lead to a correlation between nanoindentation and ring crush test techniques when applied to the SiC layer of a TRISO particle.

In the study done by Byun et al., a customized ring crushing technique utilizing a brass blanket foil at load transfer and contact (as seen previously in Fig. 21) was used to identify the fracture stress of a hemispherical SiC shell specimen. This SiC shell specimen was intended to imitate the SiC layer in TRISO particles. Final results indicate that the mean fracture stress varied between 330 and 650 MPa in the test material, as can be seen in Fig. 23 below (Byun et al., 2010).

Table II. Summary of Measured and Calculated Parameters (Data are Mean Values Except for the *m* Values and Scaling Factors for Size Effect)

Material ID	$2r_0$ (mm)	F (N)	m	σ_f^L (MPa)	Scaling factor for Size effect	σ_f^F (MPa)
DUN500S-14B	0.118	2.59	6.61	997.2	2.22	449.8
DUN500S-6B	0.125	3.60	5.49	1050.5	2.57	409.6
DUN500S-7B	0.142	5.32	7.25	1001.5	1.95	514.7
AGR-06	0.147	5.84	6.22	1016.3	2.14	475.4
AGR-10	0.113	4.20	6.40	1232.0	2.16	570.7
LEU01-46T	0.153	11.36	3.98	1203.3	3.02	399.1
LEU01-49T	0.141	8.64	6.35	1324.2	2.05	646.5
B&W-93059	0.151	6.47	6.58	923.1	1.99	463.9
B&W-93060	0.167	6.97	5.15	769.5	2.33	329.9

Figure 23. Table of values linking fracture stress to test specimen as seen in study done by Byun et al.

In the study done by Rohbeck & Xiao, elastic modulus values for the SiC layer in numerous TRISO particles were obtained by averaging the values of a minimum of 30 samples per batch and temperature conditions in a series of modified crush tests. The elastic modulus found in this study ranged from 200 to 400 GPa, as seen in Fig. 24. With this study providing the elastic modulus values over a large range of temperatures, it provides comprehensive information in regards to the SiC layer in TRISO particles (Rohbeck & Xiao, 2016).

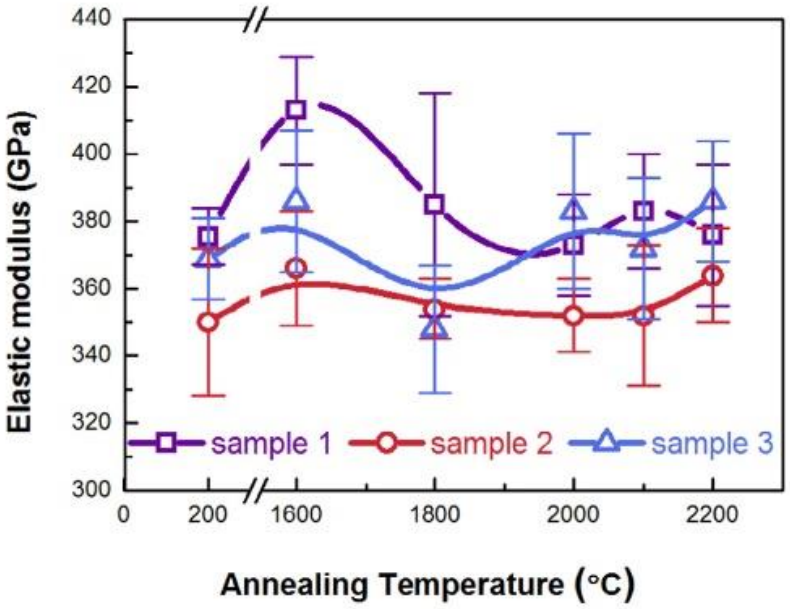

Figure 24. The elastic modulus values of the SiC layer at various temperatures (Rohbeck & Xiao, 2016).

Micro-pillar compression testing is another compression testing technique that has gained popularity in recent years. This technique involves the fabrication of a microscopic column from the desired material and then performing compression tests on the column. This technique primarily reveals the debond sheer strength and internal friction coefficient of the material. A free body diagram showing the stresses involved in micro-pillar compression testing from the work done by Shih et al. is shown in Fig. 25. The study done by Shih et al. was one of the first studies to use this technique. This study fabricated eight micro-pillar samples from inclined fiber/matrix interfaces that contained a SiC fiber reinforced SiC matrix composite. The SiC fiber was 11 ± 2 μm thick and was coated with five alternating layers consisting of 50-nm of pyrolytic carbon and 1 μm of SiC. These mini composites were then cut with a diamond saw and embedded in epoxy at 45°, 55°, and 60° angles. These pillars were further refined with a low beam current from a FIB to produce 3.5 μm diameter, 15 μm long micro-pillars. These pillars were compressed with a MTS

Nano XP indenter using a flat indenter tip. A diagram of the pillar geometry is shown in Fig. 26. Observing the compression of the micro-pillars showed that debonding occurred at the top fiber/pyrocarbon interface. The debonding shear stress and internal friction coefficient of the SiC fiber/pyrocarbon interface was observed to be 100.3 MPa and 0.73, respectively. This test determined that interfacial properties are important for characterizing the physical properties of fiber composites, which is useful in characterizing the ceramic materials contained within TRISO particle (Shih et al., 2013).

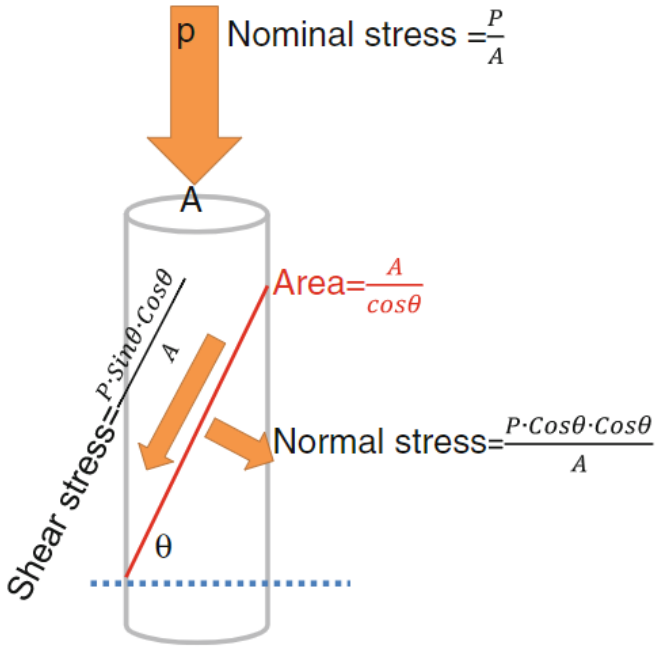

Figure 25. Forces involved in the micro-pillar compression technique (Shih et al., 2013).

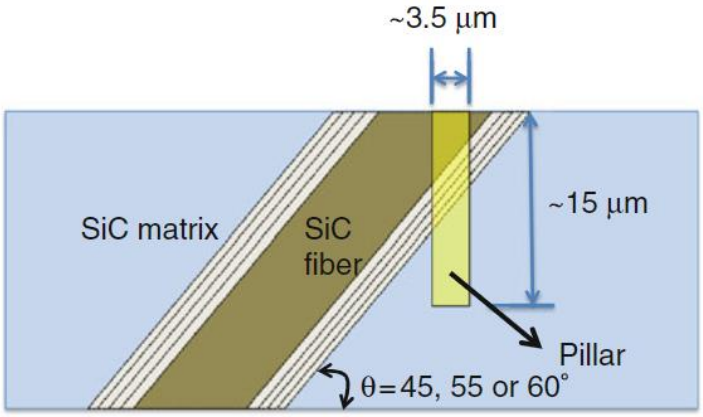

Figure 26. Illustration of final micro-pillar geometry (Shih et al., 2013).

2.14 Micro-Cantilever Beam Testing

Micro-cantilever beam testing is a scaled-down version of its macroscopic counterpart and adheres to all the same basic principles. This technique has been used for array of different materials, but is especially useful in characterizing the properties of thin films because it mitigates a lot of the shortcomings of other testing techniques (Maio & Roberts, 2005). The study done by Deng & Barnoush was pioneering in this field and demonstrates the proof of concept very well, albeit for an FeAl intermetallic alloy rather than a ceramic material. An image of the experimental micro-cantilever beam with starting notch and the final torn micro-cantilever are shown in Fig. 27 and 28. This study verified that micro-cantilever beam testing is a feasible mechanical testing technique that can be used on microscopic structures. While this technique has been used on ceramic materials such as quartz (Žagar et al., 2016) and SiC (Frazer et al., 2015), there is limited knowledge of this technique being used on PyC.

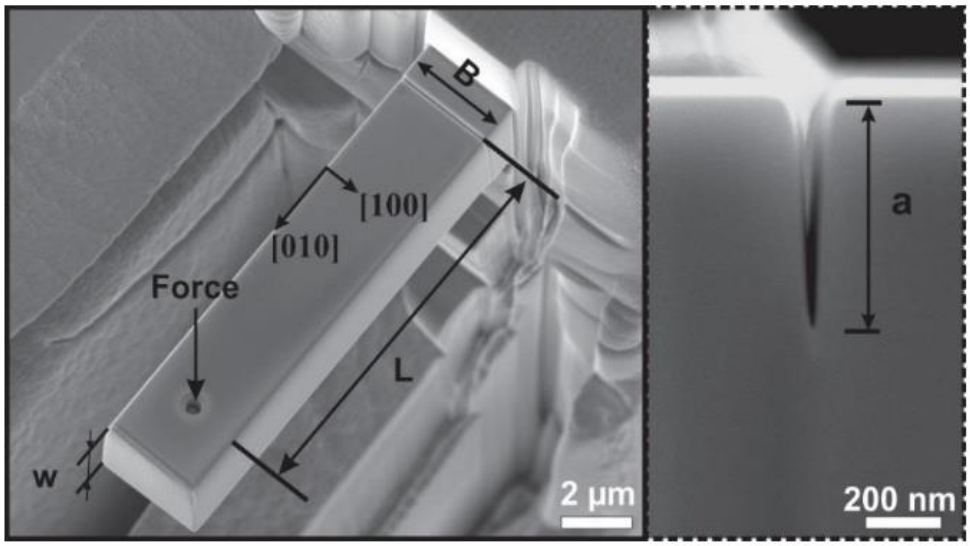

Figure 27. Image of a micro-cantilever beam to the left, closer inspection of starting notch to the right (Deng & Barnoush, n.d.).

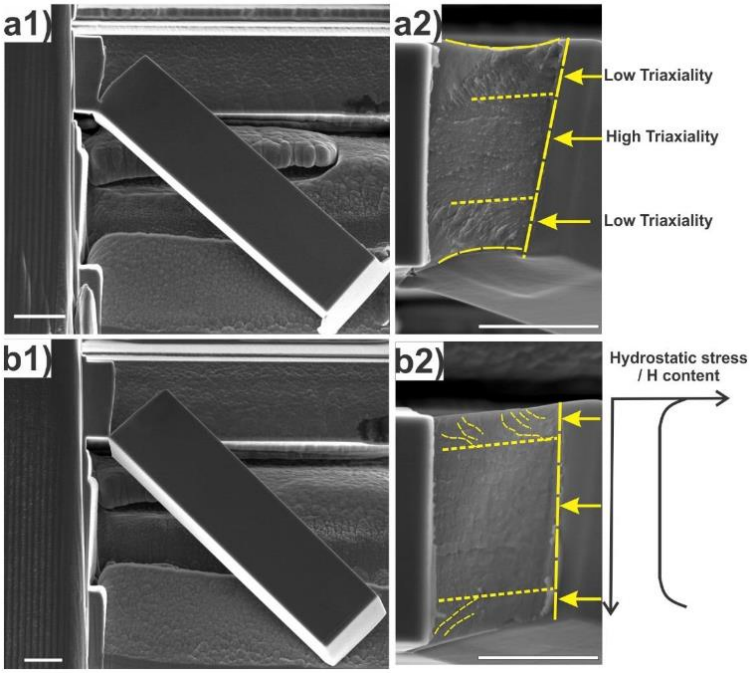

Figure 28. Image of micro-cantilever beam after fracture (Deng & Barnoush, n.d.).

2.2 Tensile Testing

Tensile testing has been extensively demonstrated in materials testing but is a relatively new concept for mechanical testing in TRISO particles. The study done by Gussev et al. shared many things in common with traditional tensile testing, while including an emphasis on designing a miniature specimen geometry suitable for irradiation in materials test reactors and post-irradiation out-of-hot cell testing. While not initially focused on TRISO fuel specimens, this study demonstrates the utility of tensile testing of nuclear materials on a miniature scale. Dog bones (SS-J and SS-Mini style) consisting of several materials - 304L stainless steel, an aluminum alloy including advanced 3D-printed material, a high nickel 718-alloy, tungsten, and an advanced fuel cladding FeCrAl alloy - were used as the tensile samples. These tensile samples were subjected to mechanical tensile tests inside a High Flux Isotope Reactor (HFIR) rabbit capsule design in order to compare the engineering mechanical properties (yield stress, ultimate tensile stress, uniform and total elongation values, and plastic behavior) between the different SS-J and SS-Mini geometries. This study is significant because it proves that acceptable mechanical property results can be obtained from miniature radioactive materials and can be consistently repeated. The dimensions of the SS-J specimen geometry and the testing apparatus for the study is shown in Fig. 29 and 30 (Gussev et al., 2017).

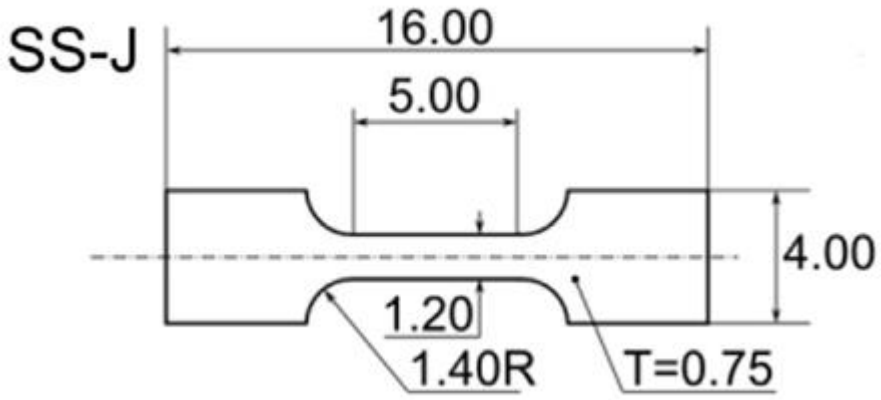

Figure 29. Dimensions of the SS-J specimen geometry, shown in millimeters. This geometry can be comprised of any given material and be subjected to radiation in this experimental design (Gussev et al., 2017).

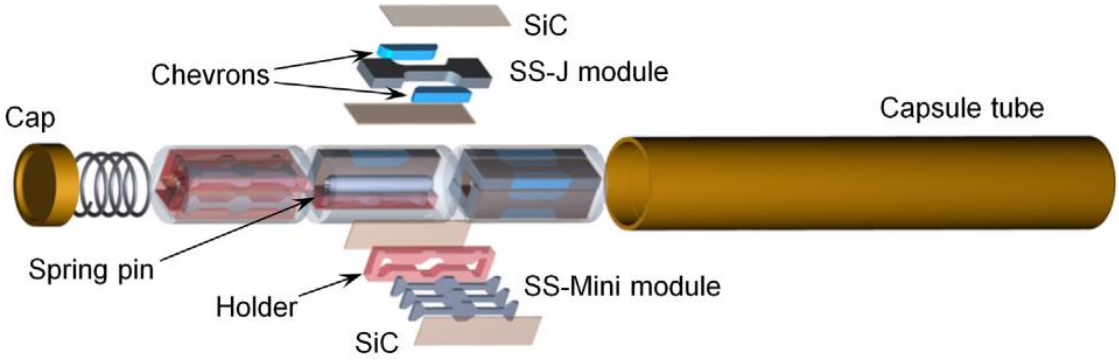

Figure 30. The HFIR rabbit capsule design for SS-J and SS-Mini tensile specimen as seen in the study done by Gussev et al. (Gussev et al., 2017).

The work shown by Lee et al. (2015) demonstrates a different miniature approach to material tensile testing than Gussev et al., with the study primarily focusing on the SiC coating layer for the TRISO particle. A novel micro-tensile testing system was developed to evaluate the high temperature fracture strength of these SiC coating layers. Scanning electron microscopy, transmission electron microscopy, x-ray diffractometry, and Raman spectroscopy techniques were used to characterize these specimens. Fig. 31 demonstrates the sample preparation process,

including SiC coating layer deposition, laser etching, and heat treatment to remove samples from bulk material. This study developed a new gripping method for tensile testing of the sample, which involves the specimen being fixed onto small ceramic holders and being held by a ceramic pin, as seen in Fig. 32. In this study, two different types of SiC layers were prepared: SiC-A and SiC-B. The SiC-A specimen had larger grain size (0.4 ~ 0.6 mm) and a round top surface, while the SiC-B specimen had smaller grain size (0.2 ~ 0.3 mm) and a flat top surface. Both coatings decreased in fracture strength when subjected to elevated temperatures. Results of this study indicated that SiC-A was a better candidate for TRISO particle material (Lee et al., 2015).

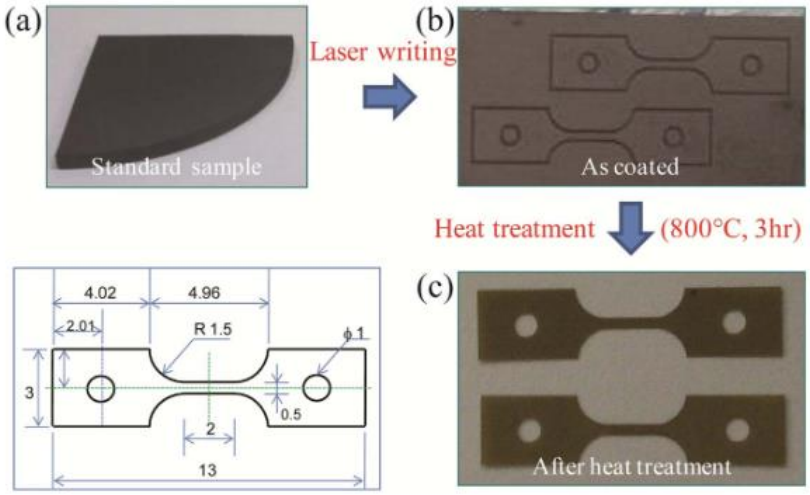

Figure 31. Tensile sample creation display. (a) Is starting sample, (b) is laser etched sample, and (c) is heat-treated sample removed from bulk material (Lee et al., 2015).

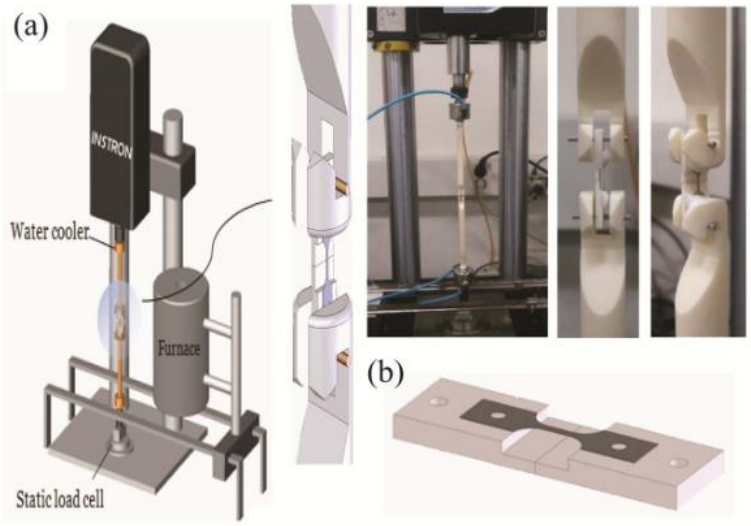

Figure 32. Diagram (a) refers to micro tensile test set up, while (b) shows sample in place (Lee et al., 2015).

The study done by Bauer et al. demonstrates a novel tensile testing technique for ceramic materials on a microscopic scale. In this particular study a nanoscale, alumina polymer composite bar is placed in between a hexagonal cellular microarchitecture. Force is applied to the top of the hexagonal cell until the tensile bar is broken, as seen in Fig. 33. The tensile strength obtained from the study was consistent with other literature regarding alumina polymers, marking this technique as a feasible method for measuring microscopic ceramic tensile strengths (Bauer et al., 2015) . One of the goals of the research being conducted for this thesis is to demonstrate the feasibility of testing applications similar to this and to create such geometries in the ceramic TRISO particle layers.

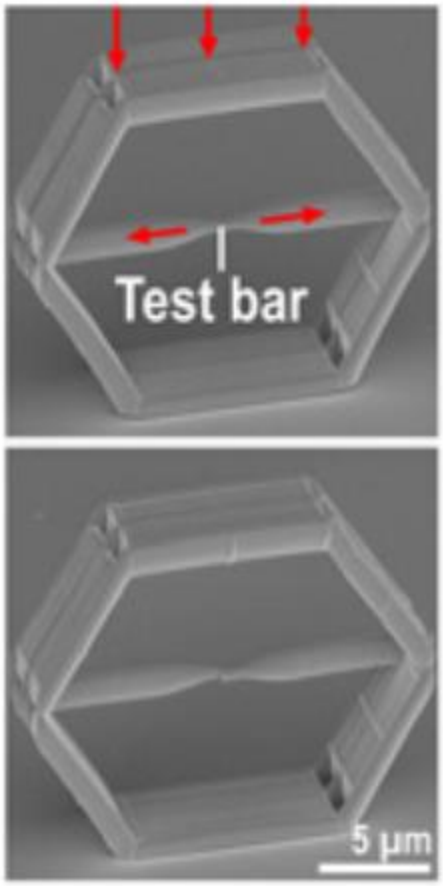

Figure 33. Image of the hexagonal cellular microarchitecture before and after tensile test (Bauer et al., 2015).

Reichardt et al. (2019) performed a unique in situ tensile test on micro-tensile samples of pure Ni single-crystal foils. The dimensions of the dog bones in this study are slightly larger yet comparable to the dimensions to the dog bones fabricated for this thesis, with the gauge length of the dog bones in the study being 25 to 30 μm and the cross sectional area being approximately 10 μm wide by 13 μm thick. This study used a unique strategy for pulling on the tensile samples. A grip in the shape of a rectangular hole was milled into the exposed end of each sample and a hook type gripper made of silicon was placed into the hole, as seen in Fig. 34. The load was applied via pulling on the hole with the gripper. Both unirradiated and irradiated Ni foils were tested. It was

determined that there was an increase in fracture stress roughly proportional to the damaging radiation dose, as was predicted (Reichardt et al., 2019). Results of this study demonstrated that successful tensile testing of irradiated material can be conducted on the micron scale.

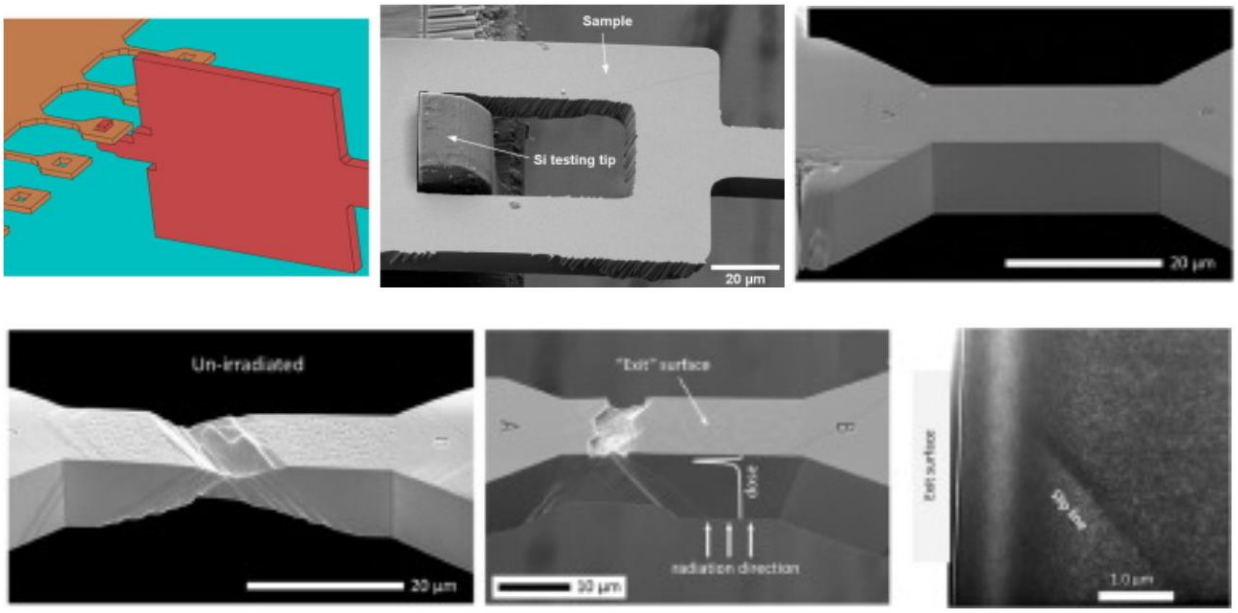

Figure 34. Visuals of the hook gripper set up and various stages of necking of the tensile sample in the study done by Reichardt et al. (Reichardt et al., 2019).

Ando et al. (2018) performed room temperature micro-tensile testing on irradiated and unirradiated F82H steel specimens. The dimensions of the tensile samples in this study are even closer to the dimensions of the tensile samples prepared for this thesis than in the study done by Reichardt et al., with the gauge section being around 10-μm long by 1-μm^2 in area. This technique uses a lift-out procedure to remove a lamella from the F82H steel sample and welds it to a SiC micro-beam using tungsten deposition. A dog bone is then milled from the lamella and the tungsten nano-manipulator needle is welded to the top of the dog bone using tungsten deposition, as seen in Fig. 35. The tensile test is performed by pulling upward on the dog bone tensile sample with the

tungsten needle. The researchers found that the change in tensile properties due to neutron irradiation is in qualitative agreement with other micrometer-and millimeter-sized F82H samples. This study demonstrated a unique technique for determining the tensile strength of micron and smaller-sized specimens and could potentially be applied to the layers of TRISO particles and compared to the work done for this thesis (Ando et al., 2018).

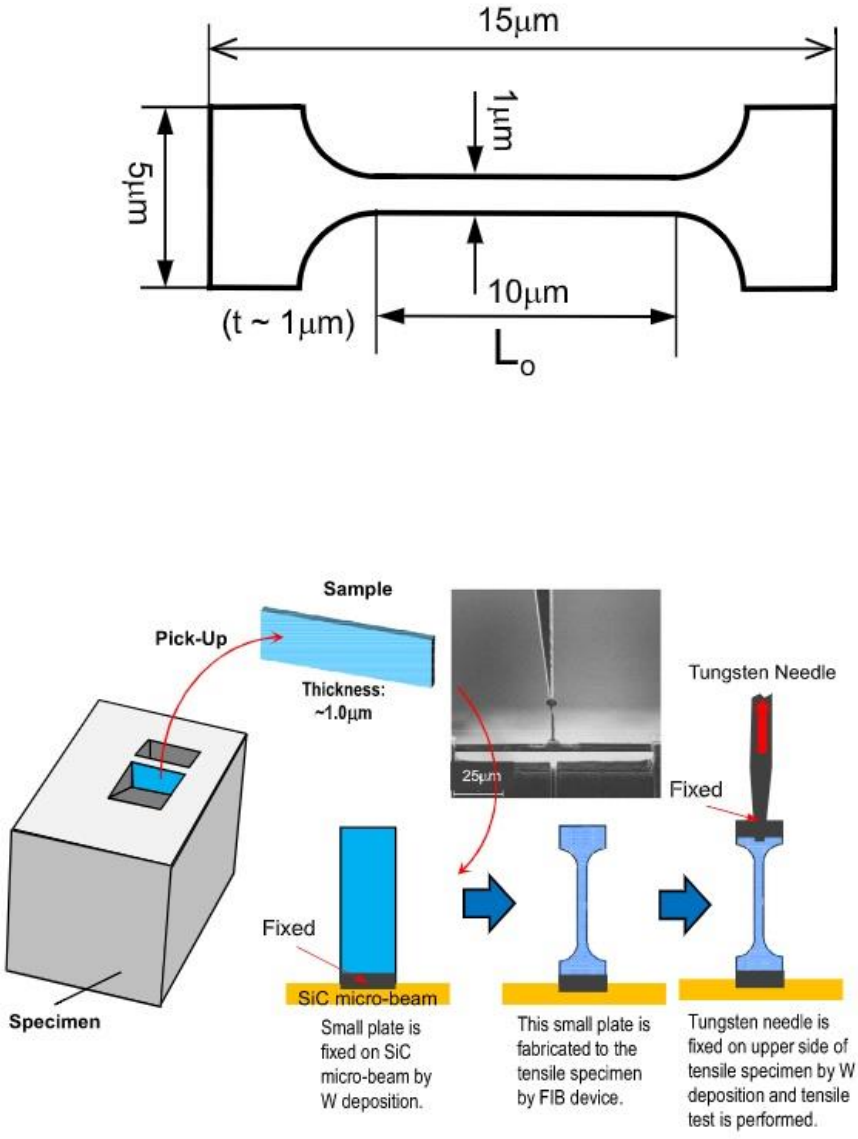

Figure 35. Top diagram shows dimensions of dog bone used for tensile testing. Bottom diagram shows procedure for tensile testing technique (Ando et al., 2018).

Testing performed for this thesis research was primarily based on work performed by Kiener & Minor (2011). Their work delved into the small-scale plasticity mechanisms that underlie the behavior of nanoscopic materials. To discover these mechanisms, they developed a novel quantitative, in situ nanotensile testing technique that is applied in a TEM setting. The material in question was monocrystalline copper formed into a dog bone shaped tensile sample 100 to 200-nm thick using FIB milling techniques. The copper dog bone was then lined up with diamond grippers and pulled on until fracture, as illustrated in Fig. 36. The forces involved in fracturing the dog bone determine the tensile strength of the sample (Kiener & Minor, 2011). The technique used for this thesis work is nearly identical to this process, with the only difference being the scale of the dog bone and diamond gripper. The dog bone and diamond gripper for this thesis work was on the order of microns, not nanometers.

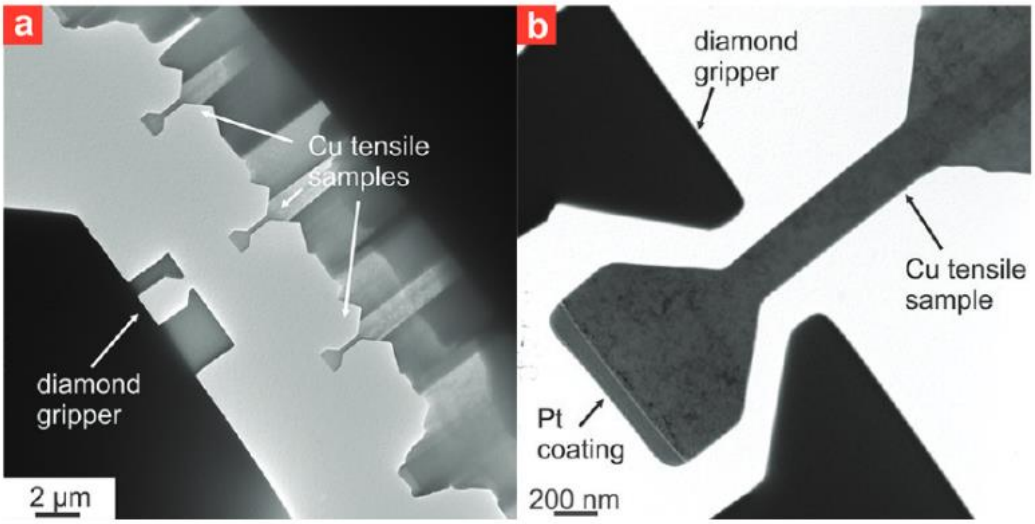

Figure 36. Display of diamond gripper and copper dog bone assembly. (a) Demonstrates a lower magnification image of the copper sample while (b) shows the copper dog bone within the diamond gripper (Kiener & Minor, 2011).

Vo et al. (2017) conducted a study with a testing procedure nearly identical to the one used for this thesis research, with the only real difference being the materials used for the gripper and the composition of the tensile samples themselves. Vo et al. makes the notable distinction that micro-tensile testing can add tremendous value to materials characterization because it can directly measure the entire stress-strain curve, including the strain to failure. The tensile samples in the study were fabricated from 304 stainless steel specimens in a FEI Quanta 3D FEG dual-beam FIB/SEM and had a final gauge length of around 4.5-μm and a cross-sectional area of around 1.3 x 1.3-μm. Three tensile specimens were created for three different conditions: as-irradiated, post-irradiation annealed (PIA), and unirradiated. The gripper used in this study was fabricated from a tungsten needle mounted on a tip adapter for use in a Hysitron PI-85 PicoIndenter system. The tensile test were conducted by selecting tension mode in the Hysitron PI-85 software and aligning the dog bone tensile samples with the gripper then pulling on the samples, as seen in Fig. 37. These tests were performed inside the SEM with displacement control and at a rate of 10 nm/s. The study found that the critical resolve shear stress (CRSS) for the unirradiated, irradiated, and PIA samples to be 213 MPa, 438 MPa, and 319 MPa, respectively. These results suggest that micron scale measured strain corresponds well with its macroscopic counterpart, with earlier literature reporting unirradiated macroscopic austenitic stainless steel having a yield strength of around 300 MPa and irradiated specimens having a yield strength of around 1000 MPa (Vo et al., 2017). With the technique used in the study sharing similarities to the technique described herein, we expected great correspondence between the micron scale measured strain and macroscopic measured strain for the TRISO particle layer materials used for this thesis.

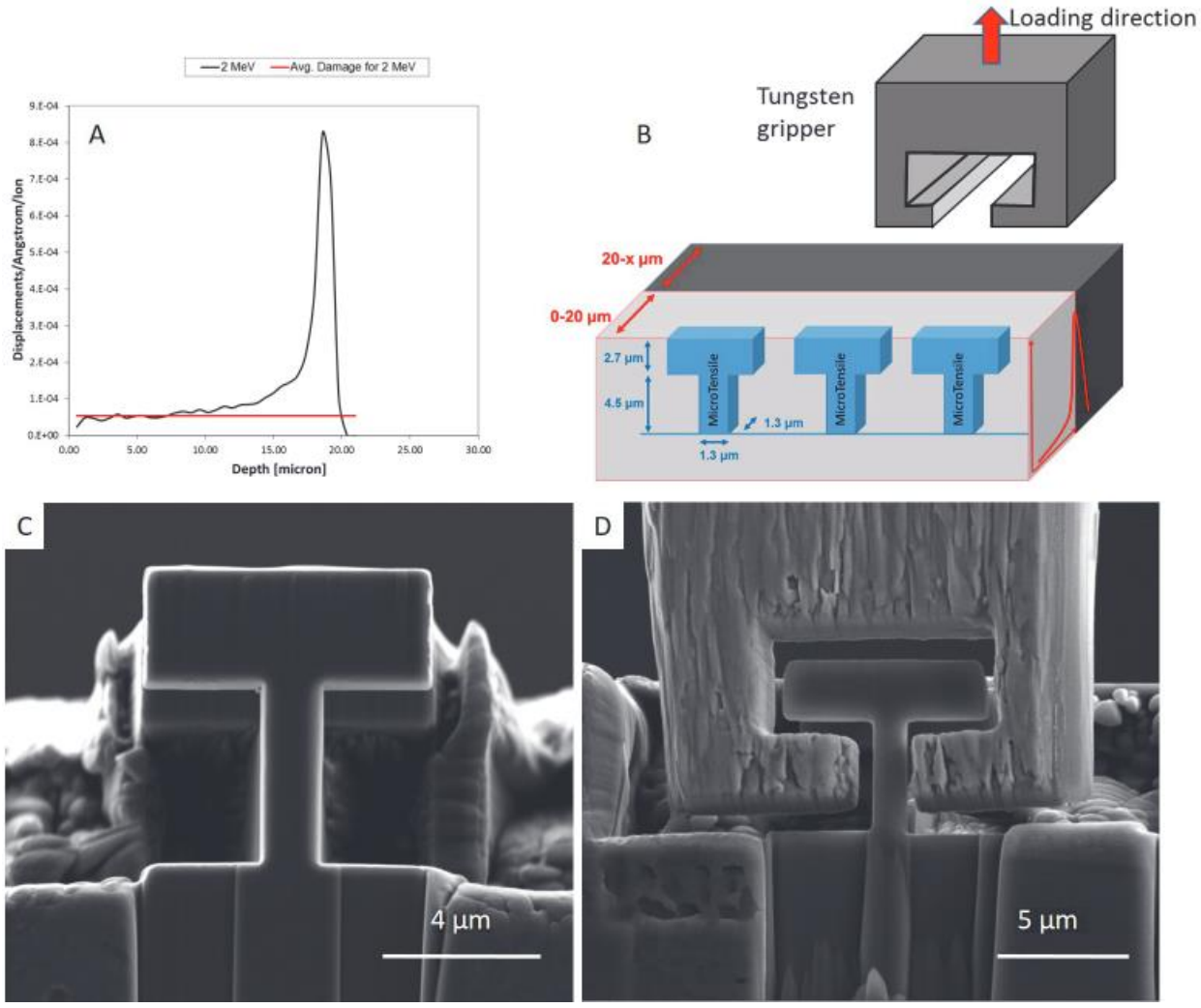

Figure 37. Experimental set up and display of tungsten gripper and steel dog bone. (A) shows a displacement versus depth curve, (B) is an illustration of the tensile testing procedure, (C) is an image of the steel dog bone, and (D) is an image of the tungsten gripper aligned with the steel dog bone. (Vo et al., 2017).

3.0 Materials and Methods

This section refers to all the materials and techniques used to fabricate and test the micro tensile samples in this thesis. Since there numerous complex steps involved in fabricating and testing the tensile samples, this section will be divided into three sub sections: instruments, sample fabrication, and sample testing.

3.1 Instruments

3.11 FEI Dual Beam 835

The instrument used for the fabrication of all the tensile samples in this thesis was a FEI Dual Beam 835 located at the Eames complex on ISU's campus in Pocatello, Idaho. This machine was built in the year 2000 and was originally meant for use in the silicon wafer industry but has since been adapted for use in micro tensile sample fabrication. The primary working components on this machine used in the tensile sample fabrication process are the gallium focused ion beam (FIB), scanning electron microscope field emission gun (SEM-FEG), tungsten and platinum gas injection systems (GIS), and nano manipulator. Fig. 38 shows the components of the Dual Beam. All samples are loaded through the front load lock and pass into the vacuum chamber with the help of a loading arm. Once inside the chamber, the sample sits on a stage that can move in the x, y, and z directions, rotate through a full 360°, and tilt beyond 52°. Using the primary working components and the maneuvering capabilities of the stage and nano manipulator, complex lift-out and tensile sample fabrication processes were possible.

Figure 38. In the top image, one can see the front view of the outside of the Dual Beam 835 with the load lock marked with the gray arrow. In the bottom image, the working components of the Dual Beam are visible with the Magnum FIB column marked with the orange arrow, the platinum GIS marked with the yellow arrow, the tungsten GIS marked with the blue arrow, the SEM column marked with the black arrow, and the Omniprobe nano manipulator marked with the green arrow.

3.12 Thermo Fisher Scientific FIB SEM Versa 3D

Originally, the instrument planned for the imaging and videoing of the tensile tests for this thesis was a FEI Quanta 200F SEM located at the Eames complex in Pocatello, Idaho. Due to technical difficulties, however, this machine was unable to be used for this thesis research. The instrument used for the imaging and videoing of the tensile tests was a Thermo Fisher Scientific FIB SEM Versa 3D located at Bruker Hysitron's headquarters in Eden Prairie, Minnesota. An image of this machine can be seen in Fig. 39. While this machine has a FIB, an SEM, and a GIS, only the SEM was used for its imaging capabilities. The chamber of this machine is accessed through the front sliding door and allows ample room for loading and unloading of the sample and the sample holder. All imaging and videoing of the tensile tests conducted during this thesis were done inside this machines vacuum chamber. Fig. 40 shows the layout and placement of the different working components typically seen inside the Versa 3D and the Dual Beam 835.

Figure 39. Image of a Versa 3D (THERMO FISHER SCIENTIFIC, 2021). The SEM column is marked with the gray arrow and the front of the vacuum chamber is marked with the orange arrow.

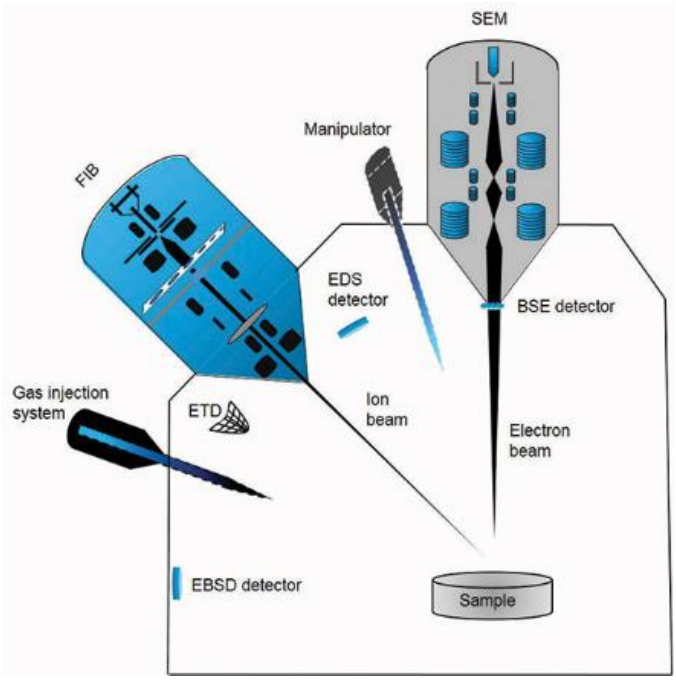

Figure 40. Illustration of the inner components typically found inside microscopes such as the Versa 3D and Dual Beam 835 (Wolff, 2020).

3.13 Bruker Hysitron PI 88 SEM PicoIndenter

The instrument used for the direct in-situ micro tensile test in this thesis was a Bruker Hysitron PI 88 SEM PicoIndenter. This machine holds the sample mount on an advanced XYZ positioning stage capable of nanometer sized movements. Opposite of the sample the machine hosts a transducer that is vacuum compatible and provides electrostatic actuation and capacitive displacement sensing on the micro newton scale. The end of the transducer contains a threaded post that allows for screw-on probes. An image of the PI 88 is shown in Fig. 41. After the sample and screw-on probe are attached, the PI 88 is mounted within a SEM or FIB/SEM for imaging of the tests being conducted. For this thesis, our PI 88 was placed within the Versa 3D mentioned in the previous section while it conducted micro tensile test of our samples.

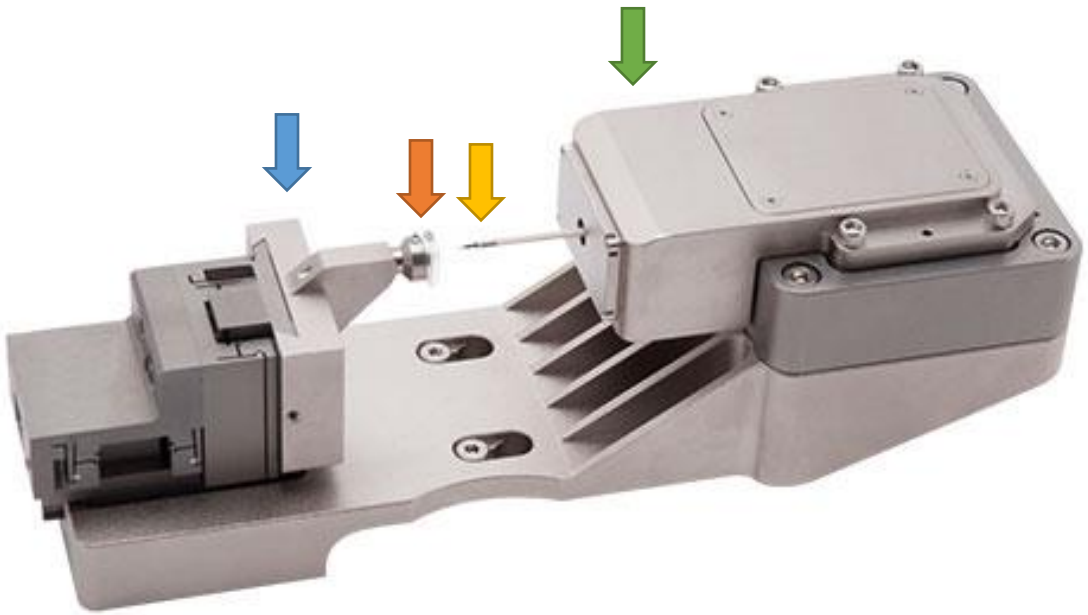

Figure 41. Image of the PI 88 SEM PicoIndenter base system. The positioning stage is marked with the blue arrow, the sample mount is marked with the orange arrow, the threaded post with screw-on probe is marked with yellow arrow, and the transducer is marked with a green arrow. *(*PI 88 SEM PicoIndenter ®, *2020)*

3.2 Sample Fabrication

Before any micro tensile samples could be fabricated, pin mounts and stub holders needed to be acquired onto which the samples would be placed. A Ted Pella 45° pin stub holder and a Ted Pella low profile 90° FIB pin mount were used to serve this purpose. Fig. 42 shows images of these holders.

Figure 42. From left to right: Ted Pella low profile 90° FIB pin mount, Ted Pella 45° pin stub holder, and pin mount in stub holder.

A challenging aspect of this work was that the Dual Beams load lock had only an 18-mm clearance from top to bottom and a 6-mm clearance above the top of the silicon wafer holder that is designed to pass through the load lock. This clearance is much too narrow for the holders in Fig. 42 to pass through on top of the silicon wafer holder. To solve this problem, a custom-made aluminum sample holder attachment composed of 20-gauge aluminum was made in the machine shop located at the Eames complex. The purpose of this sample holder attachment was to seat the Ted Pella holders low enough as to provide enough clearance to pass through the load lock. Even

with this lower seating, it was necessary to grind the Ted Pella holders to a size small enough to be able to pass through the load lock. A drawing of the custom-made aluminum sample holder attachment schematics and an image of the sample holder seated in the silicon wafer holder are shown in Fig. 43.

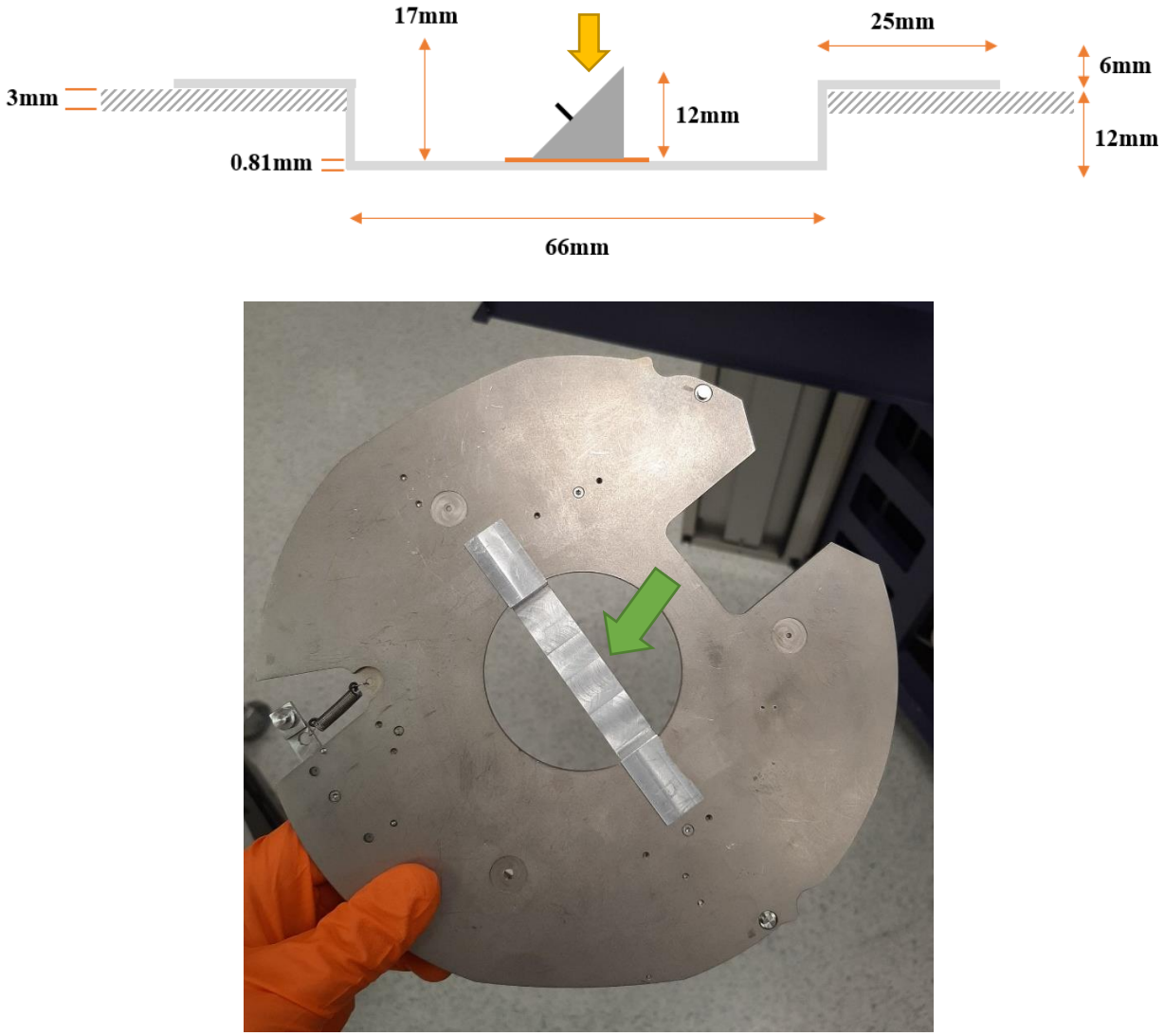

Figure 43. Drawing of the custom-made aluminum sample holder attachment schematic can be seen on top with the ground down Ted Pella holders attached with copper tape and is marked with the yellow arrow and the silicon wafer holder shown as the textured gradient. The custom holder attachment can provide 17-mm of vertical working space as seen in the schematic. Image of the custom-made aluminum sample holder attachment seated in the silicon wafer holder can be seen on the bottom marked with the green arrow and is 15-mm in width.

3.21 Diamond Gripper

A Bruker Hysitron cube cornered diamond indentation probe served as the base material for the fabrication of the diamond grippers used in the micro tensile test. This probe has a centerline-to-face angle of 35.3° and is designed to be screwed onto the threaded post of the PI 88's transducer. While the cube cornered probe performed well with our micro tensile samples, it did not perform well with other micro tensile samples with less clearance around the base. Since our micro tensile samples were protruding into open space, we did not have a problem with the base running into the bulk of the sample. Conical shaped indentation probes should be considered for future gripper fabrication because of their high centerline-to-face angle (greater than 35.3°), which will prevent the base of the probe from running into the base of low clearance tensile samples. An image of the cube cornered diamond indentation probe is shown in Fig. 44.

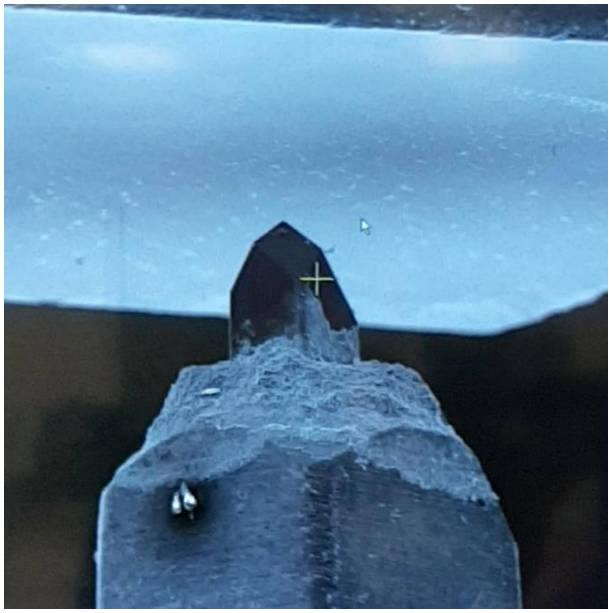

Figure 44. Image of the Bruker Hysitron diamond nano indentation probe attached to the PI 88 inside the FEI Quanta 200F SEM located at the Eames complex in Pocatello, Idaho.

The first step in fabricating the diamond gripper is properly aligning the diamond nano indentation probe onto the Ted Pella 45° pin stub holder. This is done by first screwing the probe onto the PI 88's threaded post and marking the top of the probes shaft with a black marker. This helps orient the probe relative to the PI 88. Next, after applying copper tape underneath and above the 45° pin stub holder, very carefully place the probe on top of the 45° pin stub holder with the black mark facing orthogonal to the 45° pin stub holder face and the probe tip facing upwards. Copper tape serves as an adhesive to secure the pin stub holder and to discharge any charge buildup accrued on the samples through using the FIB and SEM. The 45° pin stub holder is then placed on top of the center of the custom-made aluminum sample holder attachment. An image of proper diamond probe alignment before entering the Dual Beam for fabrication is shown in Fig. 45.

Figure 45. Diamond probe properly aligned atop 45° pin stub holder and custom-made aluminum sample holder attachment before fabrication inside the Dual Beam.

After the diamond probe enters the Dual Beams vacuum chamber, the stage is brought to eucentric height. At eucentric height the sample, ion beam, and electron beam intersect. The eucentric height is important because it allows the ion and electron beams to view the same point on the sample. After the stage is brought to eucentric height, the stage is tilted seven degrees to align the diamond probe with the ion beam. The stage needs to be tilted because the ion beam is angled exactly 52 degrees from the orthogonally positioned electron beam and the pin stub holder is angled at 45 degrees. After alignment, the first cut involved placing two 80-μm wide, 25-μm tall, 40-μm deep parallel trenches separated by a 10-μm gap with the tip of the probe placed in the center of this gap and facing directly towards the ion beam. Because this cut would be considered a large bulk cut the larger aperture (20-nA) was used. The aperture is synonymous with how powerful the ion beam is. A visualization of the alignment and cutting conducted is shown in Fig. 46. Images of the resulting cuts are shown in the Fig. 47.

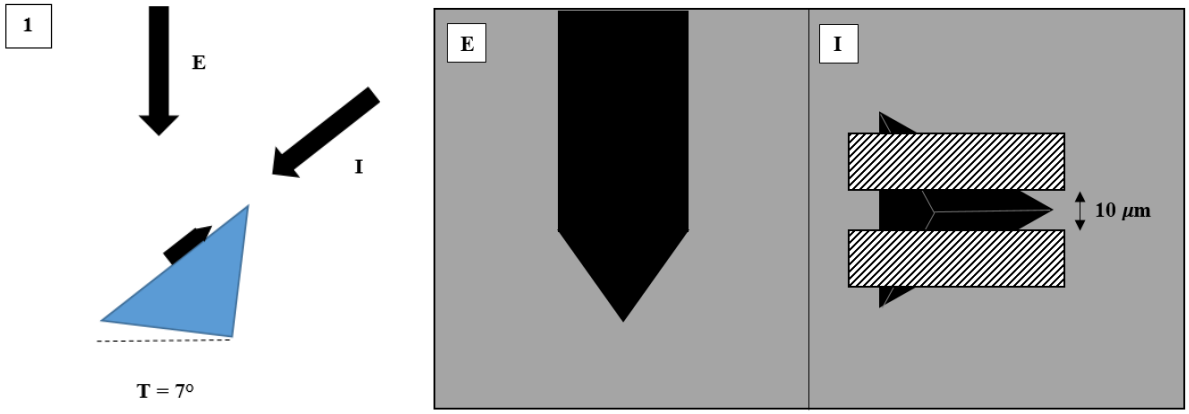

Figure 46. The graphic on the left demonstrates the alignments that were involved in the first step. The graphic on the right displays what each beam saw from this angle. T represents the stage tilt, E the electron beam, I the ion beam, and the textured gradient representing where the FIB cut into the sample.

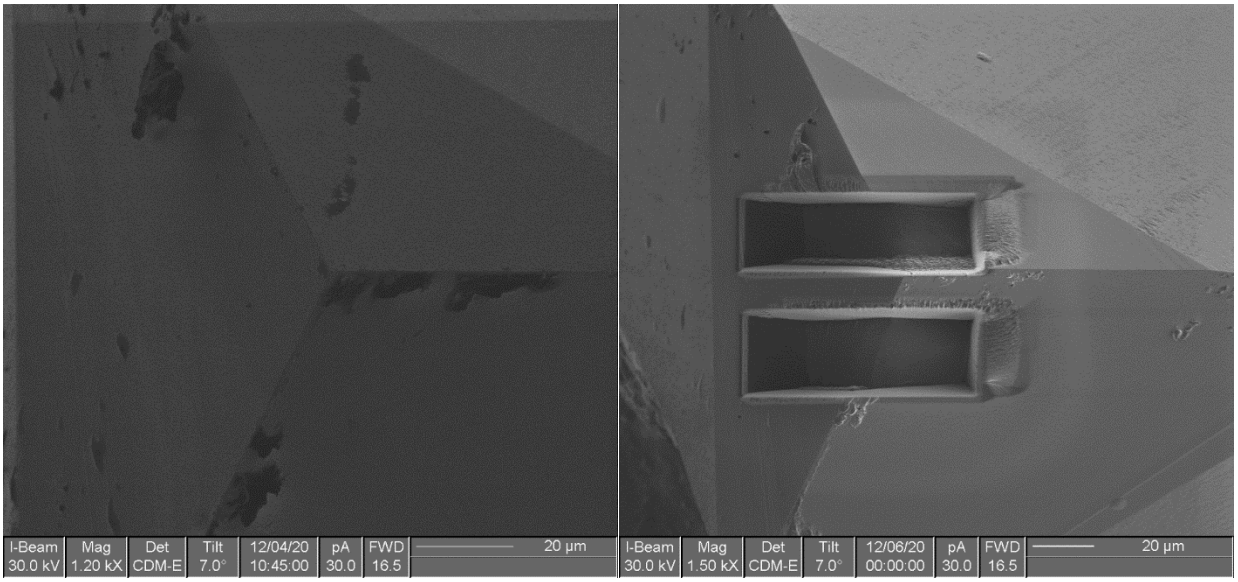

Figure 47. Image on the left is the diamond probe facing the ion beam before the first cut and the image on the right shows the parallel cuts after they have been fabricated.

After the first cut was finished, the stage was rotated 180° to face the tip perpendicular to the ion beam and expose the trench face. The second cut created a 20-μm wide by 8-μm tall block protruding from the entrenched face of the diamond tip. The five and seven nano amp apertures were used for this cut because they created finer cuts but were still powerful enough to finish the milling in a reasonable amount of time. Illistrations and images of the exposed block are shown in Fig. 48 and 49.

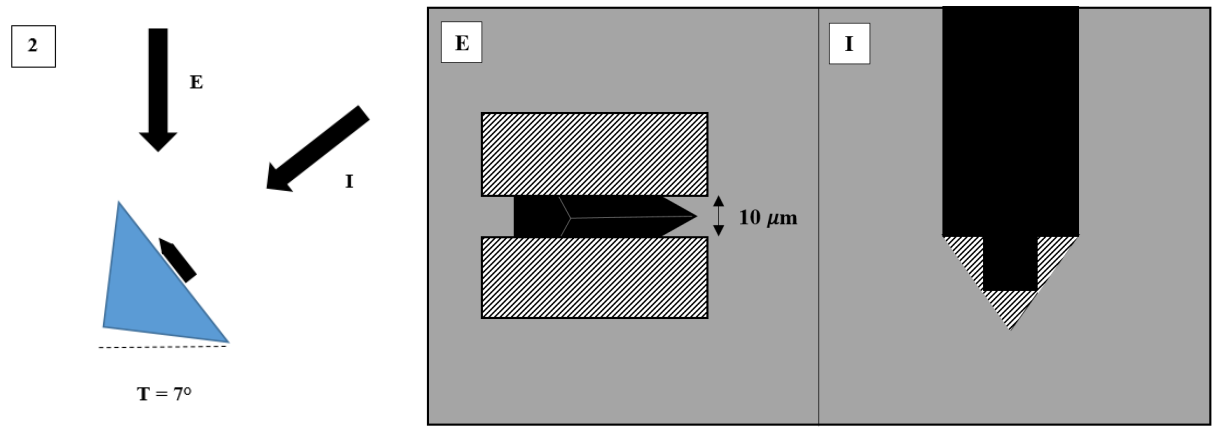

Figure 48. Alignment of the sample for the block exposing step is shown on the left while a side-by-side graphic of the electron beam and ion beam perspective during this milling step is shown on the right.

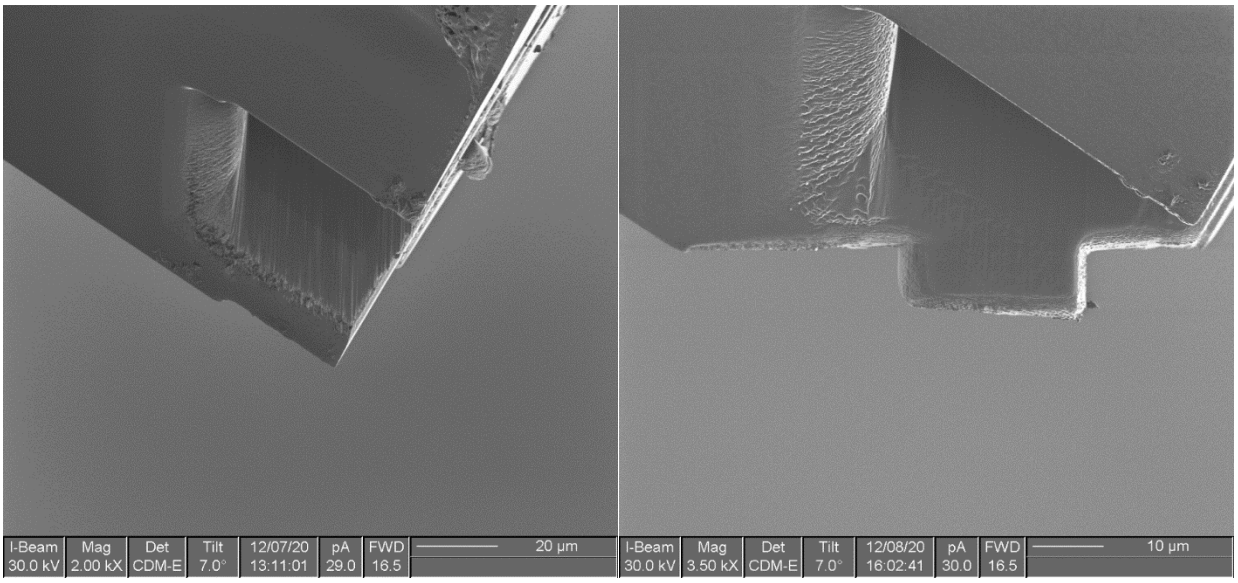

Figure 49. Images of before (left) and after (right) the block exposing step was applied to the diamond gripper from the perspective of the ion beam.

The third step involved rotating the stage 180° back to its original position facing the ion beam where the protruding block was thinned down from 10-μm thick to 5-μm thick. The smaller (1-5 nA) apertures were used for this step. It should be noted that the further along the fabrication

process progresses the smaller and smaller the apertures get. This is because the larger apertures are no longer needed to clear away a lot of material so the sharper, smaller apertures become more desirable for fine details. Fig 50. illustrates the block thinning procedure with Fig. 51 showing the block just before thinning.

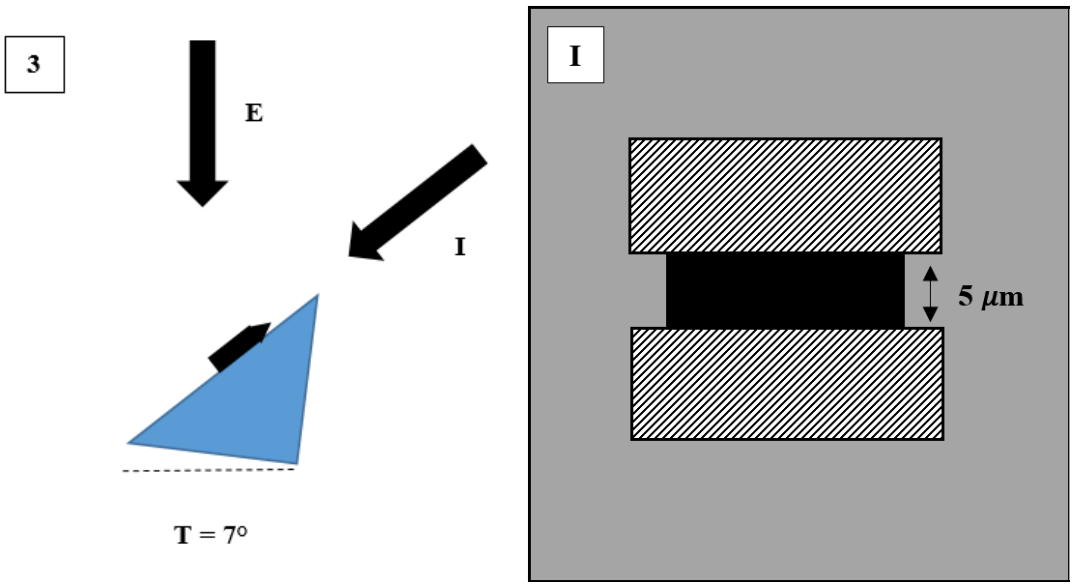

Figure 50. The alignment and visual from the ion beam perspective of the block thinning step for the fabrication of the diamond grippers.

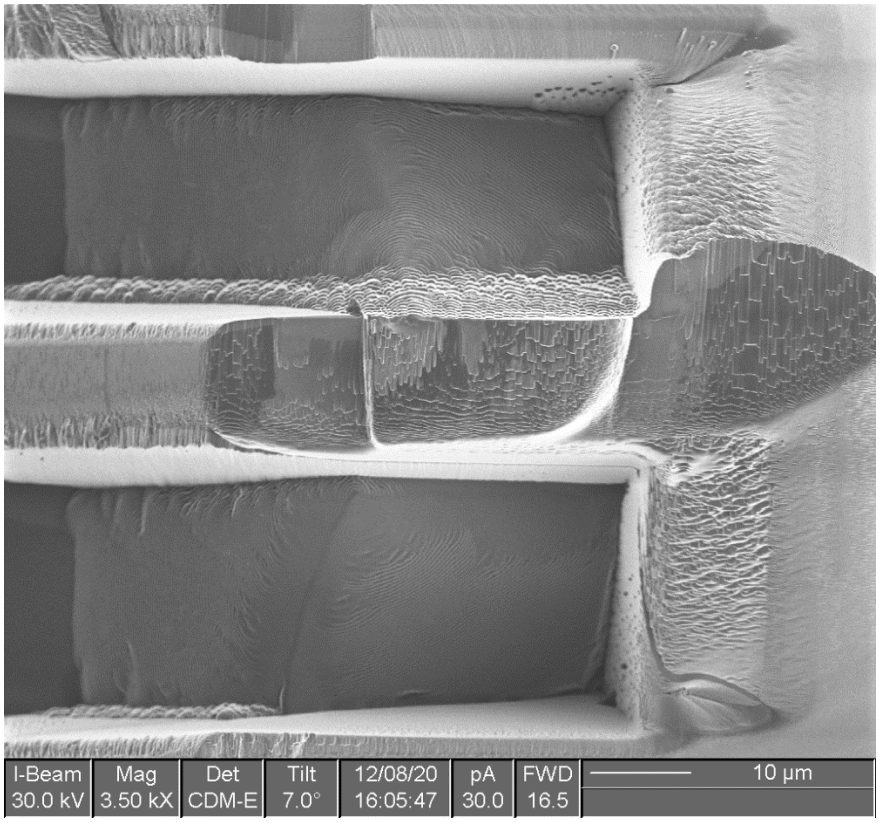

Figure 51. Image of the exposed block just prior to the thinning down process from the perspective of the ion beam.

The fourth and final step involved rotating the stage 180° back to the perpendicular facing position to the ion beam where an 11.3-μm wide by 8-μm tall square hole was extruded from the block. An additional cut was made at the bottom of the square hole to produce a 5.5-μm opening at the bottom of the block. The summation of these cuts produced a diamond gripper with gripping prongs 3.1-μm wide and 2.8-μm thick and an internal cavity 11.3-μm wide by 8-μm tall. All these final cuts were done using the one nano-meter aperture. Fig. 52 and 53 illustrate the final alignments and display the final diamond grippers used for all micro tensile tests conducted during this thesis.

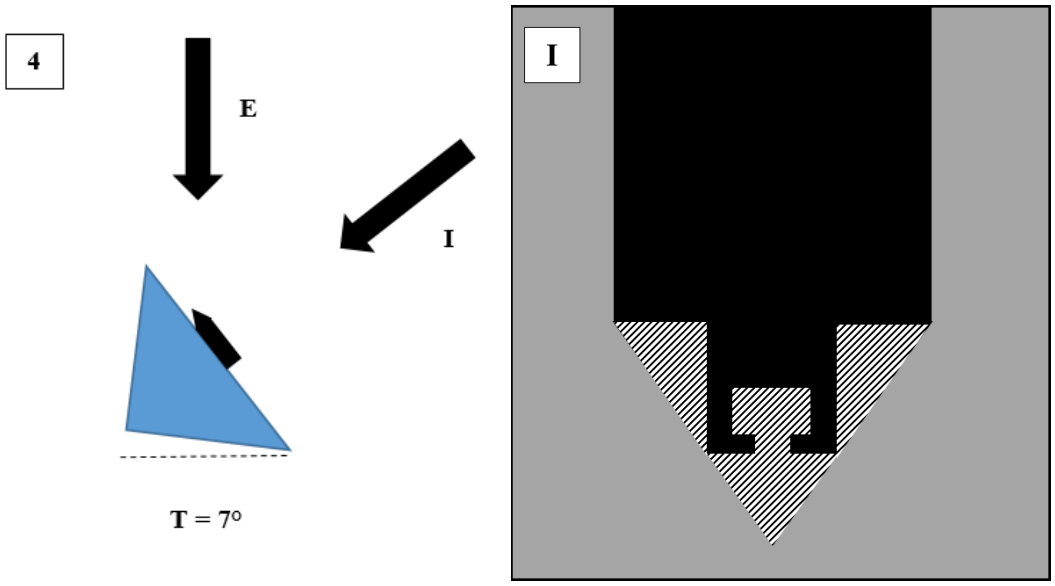

Figure 52. The final cuts and alignments involved in fabricating the diamond grippers.

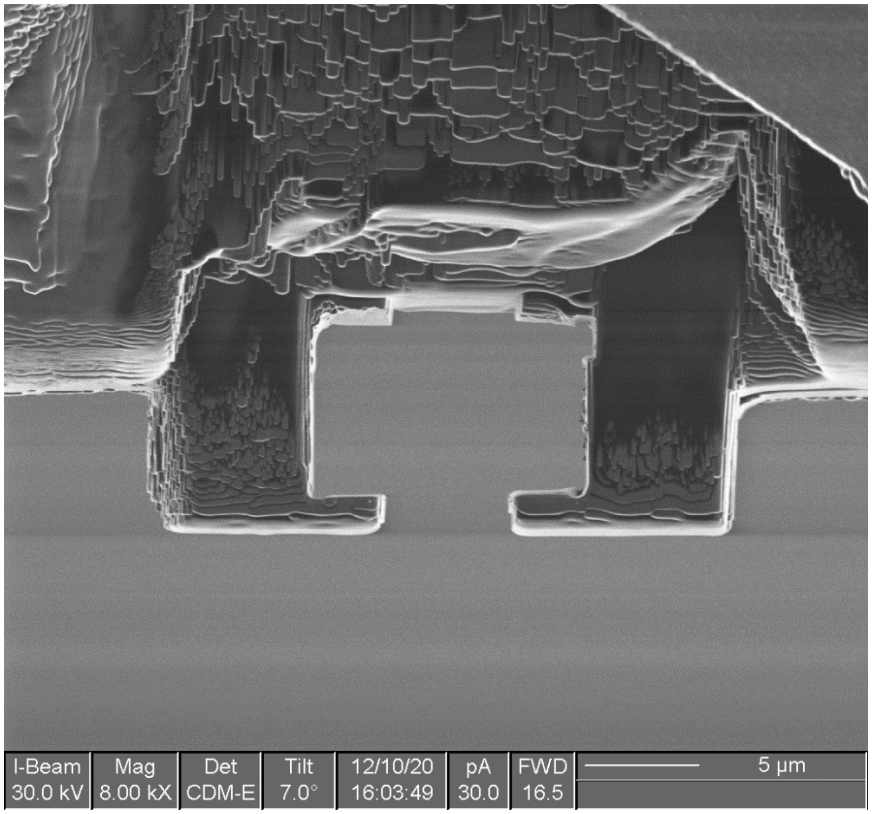

Figure 53. The completed diamond grippers used in every single micro tensile test during this thesis.

3.22 Tensile Samples for Baseline Materials

For the fabrication of the copper, molybdenum, and silicon micro tensile samples copper and molybdenum Omniprobe lift-out grids and silicon PELCO lift-out grids from Ted Pella were used as the base materials. The copper and molybdenum lift-out grids each have five posts and typically have a thickness of 25-30µm and a diameter of 3-mm. The silicon lift-out grids each have four posts, and are 80-µm wide, 100-µm thick, and 190-µm high. Images of each half-grid are shown in Fig. 43.

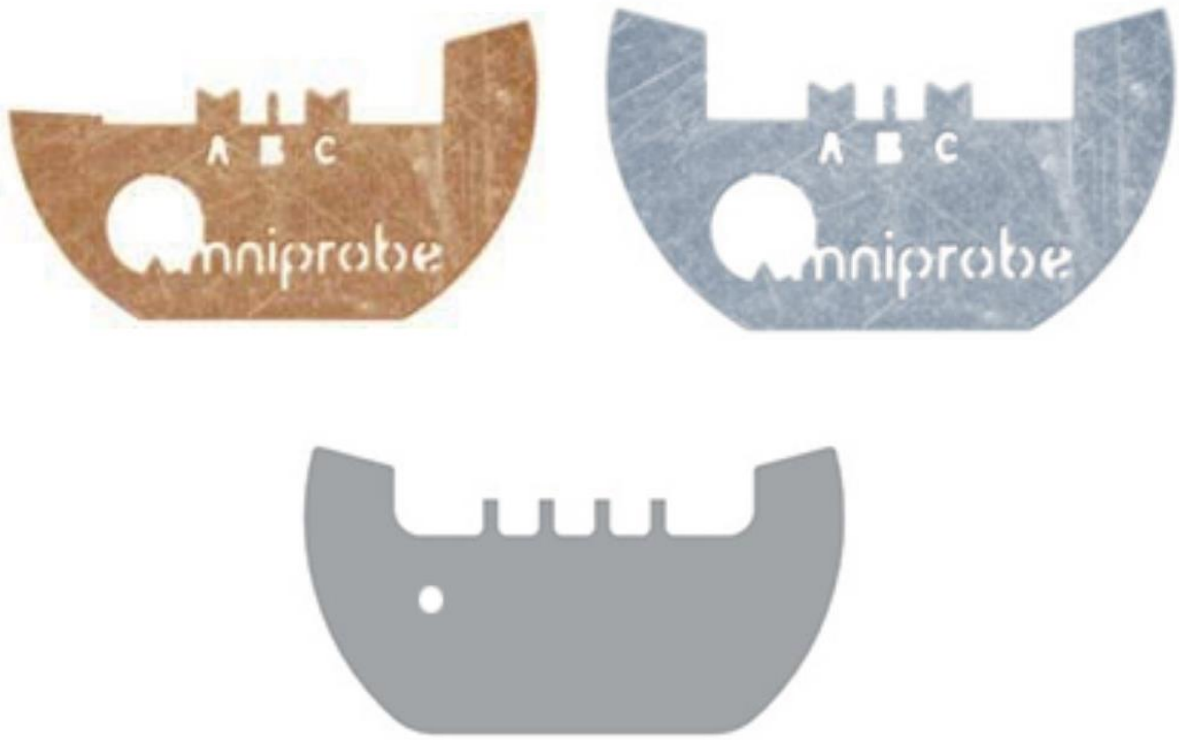

Figure 54. Images of the FIB lift-out grids. Upper left grid is copper, upper right grid is molybdenum, and bottom grid is silicon (Ted Pella, 2020).

The copper, molybdenum, and silicon dog bone shaped tensile samples were all fashioned in a similar manner, with the only differences being variance between the material hardness of the different materials (affecting mill time) and the varying thickness of the FIB lift-out grids. The samples were mounted to a 90º pin stub using copper tape and braced against a plastic box for keeping the stub steady. Two lift-out grids of each material were attached to each material's respective pin stub. The 90° pin stub was then attached to the 45° stub holder with the help of copper tape. This micro tensile sample pin set-up was then attached on top of the center of the custom-made aluminum sample holder attachment using copper tape. An image of the pin sub set-up can be seen in Fig. 55.

Figure 55. Images of a micro tensile sample pin stub set-up, with the two copper lift-out grids marked with blue arrows.

After the micro tensile sample pin stub set-up entered the Dual Beams vacuum chamber, the stage was brought to eucentric height and tilted seven degrees to align the micro tensile sample pin stub set-up with the ion beam for the same reason as described for the diamond probe. The first

step in milling the dog bones was exposing a 16-μm wide, 8-μm tall, and 20-μm deep cross-section block from the grid post tip that faces the ion beam. This was typically done with the 20 nano-amp aperture. After exposing this block the stage was rotated 180° to the perpendicular facing position where the exposed block was then refined into an 8-μm wide by 15-μm tall block. The five or seven nano-amp aperture was used for this second step. An image of the copper post and an illustration demonstrating this first step are shown in Fig. 56.

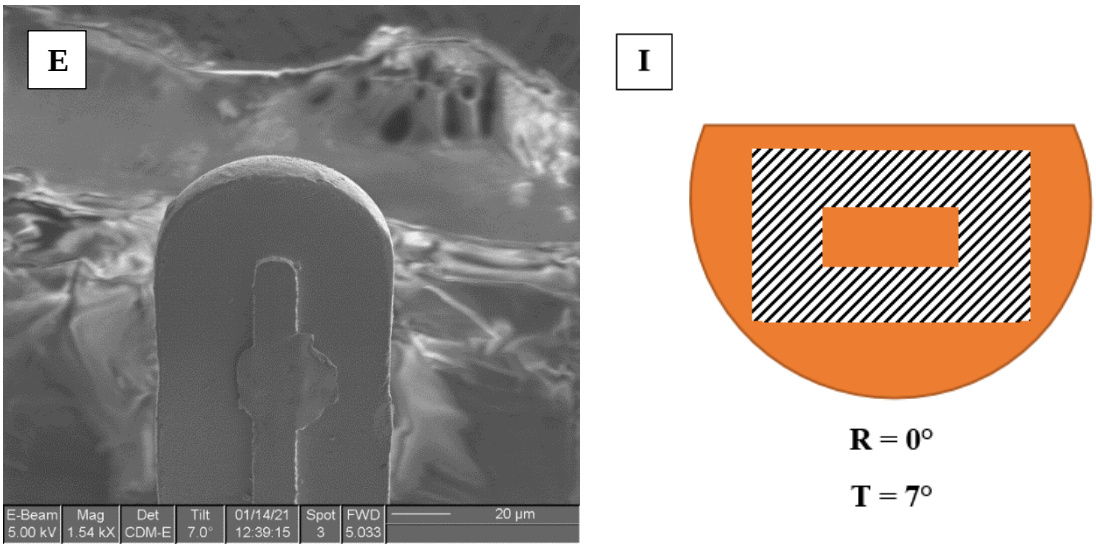

Figure 56. Image of an untouched copper lift-out grid post from the perspective of the electron beam and an illustration from the perspective of the ion beam helping to visualize where the first cuts were placed when the fabrication process began on the half-grids. The value R represents the rotation angle of the stage at the first step, T the stage tilt, and the textured gradient representing where the FIB cut into the sample.

After the block was uncovered, the stage was rotated 180° to face the ion beam and the protruding block was thinned from 8-μm to 2-μm. The three nano-amp aperture was used for this third step. The final step involved the stage being rotated 180° back to the perpendicular facing position where two 3-μm wide by 6-μm tall cuts were placed parallel to each other to create the

dog bone shape. An illustration of this can be seen in Fig. 57. It should be noted that the stage remained at a seven degree tilt throughout the entire milling process to maintain proper alignment with the ion beam. Every dog bone was designed to be 15-μm tall, 8-μm wide, and 2-μm thick with a tensile gauge section 6-μm tall by 2-μm wide and a bottom portion (head section) 4-μm tall. The analysis section of this thesis will provide the actual dimensions of each individual tensile sample. An image of one of the final dog bones and a panoramic view of one of the completed molybdenum lift-out grids is shown in Fig. 58. While the molybdenum FIB lift-out grid consisted of harder material than the copper FIB lift-out grid, it took less time to mill the dog bones because it has significantly thinner posts (25-μm vs 50-μm) tips that tapered almost to a point. The silicon FIB lift-out grid took by far the longest time, as it was the hardest material and had 100-μm thick posts. In total, 10 copper, 10 molybdenum, and 8 silicon dog bones were created.

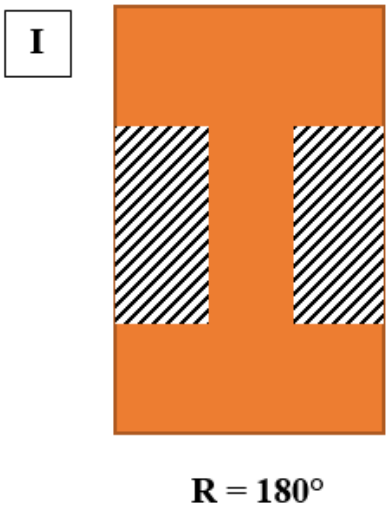

Figure 57. Illustration of the dog bone milling step, with R signifying the rotation of the stage, I demonstrating that this is from the perspective of the ion beam, and the textured gradient representing where the FIB cut into the sample.

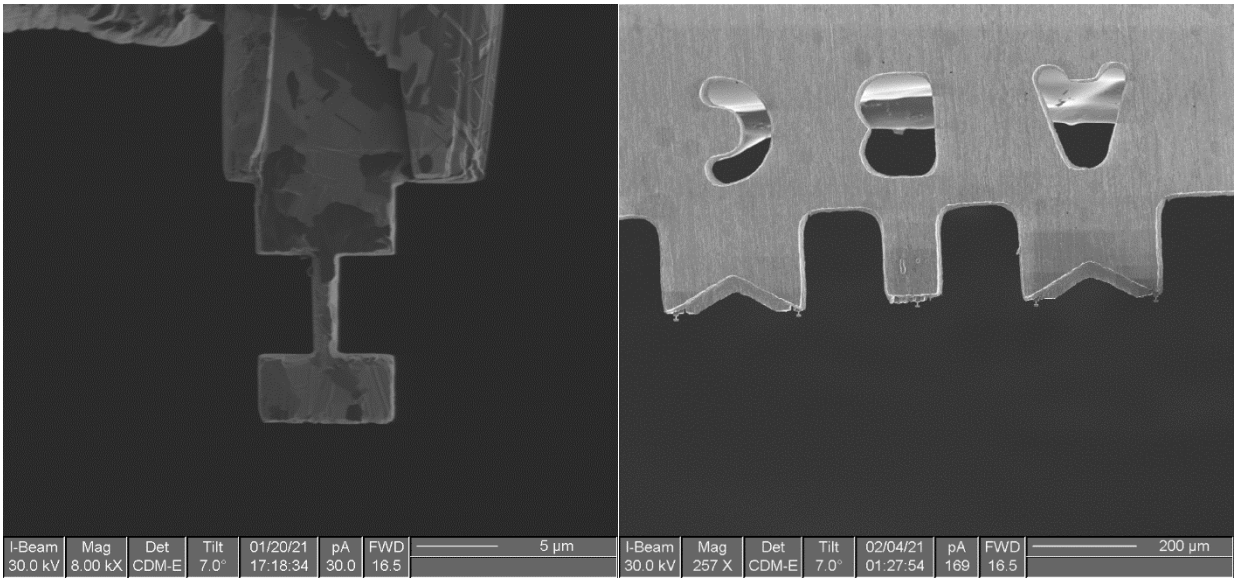

Figure 58. The image on the left is an example of a completed copper dog bone tensile sample while the image on the right displays an entire lift-out grids worth of molybdenum dog bone tensile samples.

3.23 Tensile Sample for TRISO Particles

The TRISO particles used for the fabrication of the TRISO micro tensile sample were zirconium fuel surrogate TRISO particles produced at NECSA's Advanced Coating Facility (ACF) and Research Coating Facility (RCF) in South Africa. One of the two epoxy pucks containing the TRISO particles was already polished down to expose the zirconium kernel contained within the TRISO particles. The other epoxy puck is unpolished and may be used for testing at a later date. Fig. 44 shows images of both epoxy pucks, with the image on the left being the epoxy puck with TRISO particles exposed down to the zirconium kernel (marked with blue arrow) and the image on the right is the unpolished epoxy puck.

Figure 59. Images of the two epoxy pucks containing surrogate TRISO particles from South Africa.

The TRISO particle tensile samples was fabricated using the SEM, FIB, platinum GIS, and nano-manipulator for lift-out process. The same style of micro tensile sample pin stub set-up used for the baseline material tensile samples was employed with the exposed TRISO particle epoxy puck opposite on top of the custom-made aluminum sample holder attachment. The micro tensile sample pin stub set-up used for the TRISO tensile sample was fitted with three molybdenum lift-out grids. The molybdenum lift-out grids were chosen because molybdenum is less ductile than the copper and thinner than the silicon lift-out grids. These qualities provided a stable base for the tensile samples that was relatively easy to fabricate. The exposed TRISO particle epoxy puck, measuring 4 mm thick, was placed on top of a 6 mm thick black plastic foam block to elevate the surface of the epoxy puck closer the same level as the molybdenum lift-out grids on the micro tensile sample pin stub set-up. This TRISO particle sample assembly was wrapped in copper tape running near the exposed surrogate TRISO particles to provide a discharge outlet for any buildup of charge caused by the FIB and SEM in the Dual Beam. An image of the TRISO particle tensile

sample assembly and illustration of this assembly relative to the electron and ion beams can be seen in Fig. 60. Note that while the direction of micro tensile sample pin stub set-up is different between the image and illustration, this detail is unimportant because the stage rotation can compensate.

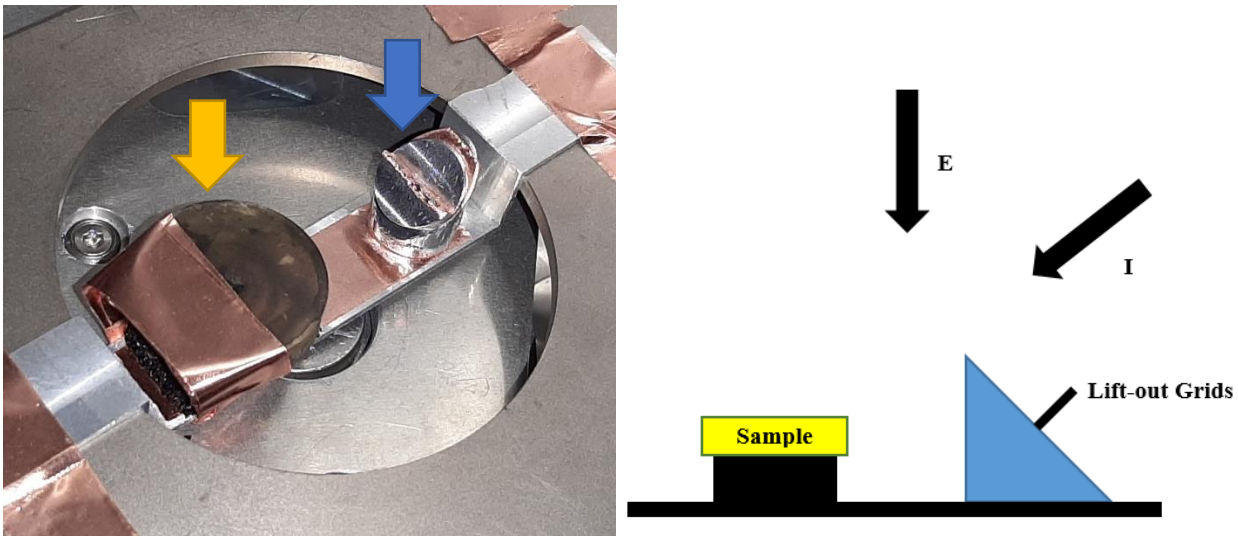

Figure 60. Image of the TRISO particle tensile sample assembly (yellow arrow) and micro tensile sample pin stub set-up (blue arrow) and an illustration of the assembly relative to the electron and ion beams.

The first step in fabricating the TRISO particle tensile sample was bringing the stage to eucentric height and tilting it 52 degrees to aim the ion beam directly at the desired location on the TRISO particle. The stage had to be tilted 52 degrees rather than 7 degrees because the TRISO particle epoxy puck was lying flat (0 degrees) on the stage rather than being placed on the 45° pin stub holder. When the stage was properly aligned, four trenches were cut into the face of the TRISO particle to expose a 50-μm wide by 30-μm tall block. The trench cuts extended 20-μm from the face of the block and were cut 20-μm deep into the sample. A 10-μm opening in the

trench cuts was left in the upper right hand corner to allow for a bridge between the block and the rest of the sample. The trench cuts utilized a regular cross-section pattern in the FEI user interface software and were conducted with the five nano-amp aperture. This particular TRISO particle micro tensile sample was cut across the buffer-IPyC boundary interface, so it was imperative that the trench cuts were aligned perfectly along the interface. An illustration of the four trench cuts around the block face aligned with the buffer-IPyC interface from the perspective of the ion beam can be seen in Fig. 61. The second step involved tilting the stage to zero degrees and aiming the ion beam 8-μm down from the face of the block and cutting a 2-µm thick section along the side of the block until the underside of the block was exposed. Because the stage is at zero degrees, the ion beam entered into the block at 52 degrees. When one side of the block was cut, the stage was rotated 180 degrees and the other side of the block was cut in a similar fashion. These cuts were conducted with the one nano-amp aperture. An image of the completed TRISO particle block from steps one and two can be seen in Fig. 62.

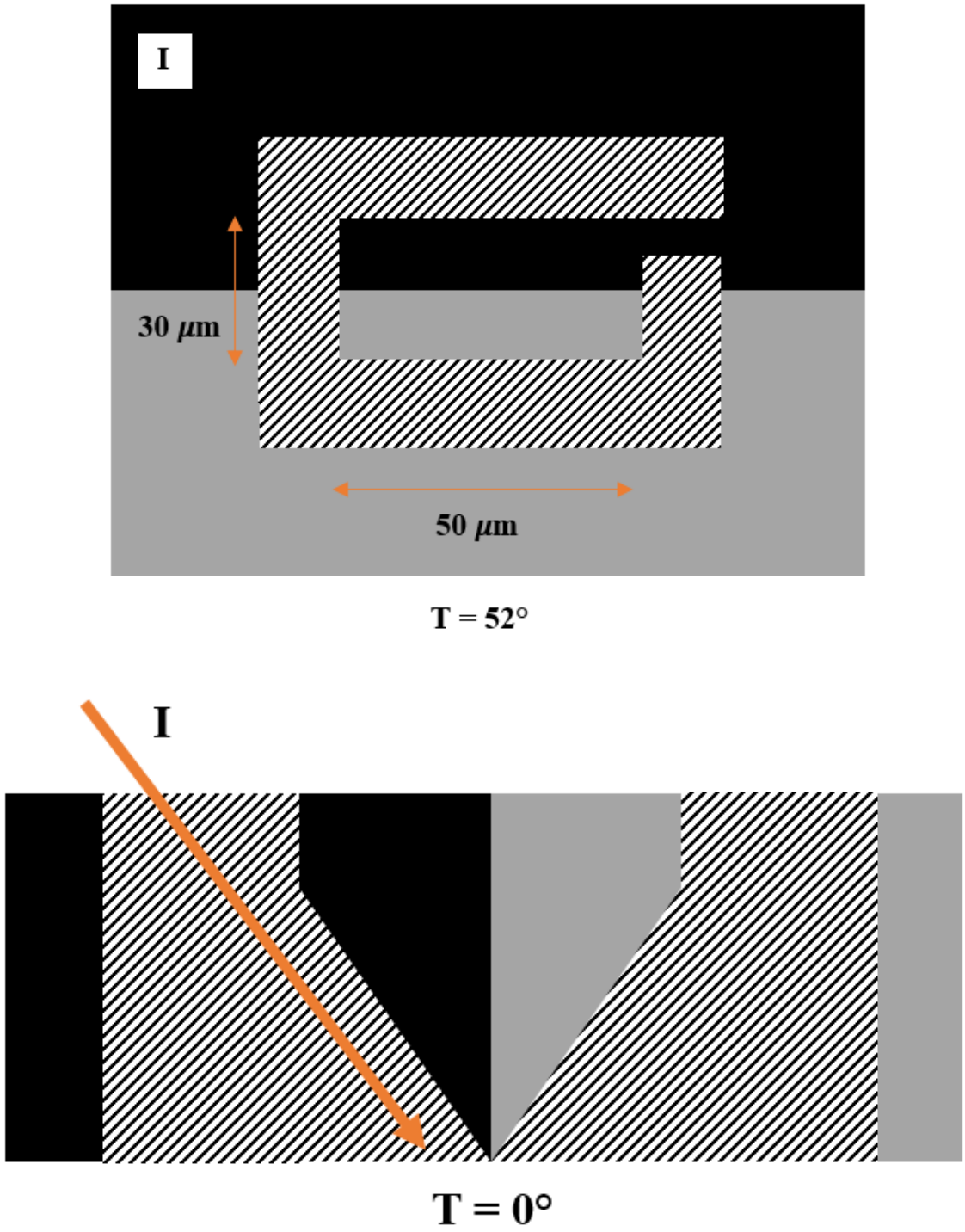

Figure 61. The illustration on top displays the dimensions of the exposed TRISO particle block and the four trench cuts from the perspective of the ion beam. The illustration on bottom displays the side view perspective of the TRISO particle block undercuts. The black background represents the IPyC layer, the gray background represents the buffer layer, and the orange arrow represents the ion beam.

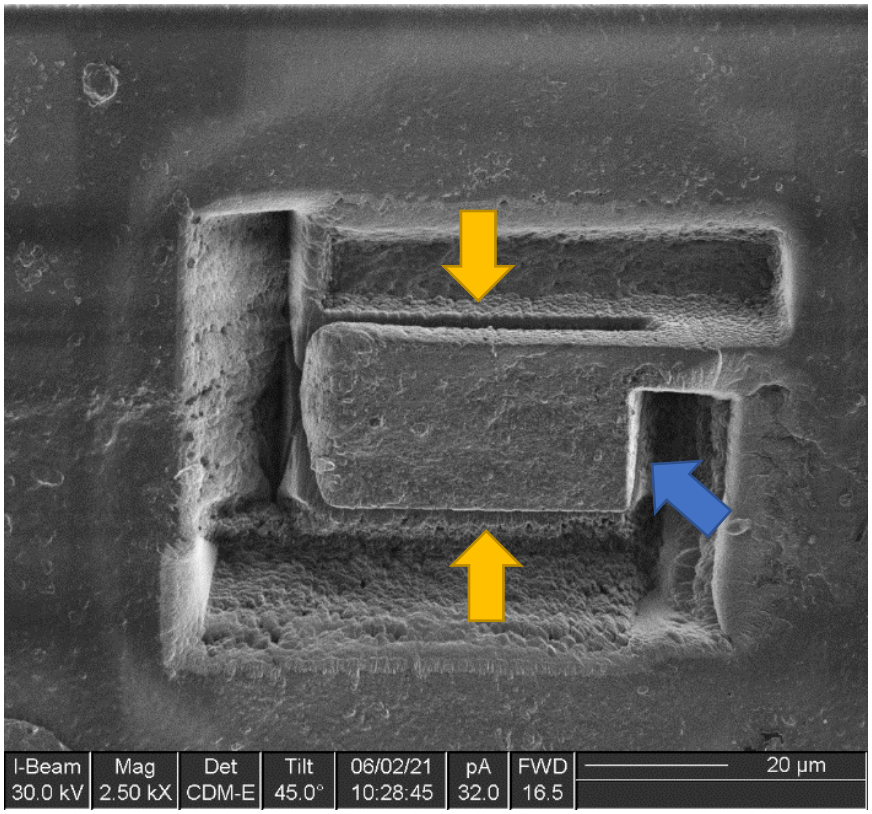

Figure 62. Image of the completed TRISO particle block from step one, with TRISO particle block surrounded by four trenches marked with a blue arrow and the side undercuts marked with yellow arrows.

The third step required tilting the stage to 45 degrees, inserting the nano-manipulator needle and attaching it to the TRISO particle block face with a platinum weld, and cutting the TRISO particle block bridge. It was necessary to tilt the stage to 45 degrees so that when the block was welded to the nano manipulator needle and later mounted to the side of one of the molybdenum lift-out grids it would be properly aligned with the micro tensile sample pin stub set-up and ion beam. After properly tilting the stage, the nano-manipulator needle was inserted and placed in contact on the side of the TRISO particle block face. It was imperative that the needle was on the side of the TRISO particle block face as to allow clean detachment from the block later. The nano manipulator needle was then welded to the TRISO particle block face using platinum GIS.

Platinum was chosen because it is a more robust and durable material for welding. When a solid weld was formed, the TRISO particle block bridge was cut from the main TRISO particle block. The bridge was holding up the entire block after the side undercuts reformed, so after the nano-manipulator needle was welded to the TRISO particle block face it was removed so as to not obstruct the lift-out process. An illustration of the stage at 45 degrees in relation to the electron ion beams and an image of the TRISO particle block during step three can be seen in Fig. 63.

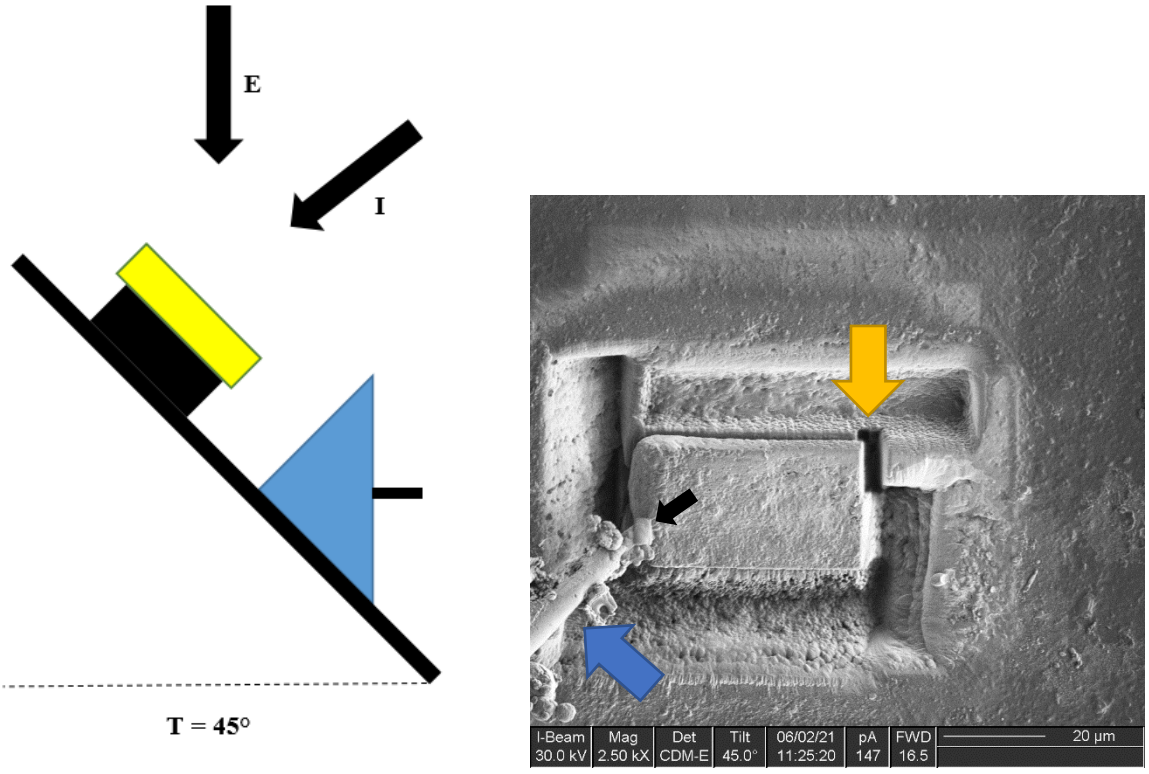

Figure 63. An illustration the stage at 45 degrees in relation to the electron ion beams and an image of the TRISO particle block during step three. The nano-manipulator needle is marked with the blue arrow, platinum weld marked with the black arrow, and cut bridge marked with the yellow arrow.

After the nano-manipulator needle was securely welded and the TRISO particle block was cut loose from the rest of the sample, the block was lifted up and out of the sample surface.

The images in Fig. 64 demonstrate the TRISO particle block being lifted from the sample surface.

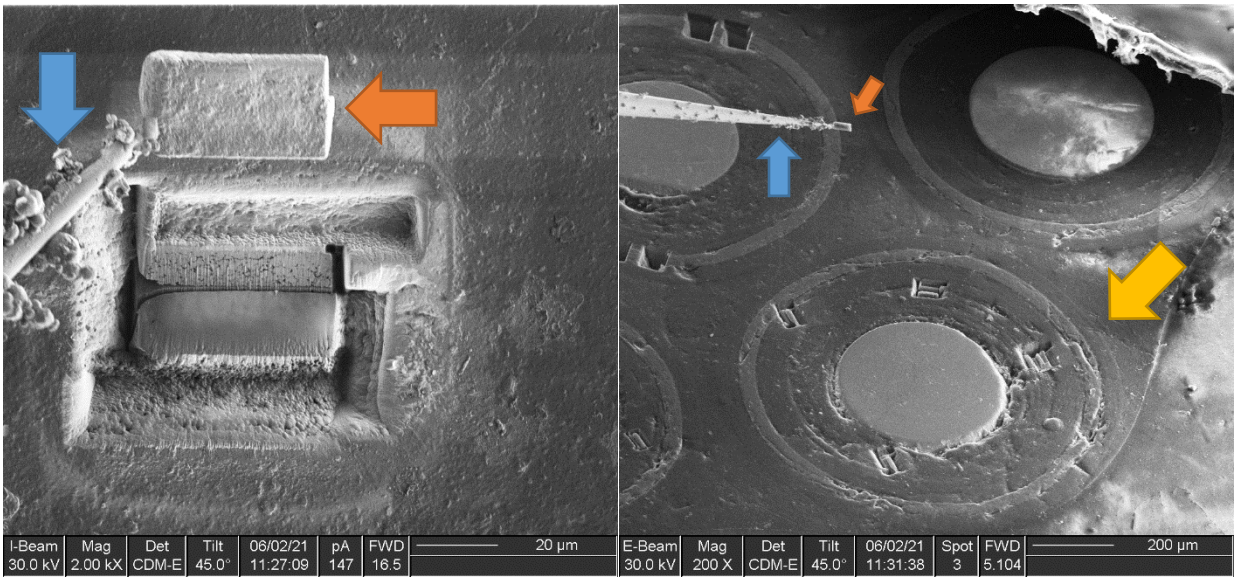

Figure 64. Image on left shows a TRISO particle block just recently lifted from the sample. Image on the right displays the lifted out block as seen from a lower magnification and further from the sample surface. The blue arrows mark the nano-manipulator needle, the orange arrows mark the TRISO particle block, and the yellow arrow marks the host TRISO particle.

The next step included retracting the nano-manipulator needle, tilting the stage to zero degrees, rotating the stage hundred 180 degrees, reinserting the nano-manipulator needle with TRISO particle block attached, and welding the TRISO particle block to the molybdenum lift-out grid. The TRISO particle block was welded further up the side of the molybdenum lift-out grid than the final TRISO particle micro tensile sample so as to prevent interference between the two. It is noted that the TRISO particle block images vary between figures in this section, because the lift-out process is difficult and not every sample survived this process. Illustrations and images of step five, TRISO particle block mounting process, can be seen in Fig. 65.

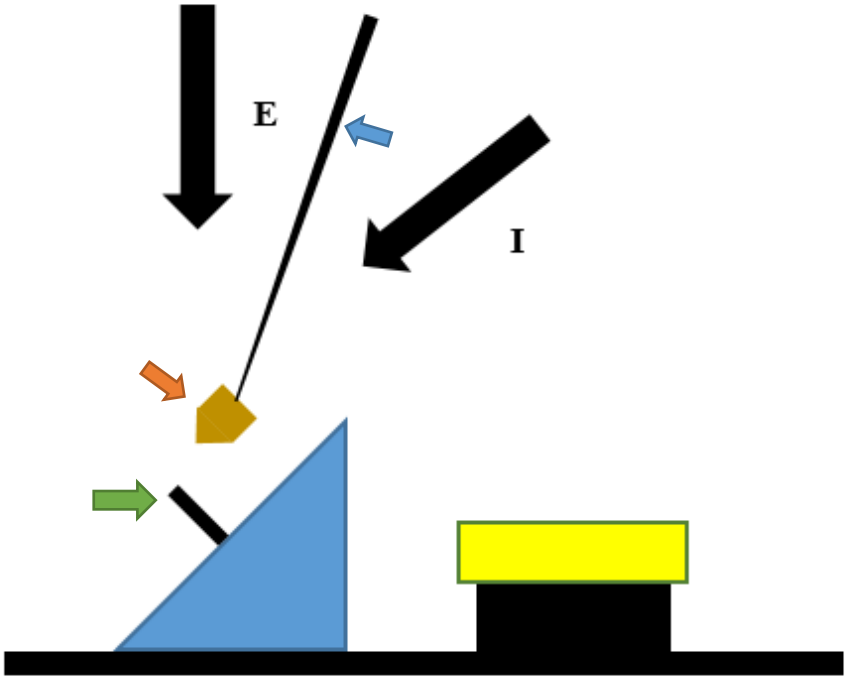

R = 180°

T = 0°

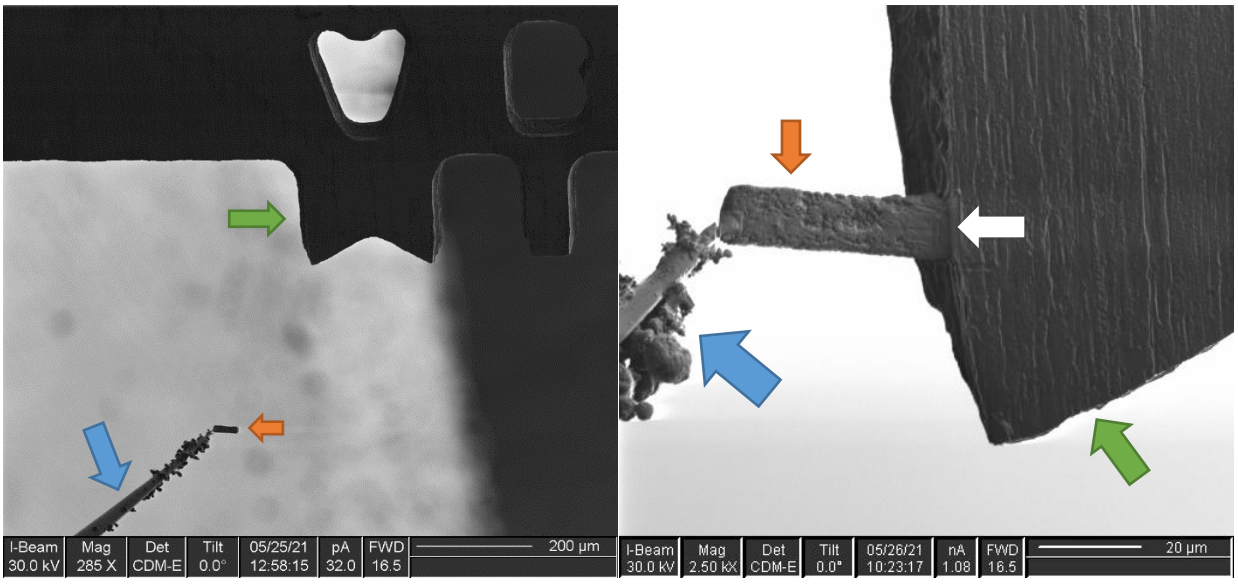

Figure 65. Illustrations and images of step five TRISO particle block mounting process. The nano-manipulator needle is by the blue arrows, the TRISO particle block marked by the orange arrows, the molybdenum lift-out grid marked by the green arrows, and the platinum weld marked by the white arrow.

After the TRISO particle block was mounted and the nano-manipulator needle was cut off from the TRISO particle block and retracted, the stage was rotated 180 degrees and tilted seven degrees to aim the side of the TRISO particle block directly at the ion beam to start the TRISO particle block thinning process. At the start of this process the block was shaped like an inverted house and was approximately 10-µm thick from top to bottom, unusable for creating lamella. To convert the TRISO particle block into a usable lamella it was thinned to 2-µm using the one nano-amp aperture. Illustrations and images of step six, the TRISO particle block thinning process, are shown in Fig. 66.

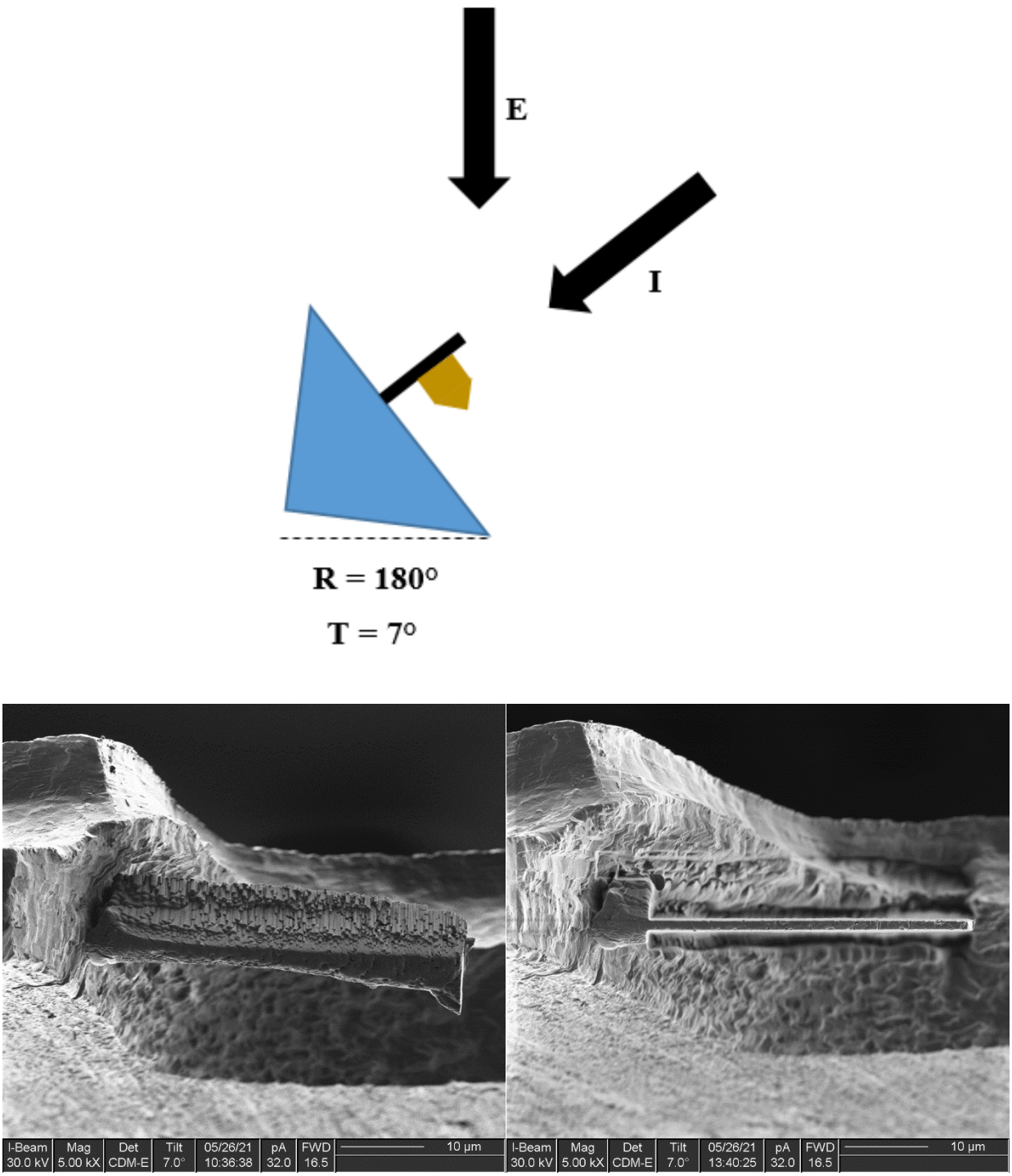

Figure 66. Illustrations and images of the step six TRISO particle block thinning process, with an illustration of the stage relative to the electron and ion beam shown on top, TRISO particle block shown on the left, and the thinned TRISO particle lamella shown on the right.

When the TRISO particle block was thinned and TRISO particle lamella created the stage was rotated 180 degrees to align the TRISO particle lamella for the final stage, the TRISO particle micro tensile sample fabrication process. Small notches 8-µm wide were cut into the tips of each of the molybdenum lift-out grid posts. One of these notches later served as the foothold placement of the TRISO particle micro tensile sample dog bone. These notches are meant to create greater surface area for the molybdenum posts and TRISO dog bones to attach to each other during the platinum weld. Images of the perpendicular view of the TRISO particle lamella and the notch used as a TRISO dog bone foothold can be seen in Fig. 67. The buffer-IPyC interface can be seen meandering horizontally through the centerline of the TRISO particle lamella.

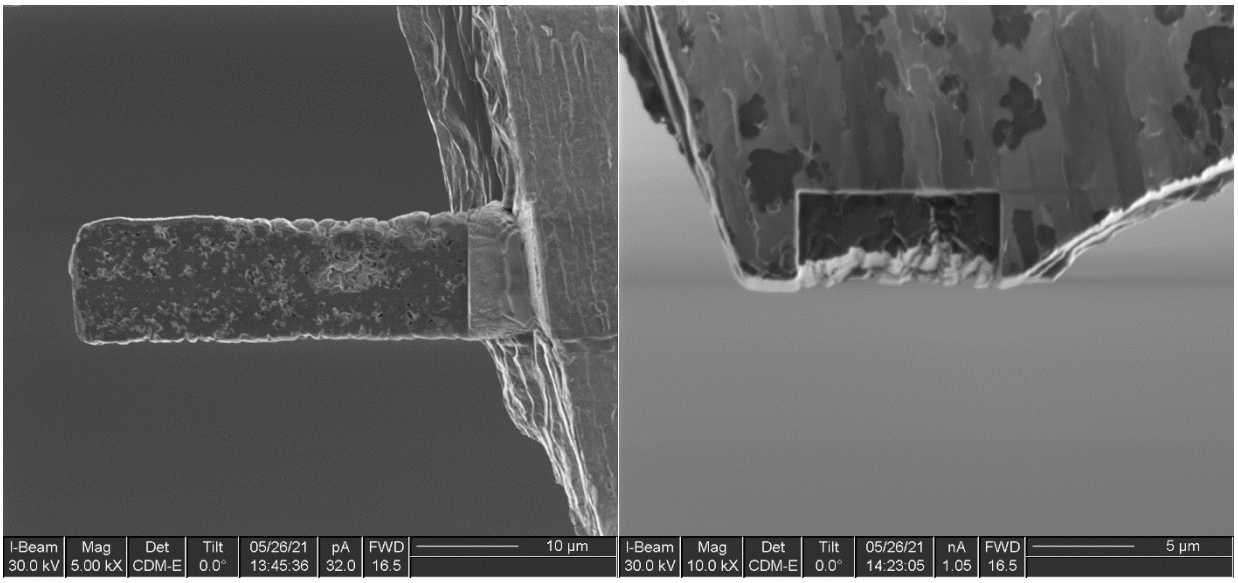

Figure 67. Images of the perpendicular view of the TRISO particle lamella and the notch used as a TRISO dog bone foothold, with the TRISO particle lamella on the left and the notch on the right.

The next step was fabricating the TRISO particle lamella piece. To achieve this the nano-manipulator needle was reinserted into the Dual Beam's vacuum chamber next to the TRISO

particle lamella. The nano-manipulator needle was welded to the side of the TRISO particle lamella and a vertical cut conducted 8-µm to the right of the needle placement using the one nano-amp aperture. From this cut an 8-µm wide piece of the TRISO particle lamella was maneuvered over to the first notch on the molybdenum lift-out grid post. With the TRISO particle lamella being 50-µm wide it can accomodate up to five TRISO particle lamella pieces. Images of the TRISO particle lamella fabrication process can be seen in Fig. 68.

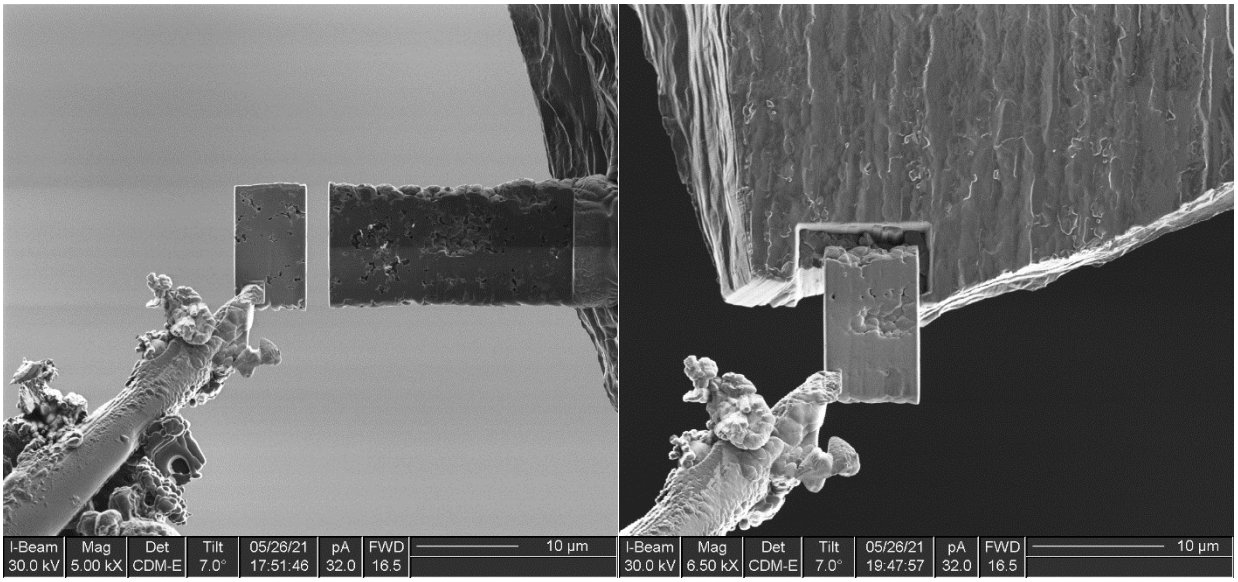

Figure 68. Image on the left displays the TRISO particle lamella piece being removed from the bulk TRISO particle lamella and the image on the right shows the TRISO particle lamella piece being the maneuvered over the molybdenum lift-out grid notch.

The final step in creating the TRISO particle micro tensile samples was creating the TRISO particle dog bone. The TRISO particle lamella was welded with platinum to the molybdenum lift-out post notch and the nano-manipulator needle was cut from the TRISO particle lamella piece. When the TRISO particle lamella piece was standing by itself, two 3-μm wide by 6-μm tall cuts were placed parallel to each other to create the dog bone shape. With the dog bone nearly complete,

the final step was rotating the stage 180 degrees and cutting away any remaining platinum weld from the depth by width cross-section of the TRISO particle dog bone. All these cuts were performed with the one nano-amp aperture. The TRISO particle dog bone was designed to be 15-μm tall, 8-μm wide, and 2-μm thick with a tensile gauge section 6-μm tall by 2-μm wide and a bottom portion (head section) 4-μm tall. Images of the final steps of the TRISO particle dog bone fabrication process can be seen in Fig. 69.

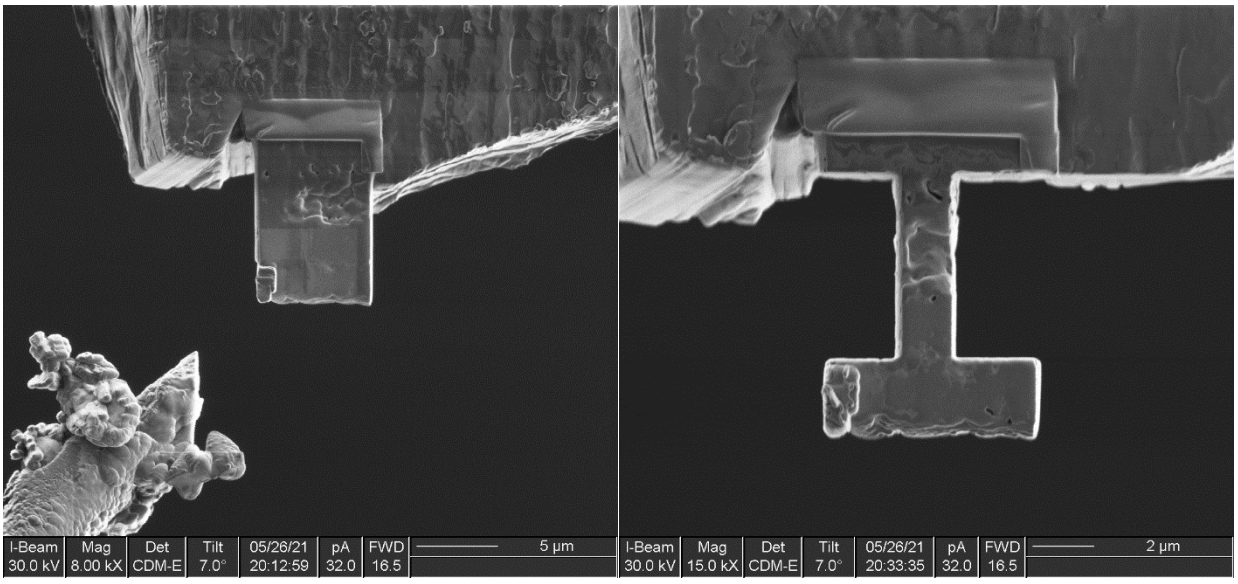

Figure 69. Image on left is the TRISO particle lamella piece platinum welded to the molybdenum lift-out grid post and the image on the right is of the completed TRISO particle dog bone.

3.3 Tensile Sample Strength Testing

After the micro tensile samples were fabricated, they were pulled with the diamond gripper inside the PI 88 PicoIndenter to determine their tensile strength and other mechanical values. This process was started by screwing the diamond gripper probe onto the transducers threaded post, making sure the black mark originally placed there was still aligned properly. The 90° pin stub

holders containing the fabricated micro tensile samples where then placed into the PI 88's sample mount. Because the lift-out grids were only attached with the copper tape, there was a chance that they would drift during the tensile test. In order to limit the possibility of this occurrence, the back of the lift-out grids was painted with silver paint to the 90° pin stub holder. The silver paint ancors the lift-out grids to the pin stub holder and provides a discharge path for any charge buildup accrued from the SEM. When the diamond gripper and pin stub holder were set properly, the PI 88 was positioned into the Versa 3D's vacuum chamber and set-up for testing. An image of the diamond gripper and 90° pin stub holder containing the fabricated micro tensile samples set in the PI 88 can be seen in Fig. 70. An image of the PI 88 being placed into the Versa 3D is shown in Fig. 71.

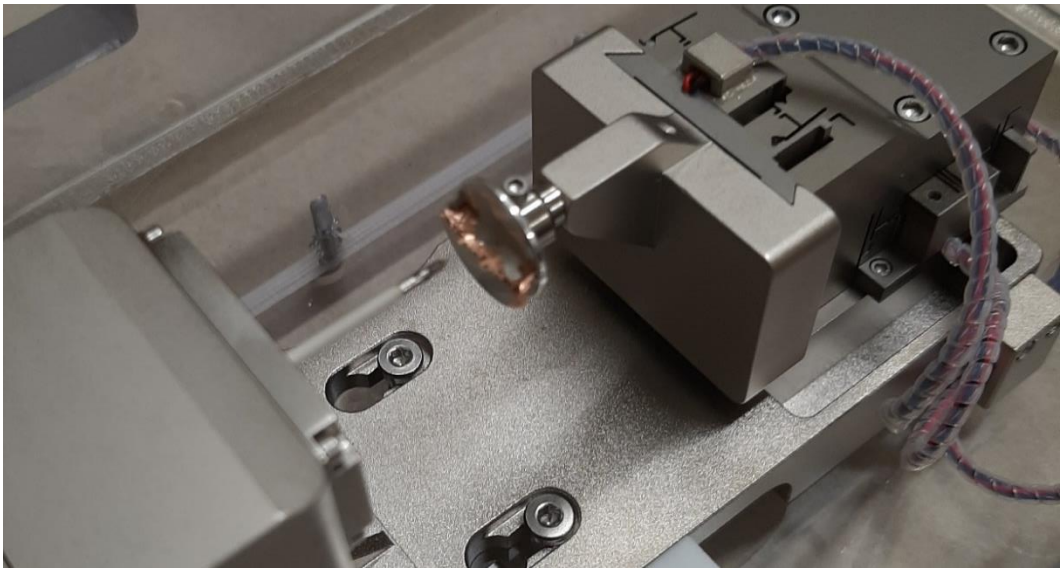

Figure 70. Image of the diamond gripper and 90° pin stub holder containing the fabricated micro tensile samples set in the PI 88.

Figure 71. Image of the PI 88, with micro tensile samples loaded, being placed into the chamber of the Versa 3D.

When the PI 88 was ready inside the Versa 3D, the diamond grippers were aligned with the dog bone tensile samples. Because the transducer's threaded post containing the diamond grippers has limited mobility, the PI 88 stage containing the dog bone micro tensile samples was used for aligning the samples. The diamond gripper and dog bone micro tensile samples were incrementally maneuvered closer together with the stage until the dog bone tensile sample rested squarely within the diamond grippers inner cavity. The images shown in Fig. 72 exhibit the diamond gripper and micro tensile samples moving closer together.

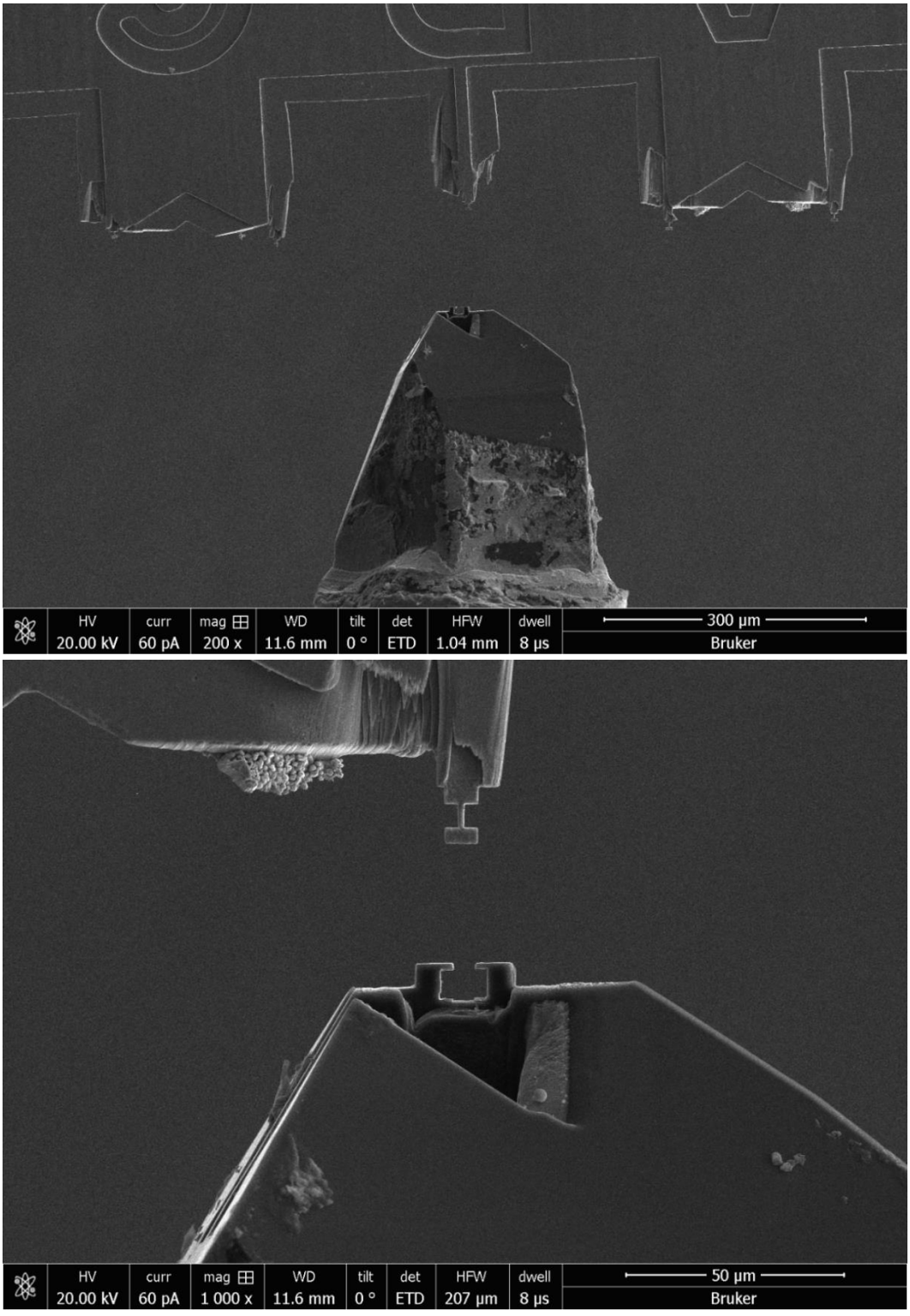

Figure 72. Diamond gripper and micro tensile samples moving closer together, with the top image being a panoramic view of the diamond gripper and one of the copper lift-out grids containing micro tensile sample dog bones and the bottom image showing a smaller distance between the diamond grippers and samples.

The dog bones were maneuvered into the inner cavity of the diamond grippers by first making sure they were not at the same height as each other (Z direction) and maneuvering the dog bone squarely into the cavity of the diamond gripper in the XY direction. This provided two benefits, the first being that the diamond gripper didn't accidentally run into the sample while maneuvering and the second being that as the sample was maneuvered one could tell whether it was above or below the diamond gripper. Once aligned in the XY direction, the sample was either raised or lowered in the Z direction until it became in focus with the diamond gripper, with the user making minor adjustments in the XY direction. One could tell that the diamond gripper and sample were closely aligned when either the sample or the gripper cast an electron shadow onto the other one. Once this electron shadow had been spotted and sample in grippers were closely aligned, a touch test was performed by lightly lowering the diamond gripper onto the head of the dog bone sample in the Y direction. Because the PI 88 is continually taking force measurements and is reporting them to the TriboScan software when it is turned on, if the force reading went up when the diamond gripper was lowered this means that the sample and diamond gripper were in contact with one another. If no change in force reading was reported the diamond gripper and sample were out of alignment and needed further adjusting. The image seen in Fig. 73 exhibits the diamond gripper and a copper dog bone tensile sample in proper alignment.

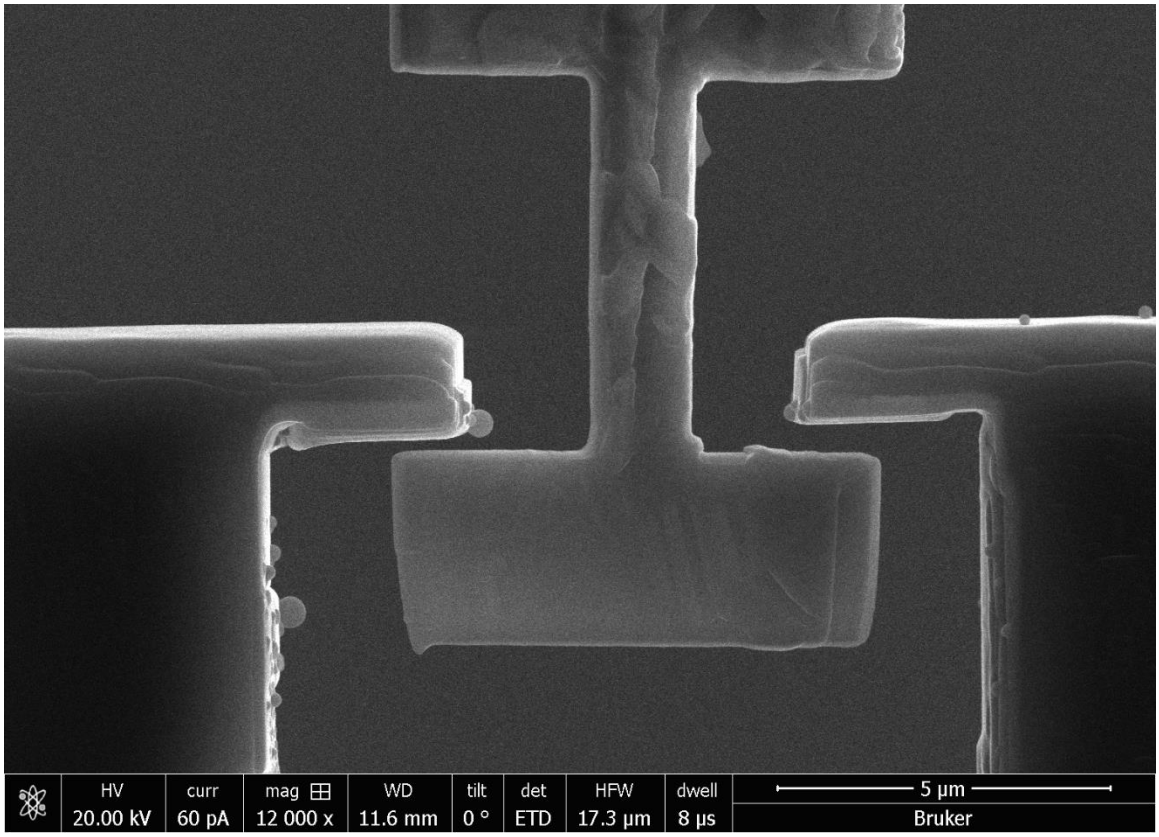

Figure 73. The diamond gripper and a copper dog bone tensile sample in proper alignment for tensile testing.

When it was confirmed that the sample was properly aligned inside the inner cavity of the diamond grippers, the inverse load function was initiated in the TriboScan software. This simply means that instead of the PI 88 PicoIndenter indenting into the sample it would pull away from the sample. This pulling action is what is required for a tensile test. The load function set the transducer to move the diamond gripper at 100-nm a second for a maximum of 33 seconds, stopping and reversing directions in the middle of the load function to return the diamond gripper to its initial position. The transducer measured the force applied to the diamond gripper in micro newtons and recorded this force throughout the totality of the load function. The results of these tests are discussed in further detail in the analysis section. The image in Fig. 74 shows one of the copper dog bone micro tensile samples after testing.

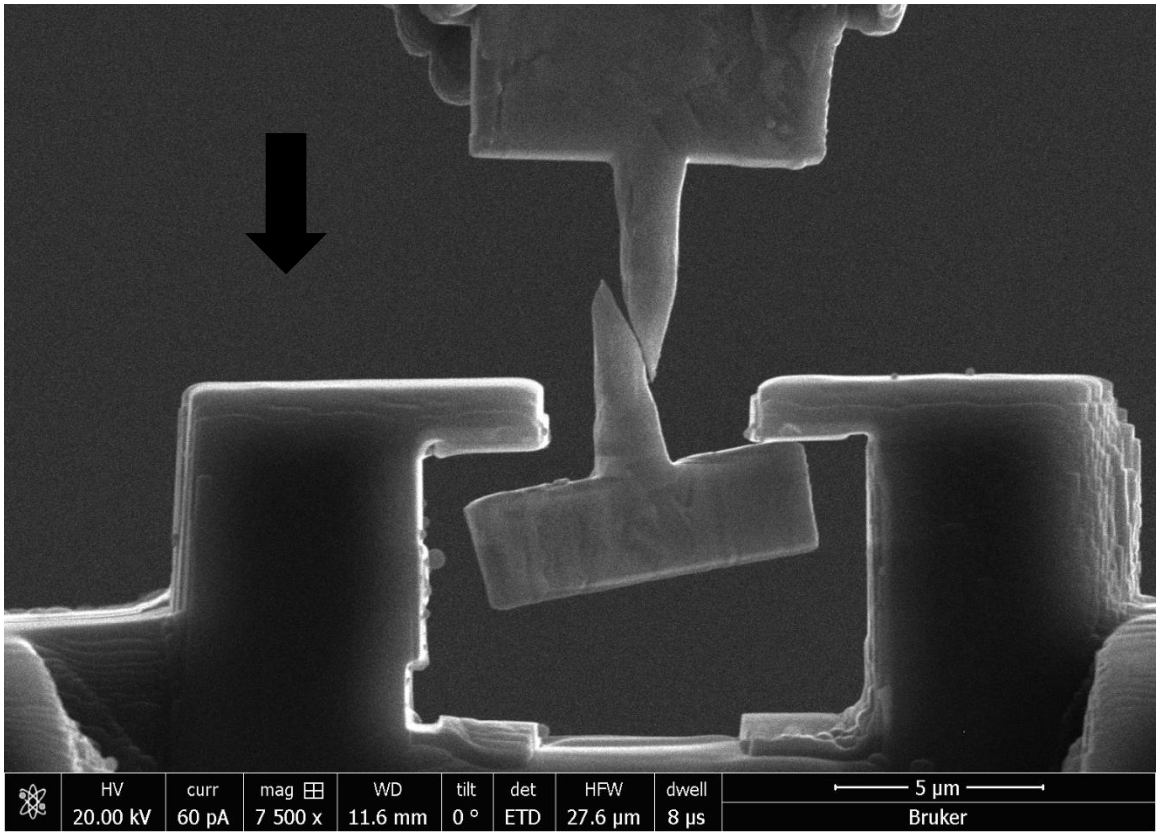

Figure 74. An example of a copper dog bone micro tensile sample post tensile test, with the black arrow pointing in the loading direction of the test.

4.0 Analysis

This section refers the results of the micro tensile tests and how they were obtained. This section also includes possible explanations as to why the micro tensile samples behaved the ways they did.

4.1 Theory

Many mechanical characteristics of a material can be determined through tensile testing. The most important values include yield strength, ultimate tensile strength, fracture strength,

modulus of elasticity, elastic deformation, uniform strain, and total strain (Dieter, 1961). In order to determine these values, we need to define some variables: depth, load, cross-sectional area, height, engineering stress, engineering strain, true stress, and true strain. Depth is the distance traveled by the gripper (and thus the sample as well) during the tensile test and load is the force detected, both being cross-referenced with time. Cross-sectional area is the surface area of the depth by width cross section of the tensile gauge section. Height is simply the height of the tensile gauge section. These four variables can be used to determine the remaining four variables. Engineering stress is defined as:

Equation 1. Engineering Stress

$$\sigma_{eng} = \frac{P}{A_0}$$

With P being the load and A_0 being the original cross-sectional area. When using metric units engineering stress will be expressed as newtons per metres squared, or pascals. Engineering strain is defined as:

Equation 2. Engineering Strain

$$\varepsilon_{eng} = \frac{\Delta L}{L_0}$$

With ΔL being the depth (current position minus original position) and L_0 being the original height of the tensile gauge section. Strain is unitless and is often expressed as a percentage. Strain is useful in that it determines how much a material has deformed in relation to its original length. True stress is defined as:

Equation 3. True Stress One

$$\boldsymbol{\sigma_{true} = \frac{P}{A}}$$

or

Equation 4. True Stress Two

$$\boldsymbol{\sigma_{true} = \sigma_{eng}(1 + \varepsilon_{eng})}$$

With $\boldsymbol{P}$ being the load, $\boldsymbol{A}$ being the current cross-sectional area, $\boldsymbol{\sigma_{eng}}$ being the engineering stress, and $\boldsymbol{\varepsilon_{eng}}$ being the engineering strain. True stress is meant to depict a more accurate measure of stress for ductile materials than engineering stress because it measures the stress as the material is deforming and thus cross-sectional area is changing. While Equation 3. represents the purest form of true stress, it is only useful if one can accurately measure the changing cross-sectional area as the tensile test progresses. This is an incredibly difficult and laborious task, so Equation 4. is much more convenient. Equation 4. attempts to predict true stress using the relationship between the already known engineering stress and engineering strain and is the method used in this thesis. True strain is defined as:

Equation 5. True Strain One

$$\boldsymbol{\varepsilon_{true} = \ln\left(\frac{L}{L_0}\right)}$$

or

Equation 6. True Strain Two

$$\boldsymbol{\varepsilon_{true} = \ln(1 + \varepsilon_{eng})}$$

With $\boldsymbol{L}$ being the current height of the tensile gauge section, $\boldsymbol{L_0}$ being the original height of the tensile gauge section, and $\boldsymbol{\varepsilon_{eng}}$ being the engineering strain. True strain is meant to depict a more accurate measure of strain in ductile materials. While Equation 5. is the most direct way to calculate true strain, it is a difficult and laborious task because of the variable $\boldsymbol{L}$. Equation 6. predicts true strain using the already known engineering strain and is the method used in this thesis.

When comparing the variables mentioned above against each other, one can make graphs that can be used to determine certain mechanical values of a material. The two graph types used in this thesis are depth and load versus time and stress versus strain (for both engineering stress/strain and true stress/strain). While the depth and load versus time graph isn't useful for directly determining the desired mechanical values, it is helpful for visualizing the forces and distances involved during the tensile test and for cropping unwanted data. The unwanted data includes pretest disturbances, post tensile sample failure ringing, and posttest unloading. The stress versus strain graph is what is used for defining the desired mechanical values. One of these values, yield strength, is defined as the amount of stress a material can handle before permanent plastic deformation takes place. Yield strength sets the stress limit for any working ductile material, since exceeding the yield strength will permanently damage the material beyond repair. Yield strength is found by locating the intercept between the stress-strain curve of the material and a linear line with the same slope as the modulus of elasticity and is typically offset by 0.002 or 0.2% of the strain. An example of this intercept interaction can be seen in Fig. 75. The modulus of elasticity is the same as Young's modulus, or the slope of the stress-strain curve in the elastic region. Elastic

deformation is the amount of deformation recovered after the tensile test is over. The maximum elastic deformation achievable is dependent on the strain value of the yield strength. The ultimate tensile strength is the maximum stress experienced by the material during the tensile test. This value is important because exceeding this value quickly leads to the failure of the material (fracture). A material should never go beyond the ultimate tensile strength in practice. Uniform strain is defined as a strain value at the ultimate tensile strength. This is an important value in determining the deformation of the material when at ultimate tensile strength. The fracture strength is when the material finally does fracture. This value is not as important as ultimate tensile strength in ductile materials but is equivalent in brittle materials. This value will always be lower than the ultimate tensile strength in ductile materials. Total strain is the strain at the fracture strength. This will determine the maximum length and deformation of the material during the test.

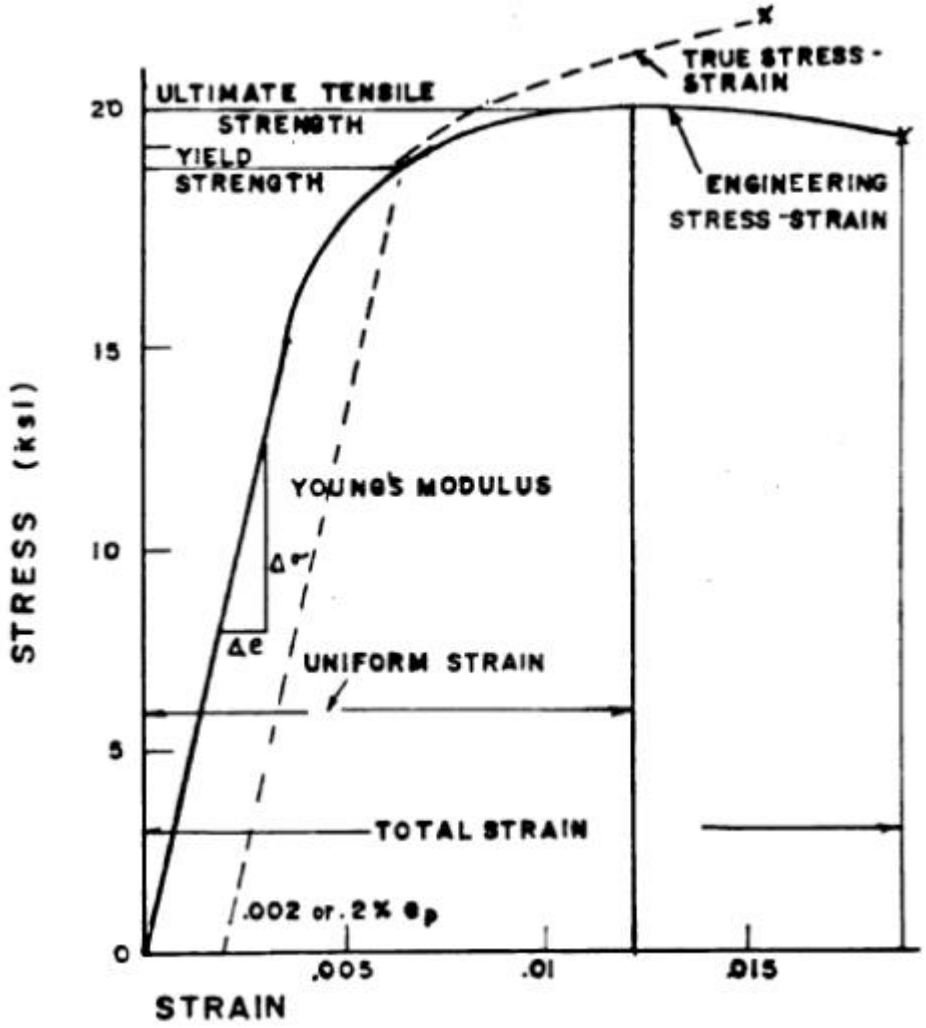

Figure 75. Example of a stress-strain curve illustrating the many important mechanical values unveiled during tensile testing (Dieter, 1961).

The mechanical values described above can be used to differentiate varying stress-strain properties between graphs, and ultimately the characteristics of materials. For instance, it should be noted that the yield strength is mostly only useful for ductile materials, since brittle materials typically do not undergo plastic deformation. So while yield strength may be one of the most important values for a ductile material such as copper, ultimate tensile strength is really the only important value for a brittle material such as silicon. The ultimate tensile strength and fracture

strength will also typically be the same value for brittle materials, since they tend to fracture abruptly. The varying importance of these values between ductile and brittle materials is important in the characterization process. Fig. 76 illustrates the differences between ductile, brittle, and variants thereof along the stress-strain curve.

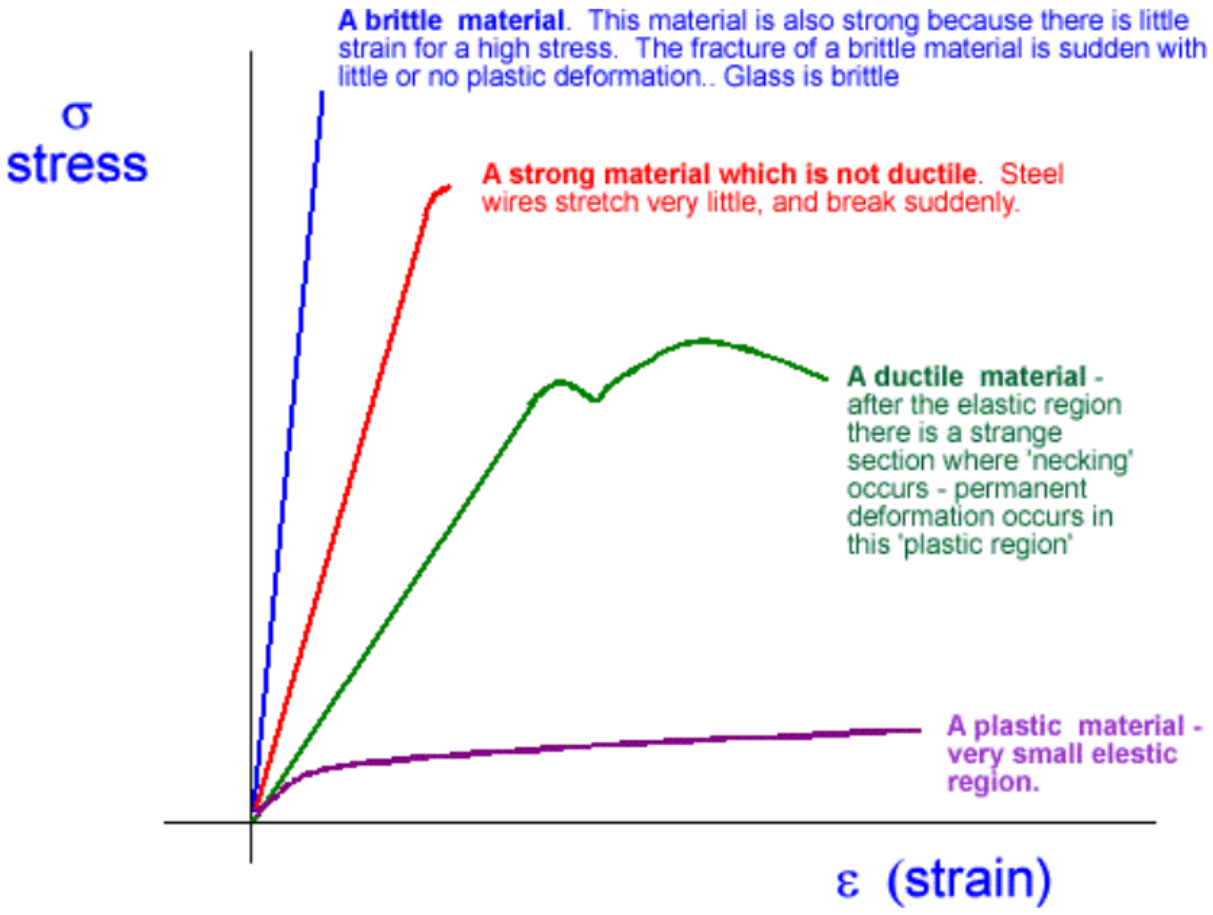

Figure 76. Stress-strain curve illustrating the differences between brittle and ductile materials (ÇAPAR, 2021).

4.2 Baseline Materials

Copper, molybdenum, and silicon tensile samples were used as the baseline materials for this thesis. Copper represents a ductile metal, molybdenum a stronger metal, and silicon a brittle material. Each sample types mechanical value results have been compared to values found in the literature. Each sample is named relative to its position on its respective half grid. For example, sample two is the second sample out of the ten samples total. A height by width cross section image, depth by width cross section image, and post failure image are shown as a reference against the dimensions of the tensile samples. The dimensions of the tensile samples were determined using the measurement tool in the Dual Beam FEI user interface software. All values displayed in the stress-strain graphs and mechanical value tables were determined using the equations shown in the theory section applied in Excel spreadsheets. The raw data (depth, load, and time) was derived from tensile tests performed with the PI 88 PicoIndenter and using TriboScan software. Of the ten copper samples made, seven yielded usable results. Of the ten molybdenum samples made, only two survived before testing. Of those two, only one was testable. Since this sample may have been damaged as well, the validity of its results are questionable. Of the eight silicon samples made, five yielded results. For the sake of convenience and to reduce redundancy, only one full set of results from each of the copper and silicon tensile samples out of all the copper and silicon samples are shown in this section. The remainder of the results from copper and silicon can be found in the appendix.

4.21 Copper Tensile Sample Six

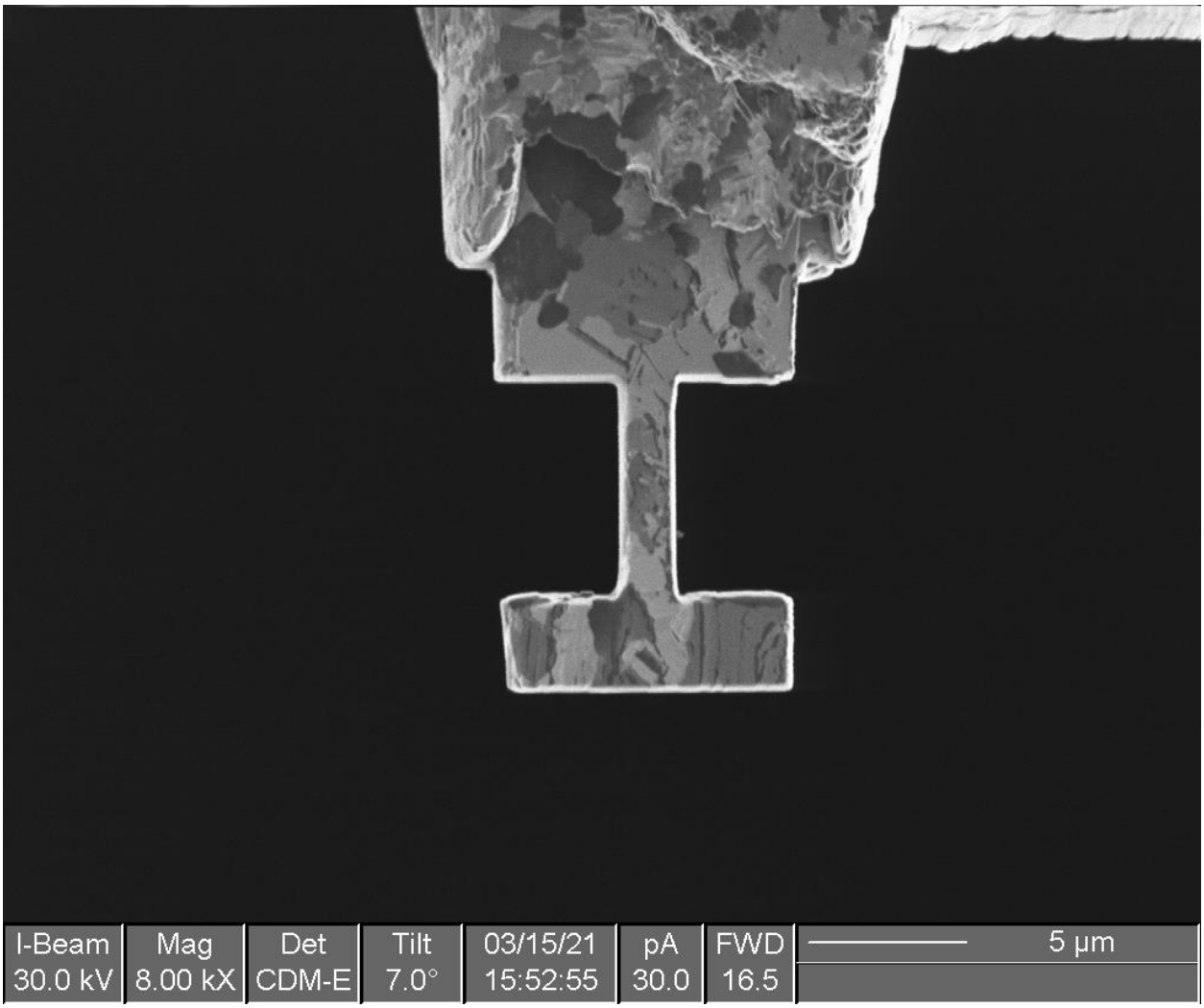

Figure 77. Copper Tensile Sample Six height by width cross section image.

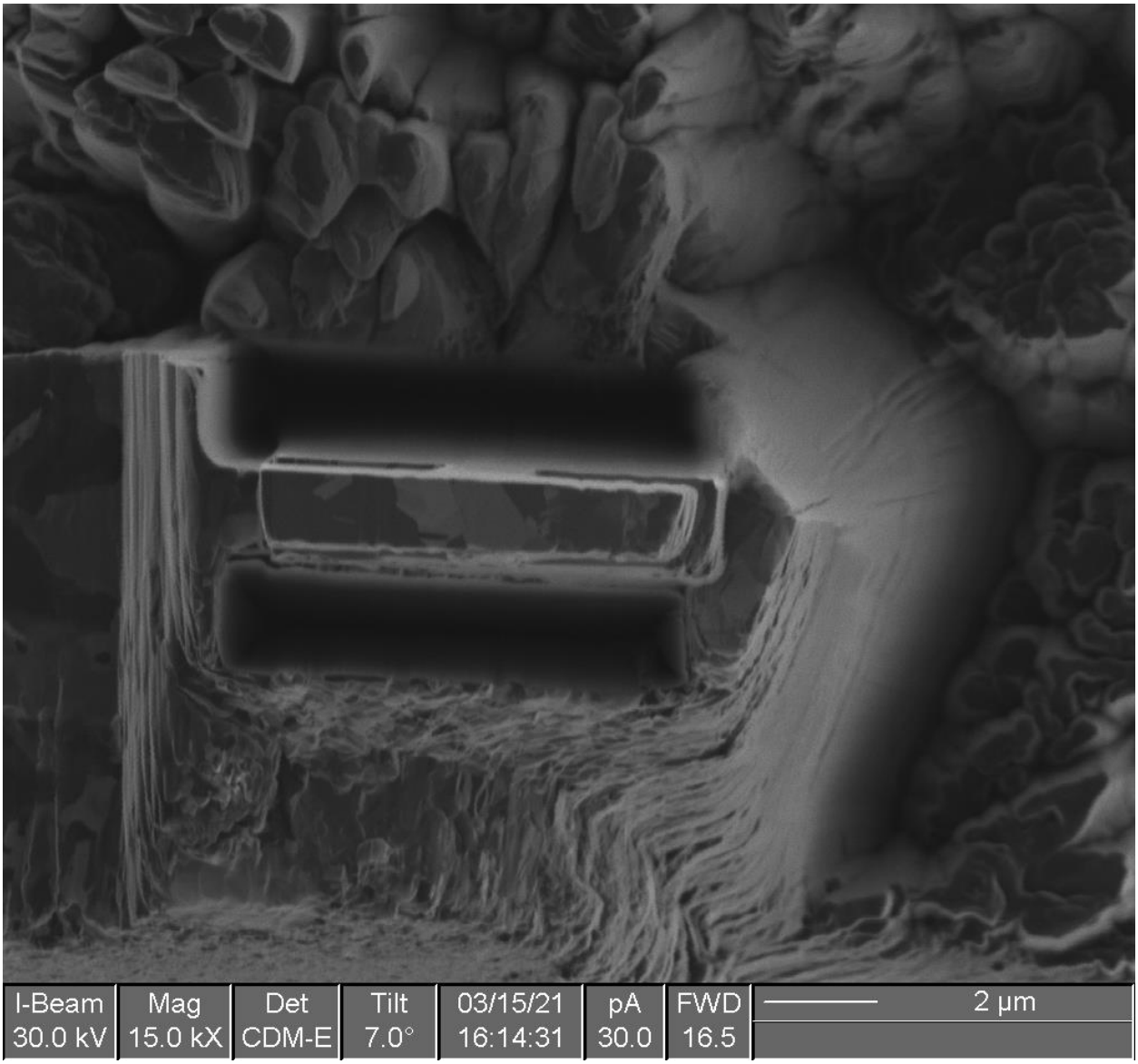

Figure 78. Copper Tensile Sample Six depth by width cross section image.

Notice the necking and deformation that the tensile gauge section experienced in Fig. 79. This is indicative of the ductility of this copper sample.

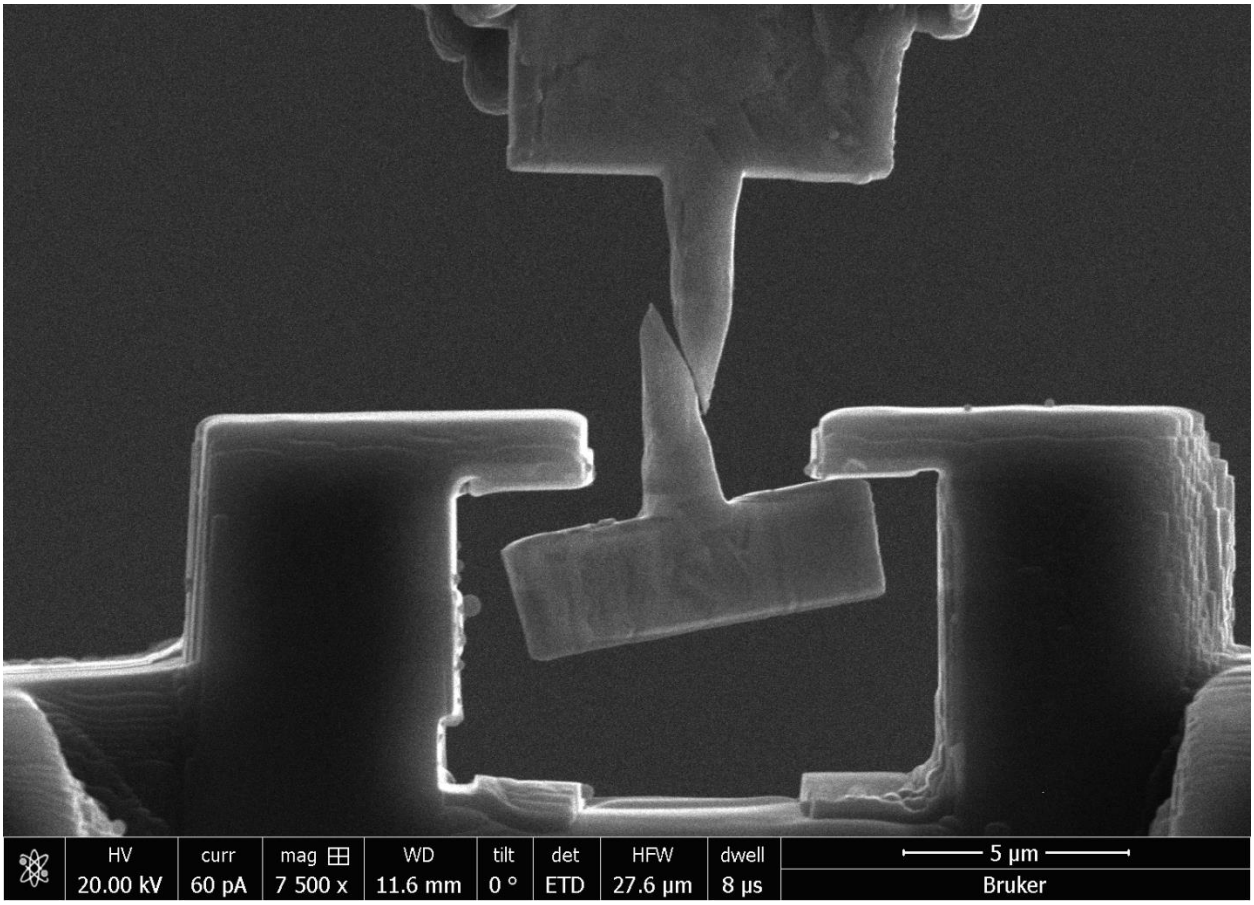

Figure 79. Copper Tensile Sample Six post failure image.

Table 1. Dimensions of Copper Tensile Sample Six, Gauge Section (μm).

Dimensions of Copper Tensile Sample Six, Gauge Section (μm)	
Height	**9.3**
Width	**1.8**
Depth	**1.9**

Notice the smooth progression in depth readings vs time in Fig. 80. This demonstrates the precision of the PI 88's transducer. The jagged portions of the load vs time curve seen in Fig. 80 are due to the relatively large size and impact of the copper crystals in relation to the size of the sample. In macroscopic samples the crystals are miniscule by comparison, so the depth vs time curve is usually smoother.

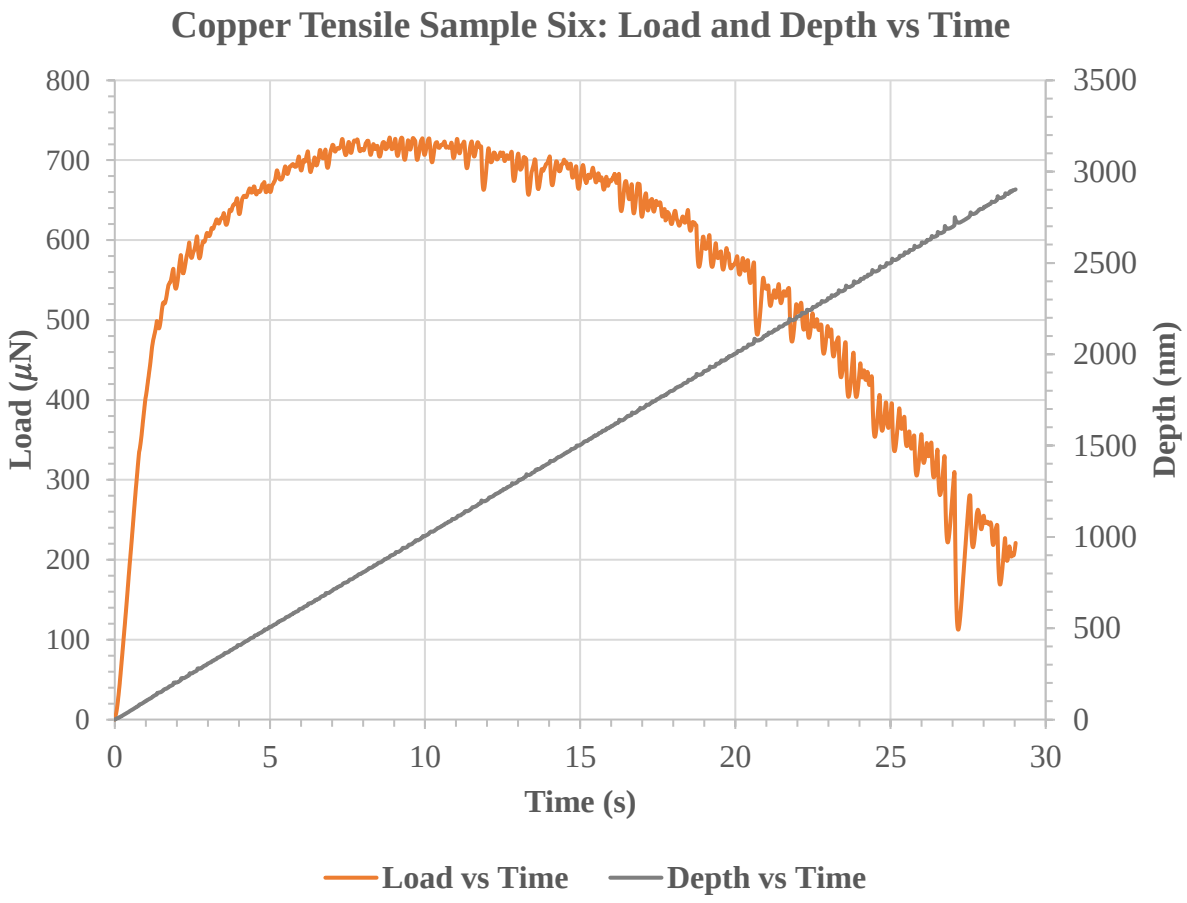

Figure 80. Copper Tensile Sample Six: Load and Depth vs Time.

Notice the large difference in engineering and true stress and the very large plastic region of this copper sample found in Fig. 81. This large plastic region indicates that this copper sample is very ductile and also shows that it deformed a significant amount. In this situation the predictive nature of true stress becomes very important for getting accurate stress readings.

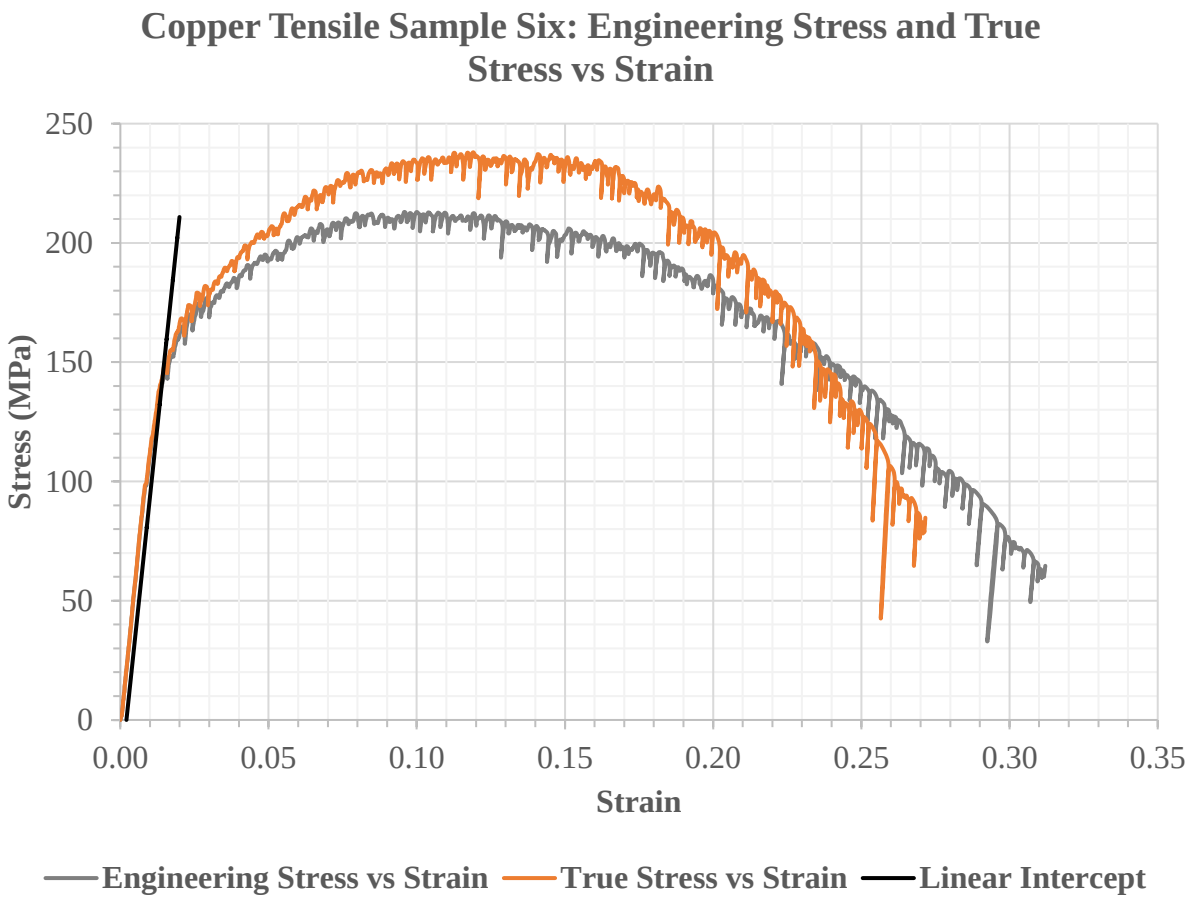

Figure 81. Copper Tensile Sample Six: Engineering Stress and True Stress vs Strain.

Table 2. Copper Tensile Sample Six: Mechanical Values.

Copper Tensile Sample Six: Mechanical Values	
Engineering Yield Strength (at 0.2% offset) (MPa)	**140.811343**
True Yield Strength (at 0.2% offset) (MPa)	**145.381995**
Engineering Max Elastic Deformation (Strain)	**0.014091**
True Max Elastic Deformation (Strain)	**0.014397**
Engineering Ultimate Tensile Strength (MPa)	**212.979903**
True Ultimate Tensile Strength (MPa)	**237.986471**
Engineering Uniform Strain	**0.095868**
True Uniform Strain	**0.119075**
Engineering Fracture Strength (MPa)	**64.622802**
True Fracture Strength (MPa)	**84.790920**
Engineering Total Strain	**0.312090**
True Total Strain	**0.271621**
Modulus of Elasticity (GPa)	**11.672954**

4.22 Copper Comparison

While the nanoscopic sample result from Kiener and Minor were dissimilar to the results in this thesis, when comparing the samples tested in this thesis to the chart seen in Fig. 82, one can see that the results derived in this thesis are in agreement with the results from Kiener and Minors microscopic results.

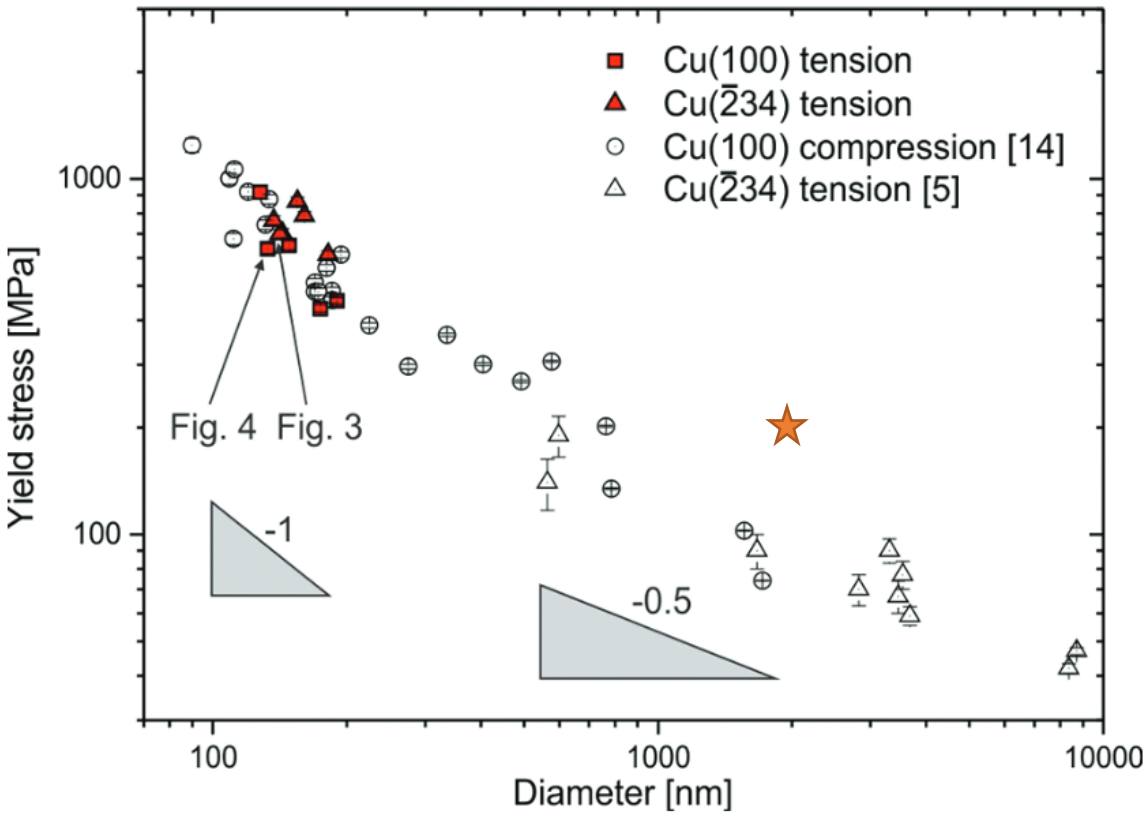

Figure 82. Yield stress (strength) vs diameter chart of nano tensile, nano compression, and micro tensile of copper tensile samples from Kiener and Minor (Kiener & Minor, 2011). The copper samples used in this thesis had diameters ranging from 1000 – 3000 nm and averaged 204 MPa for yield strength. The orange star on the graph represents the placement of the results from this thesis against the results from Kiener and Minor.

The true yield strength and ultimate tensile strength comparison between copper tensile samples from this thesis, the Copper Development Association (Copper Developement Association Inc., 2021), and Kiener and Minor nano crystalline samples (Kiener & Minor, 2011) can be seen below in Table 3. True yield strength was chosen as coppers strength metric because of coppers high ductility. While the copper tensile samples from this thesis shared similar values with the data from the Copper Development Association, neither of these results were similar to the one posted result from Kiener and Minors test. This difference in results is believed to be due to interatomic behavior exhibited by nano crystalline copper. This implies that the microscopic copper samples in this thesis share closer similarities to macroscopic copper samples than nano scopic copper samples.

Table 3. Copper Comparison

Copper Comparison		
	True Yield Strength (MPa)	**True Ultimate Tensile Strength (MPa)**
Copper Tensile Sample Two	144	204
Copper Tensile Sample Four	334	377
Copper Tensile Sample Five	189	216
Copper Tensile Sample Six	145	238
Copper Tensile Sample Seven	197	224
Copper Tensile Sample Nine	210	228
Copper Tensile Sample Ten	211	247
Copper Development Association (Cold Rolled Copper)	138 min.	221 min.
Kiener and Minor (nano crystalline)	636	-

4.23 Molybdenum Tensile Sample Eight

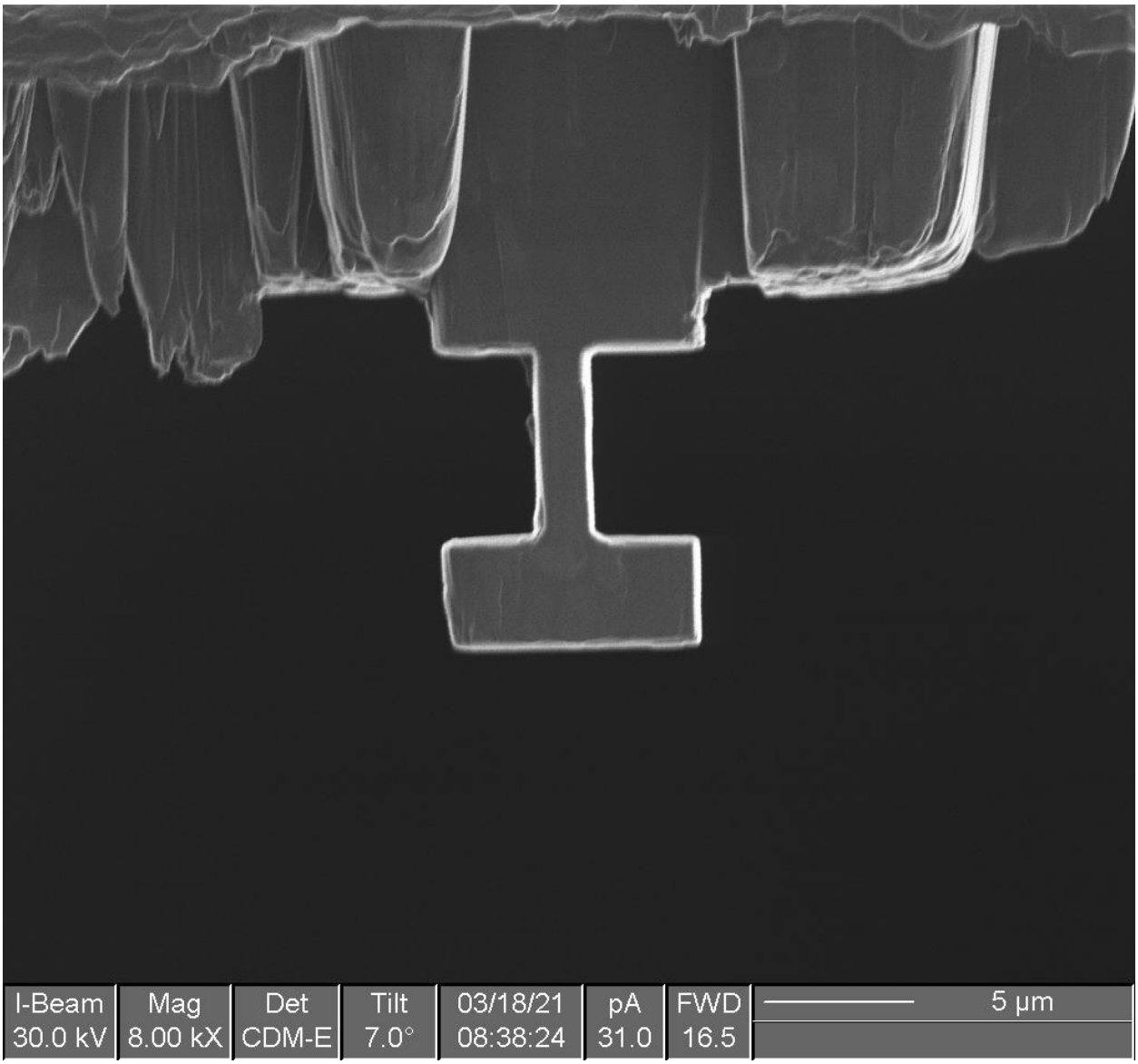

Figure 83. Molybdenum Tensile Sample Eight height by width cross section image.

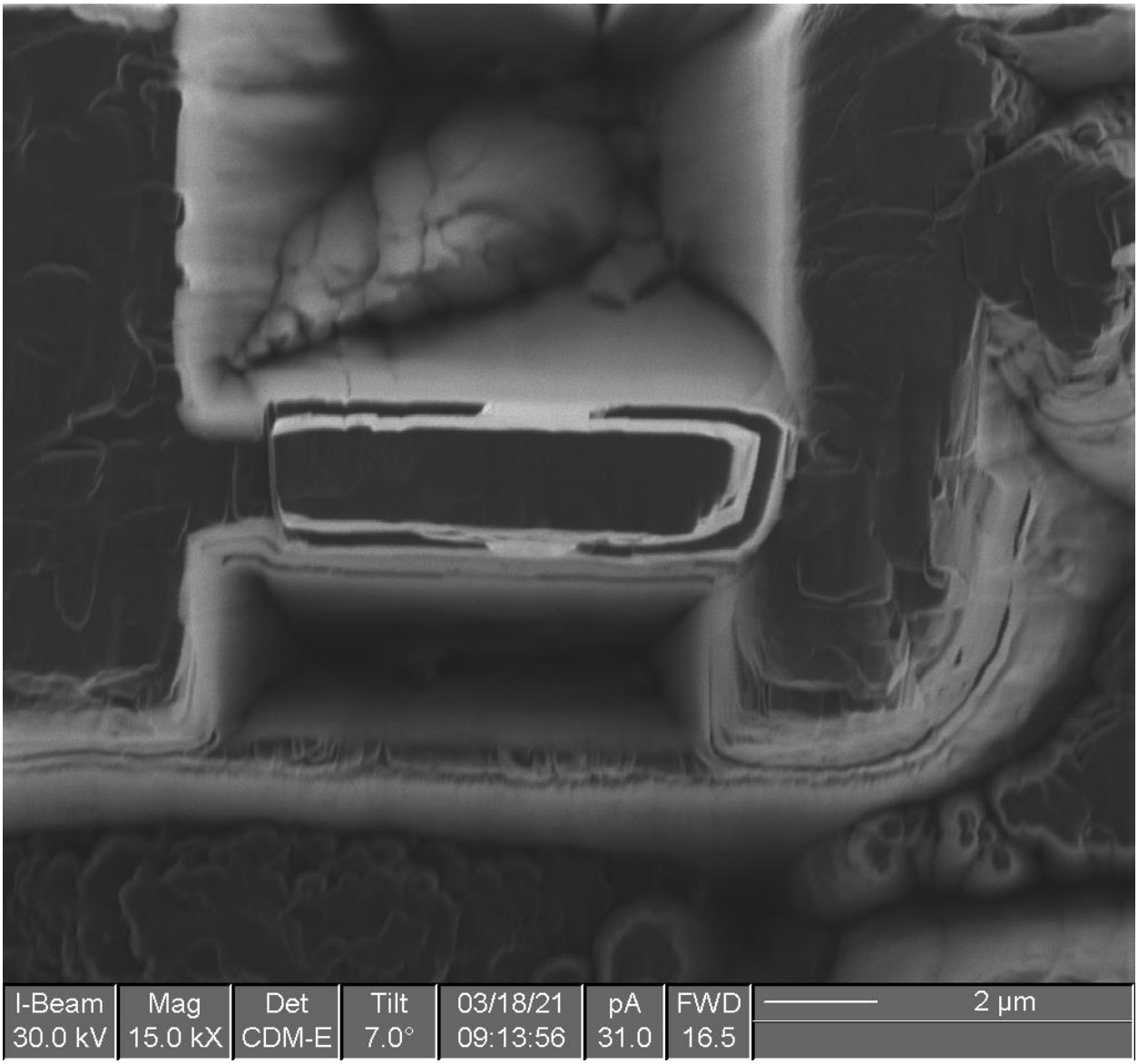

Figure 84. Molybdenum Tensile Sample Eight depth by width cross section image.

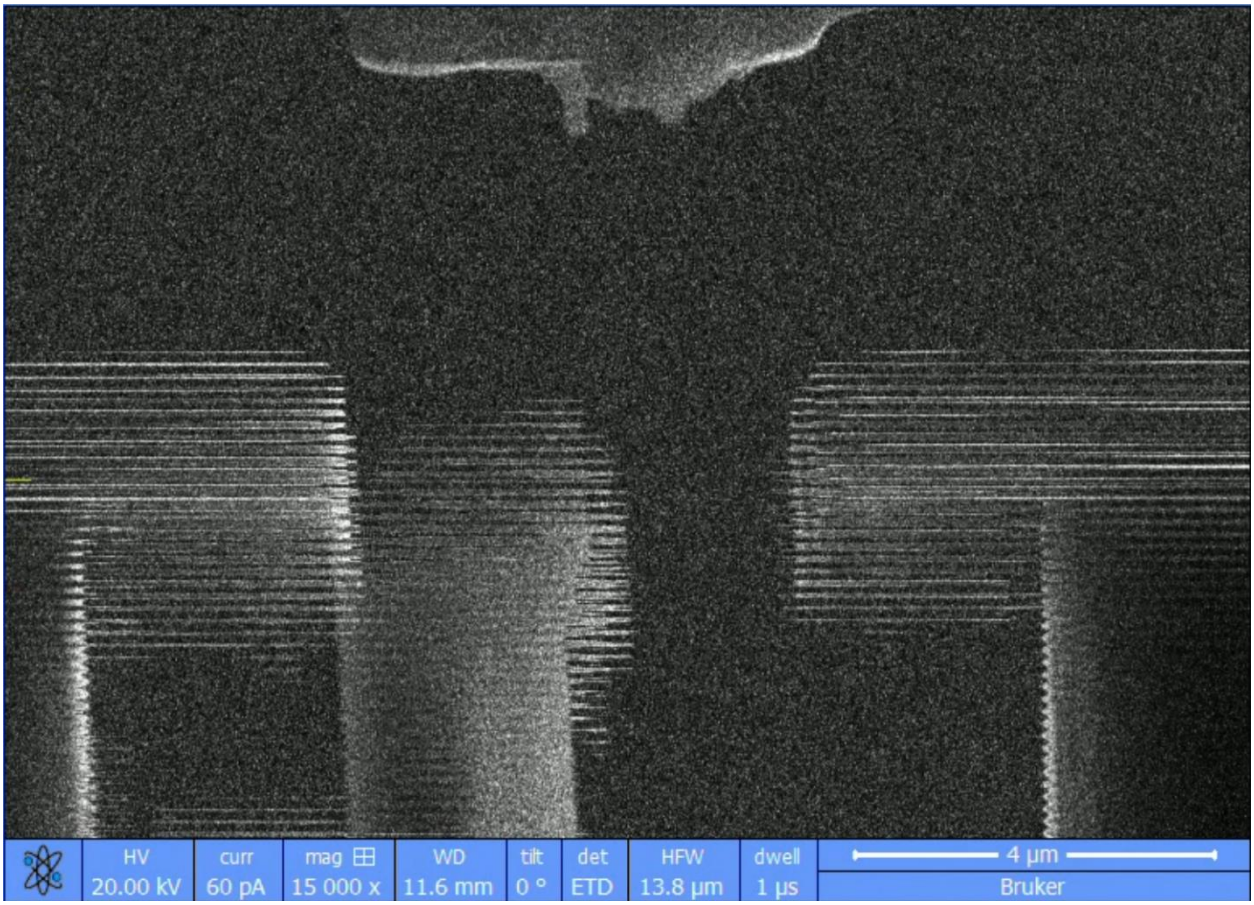

Figure 85. Molybdenum Tensile Sample Eight post failure image.

Table 4. Dimensions of Molybdenum Tensile Sample Eight, Gauge Section (μm).

Dimensions of Molybdenum Tensile Sample Eight, Gauge Section (μm)	
Height	**8.6**
Width	**2.0**
Depth	**2.9**

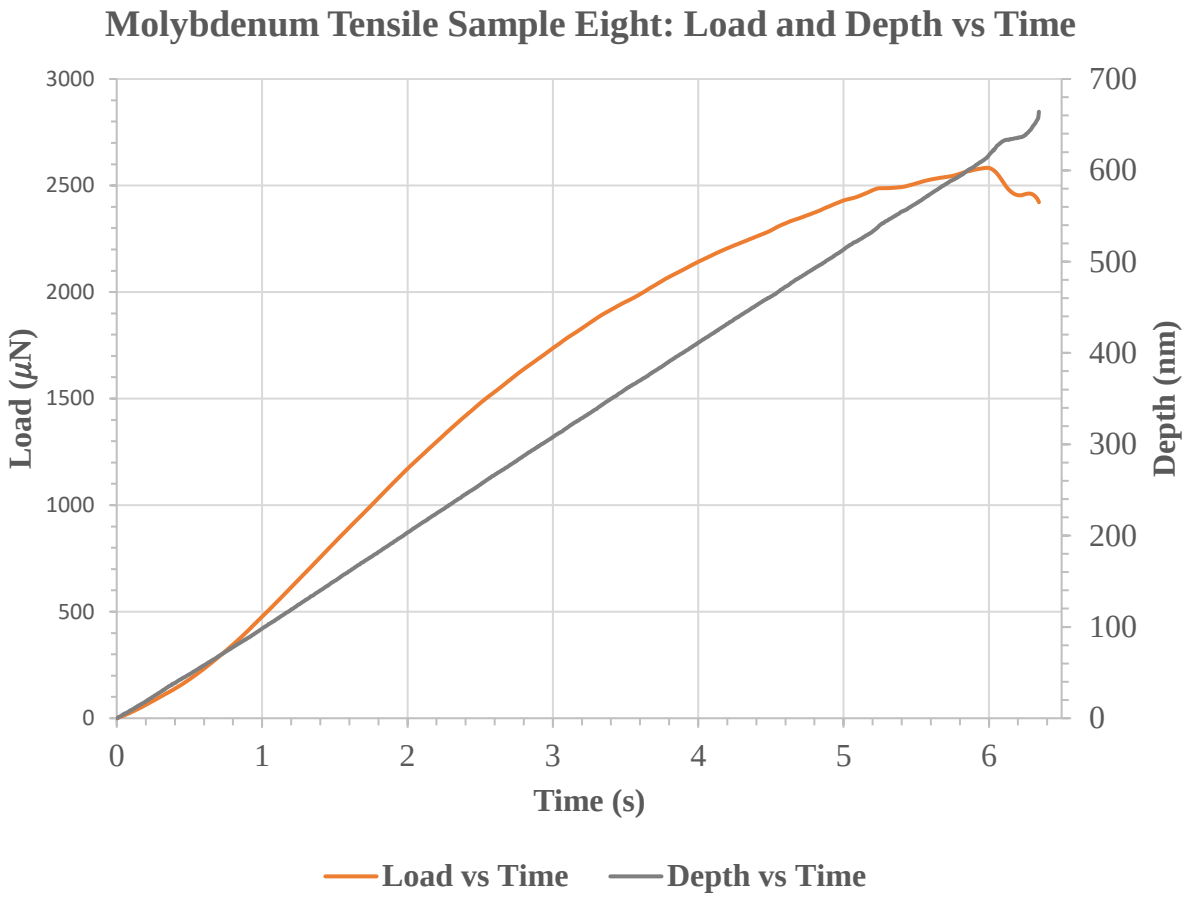

Figure 86. Molybdenum Tensile Sample Eight: Load and Depth vs Time.

The stress-strain curve in Fig. 87 implies that this molybdenum sample is more brittle than copper, but still retains a respectable plastic region.

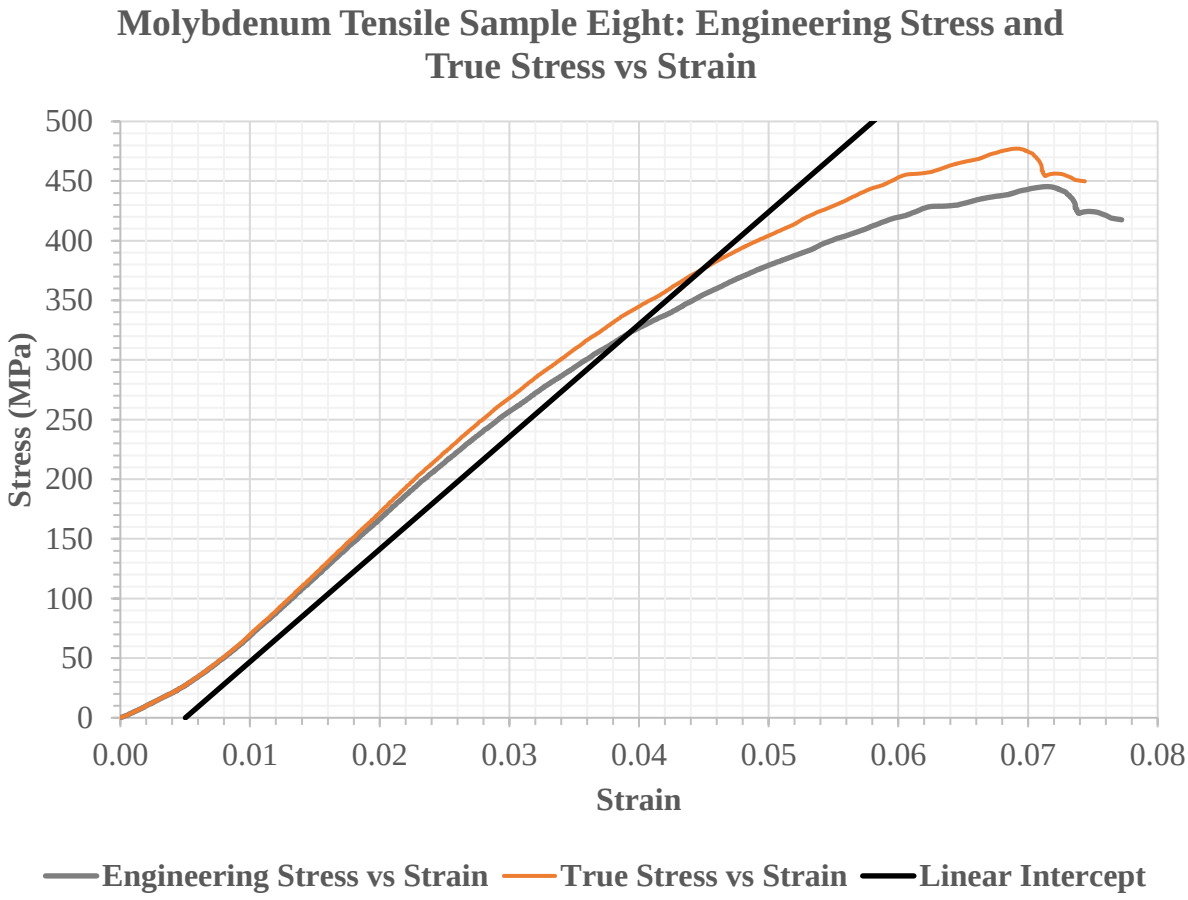

Figure 87. Molybdenum Tensile Sample Eight: Engineering Stress and True Stress vs Strain.

Since there was only one sample tested, the sample was potentially damaged, and there is limited literature on molybdenum, the mechanical values of molybdenum will be stand alone and not be compared to other results outside of this thesis.

Table 5. Molybdenum Tensile Sample Eight: Mechanical Values.

Molybdenum Tensile Sample Eight: Mechanical Values	
Engineering Yield Strength (at 0.5% offset) (MPa)	**333.642961**
True Yield Strength (at 0.5% offset) (MPa)	**376.170496**
Engineering Elastic Deformation	**0.041232**
True Elastic Deformation	**0.044917**
Engineering Ultimate Tensile Strength (MPa)	**445.347701**
True Ultimate Tensile Strength (MPa)	**477.212447**
Engineering Uniform Strain	**0.071419**
True Uniform Strain	**0.069124**
Engineering Fracture Strength (MPa)	**417.546671**
True Fracture Strength (MPa)	**449.791515**
Engineering Total Strain	**0.077225**
True Total Strain	**0.074388**
Modulus of Elasticity (GPa)	**6.783684**

4.24 Silicon Tensile Sample One

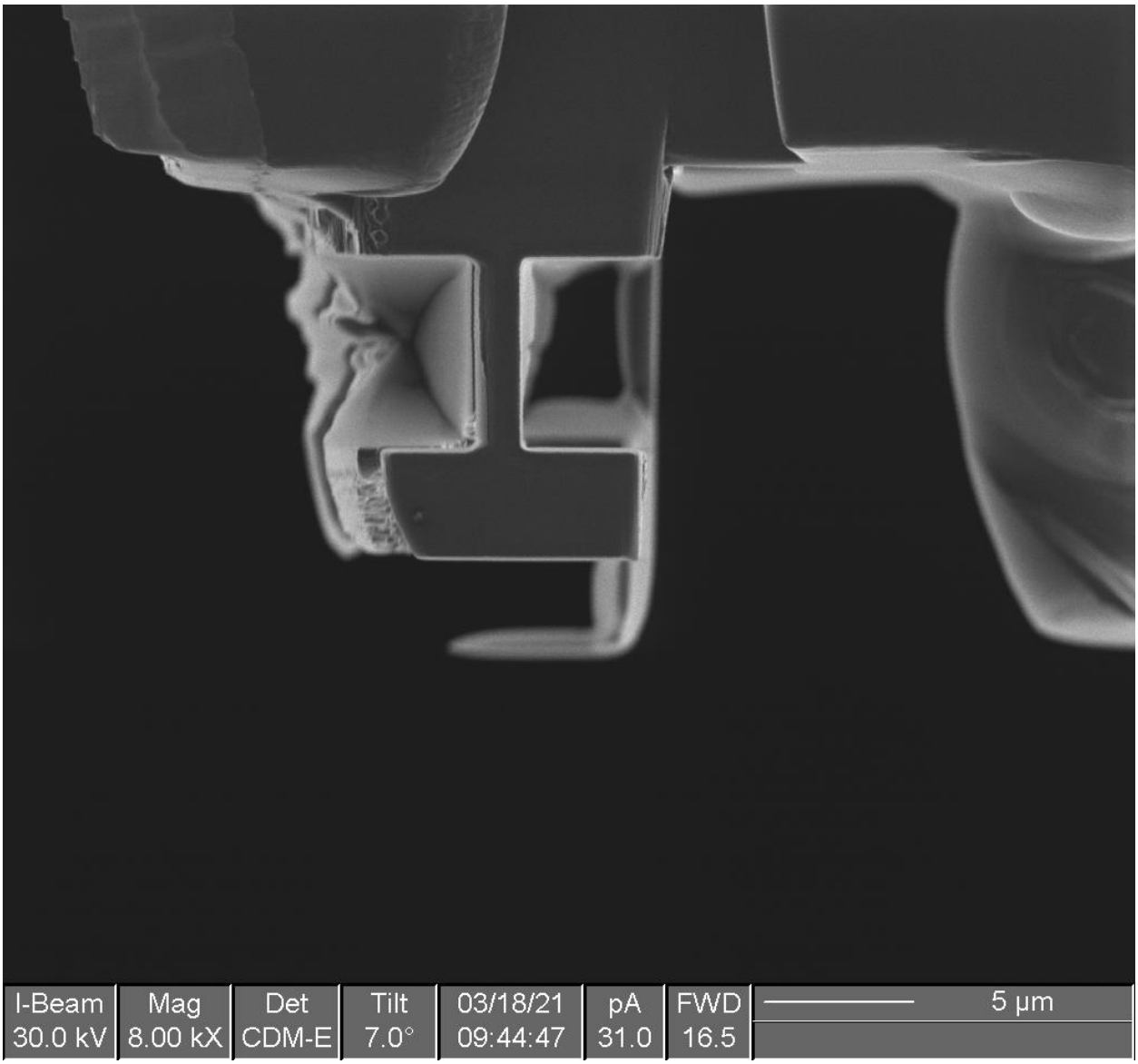

Figure 88. Silicon Tensile Sample One height by width cross section image.

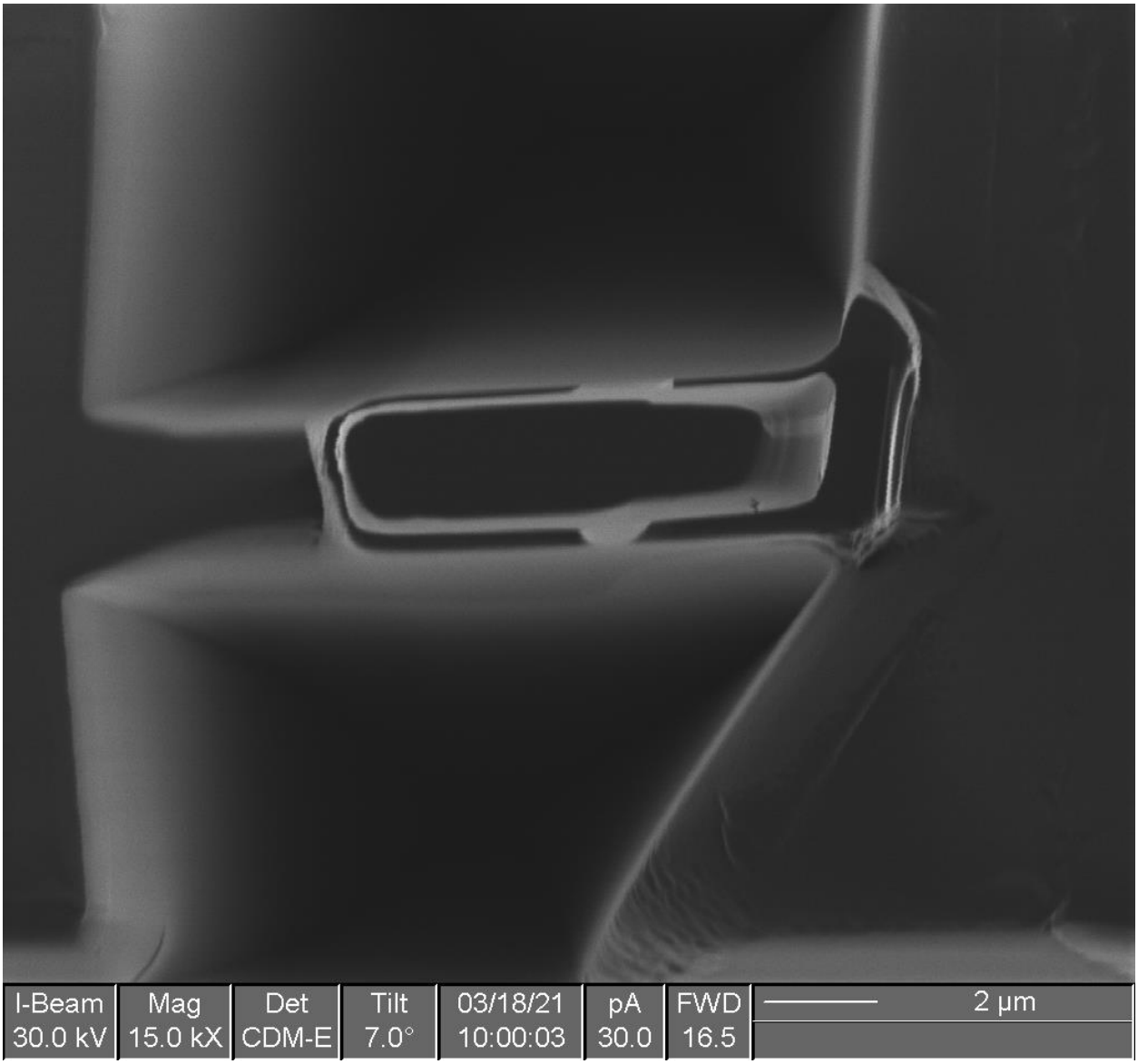

Figure 89. Silicon Tensile Sample One depth by width cross section image.

Notice the clean fracture and ringing of the diamond grippers in Fig. 90. This is indicative of the abrupt fracture experienced by the brittle silicon sample.

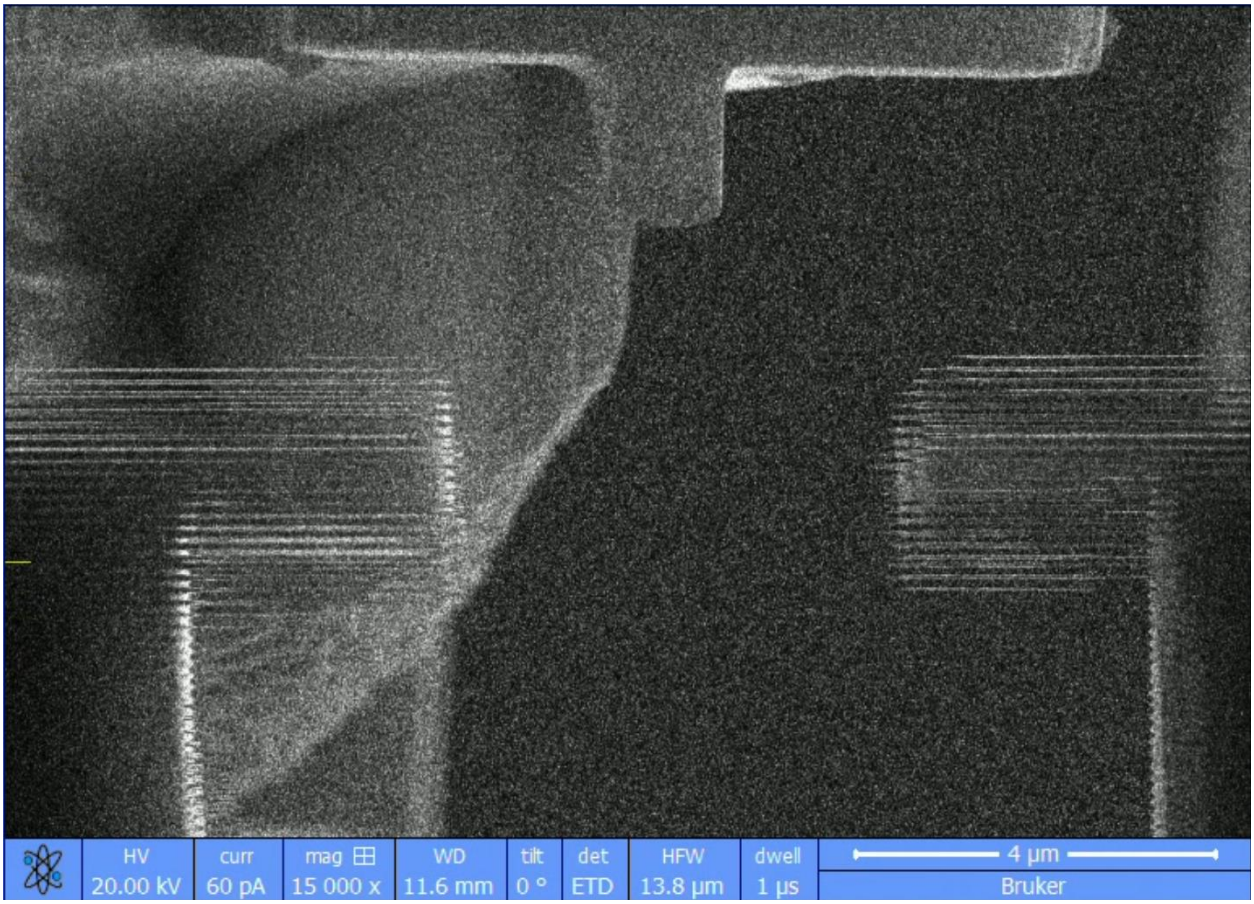

Figure 90. Silicon Tensile Sample One post failure image.

Table 6. Dimensions of Silicon Tensile Sample One, Gauge Section (μm).

Dimensions of Silicon Tensile Sample One, Gauge Section (μm)	
Height	**9.1**
Width	**1.5**
Depth	**3.3**

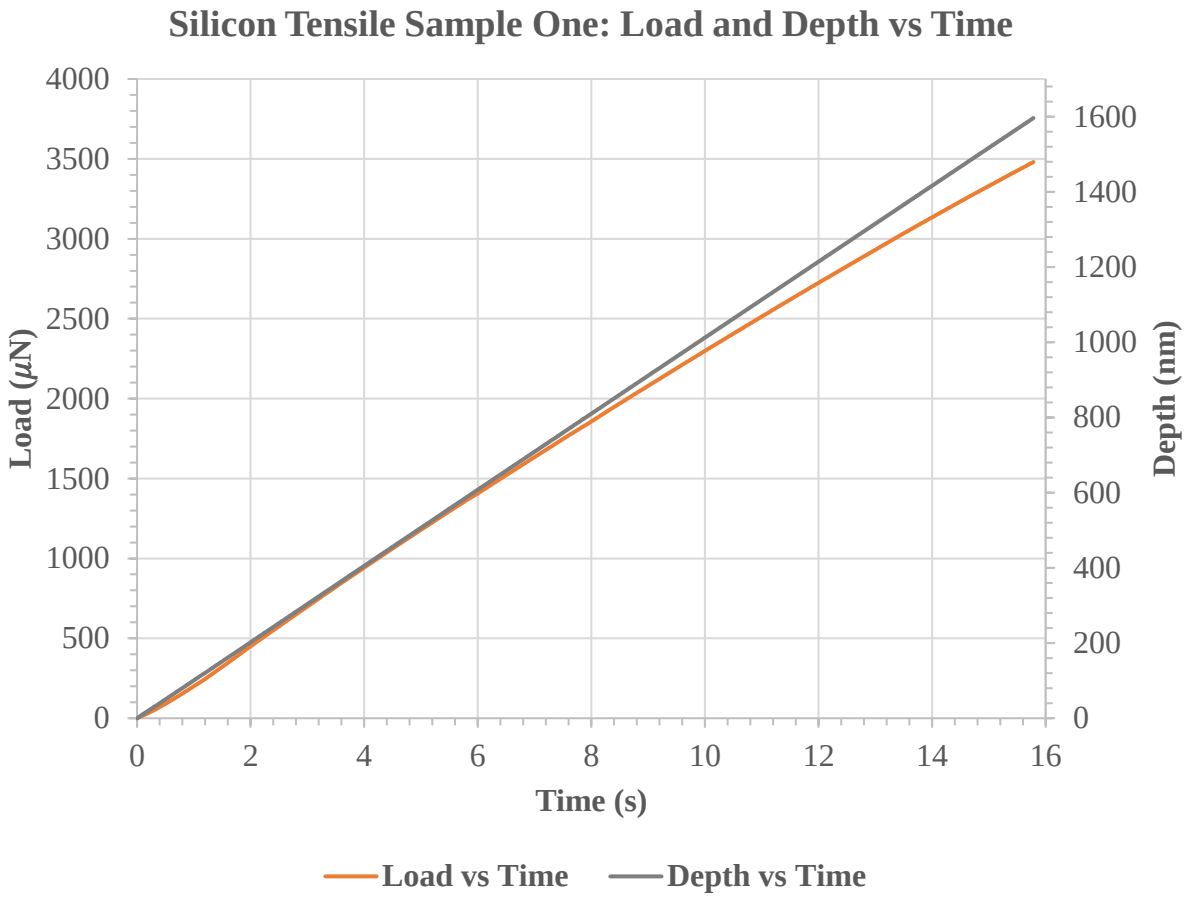

Figure 91. Silicon Tensile Sample One: Load and Depth vs Time.

Notice how straight the stress-strain curve is in Fig. 92. This is a strong indicator that silicon is a brittle material. Also notice the difference in magnitude between engineering stress and true stress. Since silicon is a brittle material it does not deform much if at all before fracture, so the predictive nature of true stress becomes inaccurate. Engineering stress more accurately predicts the stress of a brittle material like silicon than true stress.

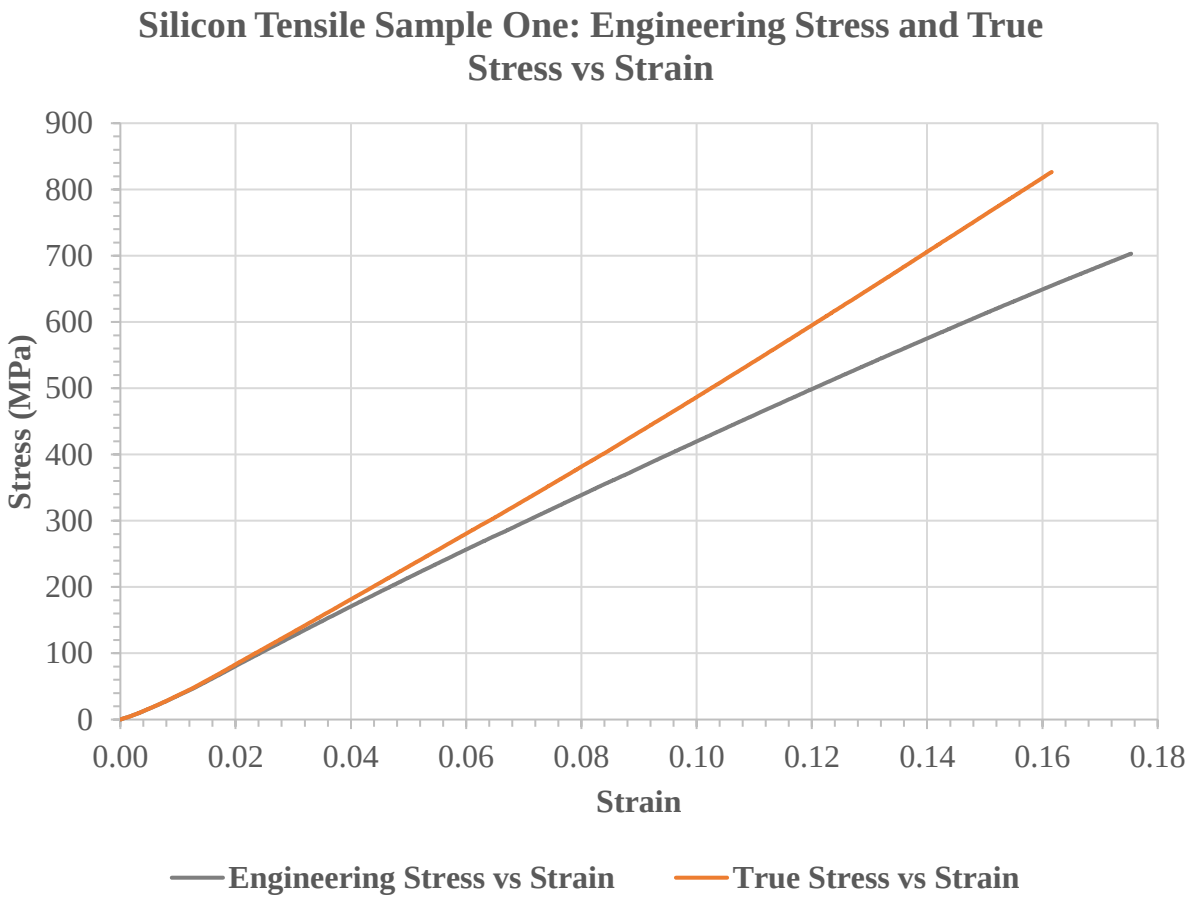

Figure 92. Silicon Tensile Sample One: Engineering Stress and True Stress vs Strain.

Table 7. Silicon Tensile Sample One: Mechanical Values.

Silicon Tensile Sample One: Mechanical Values	
Engineering Fracture Strength (MPa)	**703.080825**
True Fracture Strength (MPa)	**826.401586**
Engineering Total Strain	**0.175401**
True Total Strain	**0.161609**
Modulus of Elasticity (GPa)	**4.249089**

4.25 Silicon Comparison

Since silicon's fracture behavior follows a Weibull distribution, more samples will be needed for an accurate measure of its fracture strength (Bohm et al., 2004). The metric chosen for assessing silicon's strength value was engineering fracture strength because of silicon's brittle nature. The samples that have been tested are compared against an AZO Materials silicon catalog as reference (AZO Materials, 2021).

Table 8. Silicon Comparison.

Silicon Comparison	
	Engineering Fracture Strength (MPa)
Silicon Tensile Sample One	703
Silicon Tensile Sample Four	372
Silicon Tensile Sample Five	780
Silicon Tensile Sample Seven	785
Silicon Tensile Sample Eight	369
AZO Materials	165 - 180

4.3 South African Surrogate TRISO Particle

One lift-out sample of the buffer-IPyC interface was fabricated successfully before the writing of this thesis. A height by width cross section image, depth by width cross section image, and post failure image are shown as a reference against the dimensions of the tensile samples. The dimensions of the tensile samples were determined using the measurement tool in the Dual Beams FEI user interface software. All values displayed in the stress-strain graph and mechanical value tables were determined using the equations shown in the theory section applied in Excel spreadsheets. The raw data (depth, load, and time) was derived from a tensile test done inside the PI 88 PicoIndenter and using TriboScan software.

4.31 TRISO Tensile Sample One

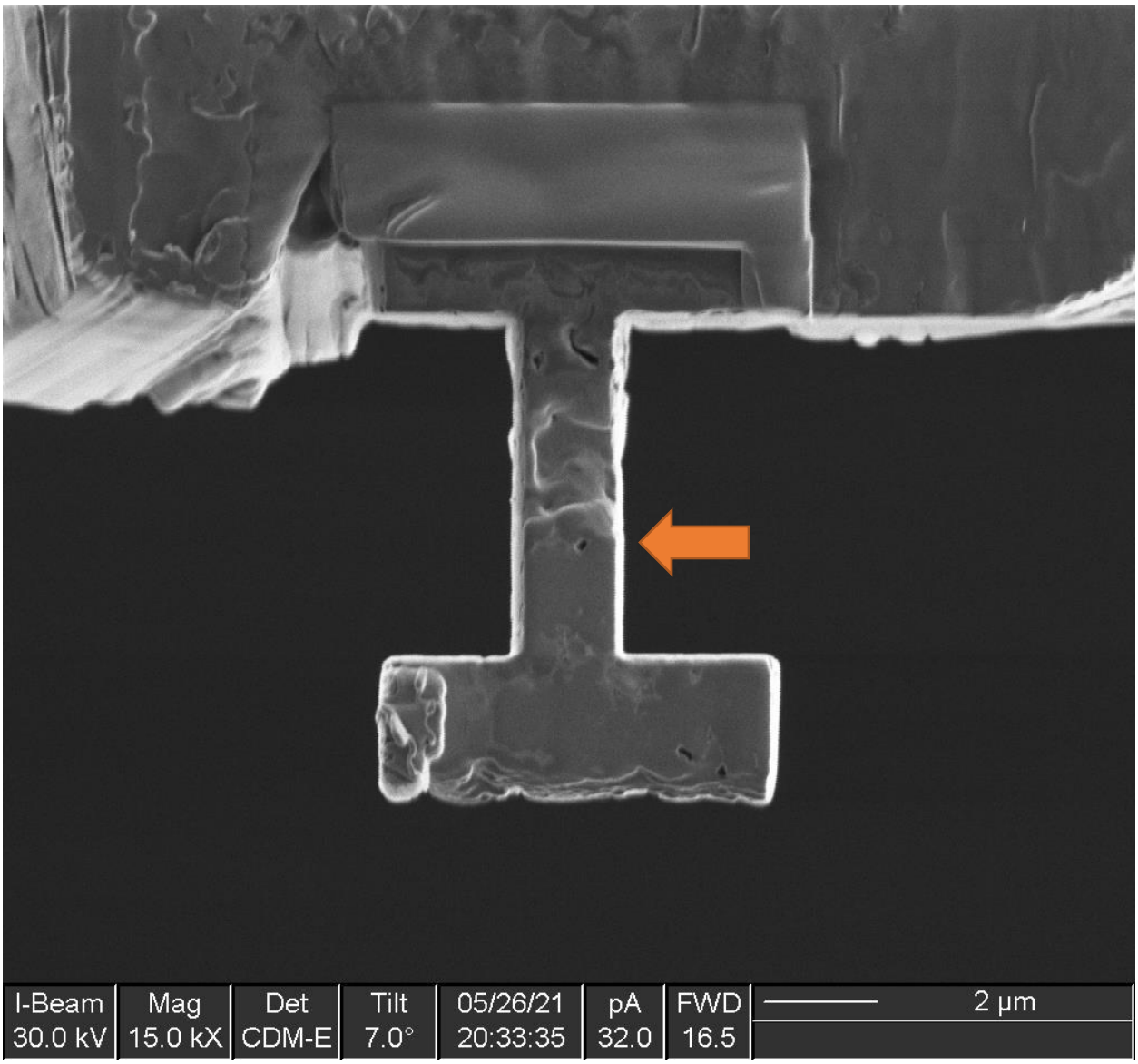

Figure 93**.** TRISO Tensile Sample One height by width cross section image. Notice the interlayer boundary between the buffer layer in the upper region and the IPyC layer in the lower region, as seen marked with the orange arrow

Leftover platinum from the lift-out process was remained on the face of the TRISO tensile sample, so it needed to be removed through FIBing, as seen in Fig. 94

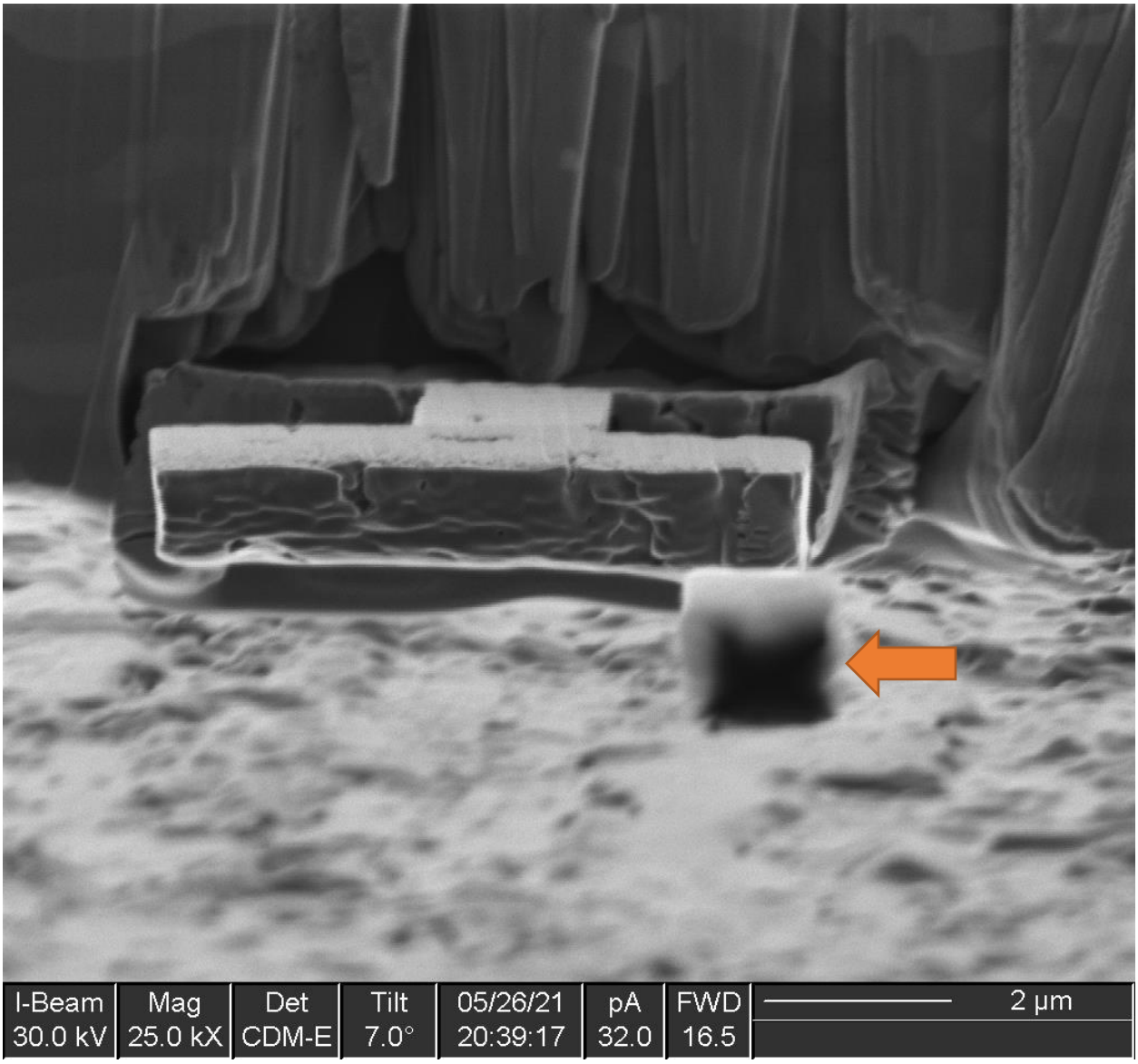

Figure 94. TRISO Tensile Sample One depth by width cross section image. The hole leftover by this cut can be seen marked with the orange arrow.

In the one test conducted, the tensile sample broke deep in the buffer layer portion of the sample. The fracture location was believed to be caused by the buffer layers high porosity, which has a relatively low cross-sectional area containing solid material in comparison to the IPyC layer. This is due to the open cavities inside the buffer layers structure. This reduced cross-sectional area increased the local stresses on the buffer layer causing it to fracture before the IPyC layer. An image of the fractured buffer layer can be seen in Fig. 95.

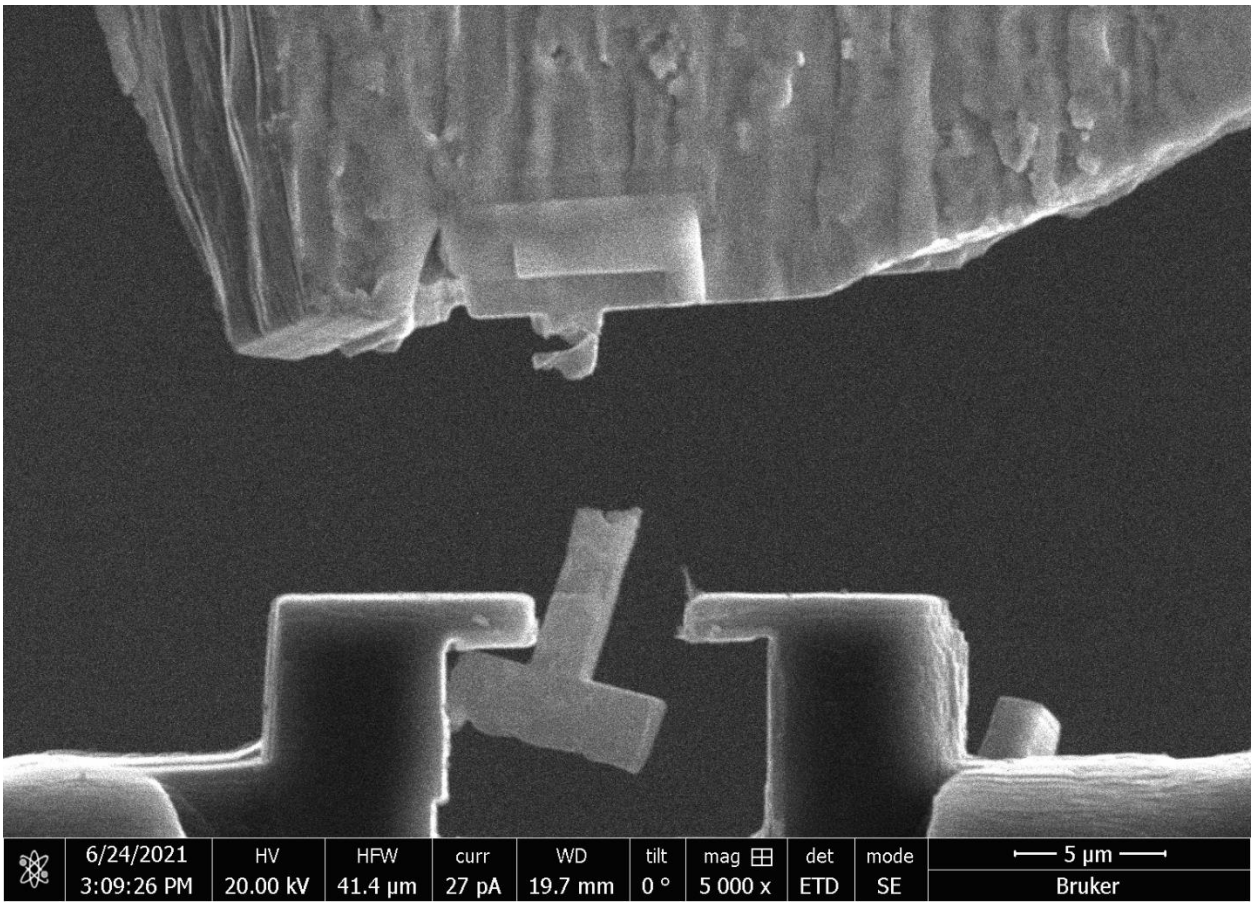

Figure 95. TRISO Tensile Sample One post failure image.

Notice the difference in porosity between the upper and lower portions of the tensile sample (buffer and IPyC) in Fig. 96. This texture gradient is what is believed to have caused the buffer layer to fracture in this test.

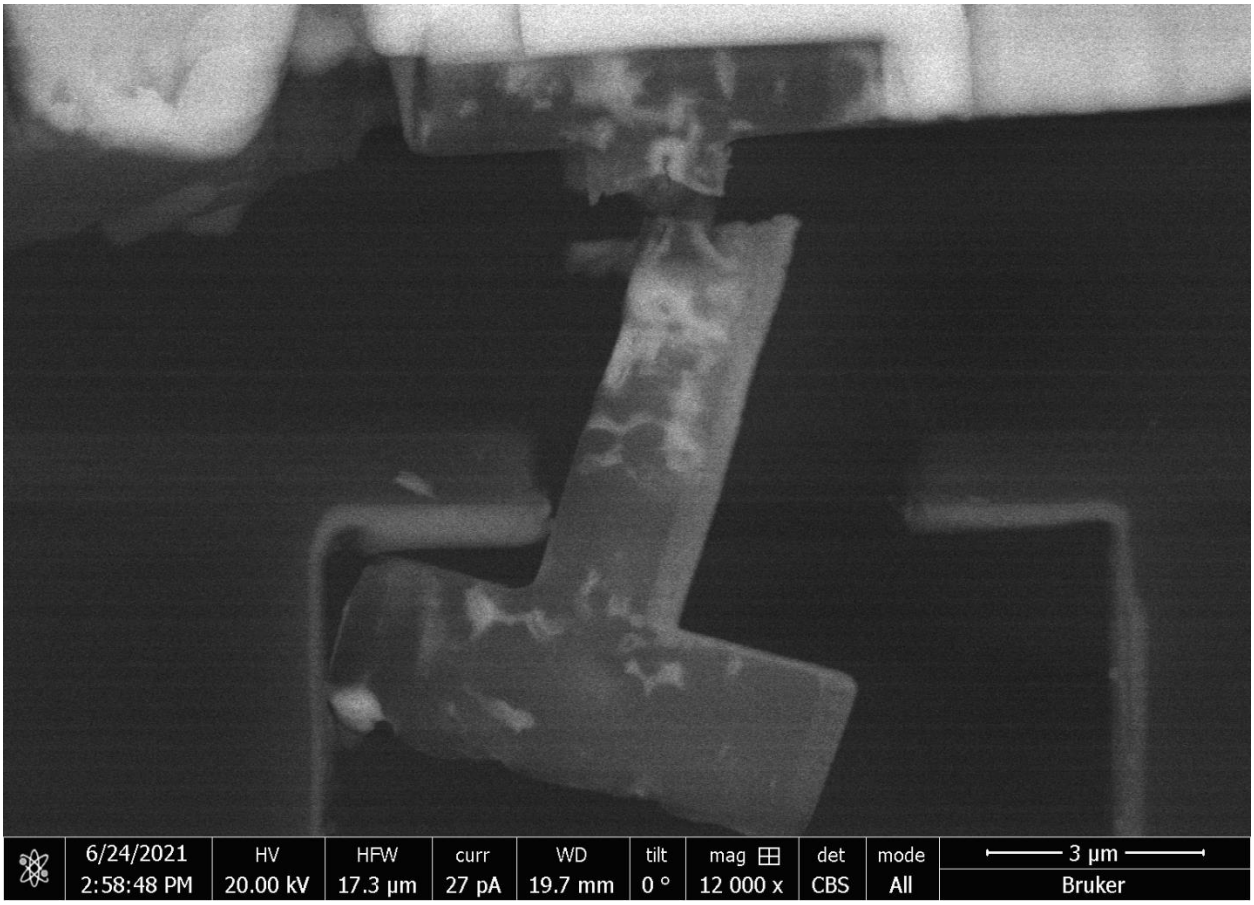

Figure 96. TRISO Tensile Sample One post failure image as seen through the Circular Backscatter Detector (CBS), with the white texture showcasing the nuances of the buffer layers porosity.

Notice the jagged fracture pattern caused by the porosity of the buffer layer in Fig. 97.

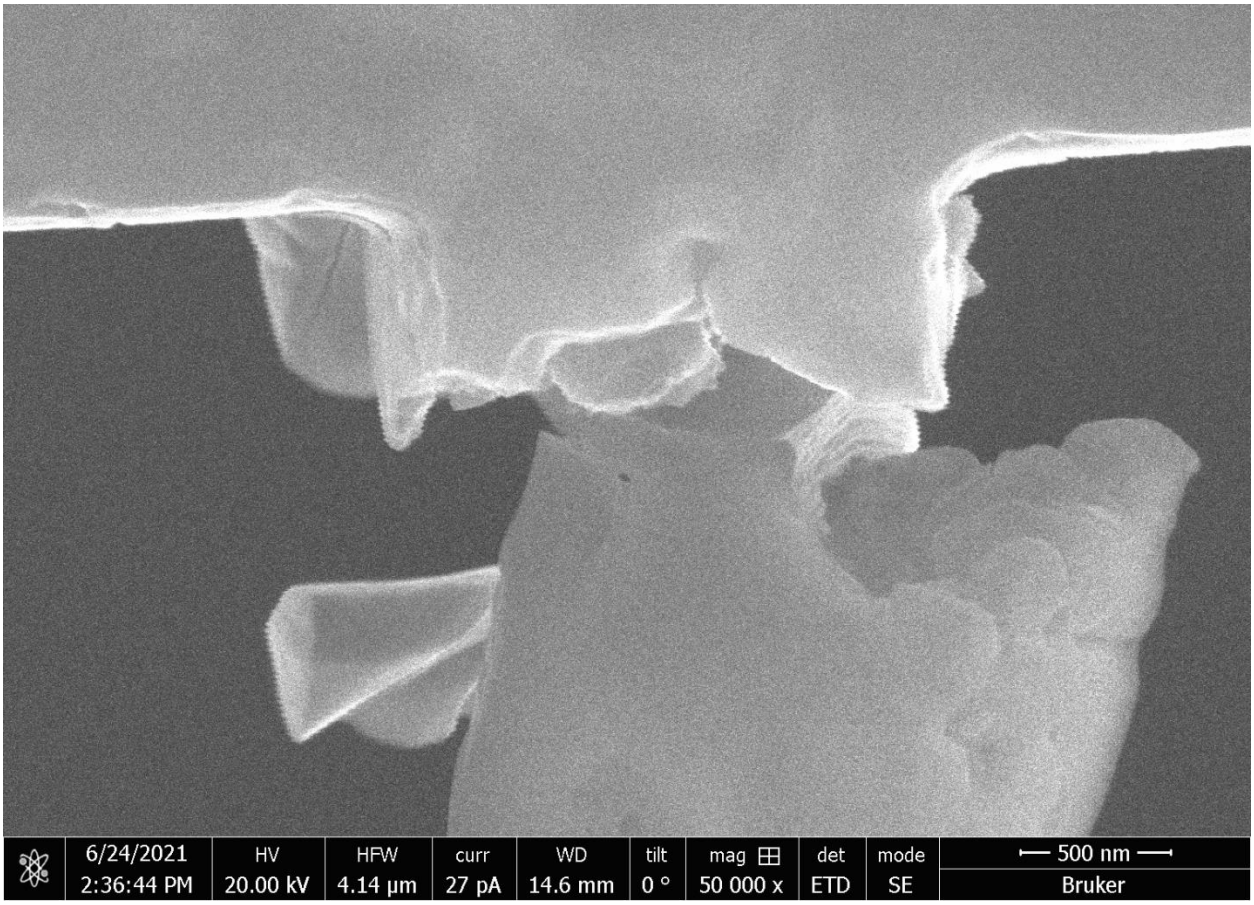

Figure 97. Zoomed in view of the point of fracture on the tensile sample.

Table 9. Dimensions of TRISO Tensile Sample One, Gauge Section (μm).

Dimensions of TRISO Tensile Sample One, Gauge Section (μm)	
Height	**8.5**
Width	**2.0**
Depth	**2.0**

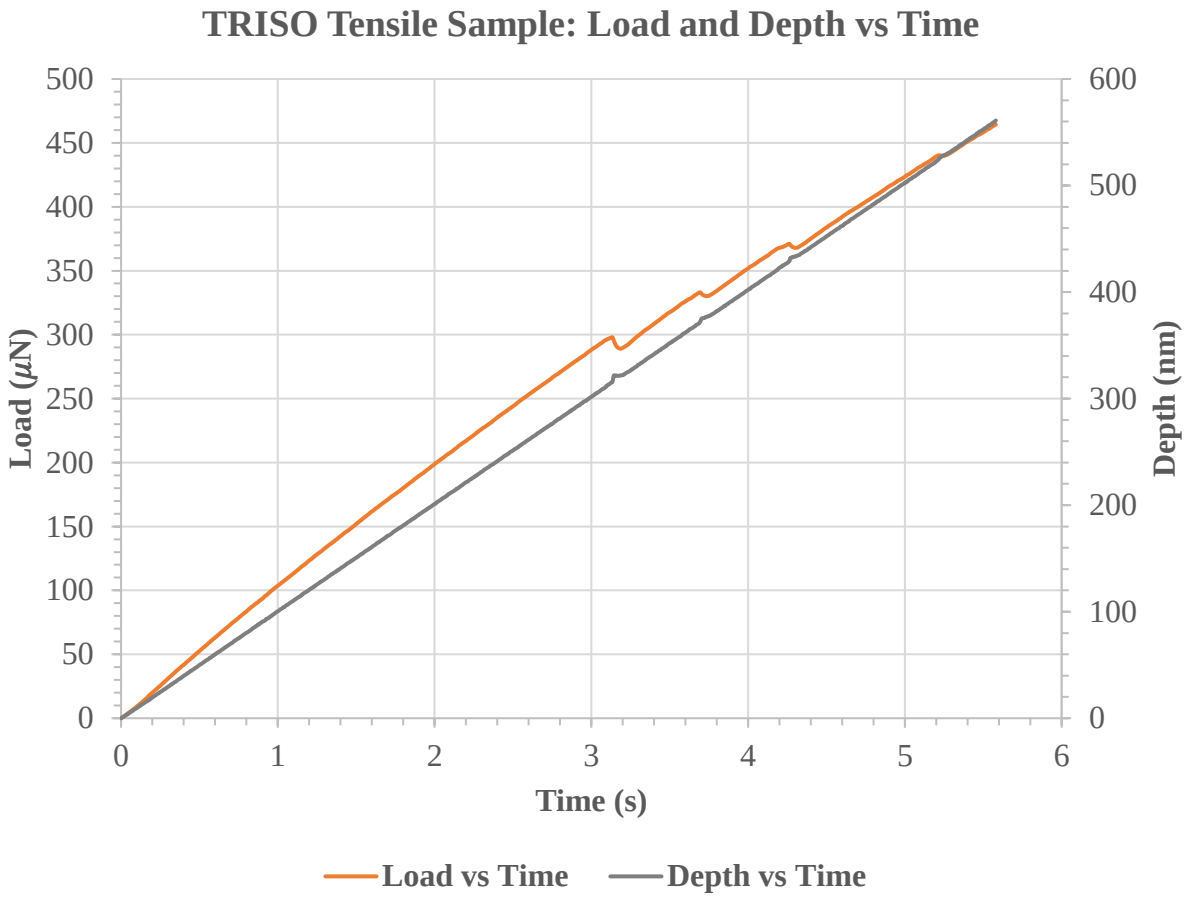

Figure 98. TRISO Tensile Sample: Load and Depth vs Time.

Notice the deviations in the stress-strain curve starting near the 90 MPa in Fig. 99. These deviations were believed to be caused by the fracture lines being slowed down by the open pores in the buffer layer of the TRISO tensile sample. The beginning of the graph is shown in this example to demonstrate that there is a preloading period on all the test conducted, with this period cropped for all the other graphs in this thesis.

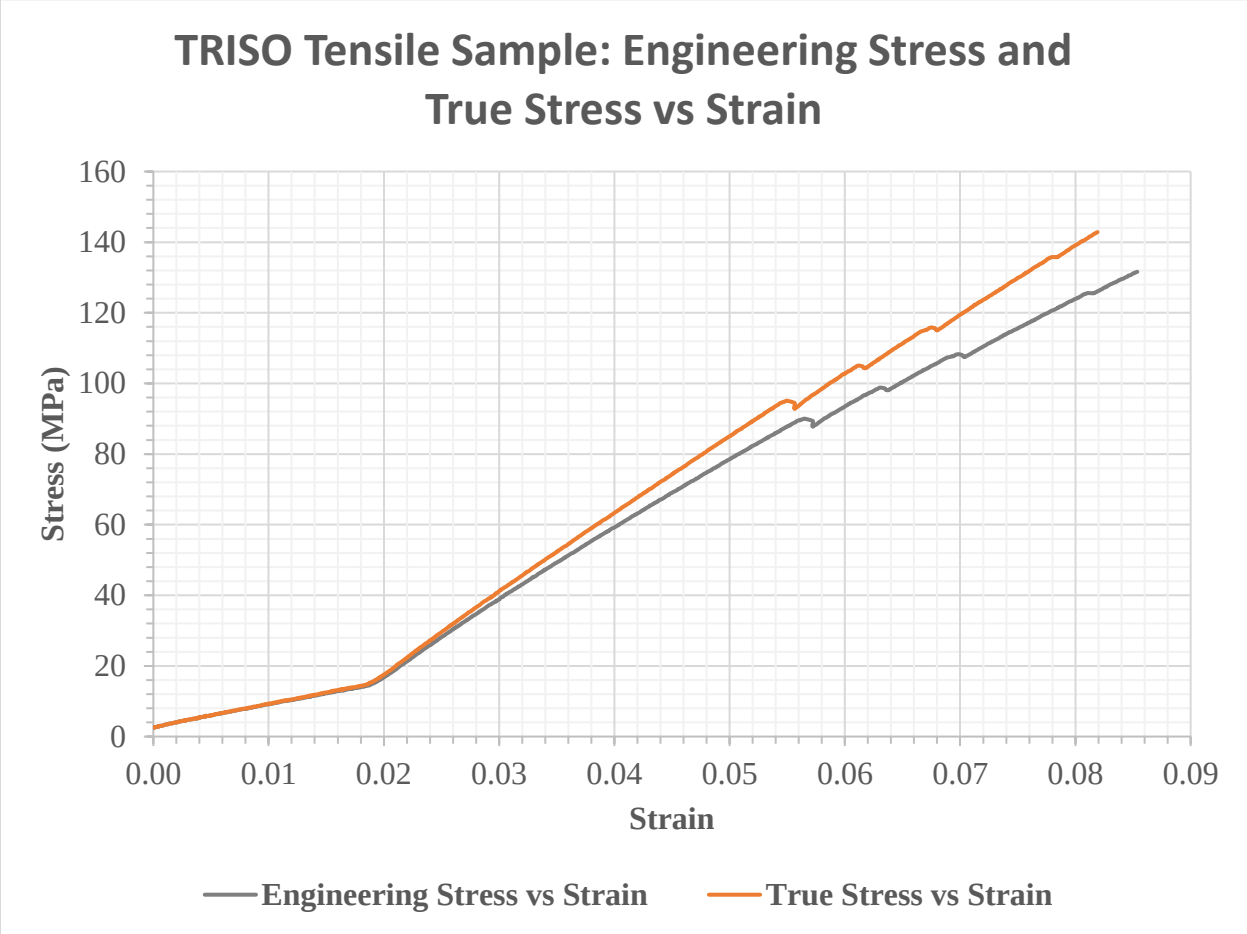

Figure 99. TRISO Tensile Sample: Engineering Stress and True Stress vs Strain.

Since only one TRISO sample was tested and there is limited literature, there is not enough data to make a useful comparison. The maximum values for this example are based-off the stress-strain curve without the preloading period taken into account. All other graphs take the preloading period off as well.

Table 10. TRISO Tensile Sample: Mechanical Values.

TRISO Tensile Sample: Mechanical Values	
Engineering Fracture Strength (MPa)	**116.079854**
True Fracture Strength (MPa)	**123.741345**
Engineering Total Strain	**0.066002**
True Total Strain	**0.063915**
Modulus of Elasticity (GPa)	**2.180585**

5.0 Conclusion

Through the work done in this thesis, an innovative new sample preparation technique for determining the tensile strength of select layers and layer interfaces of TRISO particles was developed. The tensile strength results derived from the copper micro tensile samples tested in this thesis were compared to the results of Kiener and Minors copper micro tensile tests and the results of both tests appear to be in agreement with each other. The similarity between these two tests verifies the accuracy of the methods used in this thesis. The microscopic copper tensile strength results from this thesis showed greater correspondence with results from macroscopic copper tensile tests than they did with nanoscopic copper tensile tests. This correspondence implies that

by using the methods in this thesis an accurate representation of the tensile strength of macroscopic TRISO particle layer materials can be determined from the tensile strength of microscopic TRISO particle layer materials. While the tensile strength results derived from the molybdenum and silicon micro tensile samples did not add any significant value in terms of tensile strength accuracy verification, they added further proof that the sample preparation technique used in this thesis works for fabricating micro tensile samples. The TRISO particle tensile sample containing the buffer and IPyC layers was tested and fractured deep inside the buffer layer. While only one TRISO particle sample was tested, the fracture behavior exhibited by this sample suggest that the buffer layer is the weakest area in the buffer-IPyC interface. The work exhibited in this thesis established a new method for characterizing the mechanical behavior of individual layers and interlayer bonds of TRISO particles that can be used to further develop TRISO particles for deployment in the nuclear reactors of tomorrow.

5.1 Future Works

At the time of writing this thesis, only one TRISO particle micro tensile sample from the South African surrogate TRISO particles was fabricated and tested. The goal is to continue fabricating and testing samples from the South African surrogate TRISO particles and to eventually start fabricating and testing samples from U.S. Adavanced Test Reactor (ATR) surrogate TRISO particles, unirradiated fueled TRISO particles, and irradiated fueled TRISO particles. The testing of these particles will help in our understanding of the thermomechanical behaviors of TRISO particles for use in future HTGRs.

6.0 References

Ando, M., Tanigawa, H., Kurotaki, H., & Katoh, Y. (2018). Mechanical properties of neutron irradiated F82H using micro-tensile testing. *Nuclear Materials and Energy*, *16*, 258–262. https://doi.org/10.1016/j.nme.2018.07.008

AZO Materials. (2021). Properties: A Background to Silicon and its Applications. https://www.azom.com/properties.aspx?ArticleID=599

Bauer, J., Schroer, A., Schwaiger, R., Tesari, I., Lange, C., Valdevit, L., & Kraft, O. (2015). Push-to-pull tensile testing of ultra-strong nanoscale ceramic-polymer composites made by additive manufacturing. *Extreme Mechanics Letters*, *3*, 105–112. https://doi.org/10.1016/j.eml.2015.03.006

Bellan, C., & Dhers, J. (2004). Evaluation of Young modulus of CVD coatings by different techniques. *Thin Solid Films*, *469–470*(SPEC. ISS.), 214–220. https://doi.org/10.1016/j.tsf.2004.08.182

Bohm, C., Hauck, T., Juritza, A., & Müller, W. H. (2004). Weibull statistics of silicon die fracture. Proceedings of 6th Electronics Packaging Technology Conference, EPTC 2004, 782–786. https://doi.org/10.1109/eptc.2004.1396714

Bower, G. R., Demkowicz, P. A., Ploger, S. A., & Hunn, J. D. (2017). *Measurement of kernel swelling and buffer densification in irradiated UCO-TRISO particles.* http://www.inl.gov

Byun, T. S., Hunn, J. D., Miller, J. H., Snead, L. L., & Kim, J. W. (2010). Evaluation of fracture stress for the SiC layer of TRISO-coated fuel particles using a modified crush test method.

International Journal of Applied Ceramic Technology, *7*(3), 327–337. https://doi.org/10.1111/j.1744-7402.2009.02462.x

Byun, T. S., Kim, J. W., Dunbar, I., & Hunn, J. D. (2008). *Fracture Stress Data for SiC Layers in TRISO-Coated Fuel Particles*.

ÇAPAR, Y. (2021). Engineering Stress/Strain vs True Stress/Strain. https://yasincapar.com/engineering-stress-strain-vs-true-stress-strain/

Chapin, D., Kiffer, S., & Nestell, J. (2004). *The Very High Temperature Reactor: A Technical Summary*.

Copper Developement Association Inc. (2021). Fundamentals: Types of Copper and Properties. https://www.copper.org/applications/architecture/arch_dhb/technical-discussion/fundamentals/intro.html

Deng, Y., & Barnoush, A. (n.d.). *Hydrogen embrittlement revealed via novel in situ fracture experiments using notched micro-cantilever specimens*.

Dieter, G. E. (1961). Mechanical Metallurgy (R. F. Mehl & M. B. Bever, Eds.).

Frazer, D., Abad, M. D., Krumwiede, D., Back, C. A., Khalifa, H. E., Deck, C. P., & Hosemann, P. (2015). Localized mechanical property assessment of SiC/SiC composite materials. *Composites Part A: Applied Science and Manufacturing*, *70*, 93–101. https://doi.org/10.1016/j.compositesa.2014.11.008

Frazer, D., Szornel, J., Krumwiede, D. L., Terrani, K. A., & Hosemann, P. (2017). Evaluation of the Mechanical Properties of TRISO Particles Using Nanoindentation and Ring Compression

Testing. *Experimental Mechanics*, *57*(7), 1081–1090. https://doi.org/10.1007/s11340-017-0277-z

Gussev, M. N., Howard, R. H., Terrani, K. A., & Field, K. G. (2017). Sub-size tensile specimen design for in-reactor irradiation and post-irradiation testing. *Nuclear Engineering and Design*, *320*, 298–308. https://doi.org/10.1016/j.nucengdes.2017.06.008

Hales, J. D., Williamson, R. L., Novascone, S. R., Perez, D. M., Spencer, B. W., & Pastore, G. (2013). Multidimensional multiphysics simulation of TRISO particle fuel. *Journal of Nuclear Materials*, *443*(1–3), 531–543. https://doi.org/10.1016/j.jnucmat.2013.07.070

Honorato, E. (2011). *The High Temperature Reactor and the TRISO coated fuel particle (Part I) | GrInAEr-Lab*. https://eddiehonorato.wordpress.com/2011/11/04/the-high-temperature-reactor-and-the-triso-coated-fuel-particle-part-i/

Hosemann, P., Hosemann, P., Kaoumi, D., Chrzan, D., & Maloy, S. A. (2018). *Developing Ultra-small Scale Mechanical Testing Methods and Microstructural Investigation Procedures for Irradiated Materials Fuel Cycle Research and Development Final report on the NEUP project: Developing ultra-small scale mechanical testing methods and microstructural investigation procedures for irradiated materials*.

Hunn, J. D., & Lowden, R. A. (n.d.). *Property Versus Process Trends for Inner-Pyrocarbon Layers in TRISO-Coated Particle Fuel*.

IAEA. (n.d.). *PrismaticHTR*.

Jiang, S., Tu, J., Yang, X., & Gui, N. (2019). A review of pebble flow study for pebble bed high temperature gas-cooled reactor. *Experimental and Computational Multiphase Flow*, *1*(3), 159–176. https://doi.org/10.1007/s42757-019-0006-1

Kallman, B. (2013). *The Very High Temperature Reactor*. http://large.stanford.edu/courses/2013/ph241/kallman1/

Kiener, D., & Minor, A. M. (2011). Source truncation and exhaustion: Insights from quantitative in situ TEM tensile testing. *Nano Letters*, *11*(9), 3816–3820. https://doi.org/10.1021/nl201890s

Lee, H. M., Park, K. il, Park, J. Y., Kim, W. J., & Kim, D. K. (2015). High-temperature fracture strength of a CVD-SiC coating layer for TRISO nuclear fuel particles by a micro-tensile test. *Journal of the Korean Ceramic Society*, *52*(6), 441–448. https://doi.org/10.4191/kcers.2015.52.6.441

López-Honorato, E., Meadows, P. J., Shatwell, R. A., & Xiao, P. (2010). Characterization of the anisotropy of pyrolytic carbon by Raman spectroscopy. *Carbon*, *48*(3), 881–890. https://doi.org/10.1016/j.carbon.2009.11.010

Maio, D. di, & Roberts, S. G. (2005). Measuring fracture toughness of coatings using FIB-machined microbeams. In *J. Mater. Res* (Vol. 20, Issue 2). www.feicompany.com

Moradkhani, A., Baharvandi, H., Tajdari, M., Latifi, H., & Martikainen, J. (2013). Determination of fracture toughness using the area of micro-crack tracks left in brittle materials by Vickers indentation test. *Journal of Advanced Ceramics*, *2*(1), 87–102. https://doi.org/10.1007/s40145-013-0047-z

NanoScan. (2018). *Nanoindentation - Nanohardness testers NanoScan*. http://nanoscan.info/eng/methods/nanoindentation

Nanoscience Instruments. (2021). Nanoindentation. In *Nanoindentation*. https://www.nanoscience.com/techniques/nanoindentation/

NRC. (n.d.). *3-2 3.2.2. Chemical Reaction at the Fuel Kernel Boundary*.

Office of Nuclear Energy. (2009). Advanced Gas Reactor Fuel Program's TRISO Particle Fuel Sets A New World Record For Irradiation Performance | Department of Energy. In *U.S. Department of Energy*. https://www.energy.gov/ne/articles/advanced-gas-reactor-fuel-programs-triso-particle-fuel-sets-new-world

Parma, E. J., Pickard, P. S., & Suo-Anttila, A. J. (2003). *SANDIA REPORT Concepts for Electrical Power Generation and Hydrogen Production*. http://www.doe.gov/bridge

PBMR. (2017). *PBMR - How the PBMR fuel works*. http://www.pbmr.co.za/index2.asp?Content=224

PI 88 SEM PicoIndenter ®. (2020). https://airtable.com/shrrfypV1Wg7J9ULa

Reichardt, A., Ionescu, M., Davis, J., Edwards, L., Harrison, R. P., Hosemann, P., & Bhattacharyya, D. (2019). *In situ Micro tensile testing of He +2 ion irradiated and implanted single crystal nickel film*. https://www.sciencedirect.com/science/article/pii/S1359645415006059e8d1b9e18a5dfbb60ac5b2b0547f3cedhttps://www.elsevier.com/open-access/userlicense/1.0/2

Reznik, B., & Hüttinger, K. J. (2002). On the terminology for pyrolytic carbon. In *Carbon* (Vol. 40, Issue 4, pp. 621–624). Elsevier Ltd. https://doi.org/10.1016/S0008-6223(01)00282-2

Rohbeck, N., & Xiao, P. (2016). Evaluation of the mechanical performance of silicon carbide in TRISO fuel at high temperatures. *Nuclear Engineering and Design*, *306*, 52–58. https://doi.org/10.1016/j.nucengdes.2016.05.040

Shih, C., Katoh, Y., Leonard, K. J., Bei, H., & Lara-Curzio, E. (2013). Determination of interfacial mechanical properties of ceramic composites by the compression of micro-pillar test specimens. *Journal of Materials Science*, *48*(15), 5219–5224. https://doi.org/10.1007/s10853-013-7311-z

Ted Pella. (2020). Focused Ion Beam Sample Holder, FIB Lift-out Grids, Silicon Aperture Frames. In Ted Pella, Inc. https://www.tedpella.com/grids_html/4510half.htm.aspx#10FIBC05

THERMO FISHER SCIENTIFIC. (2021). Focused ion beam scanning electron microscope - Versa 3D. https://www.directindustry.com/prod/thermo-fisher-scientific-materials-structural/product-123345-1401265.html

van Rooyen, G. T., du Preez, R., de Villiers, J., & Cromarty, R. (n.d.). *The Fracture Strength of TRISO-Coated Particles determined by Compression Testing between Soft Aluminium Anvils*.

van Rooyen, I. J., Dunzik-Gougar, M. L., Van, P. M., Trowbridge, R. T., van Rooyen, P. M., & Trowbridge, T. (2012). *On Techniques to Characterize and Correlate Grain Size, Grain Boundary Orientation and the Strength of the SiC Layer of TRISO Coated Particles: A Preliminary Study HTR 2012 On Techniques to Characterize and Correlate Grain Size, Grain Boundary Orientation and the Strength of the SiC Layer of TRISO Coated Particles: A Preliminary Study*.

Verfondern, K., Nabielek, H., Kania, M. J., ALLELEIN, H.-J., & Institut für Energie- und Klimaforschung Nukleare Entsorgung und Reaktorsicherheit (IEK-6). (2013). *High-quality Thorium TRISO fuel performance in HTGRs*.

Vo, H. T., Reichardt, A., Frazer, D., Bailey, N., Chou, P., & Hosemann, P. (2017). *In Situ Micro-Tensile Testing on Proton Beam-Irradiated Stainless Steel*. http://www.elsevier.com/open-access/userlicense/1.0/

Wolff, A. (2020). Focused ion beams: An overview of the technology and its capabilities - 2020 - Wiley Analytical Science. https://analyticalscience.wiley.com/do/10.1002/was.00070009

Žagar, G., Pejchal, V., Mueller, M. G., Michelet, L., & Mortensen, A. (2016). Fracture toughness measurement in fused quartz using triangular chevron-notched micro-cantilevers. *Scripta Materialia*, *112*, 132–135. https://doi.org/10.1016/j.scriptamat.2015.09.032

Zhang, H., Lõpez-Honorato, E., Javed, A., Shapiro, I., & Xiao, P. (2012). A study of the microstructure and vickers indentation fracture toughness of silicon carbide coatings on triso fuel particles. *Journal of the American Ceramic Society*, *95*(3), 1086–1092. https://doi.org/10.1111/j.1551-2916.2011.05044.x

7.0 Appendix

7.1 Copper Tensile Sample Two

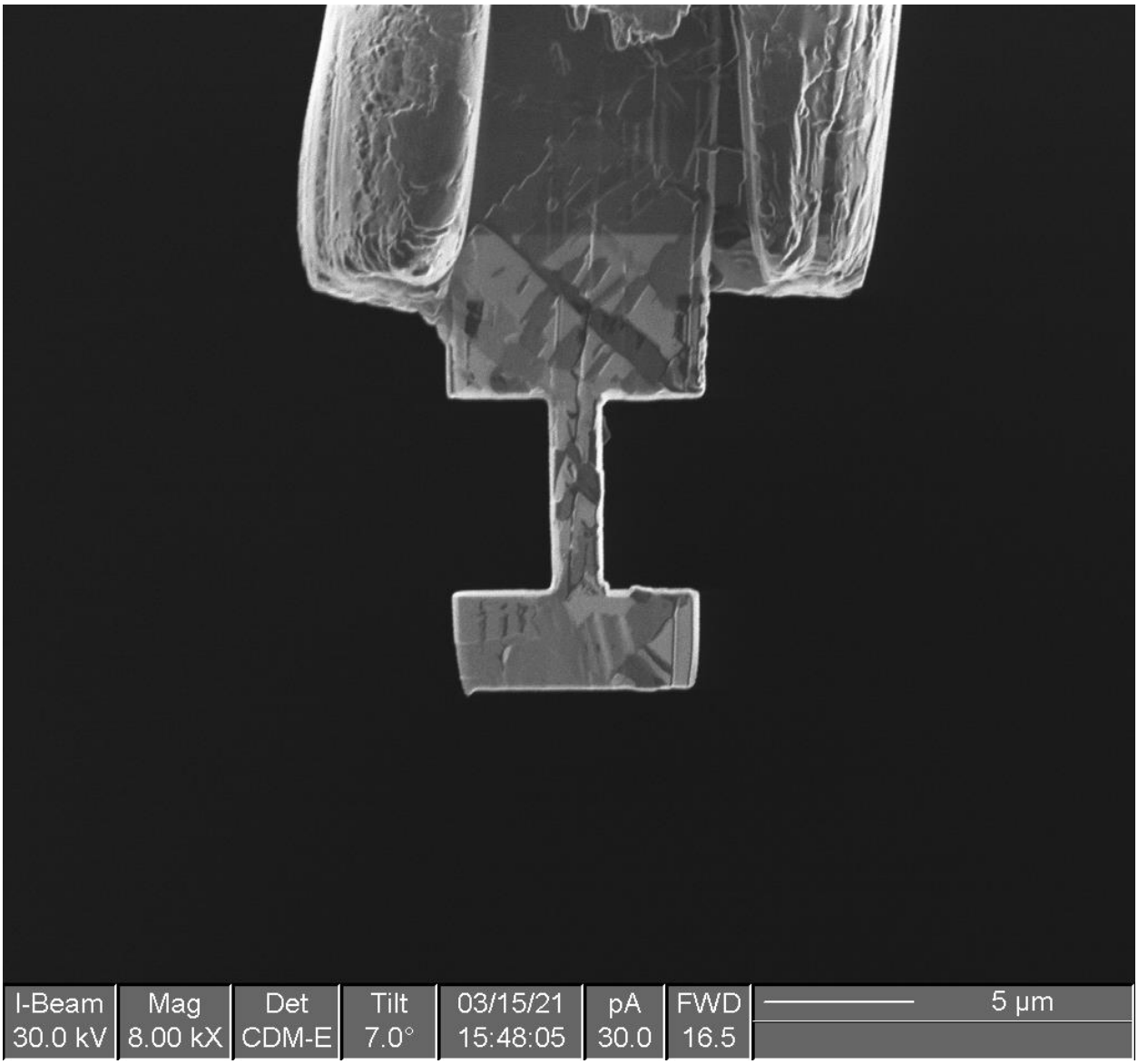

Figure 100. Copper Tensile Sample Two height by width cross section image.

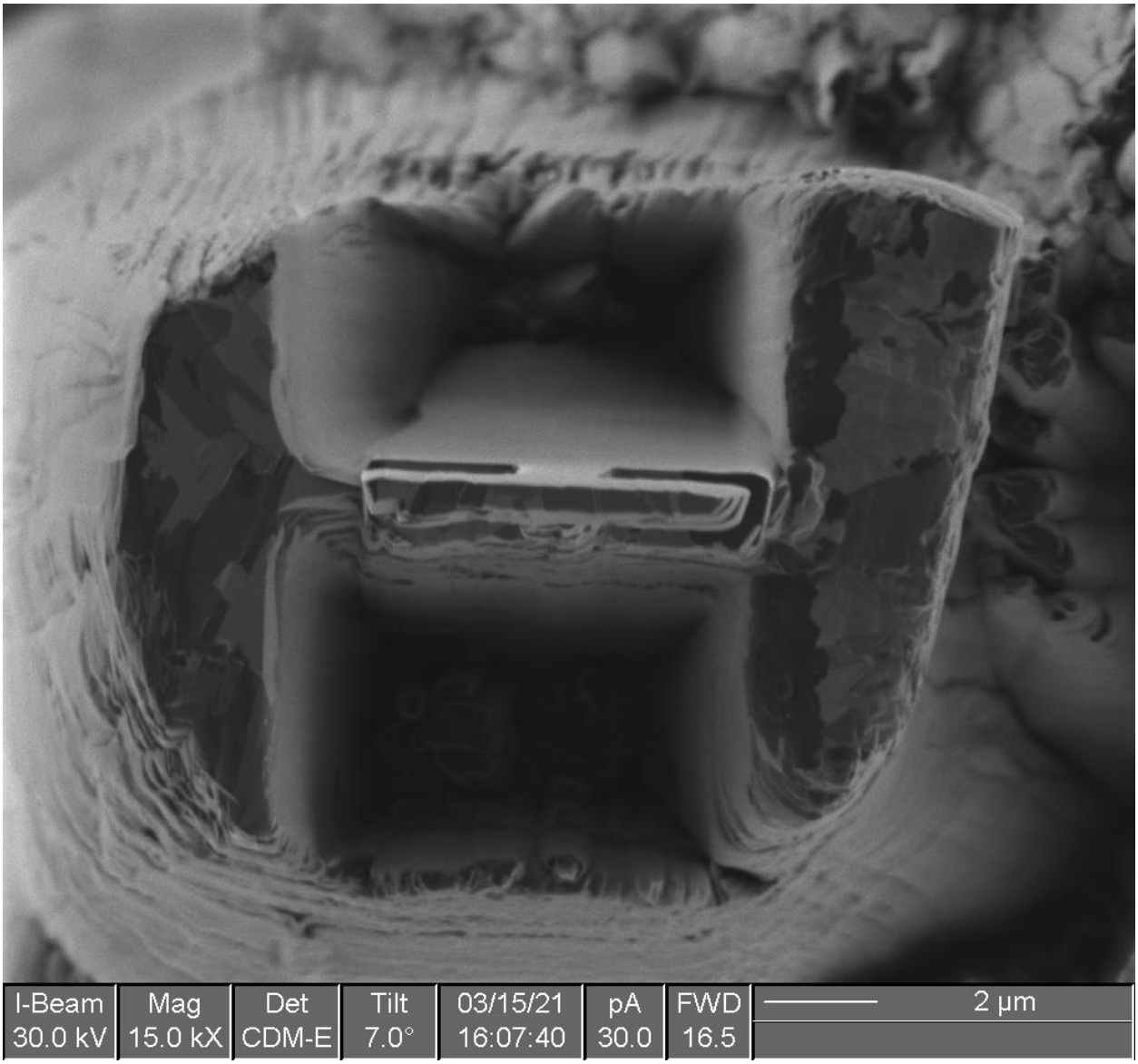

Figure 101. Copper Tensile Sample Two depth by width cross section image.

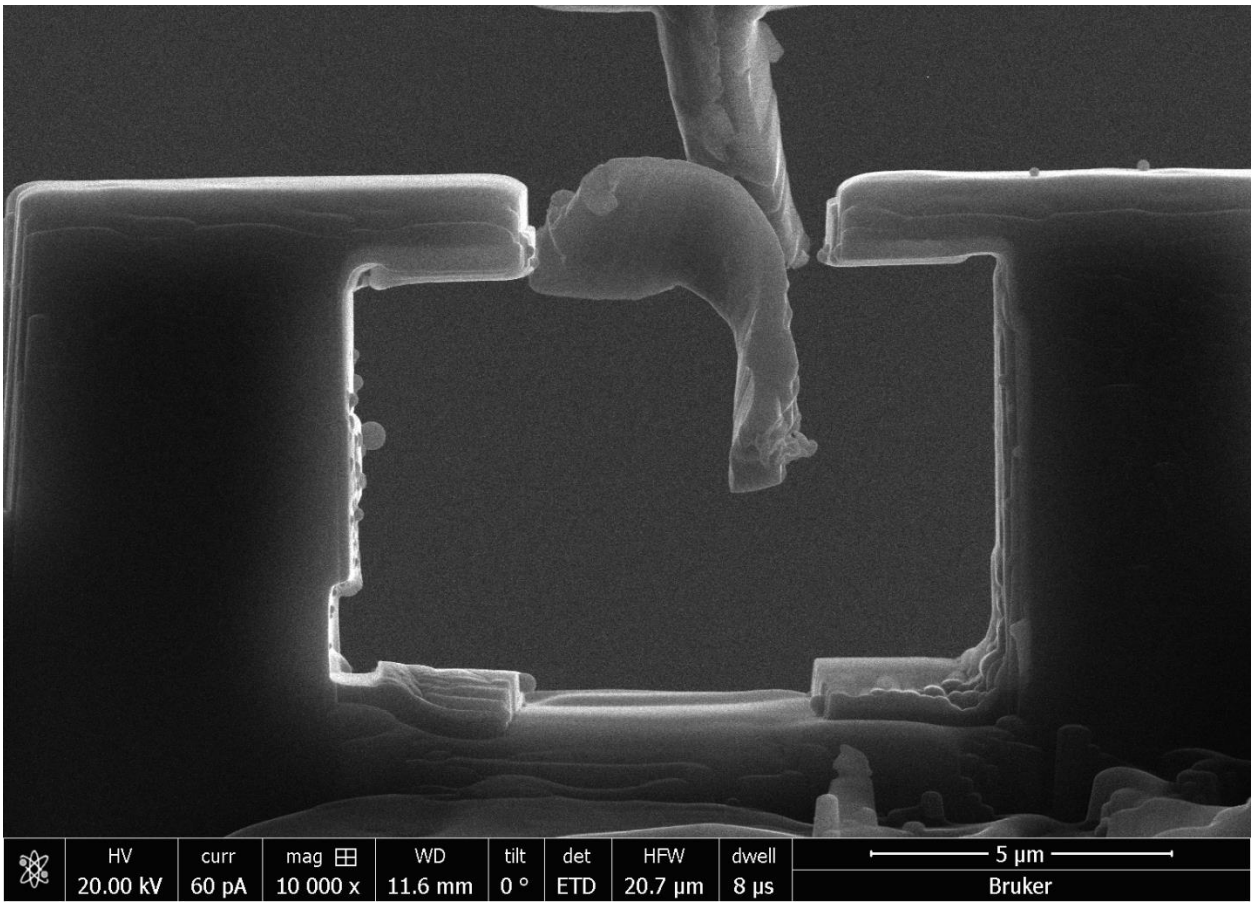

Figure 102. Copper Tensile Sample Two post failure image.

Table 11. Dimensions of Copper Tensile Sample Two, Gauge Section (μm).

Dimensions of Copper Tensile Sample Two, Gauge Section (μm)	
Height	**9.1**
Width	**1.6**
Depth	**1.7**

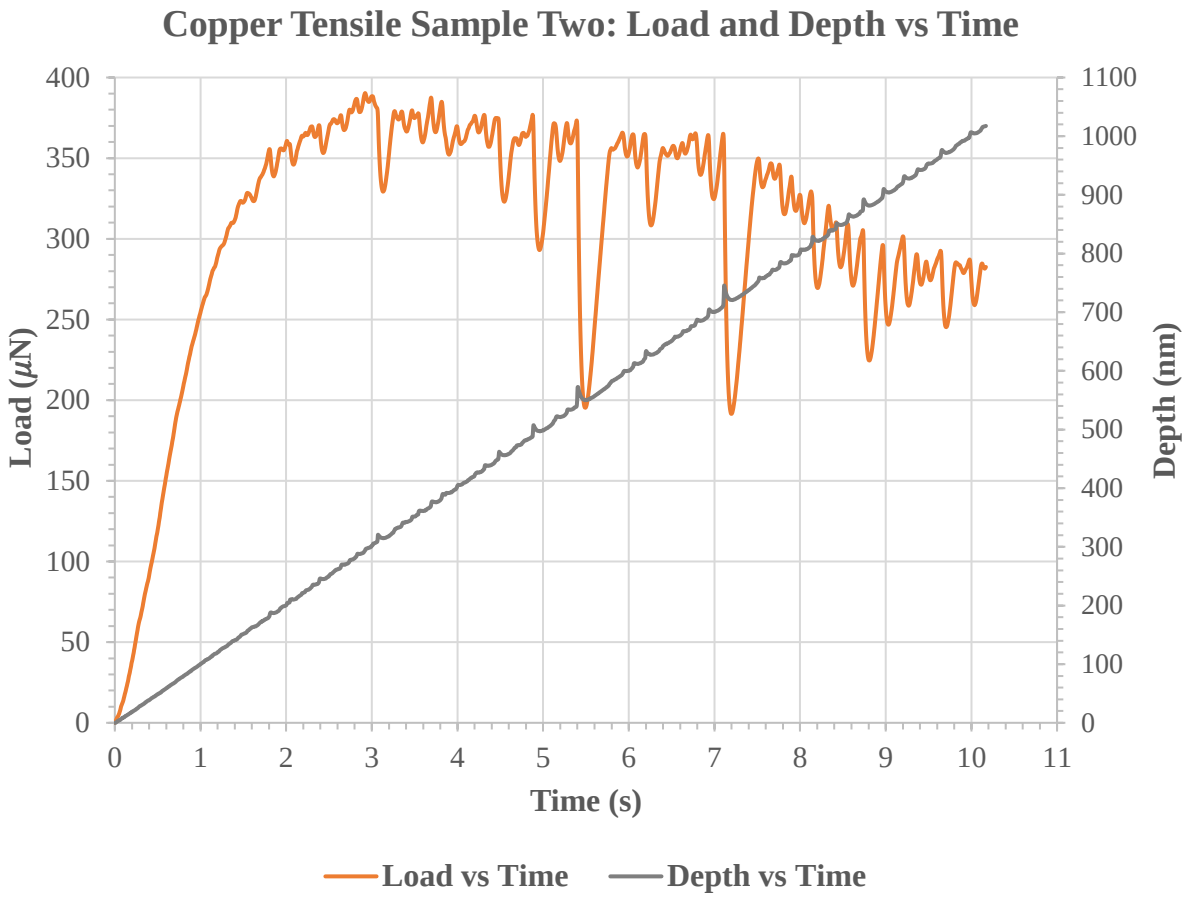

Figure 103. Copper Tensile Sample Two: Load and Depth vs Time.

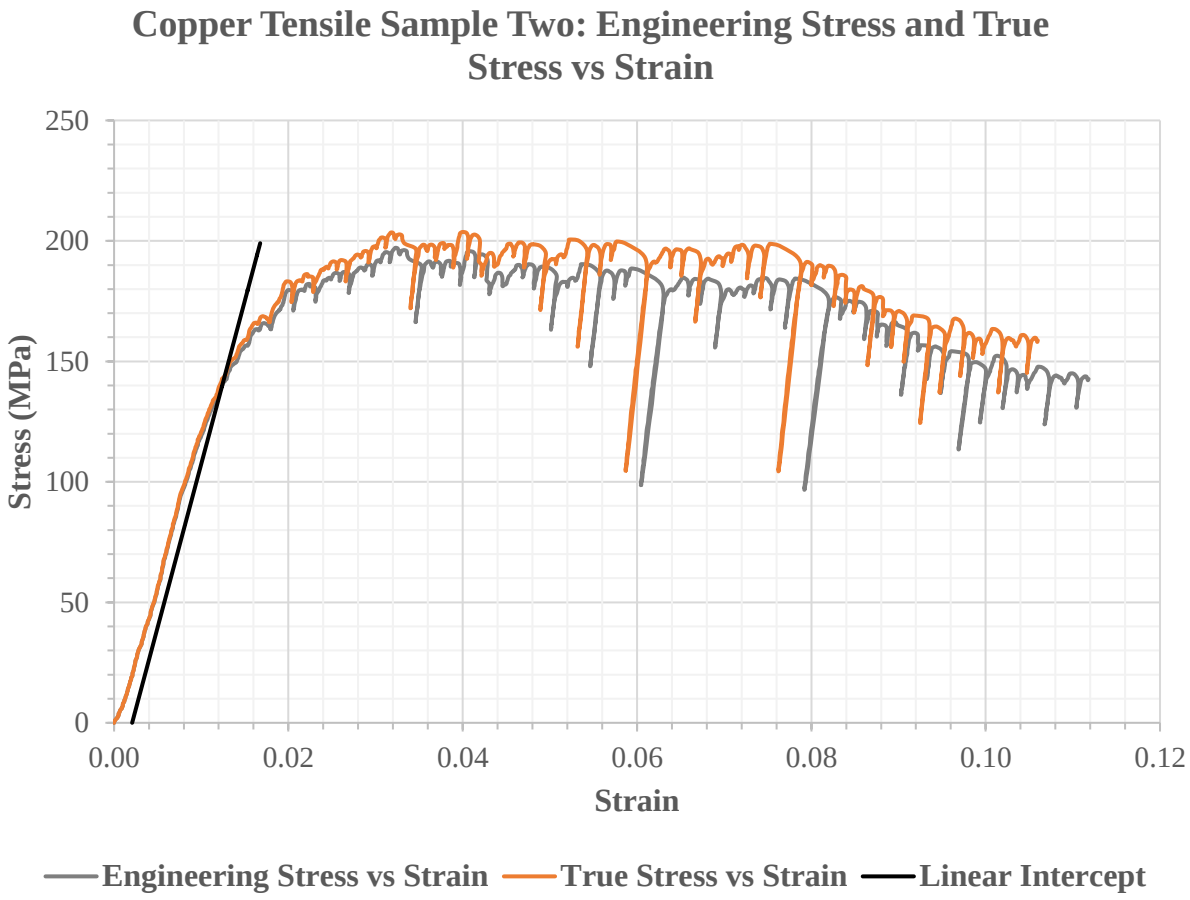

Figure 104. Copper Tensile Sample Two: Engineering Stress and True Stress vs Strain.

Table 12. Copper Tensile Sample Two: Mechanical Values.

Copper Tensile Sample Two: Mechanical Values	
Engineering Yield Strength (at 0.2% offset) (MPa)	**141.451935**
True Yield Strength (at 0.2% offset) (MPa)	**144.099793**
Engineering Max Elastic Deformation (Strain)	**0.012611**
True Max Elastic Deformation (Strain)	**0.012699**
Engineering Ultimate Tensile Strength (MPa)	**197.149261**
True Ultimate Tensile Strength (MPa)	**203.709166**
Engineering Uniform Strain	**0.032285**
True Uniform Strain	**0.039988**
Engineering Fracture Strength (MPa)	**142.708325**
True Fracture Strength (MPa)	**158.663863**
Engineering Total Strain	**0.111805**
True Total Strain	**0.105985**
Modulus of Elasticity (GPa)	**11.635009**

7.2 Copper Tensile Sample Four

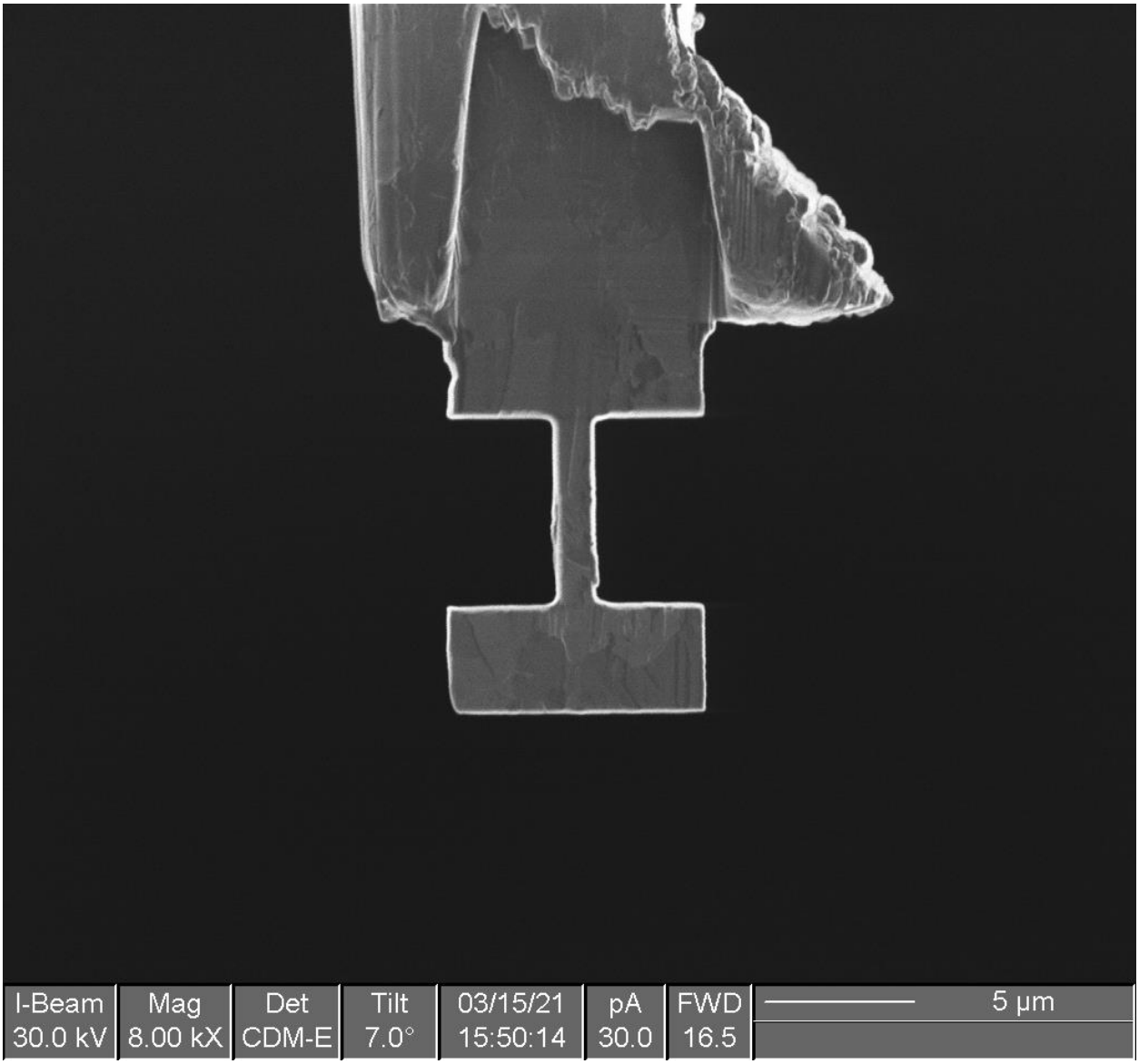

Figure 105. Copper Tensile Sample Four height by width cross section image.

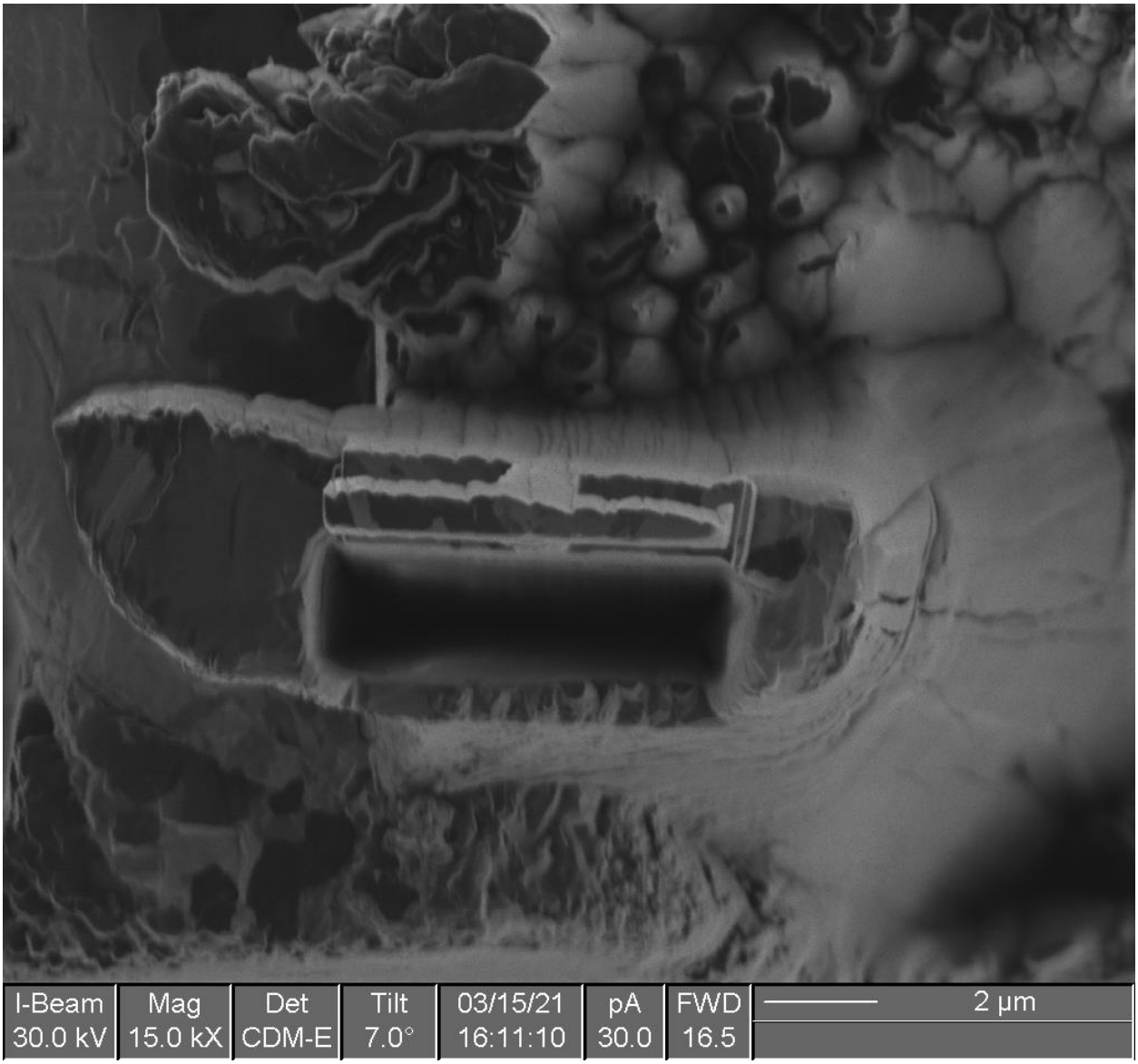

Figure 106**.** Copper Tensile Sample Four depth by width cross section image.

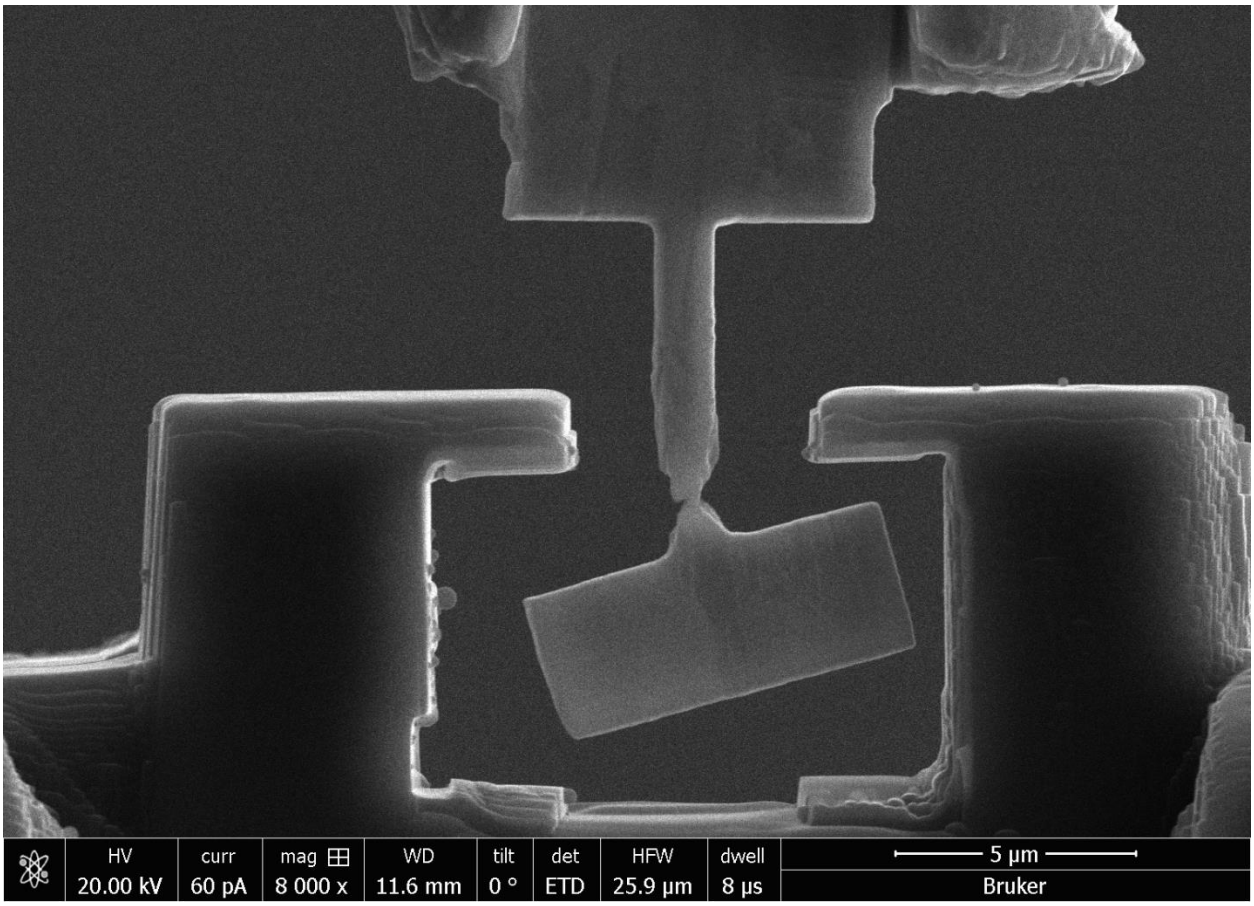

Figure 107. Copper Tensile Sample Two post failure image.

Table 13. Dimensions of Copper Tensile Sample Four, Gauge Section (μm).

Dimensions of Copper Tensile Sample Four, Gauge Section (μm)	
Height	**8.7**
Width	**1.4**
Depth	**1.3**

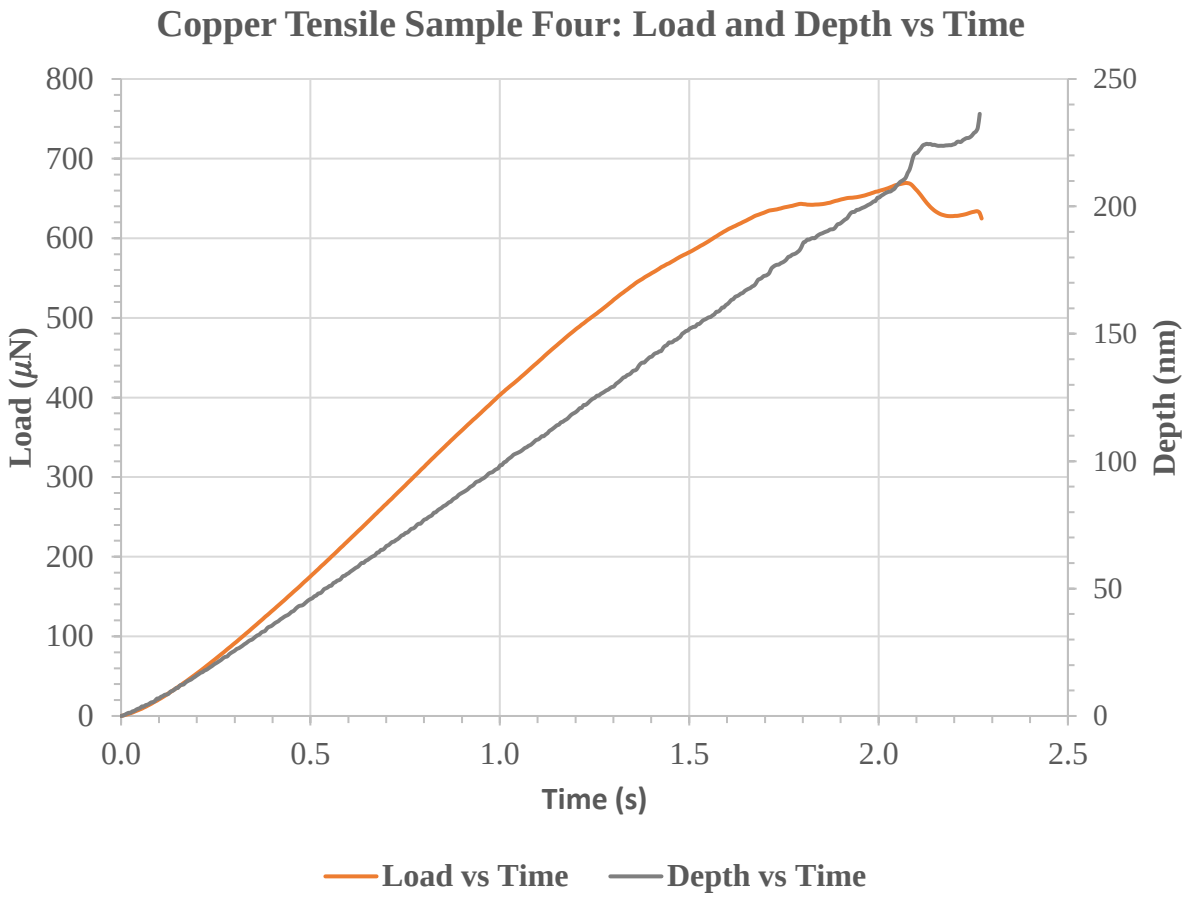

Figure 108. Copper Tensile Sample Four: Load and Depth vs Time.

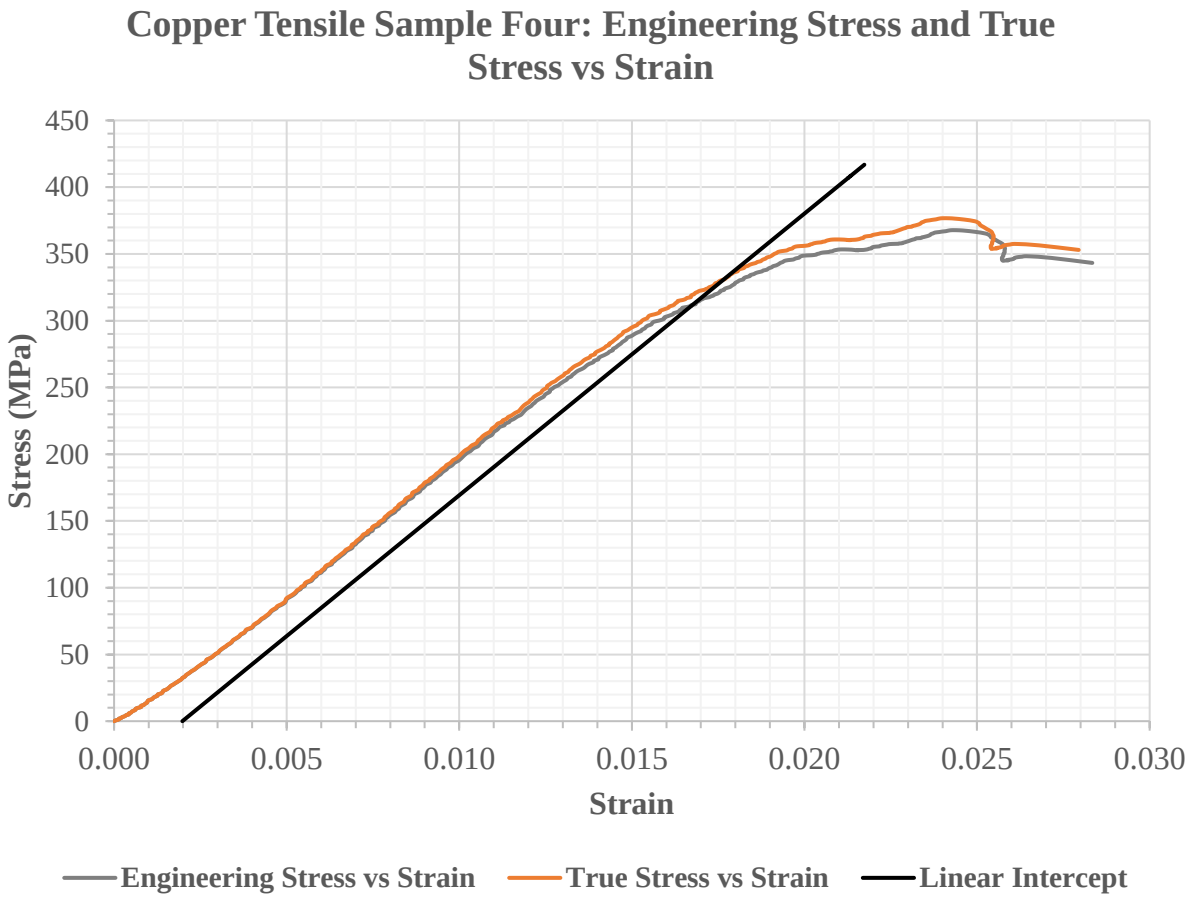

Figure 109. Copper Tensile Sample Four: Engineering Stress and True Stress vs Strain.

Table 14. Copper Tensile Sample Four: Mechanical Values.

Copper Tensile Sample Four: Mechanical Values	
Engineering Yield Strength (at 0.2% offset) (MPa)	**316.933935**
True Yield Strength (at 0.2% offset) (MPa)	**334.389540**
Engineering Max Elastic Deformation (Strain)	**0.017105**
True Max Elastic Deformation (Strain)	**0.017839**
Engineering Ultimate Tensile Strength (MPa)	**367.823640**
True Ultimate Tensile Strength (MPa)	**376.758009**
Engineering Uniform Strain	**0.024290**
True Uniform Strain	**0.024000**
Engineering Fracture Strength (MPa)	**346.990445**
True Fracture Strength (MPa)	**356.415714**
Engineering Total Strain	**0.027163**
True Total Strain	**0.026801**
Modulus of Elasticity (GPa)	**18.609483**

7.3 Copper Tensile Sample Five

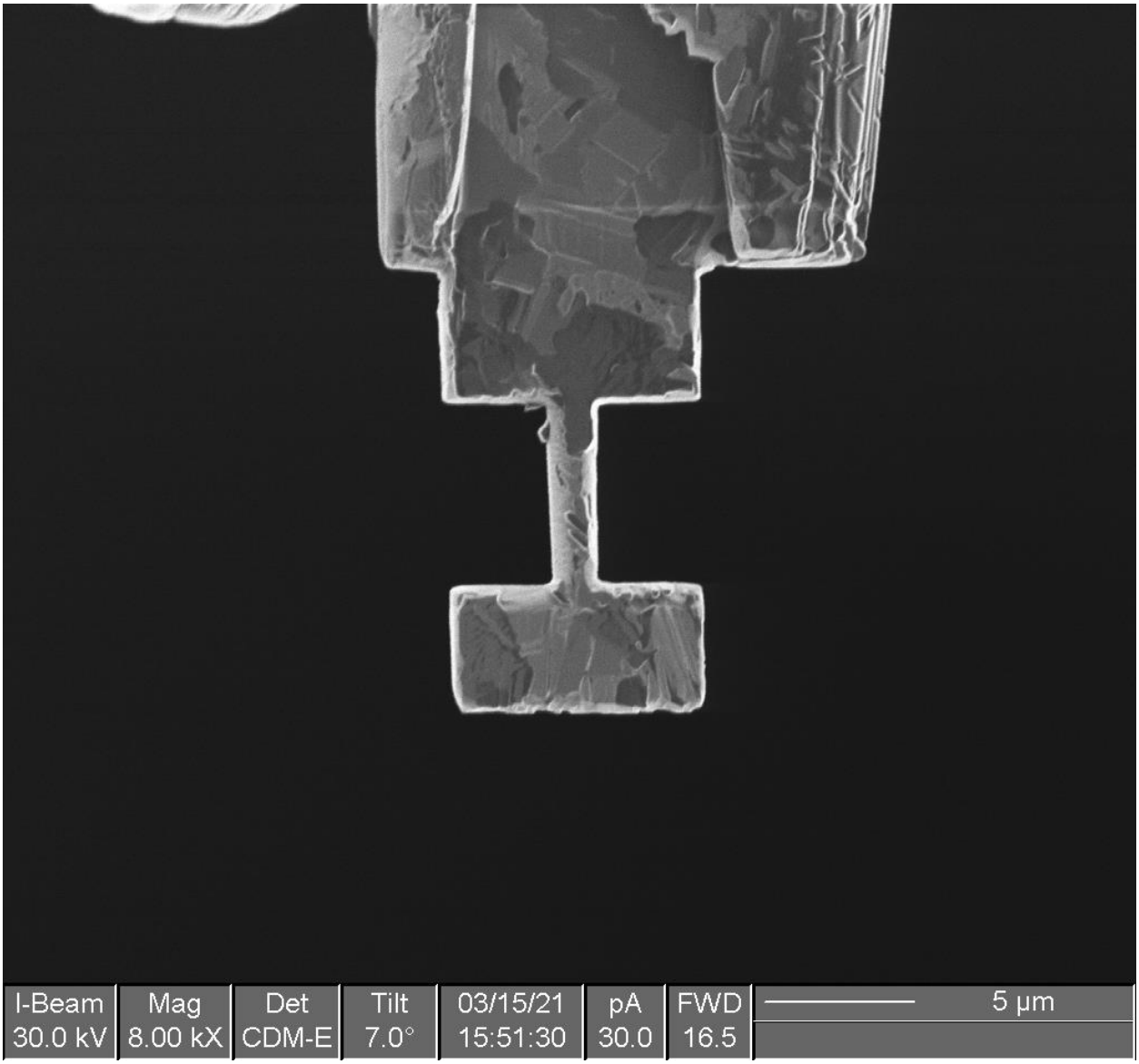

Figure 110. Copper Tensile Sample Five height by width cross section image.

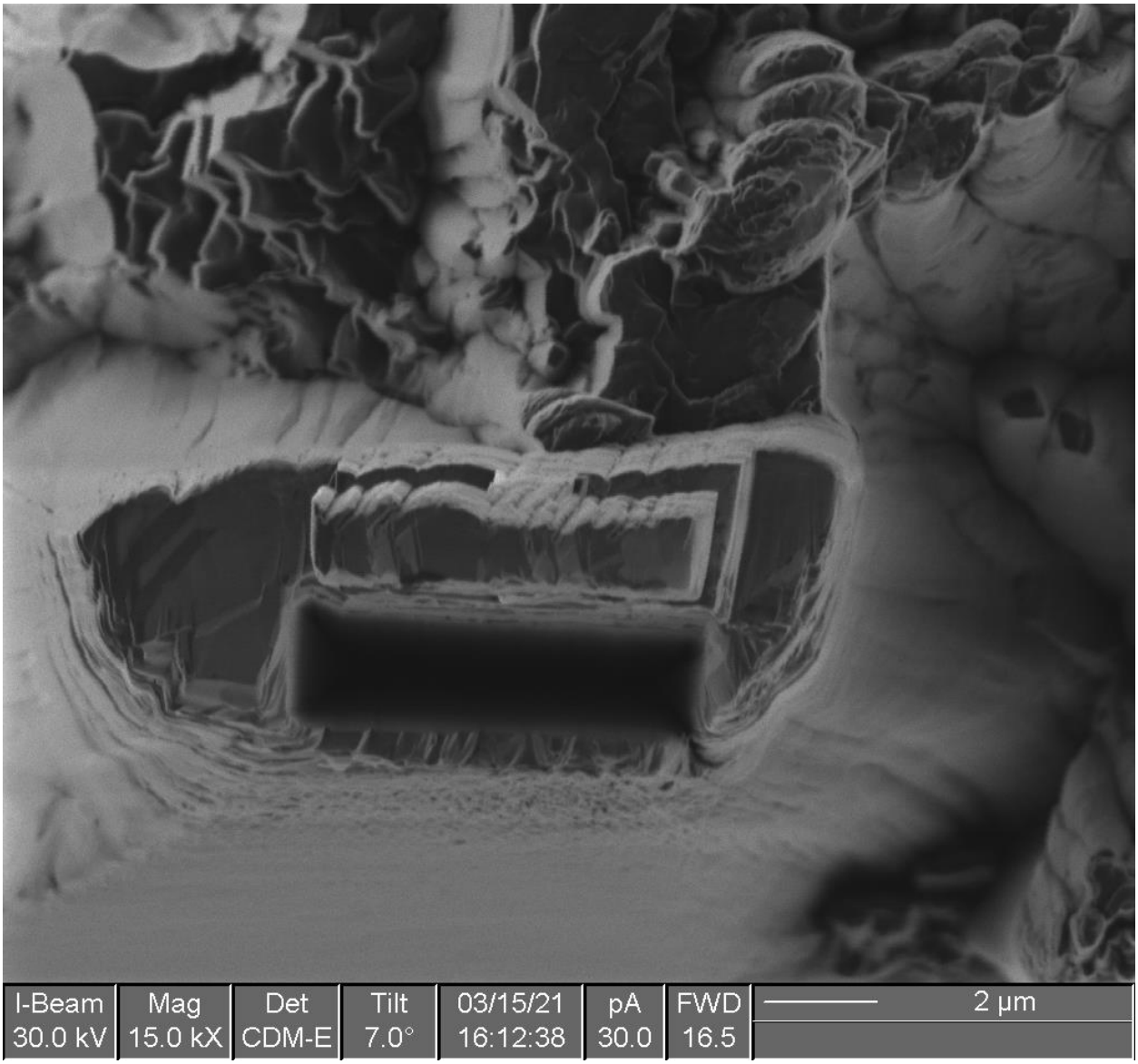

Figure 111. Copper Tensile Sample Five depth by width cross section image.

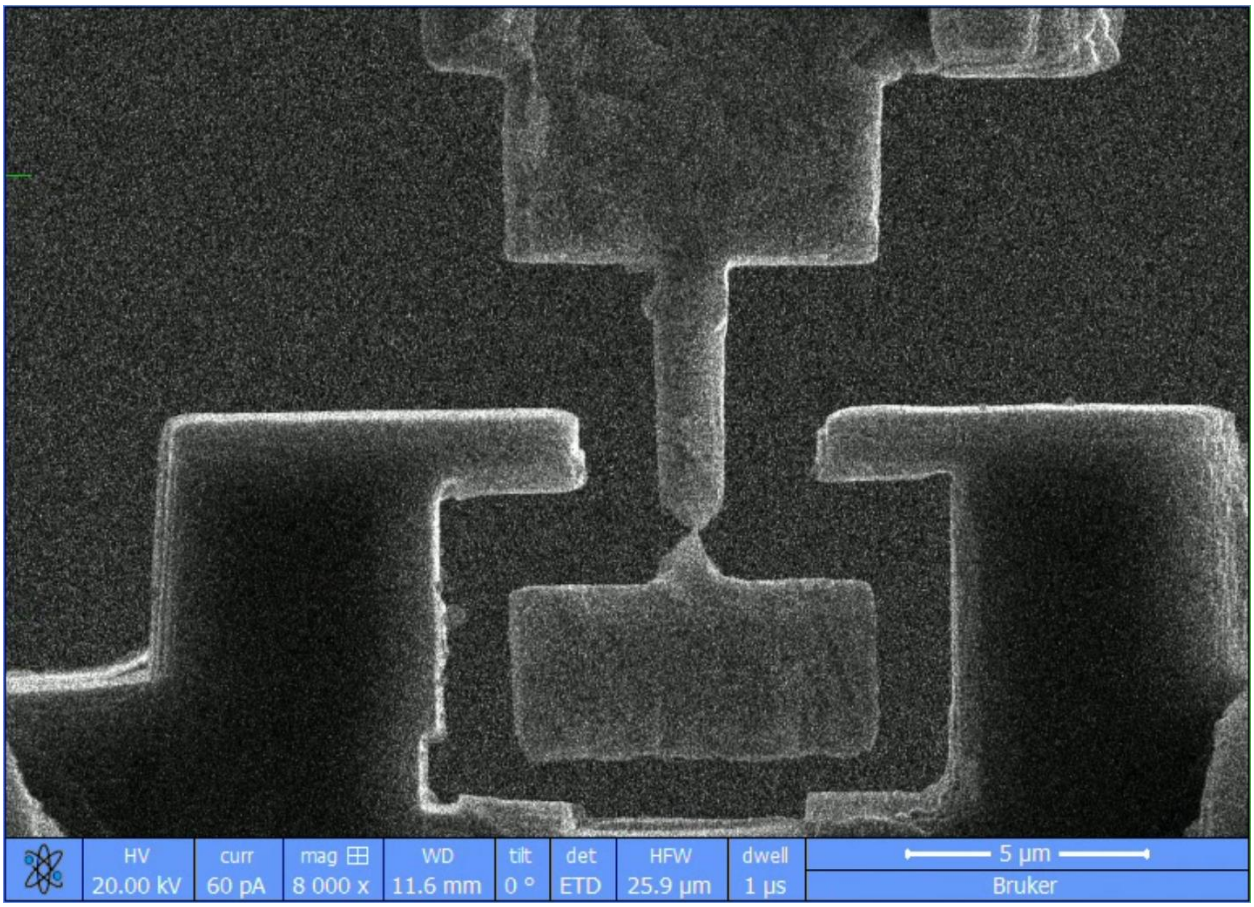

Figure 112. Copper Tensile Sample Five post failure image.

Table 15. Dimensions of Copper Tensile Sample Five, Gauge Section (μm).

Dimensions of Copper Tensile Sample Five, Gauge Section (μm)	
Height	**8.4**
Width	**1.6**
Depth	**2.3**

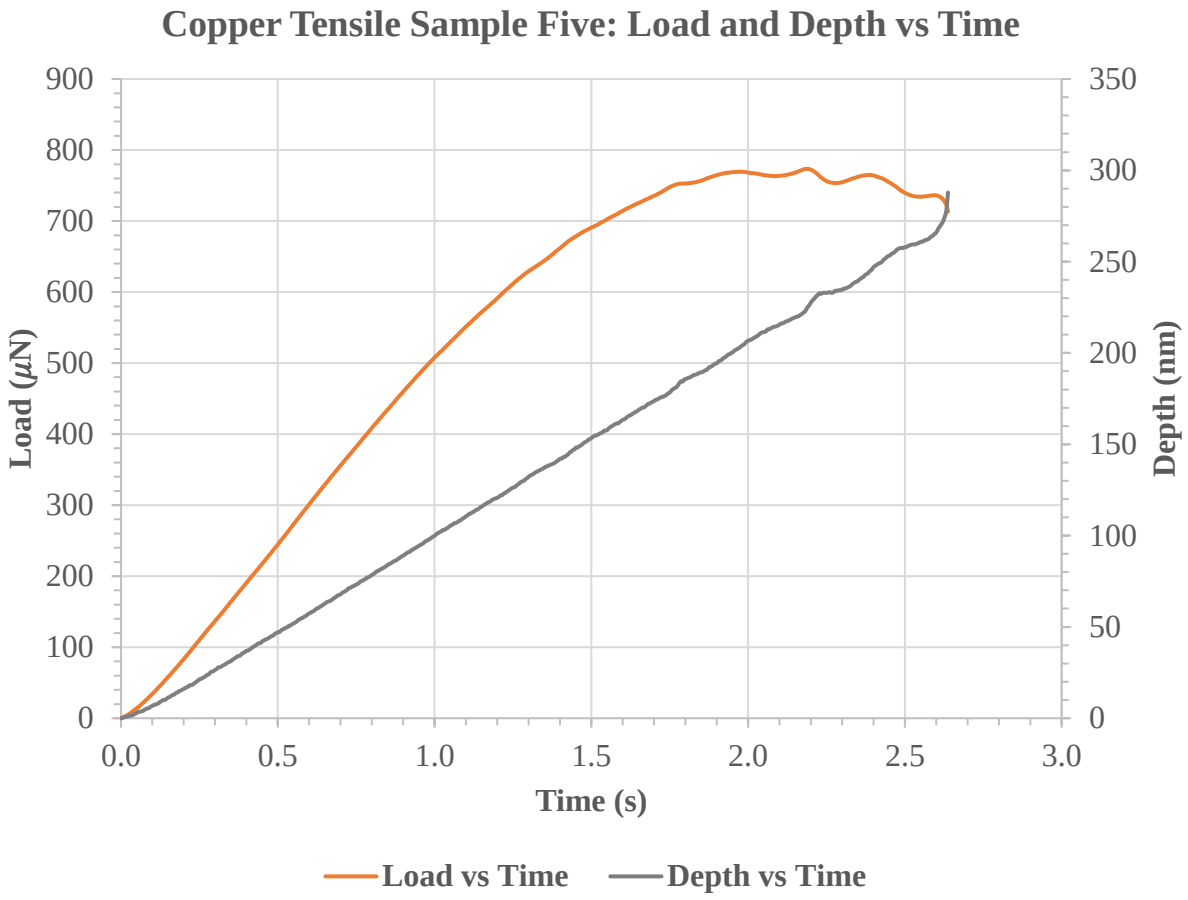

Figure 113. Copper Tensile Sample Five: Load and Depth vs Time.

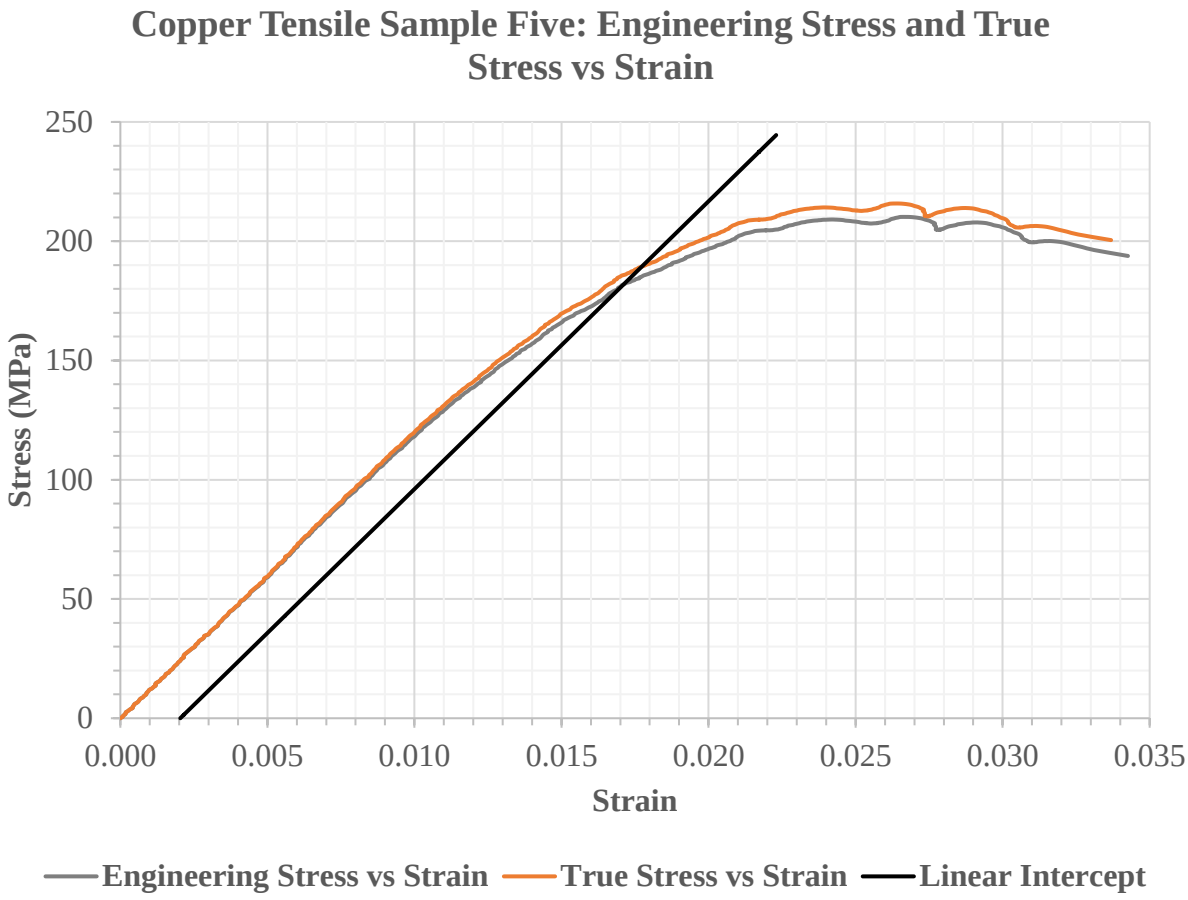

Figure 114. Copper Tensile Sample Five: Engineering Stress and True Stress vs Strain.

Table 16. Copper Tensile Sample Five: Mechanical Values.

Copper Tensile Sample Five: Mechanical Values	
Engineering Yield Strength (at 0.2% offset) (MPa)	**183.306209**
True Yield Strength (at 0.2% offset) (MPa)	**188.849712**
Engineering Max Elastic Deformation (Strain)	**0.017389**
True Max Elastic Deformation (Strain)	**0.017621**
Engineering Ultimate Tensile Strength (MPa)	**210.176200**
True Ultimate Tensile Strength (MPa)	**215.791699**
Engineering Uniform Strain	**0.026718**
True Uniform Strain	**0.026367**
Engineering Fracture Strength (MPa)	**193.811611**
True Fracture Strength (MPa)	**200.451887**
Engineering Total Strain	**0.034261**
True Total Strain	**0.033688**
Modulus of Elasticity (GPa)	**11.869549**

7.4 Copper Tensile Sample Seven

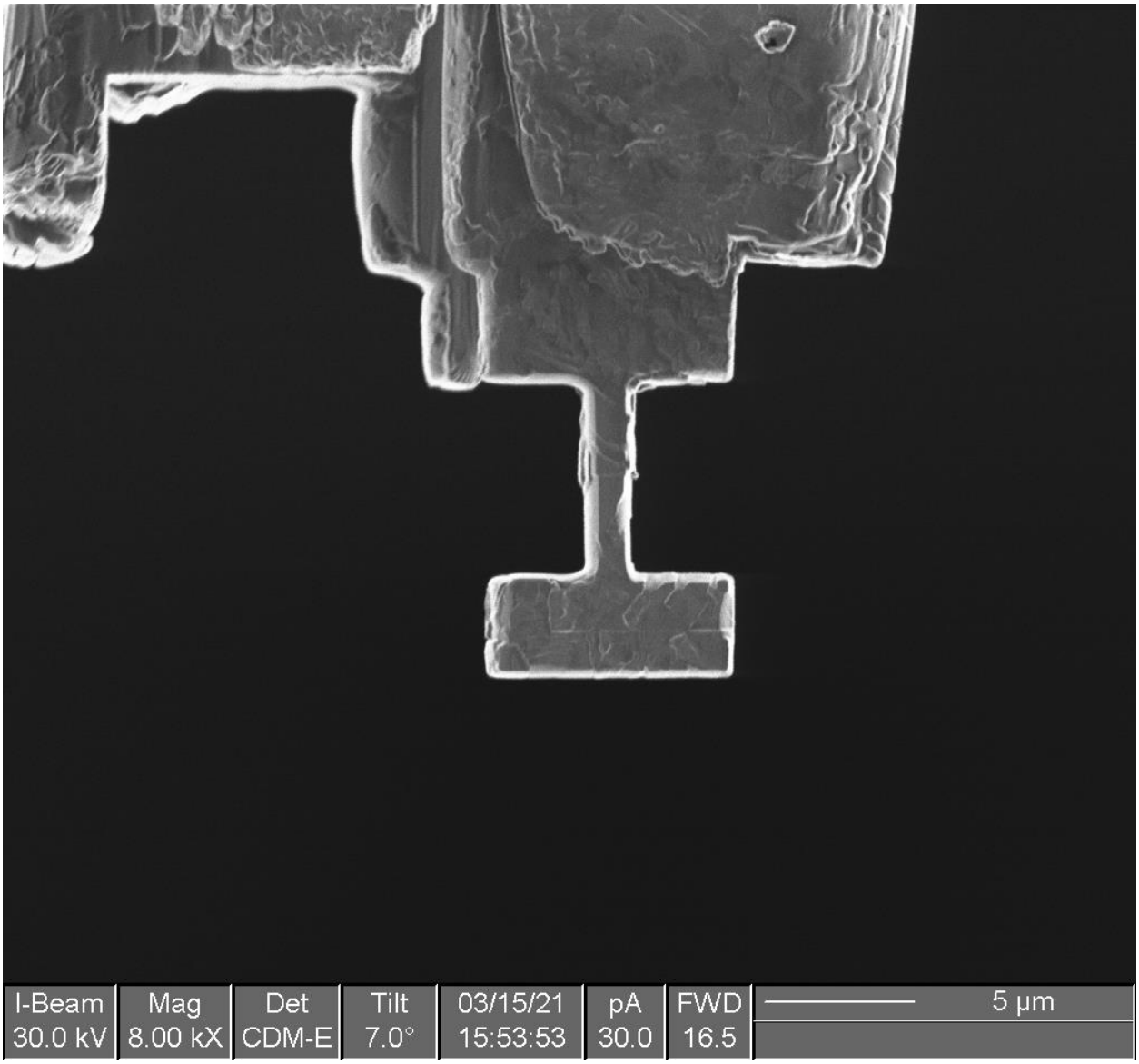

Figure 115. Copper Tensile Sample Seven height by width cross section image.

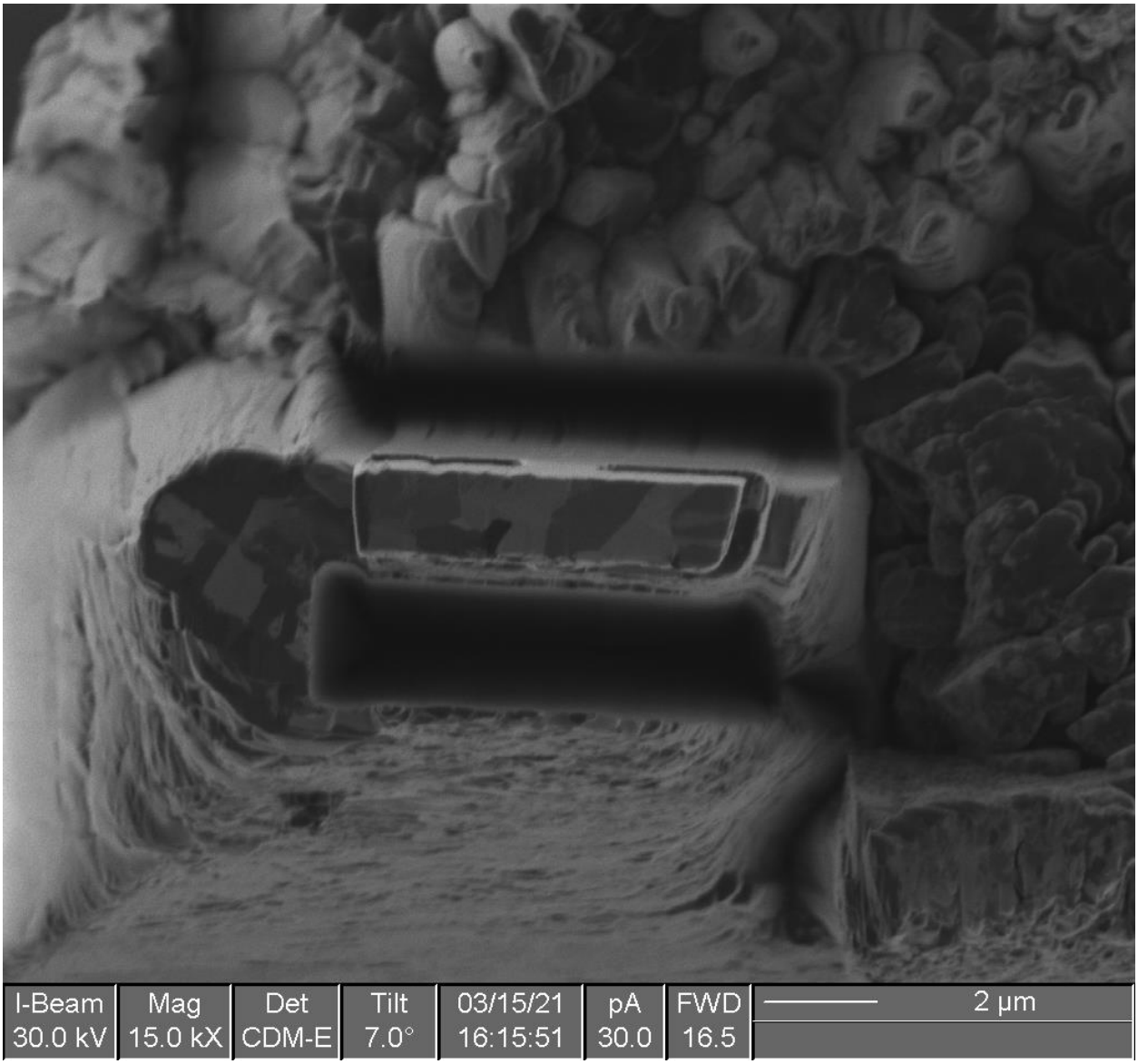

Figure 116. Copper Tensile Sample Seven depth by width cross section image.

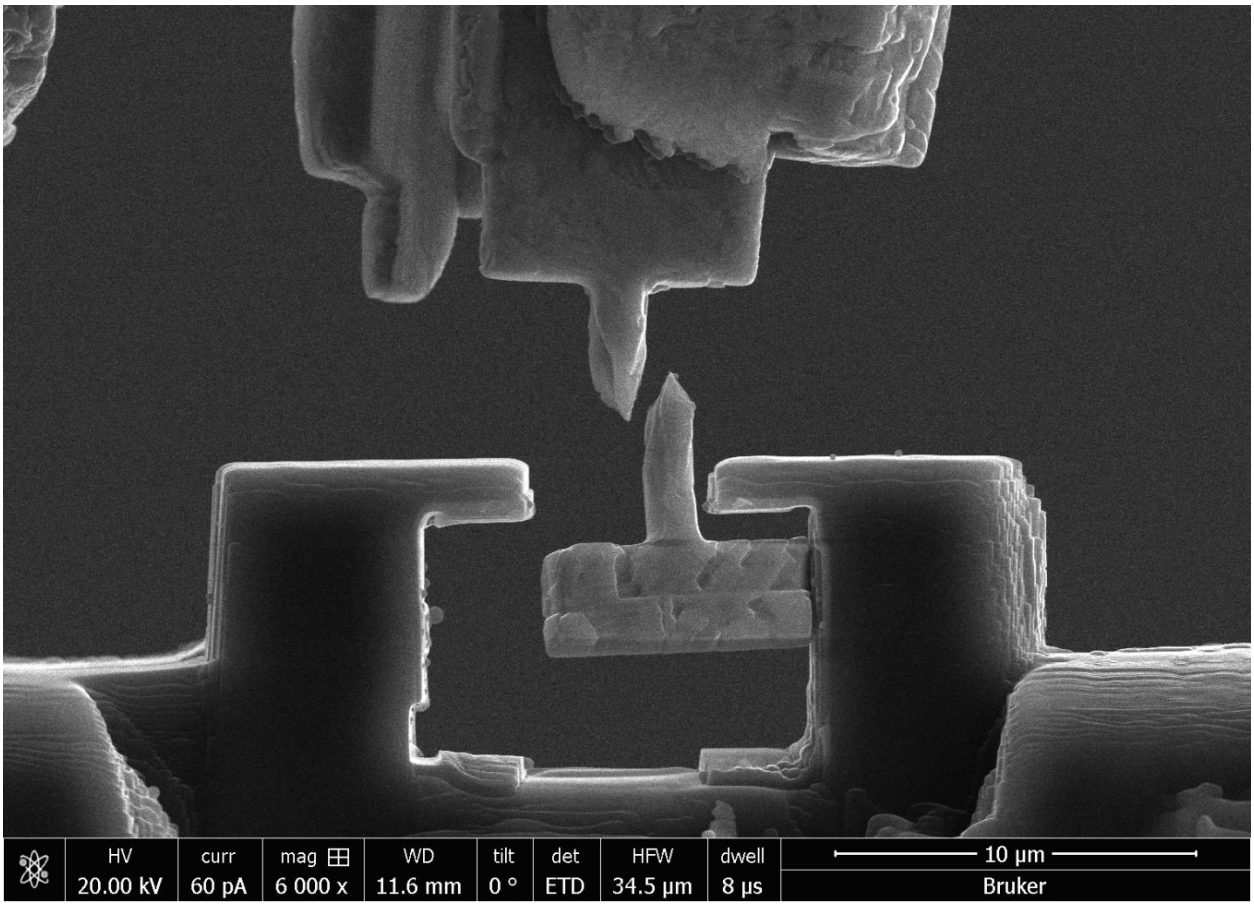

Figure 117. Copper Tensile Sample Two post failure image.

Table 17. Dimensions of Copper Tensile Sample Seven, Gauge Section (μm).

Dimensions of Copper Tensile Sample Seven, Gauge Section (μm)	
Height	**8.9**
Width	**1.8**
Depth	**2.3**

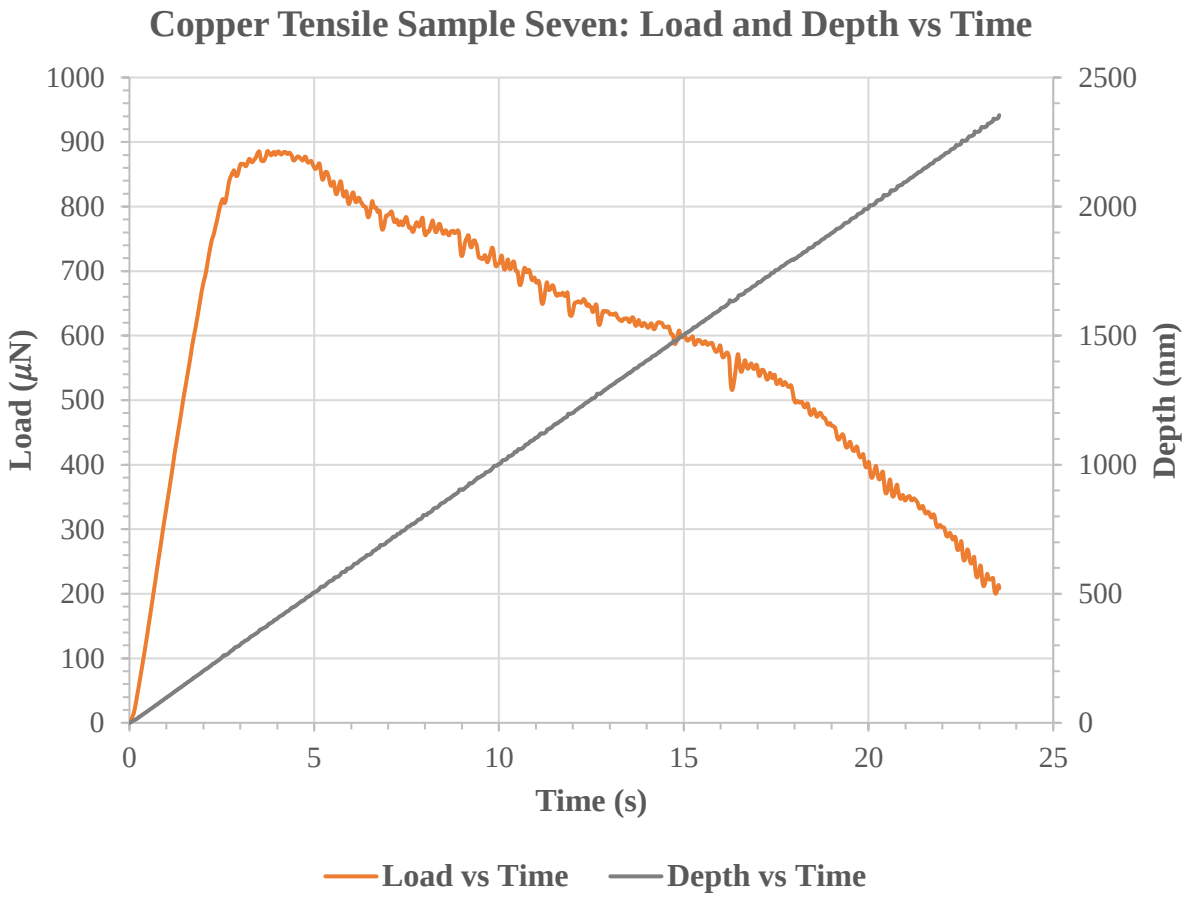

Figure 118. Copper Tensile Sample Seven: Load and Depth vs Time.

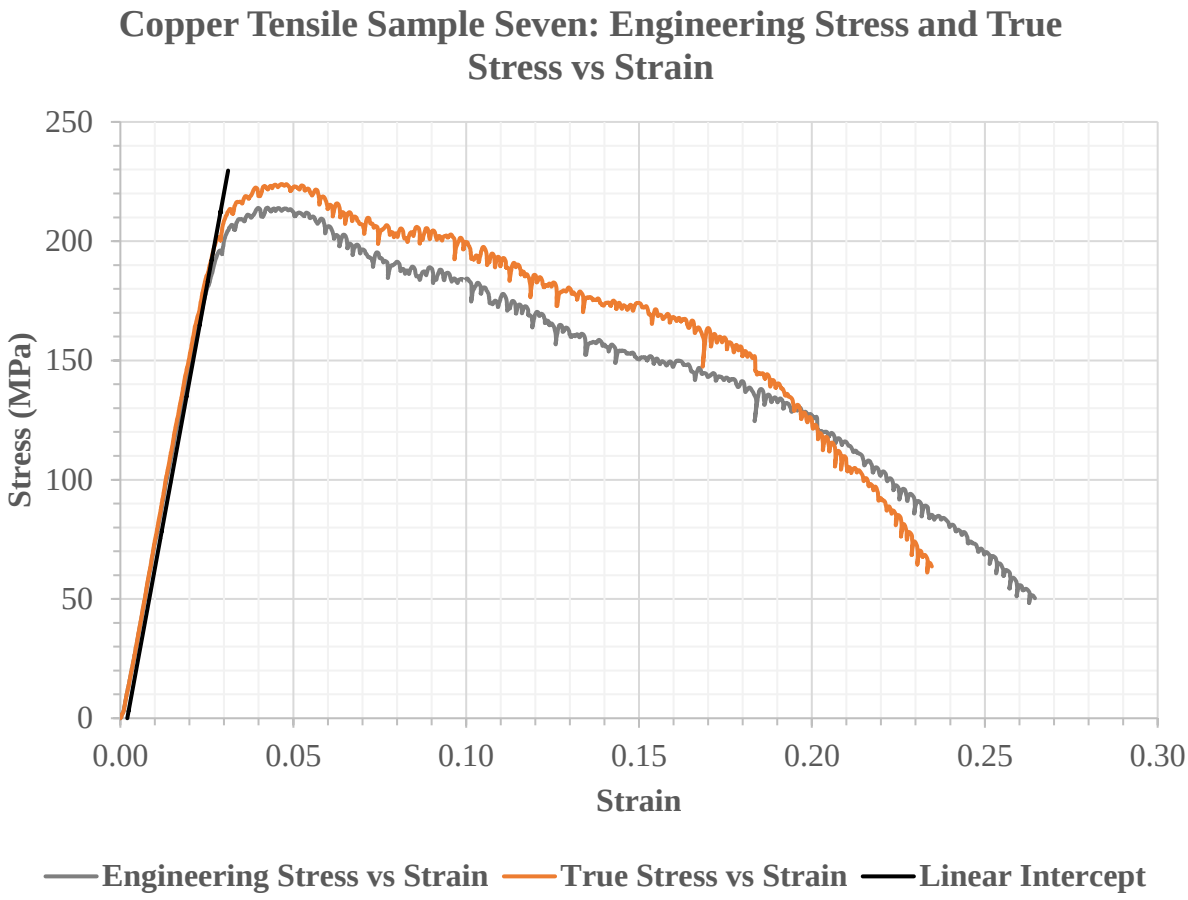

Figure 119. Copper Tensile Sample Seven: Engineering Stress and True Stress vs Strain.

Table 18. Copper Tensile Sample Seven: Mechanical Values.

Copper Tensile Sample Seven: Mechanical Values	
Engineering Yield Strength (at 0.2% offset) (MPa)	**180.924111**
True Yield Strength (at 0.2% offset) (MPa)	**196.800966**
Engineering Max Elastic Deformation (Strain)	**0.025212**
True Max Elastic Deformation (Strain)	**0.026996**
Engineering Ultimate Tensile Strength (MPa)	**214.050029**
True Ultimate Tensile Strength (MPa)	**223.906892**
Engineering Uniform Strain	**0.042531**
True Uniform Strain	**0.046788**
Engineering Fracture Strength (MPa)	**50.322574**
True Fracture Strength (MPa)	**63.633549**
Engineering Total Strain	**0.264513**
True Total Strain	**0.234687**
Modulus of Elasticity (GPa)	**7.560844**

7.5 Copper Tensile Sample Nine

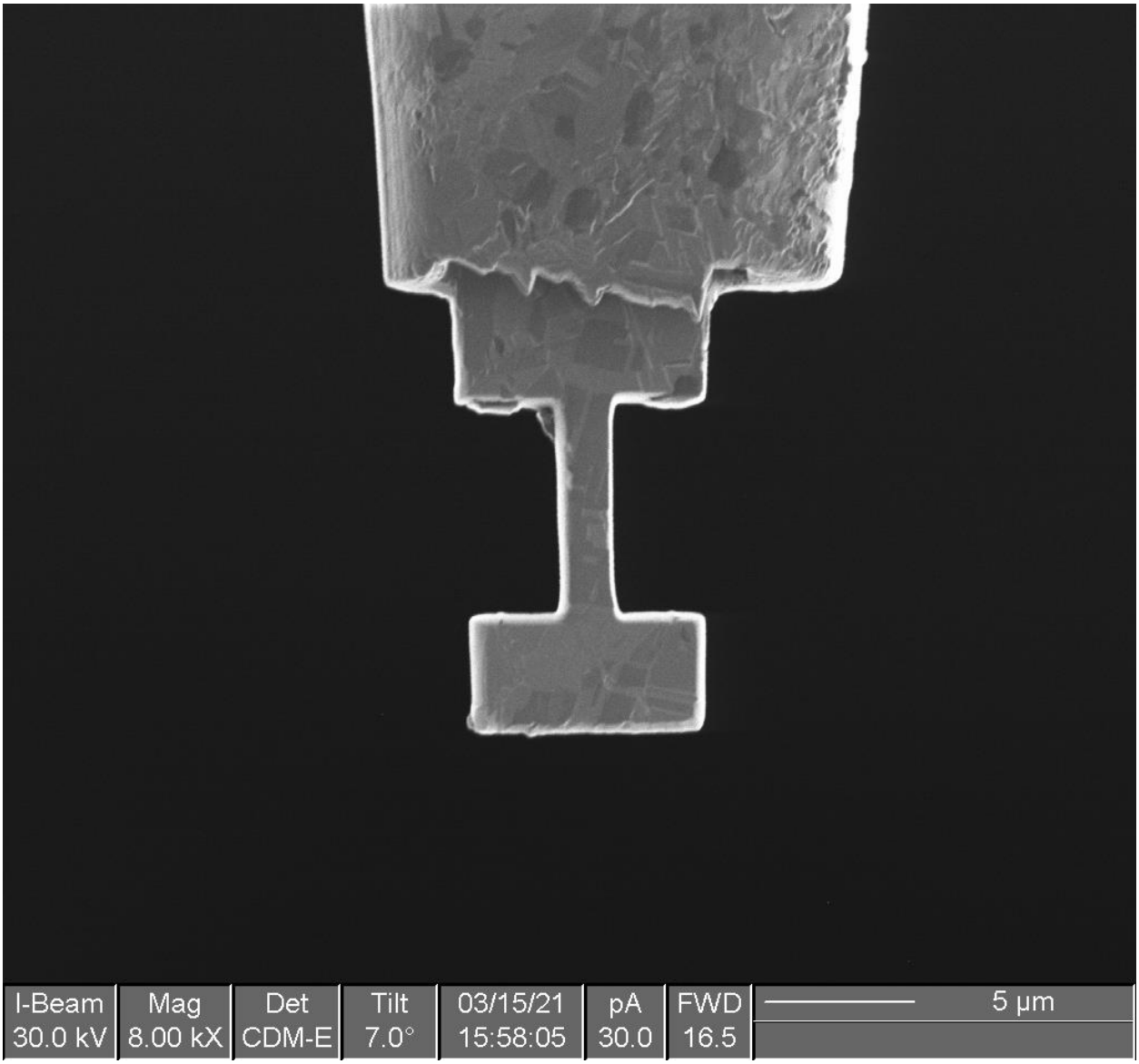

Figure 120. Copper Tensile Sample Nine height by width cross section image.

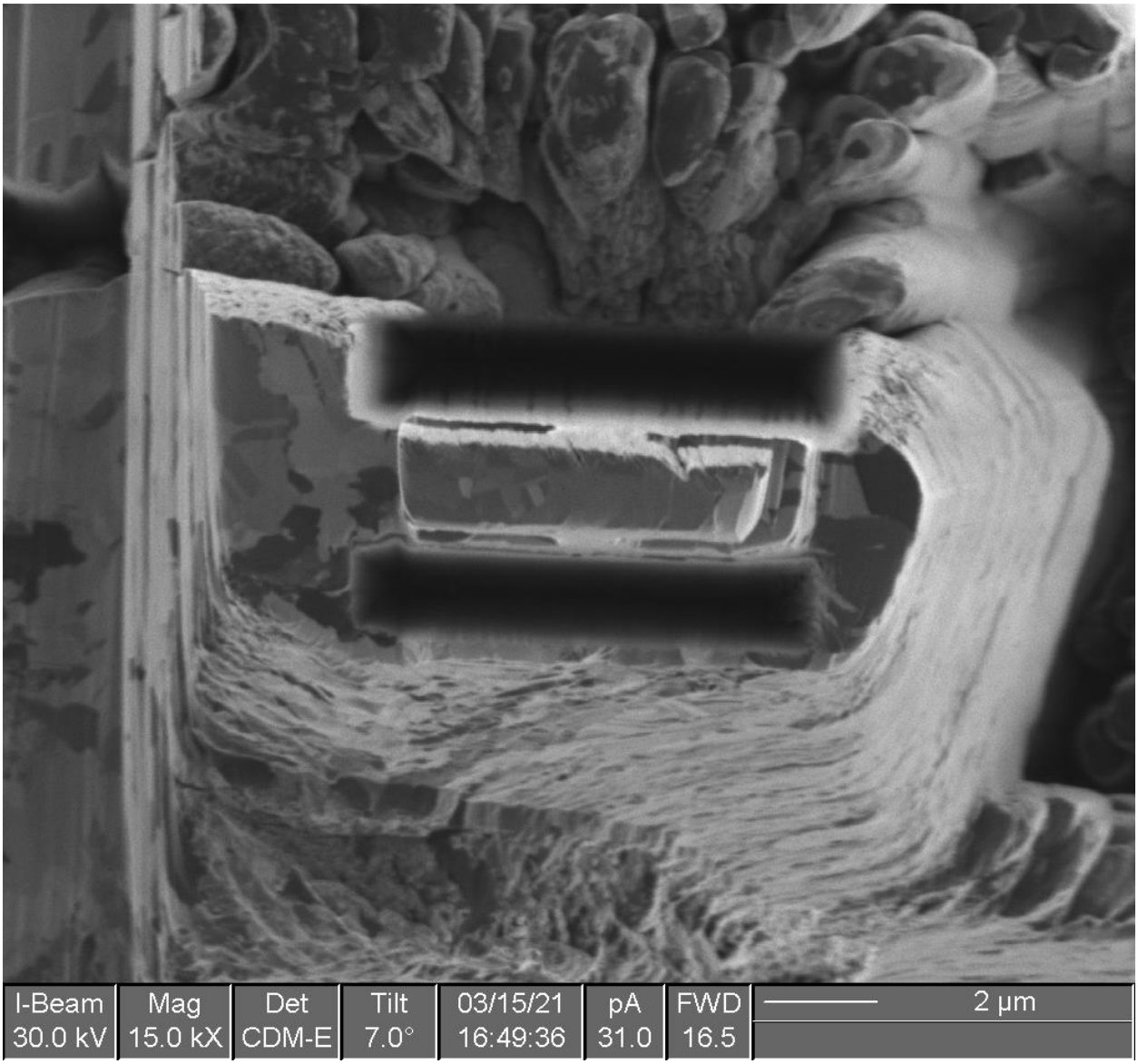

Figure 121. Copper Tensile Sample Nine depth by width cross section image.

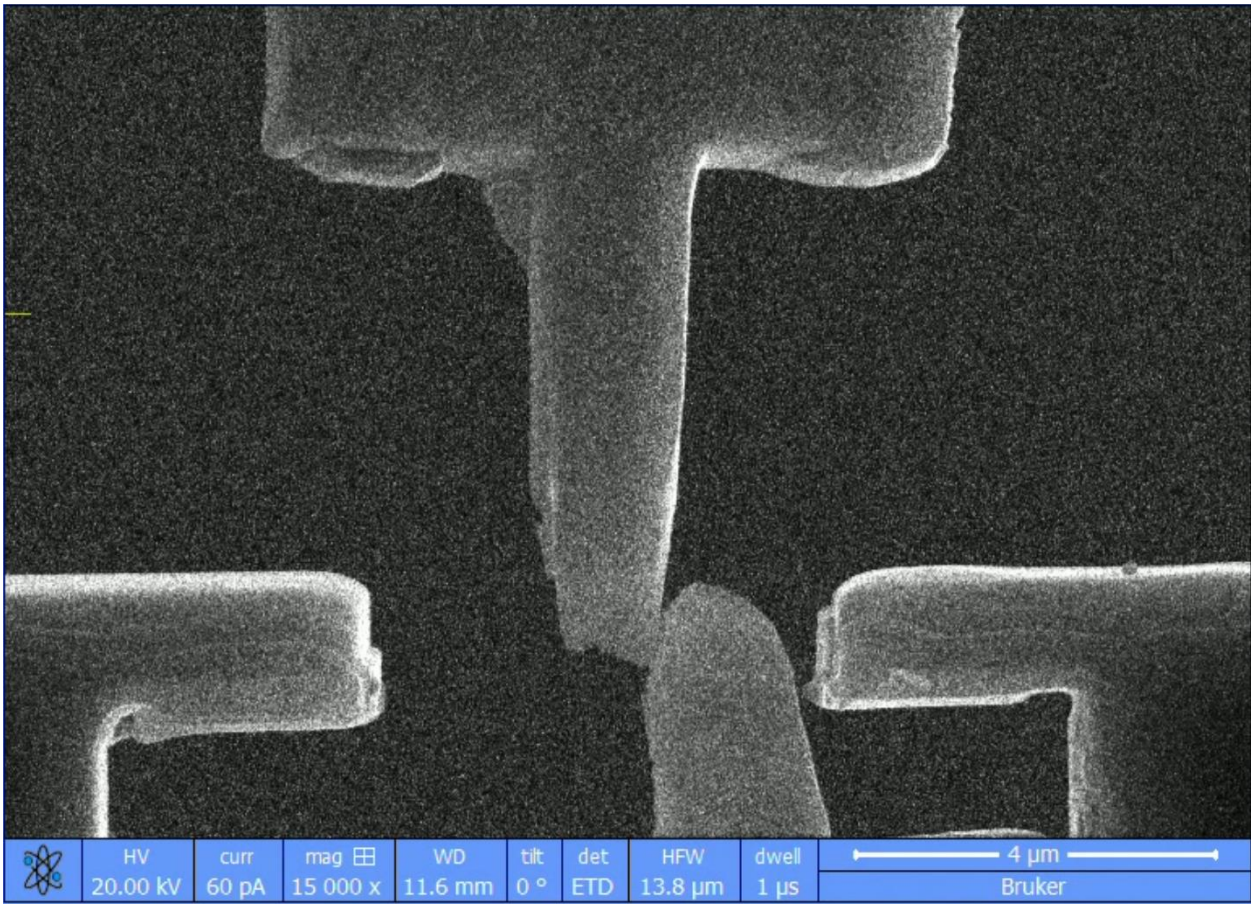

Figure 122. Copper Tensile Sample Nine post failure image.

Table 19. Dimensions of Copper Tensile Sample Nine, Gauge Section (μm).

Dimensions of Copper Tensile Sample Nine, Gauge Section (μm)	
Height	**9.8**
Width	**1.9**
Depth	**2.4**

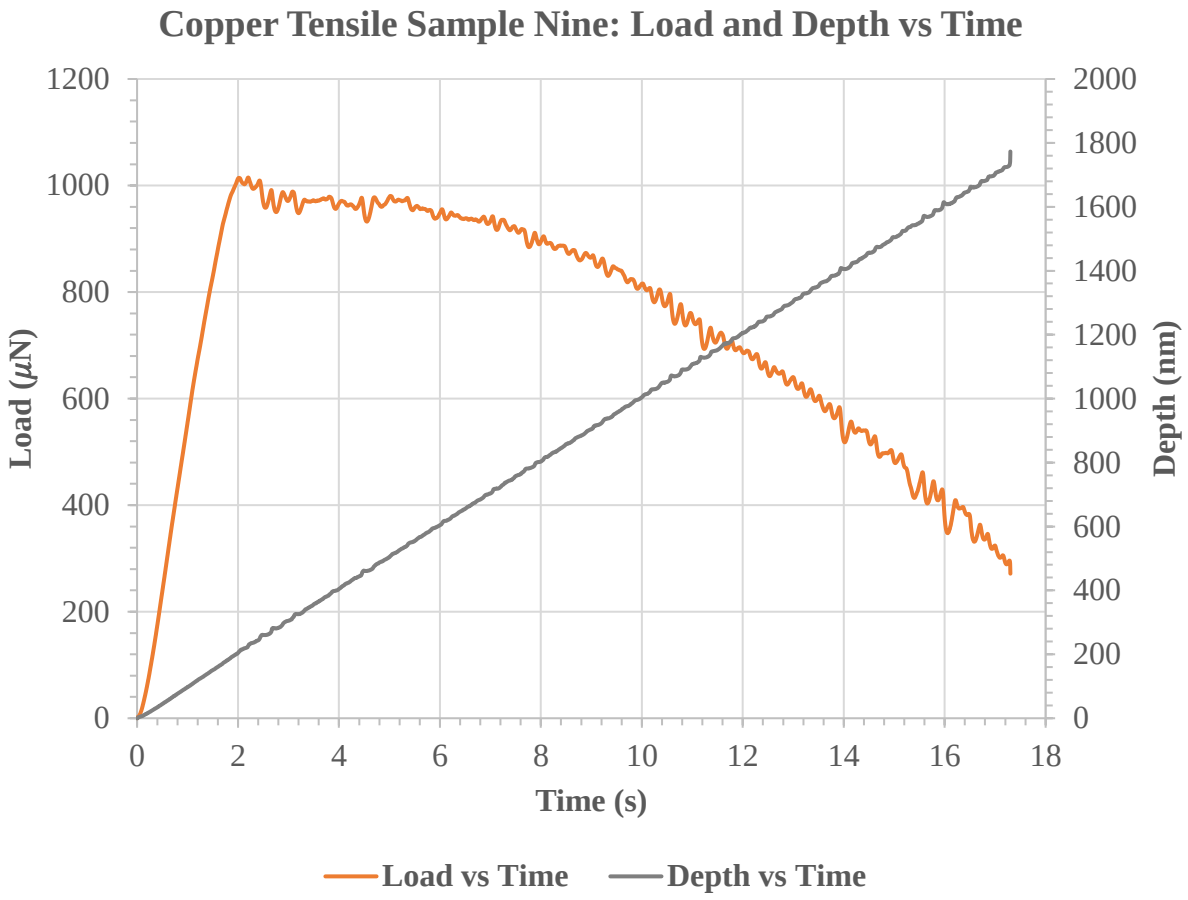

Figure 123. Copper Tensile Sample Nine: Load and Depth vs Time.

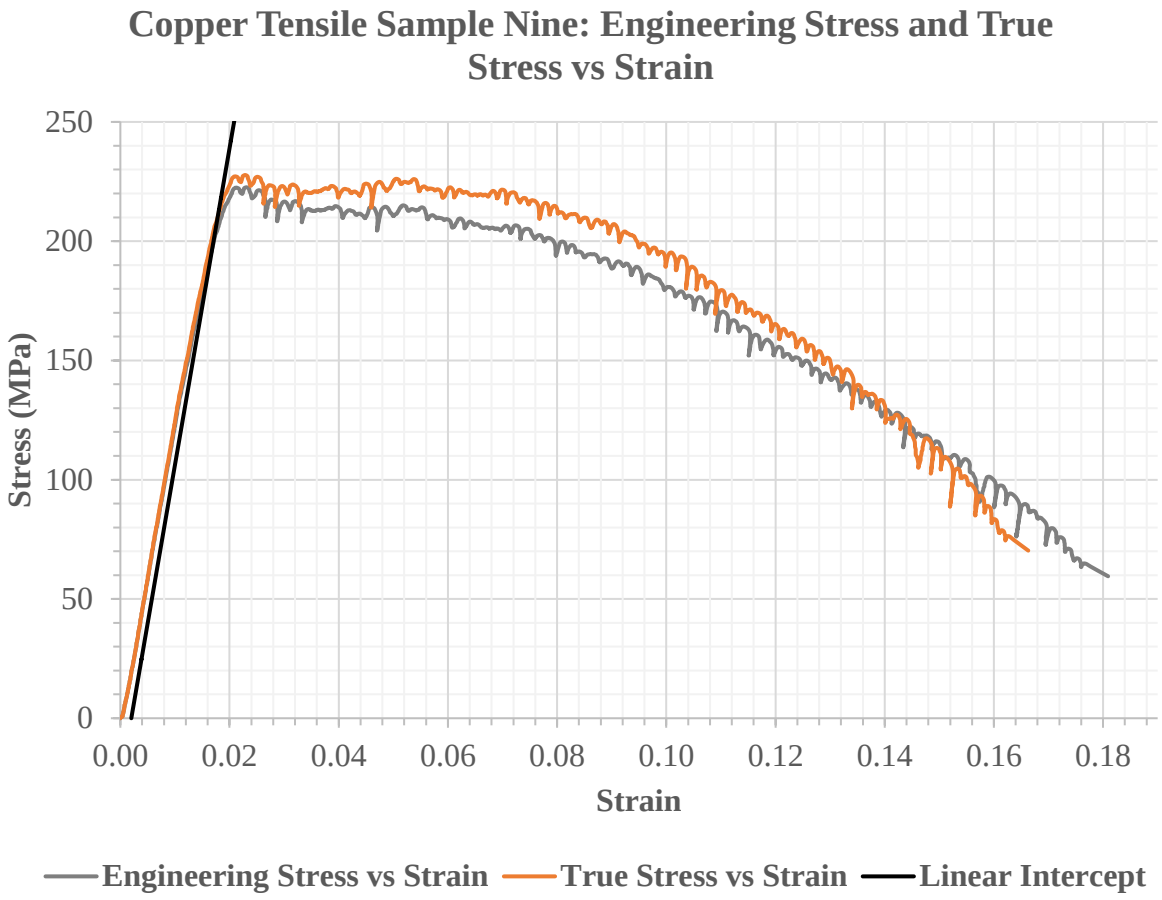

Figure 124. Copper Tensile Sample Nine: Engineering Stress and True Stress vs Strain.

Table 20. Copper Tensile Sample Nine: Mechanical Values.

Copper Tensile Sample Nine: Mechanical Values	
Engineering Yield Strength (at 0.2% offset) (MPa)	**203.093027**
True Yield Strength (at 0.2% offset) (MPa)	**210.384151**
Engineering Max Elastic Deformation (Strain)	**0.017467**
True Max Elastic Deformation (Strain)	**0.017855**
Engineering Ultimate Tensile Strength (MPa)	**222.592977**
True Ultimate Tensile Strength (MPa)	**227.734978**
Engineering Uniform Strain	**0.023100**
True Uniform Strain	**0.022838**
Engineering Fracture Strength (MPa)	**59.518109**
True Fracture Strength (MPa)	**70.286250**
Engineering Total Strain	**0.180922**
True Total Strain	**0.166296**
Modulus of Elasticity (GPa)	**12.148202**

7.6 Copper Tensile Sample Ten

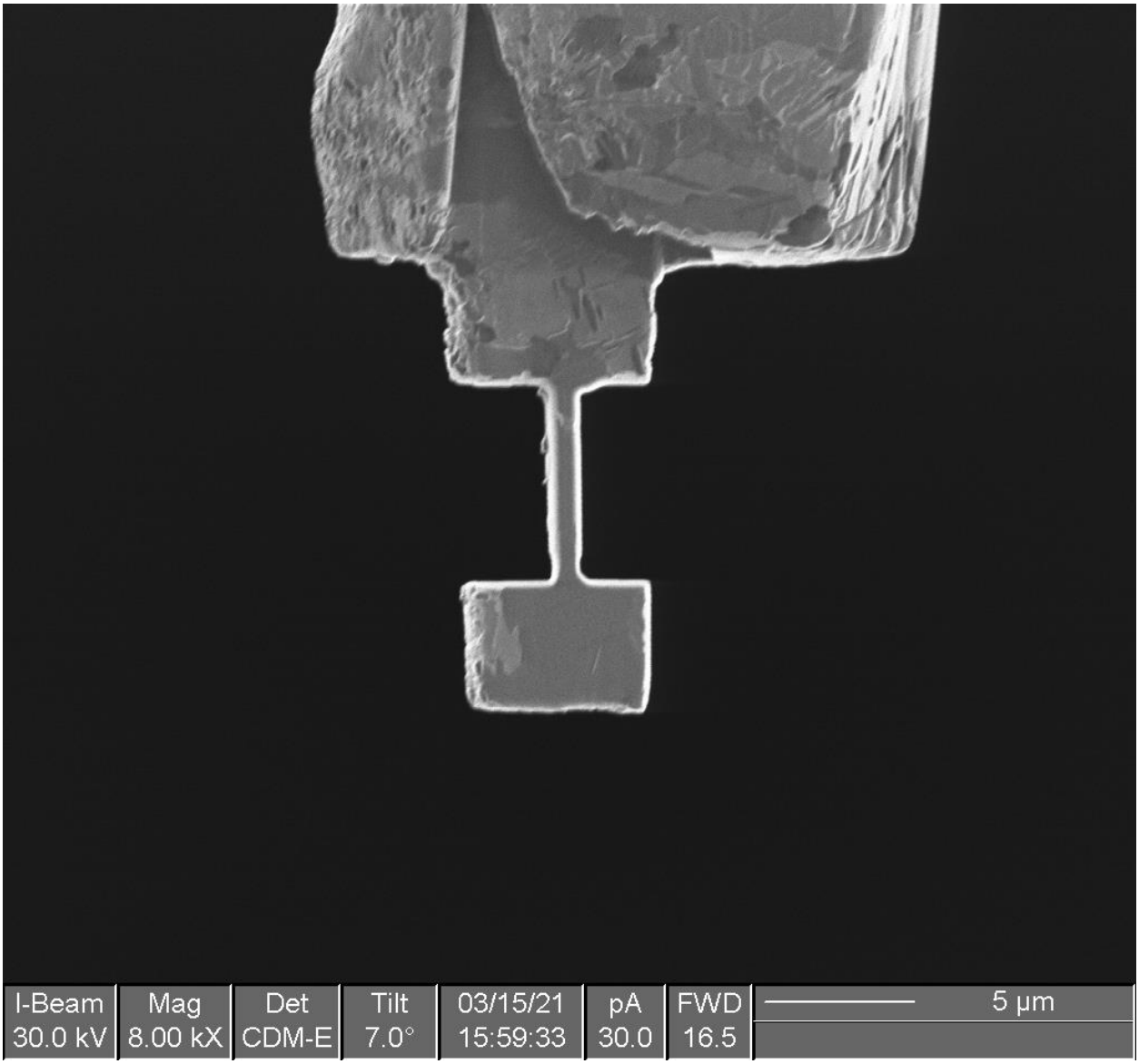

Figure 125. Copper Tensile Sample Ten height by width cross section image.

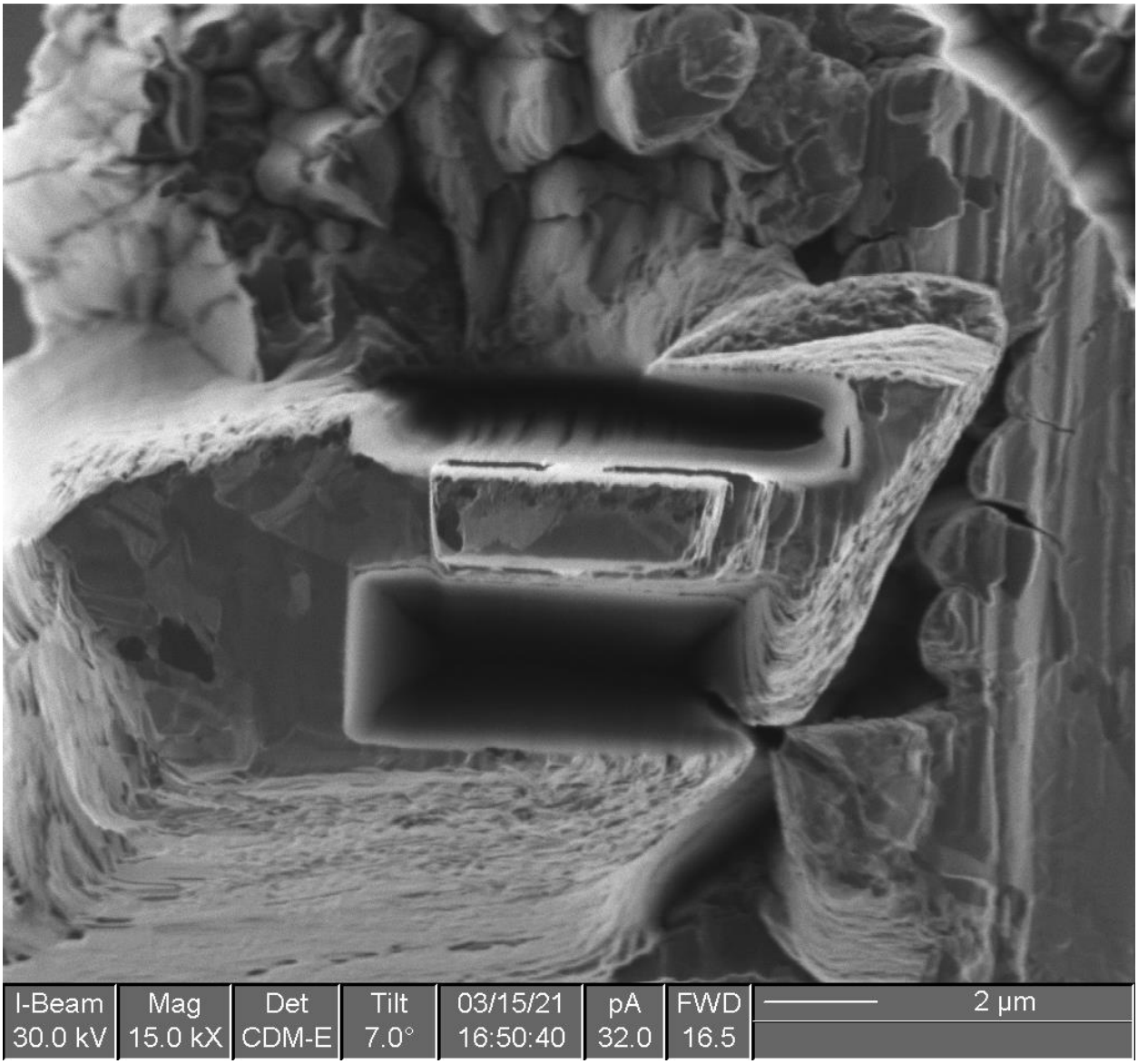

Figure 126. Copper Tensile Sample Ten depth by width cross section image.

Note that this sample experienced some slippage on the right side of the head section, as can be seen in Fig. 127. This can be seen as variance in the plastic region of the stress-strain curve.

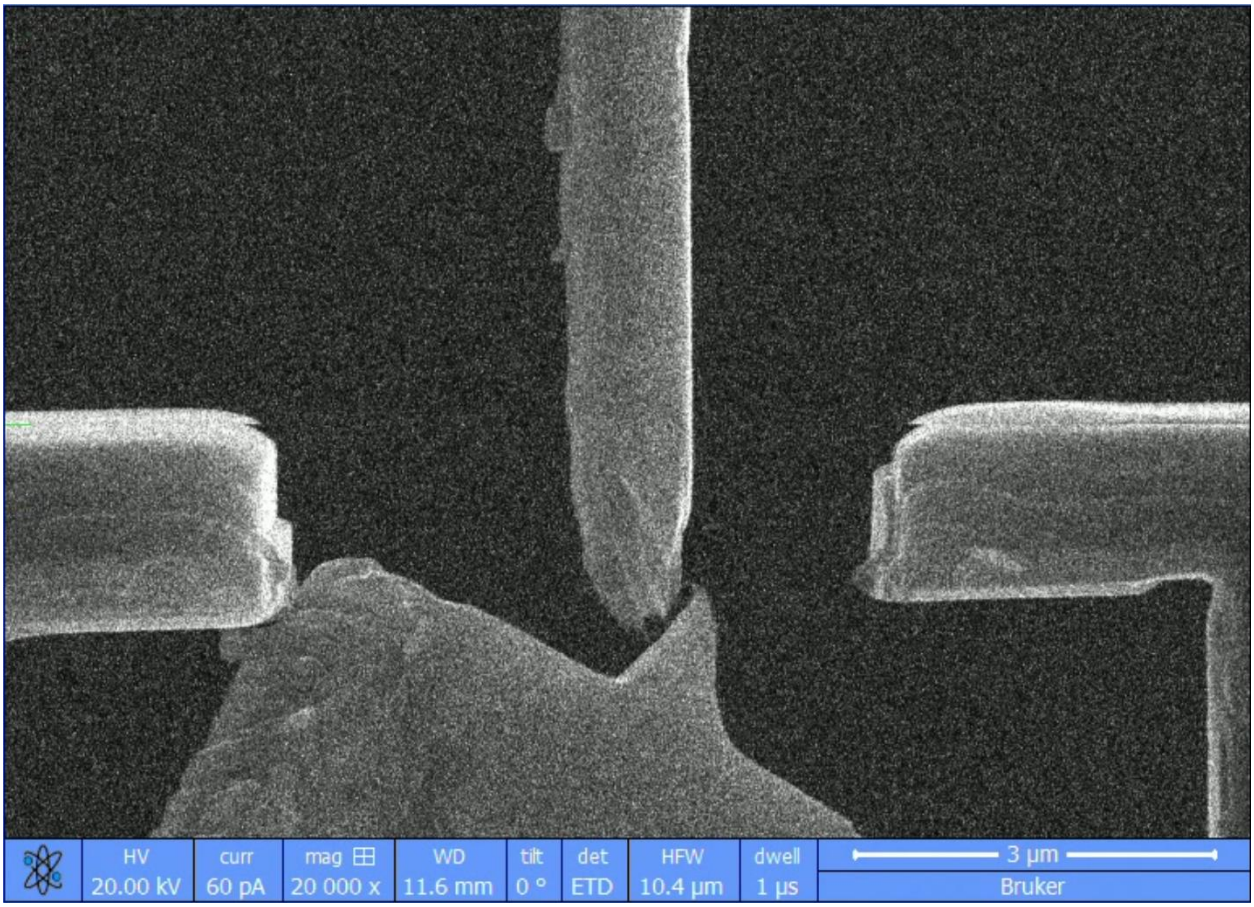

Figure 127. Copper Tensile Sample Ten post failure image.

Table 21. Dimensions of Copper Tensile Sample Ten, Gauge Section (μm).

Dimensions of Copper Tensile Sample Ten, Gauge Section (μm)	
Height	**9.0**
Width	**1.0**
Depth	**2.4**

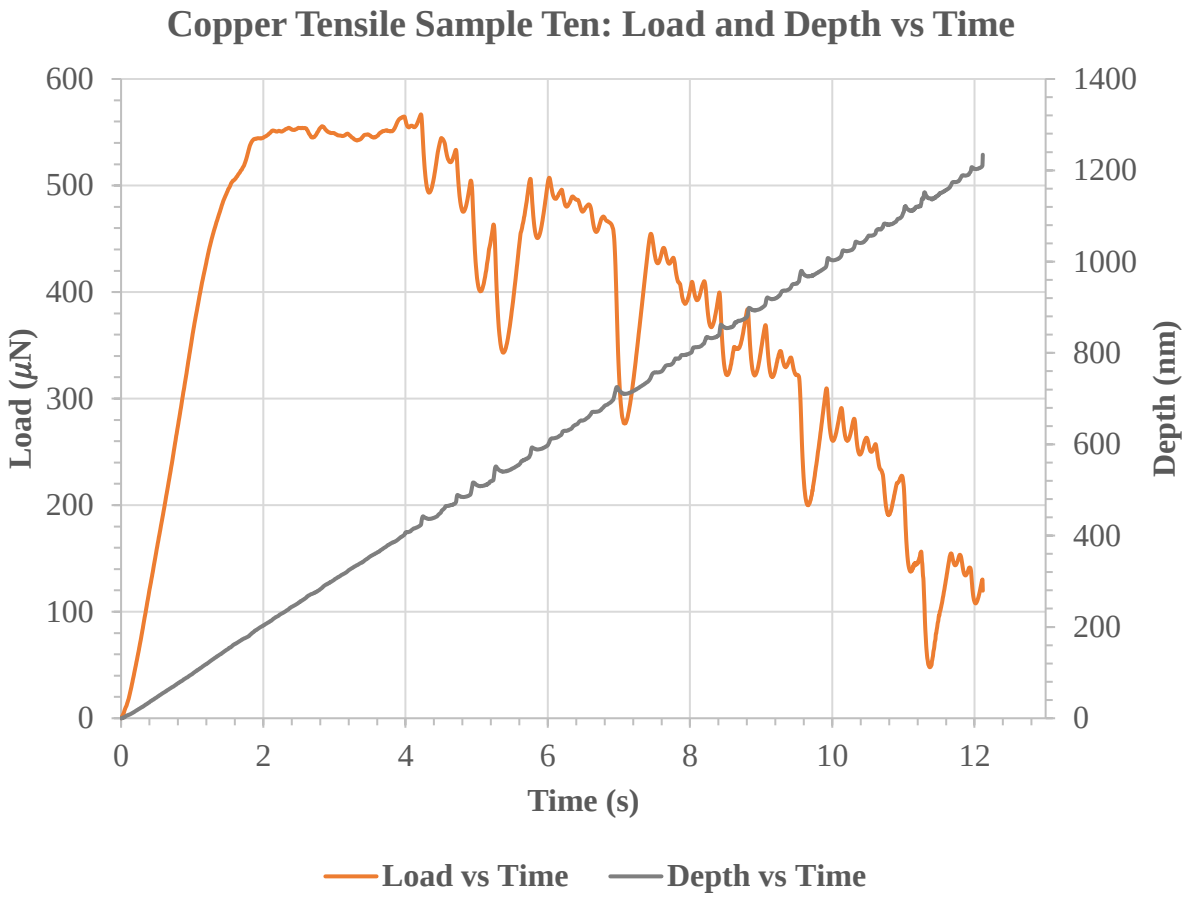

Figure 128. Copper Tensile Sample Ten: Load and Depth vs Time.

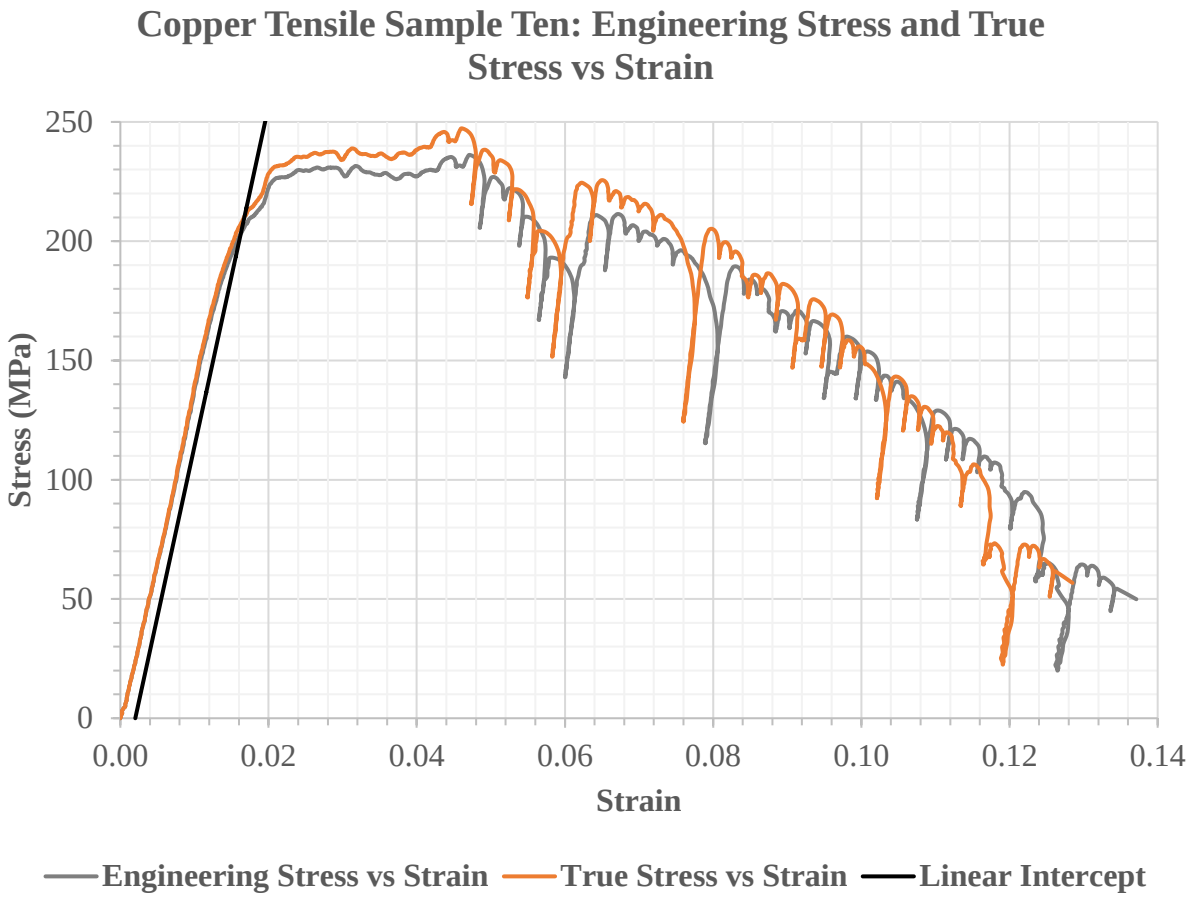

Figure 129. Copper Tensile Sample Ten: Engineering Stress and True Stress vs Strain.

Table 22. Copper Tensile Sample Ten: Mechanical Values.

Copper Tensile Sample Ten: Mechanical Values	
Engineering Yield Strength (at 0.2% offset) (MPa)	**204.506918**
True Yield Strength (at 0.2% offset) (MPa)	**210.627748**
Engineering Max Elastic Deformation (Strain)	**0.016493**
True Max Elastic Deformation (Strain)	**0.016818**
Engineering Ultimate Tensile Strength (MPa)	**236.125795**
True Ultimate Tensile Strength (MPa)	**247.276476**
Engineering Uniform Strain	**0.047223**
True Uniform Strain	**0.046142**
Engineering Fracture Strength (MPa)	**49.893636**
True Fracture Strength (MPa)	**56.735203**
Engineering Total Strain	**0.137123**
True Total Strain	**0.128501**
Modulus of Elasticity (GPa)	**13.201224**

7.7 Silicon Tensile Sample Four

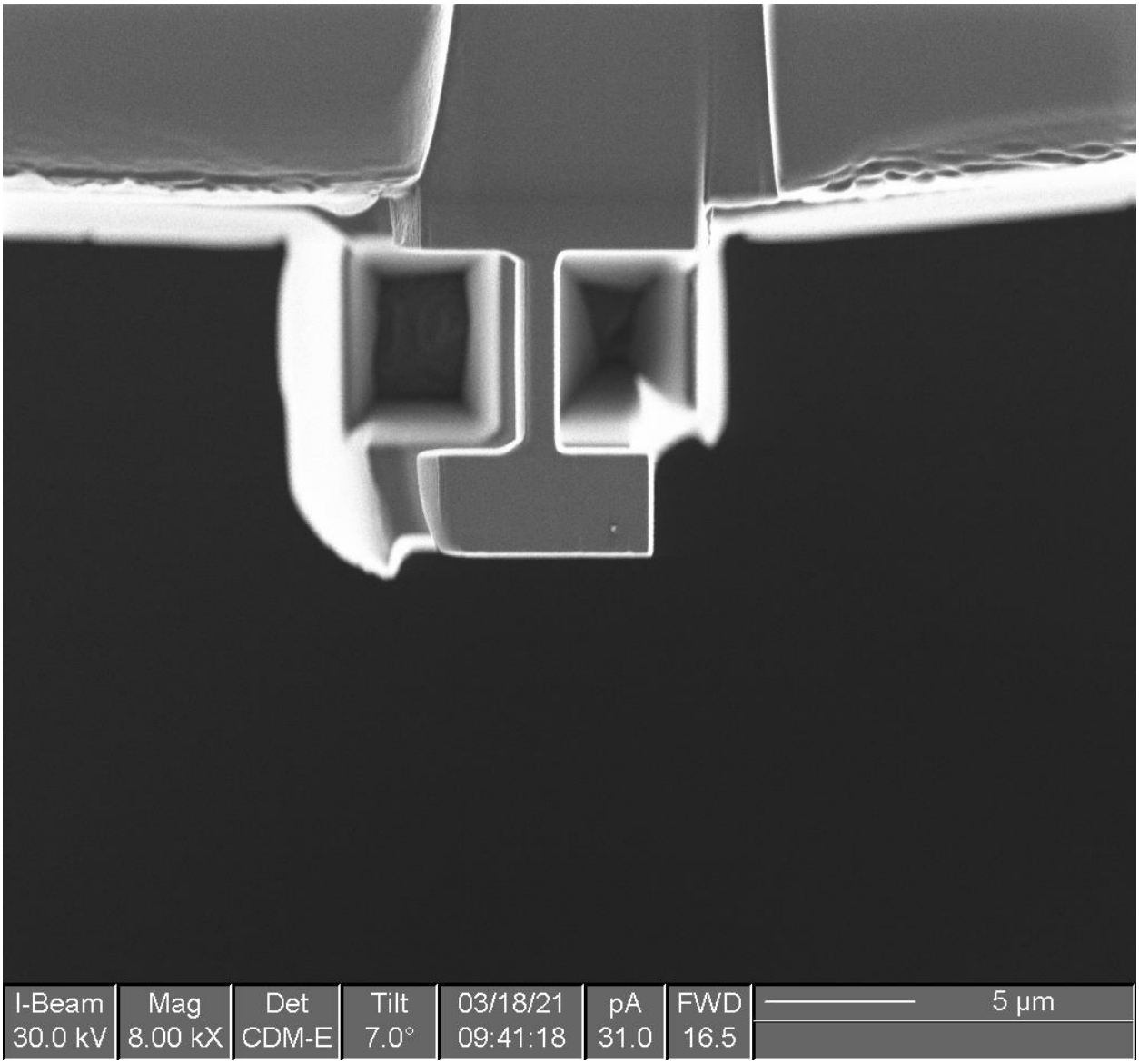

Figure 130. Silicon Tensile Sample Four height by width cross section image.

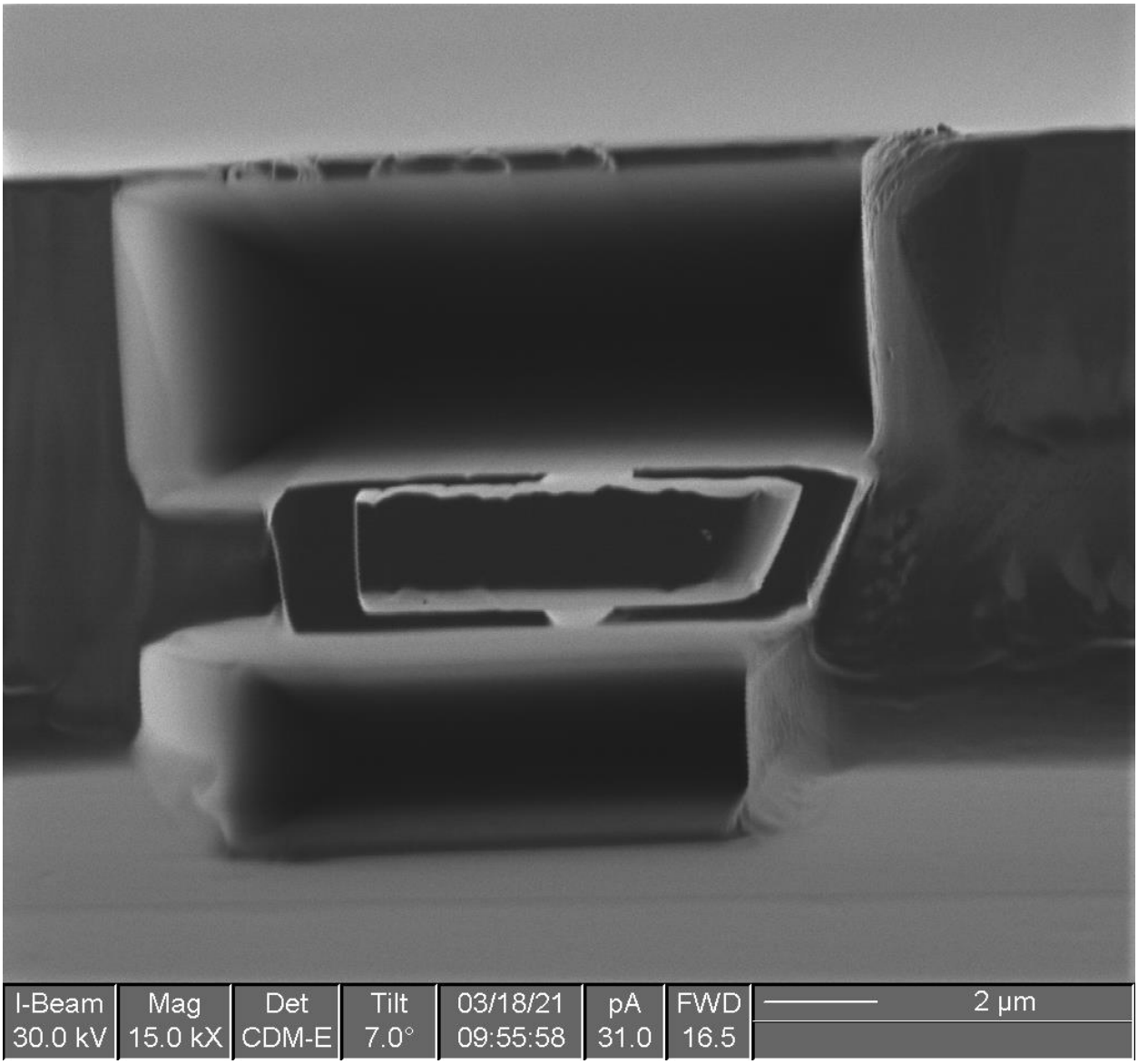

Figure 131. Silicon Tensile Sample Four depth by width cross section image.

Notice the sample in Fig. 132 experienced slippage during its test that can be seen as variance in the stress-strain curve.

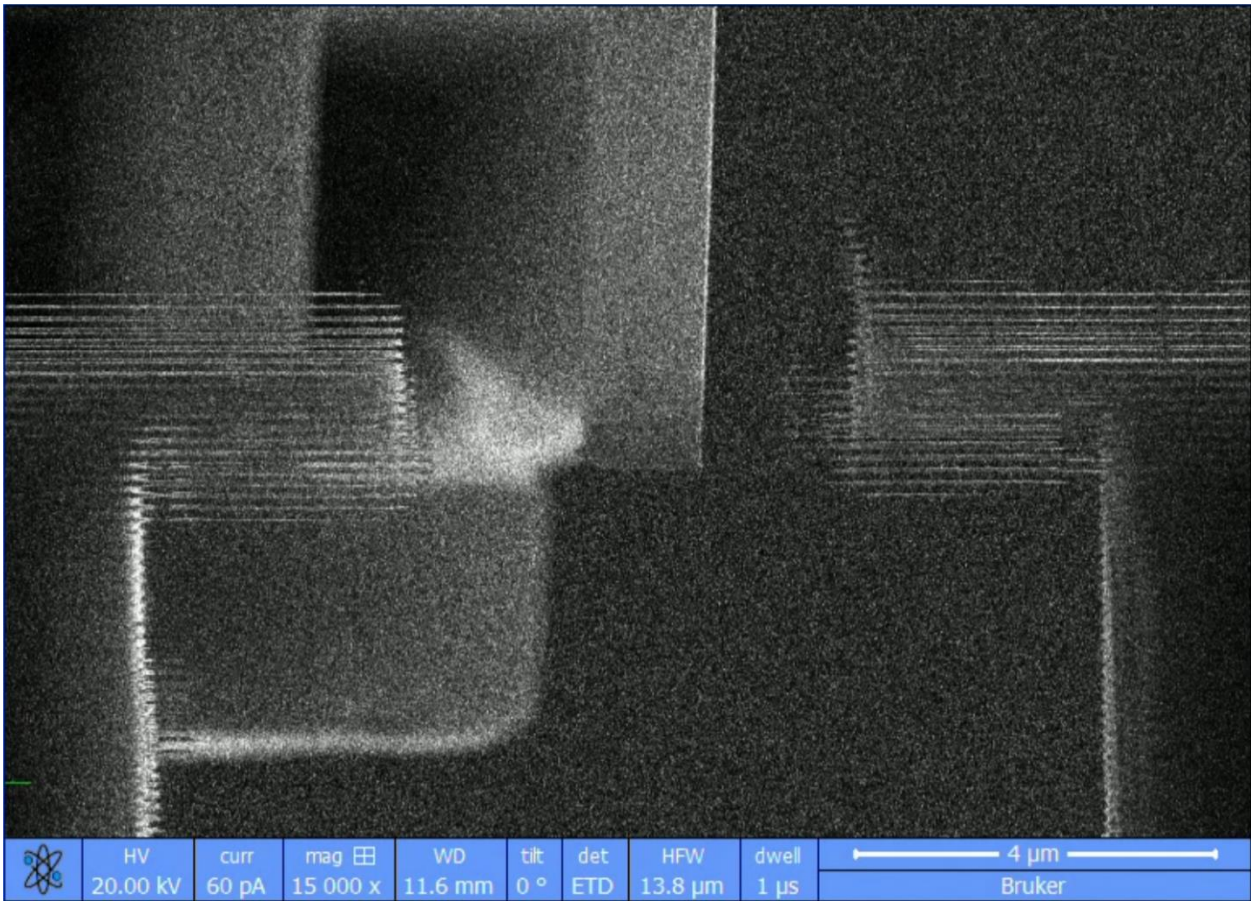

Figure 132. Silicon Tensile Sample Four post failure image.

Table 23. Dimensions of Silicon Tensile Sample Four, Gauge Section (μm).

Dimensions of Silicon Tensile Sample Four, Gauge Section (μm)	
Height	**9.3**
Width	**1.5**
Depth	**3.0**

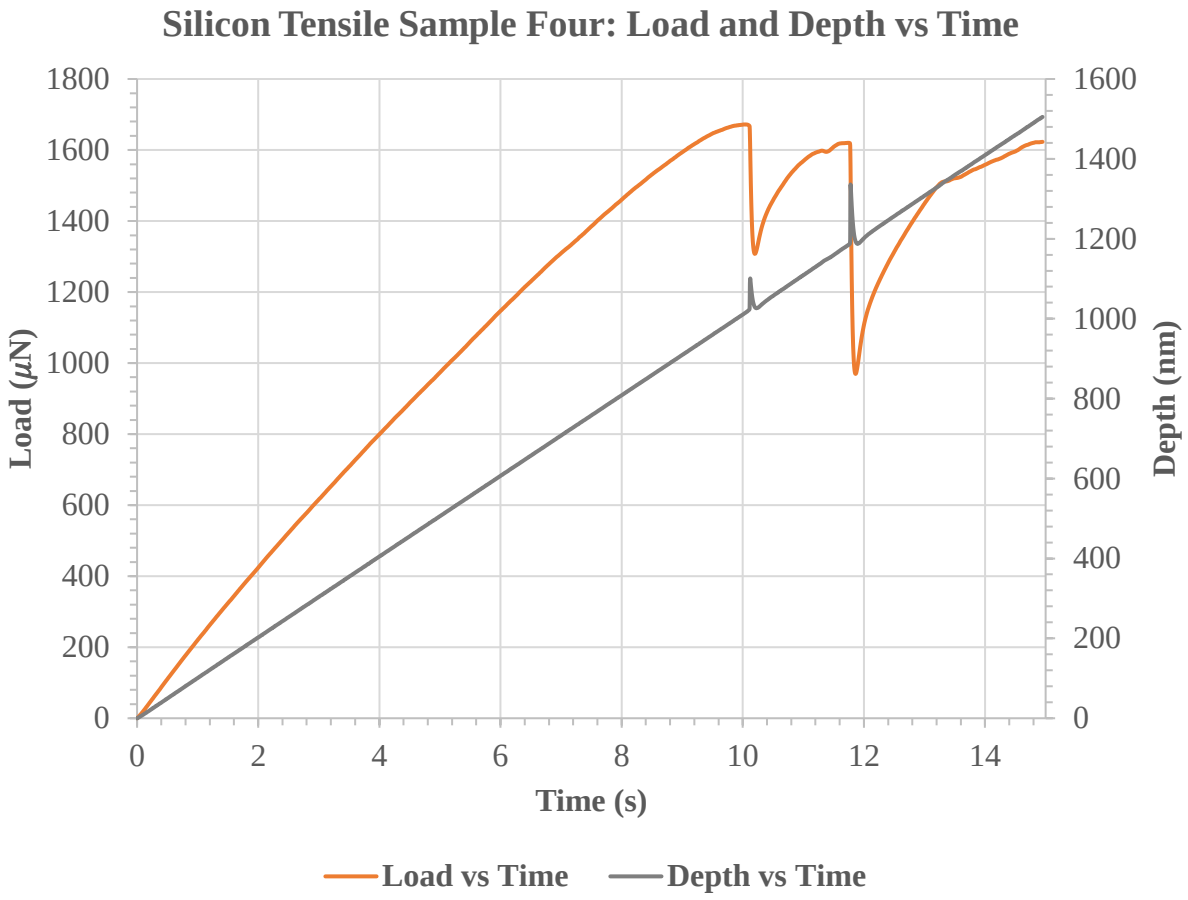

Figure 133. Silicon Tensile Sample Four: Load and Depth vs Time.

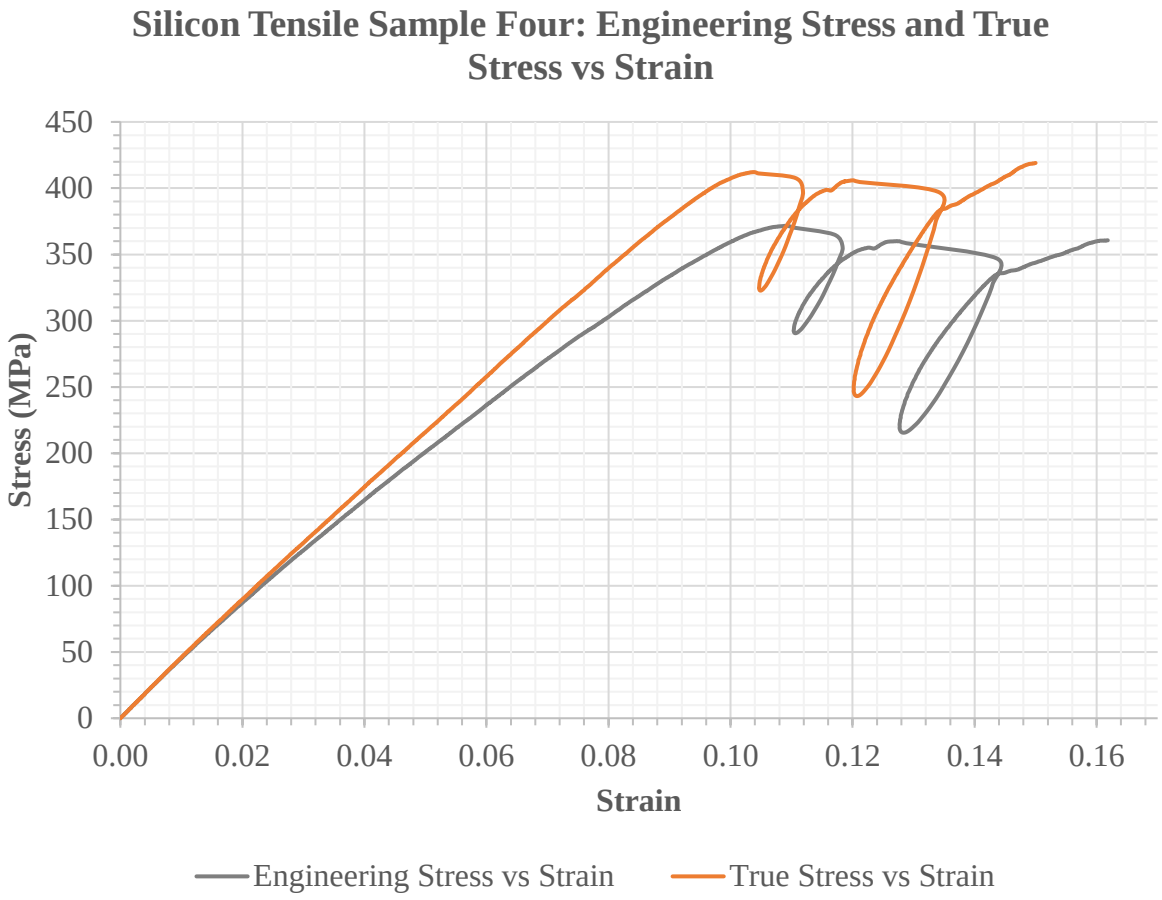

Figure 134. Silicon Tensile Sample Four: Engineering Stress and True Stress vs Strain.

Table 24. Silicon Tensile Sample Four: Mechanical Values.

Silicon Tensile Sample Four: Mechanical Values	
Engineering Fracture Strength (MPa)	**371.553813**
True Fracture Strength (MPa)	**419.021378**
Engineering Total Strain	**0.357501**
True Total Strain	**0.305645**
Modulus of Elasticity (GPa)	**4.494179**

7.8 Silicon Tensile Sample Five

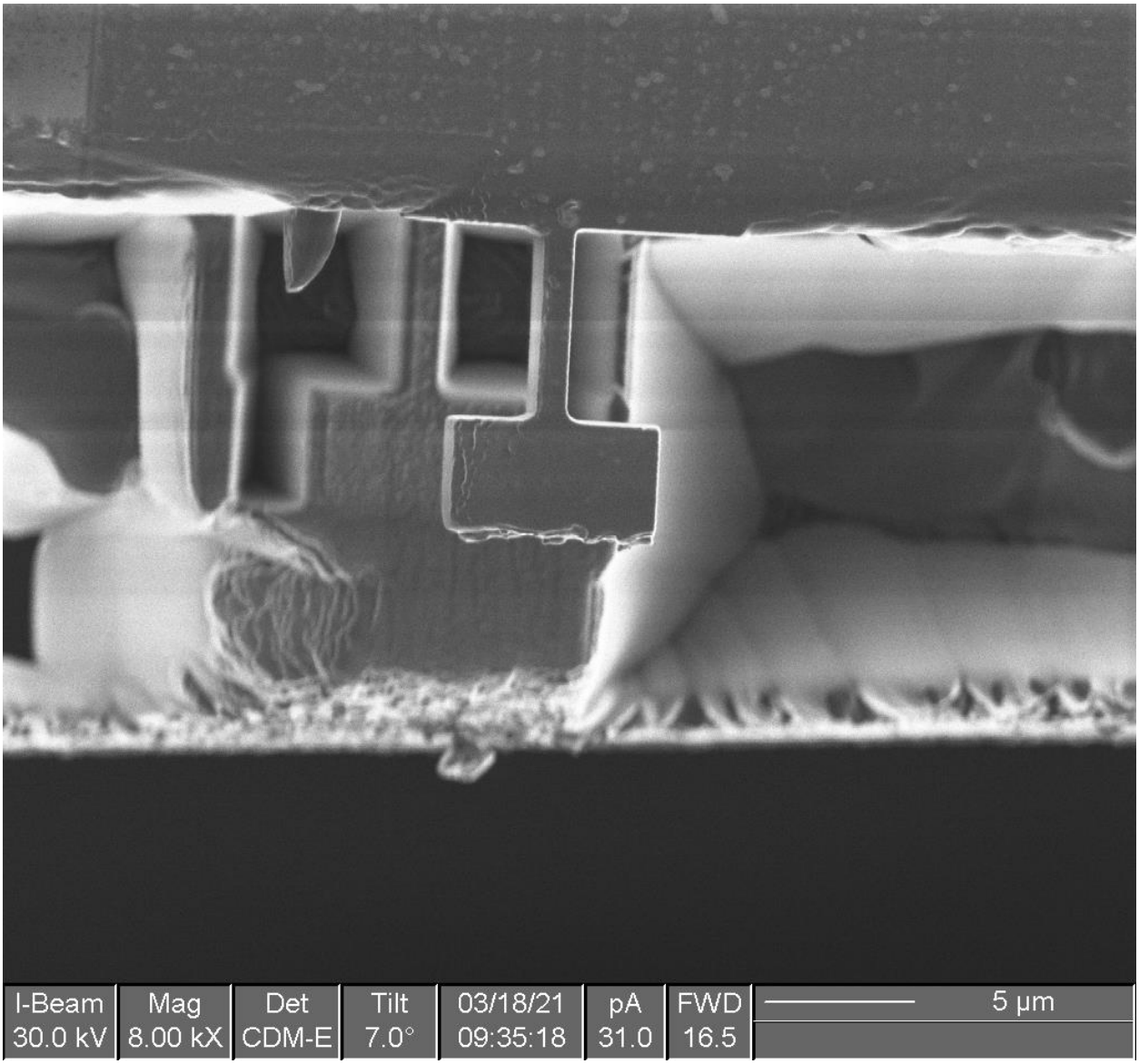

Figure 135. Silicon Tensile Sample Five height by width cross section image.

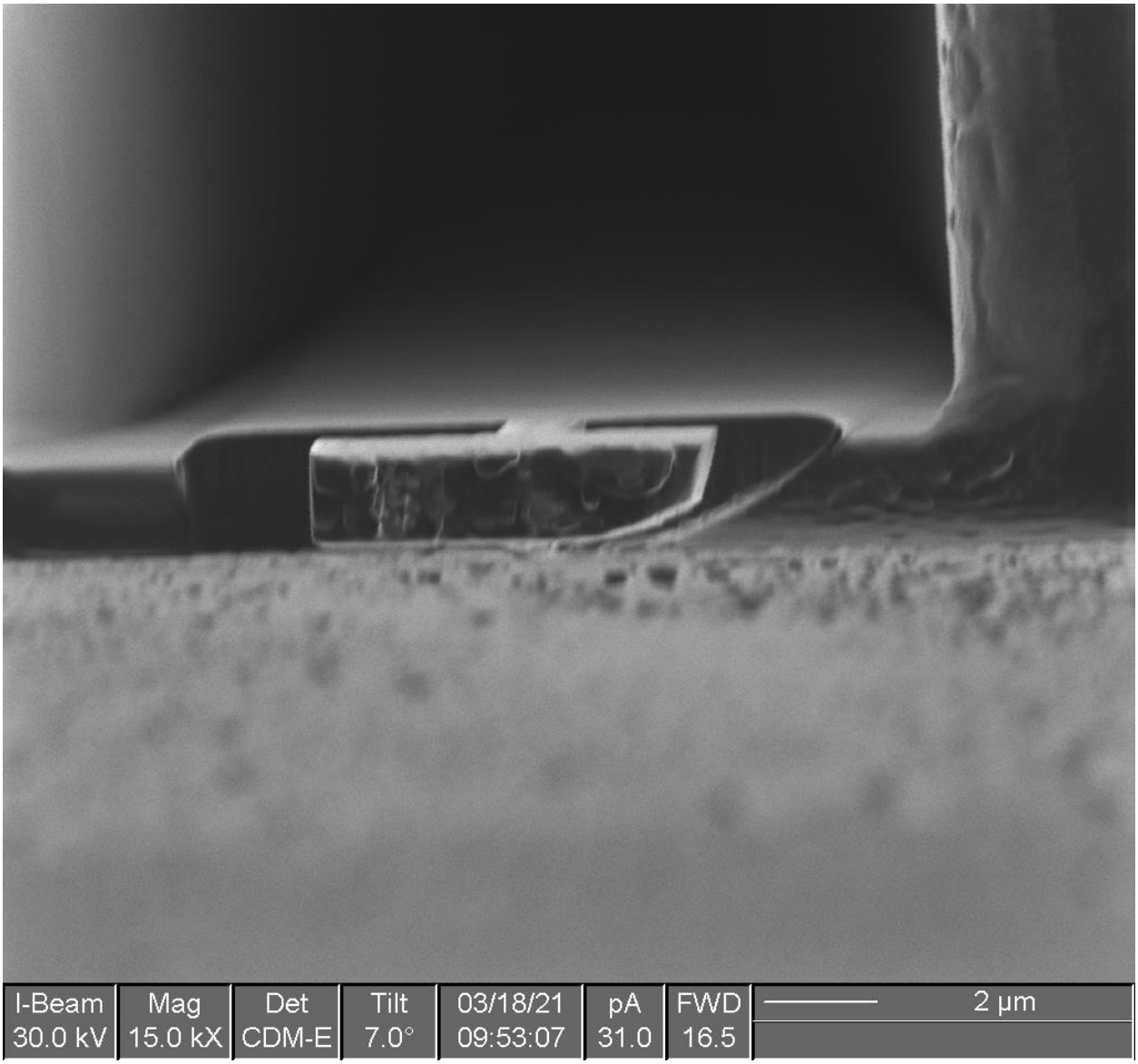

Figure 136. Silicon Tensile Sample Five depth by width cross section image.

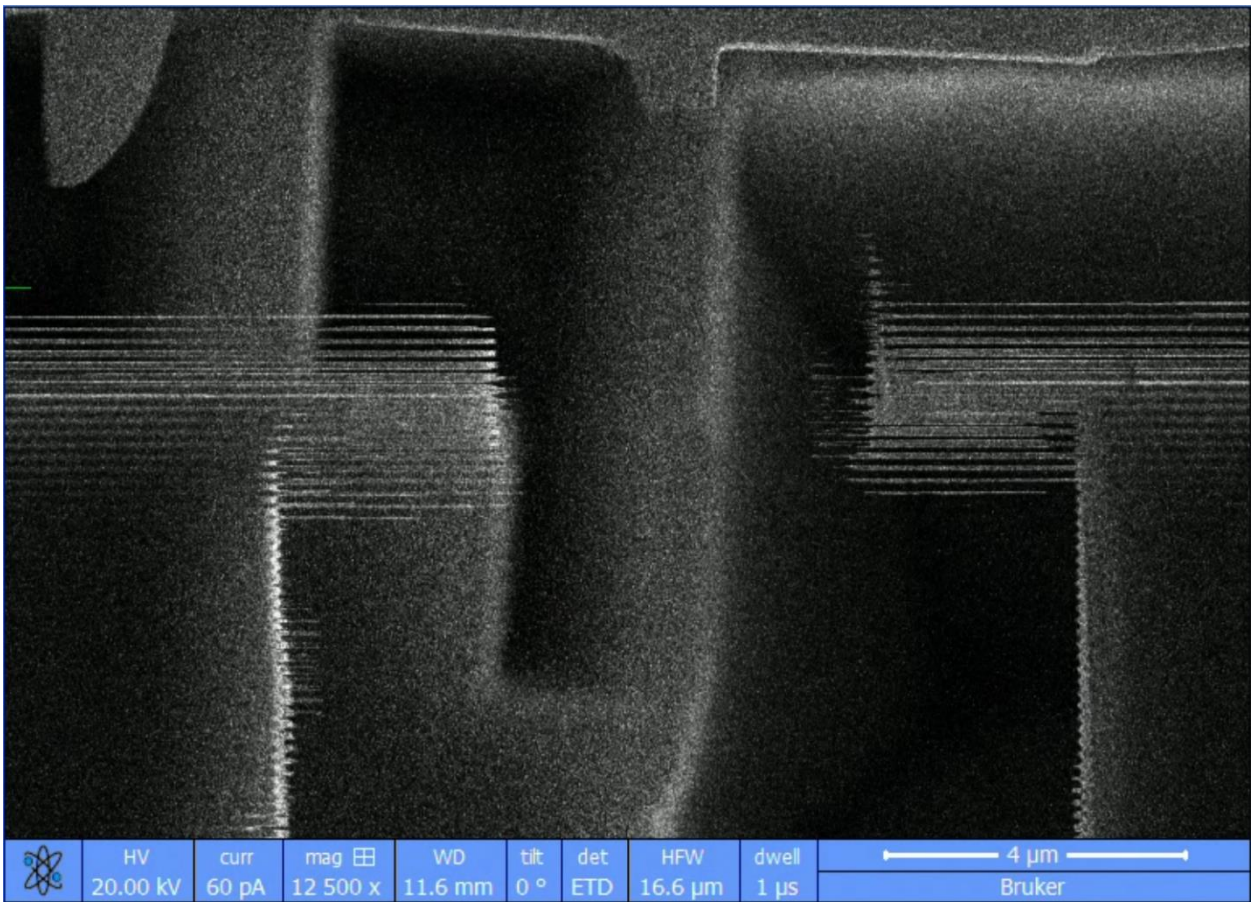

Figure 137. Silicon Tensile Sample Five post failure image.

Table 25. Dimensions of Silicon Tensile Sample Five, Gauge Section (μm).

Dimensions of Silicon Tensile Sample Five, Gauge Section (μm)	
Height	**9.0**
Width	**1.4**
Depth	**2.5**

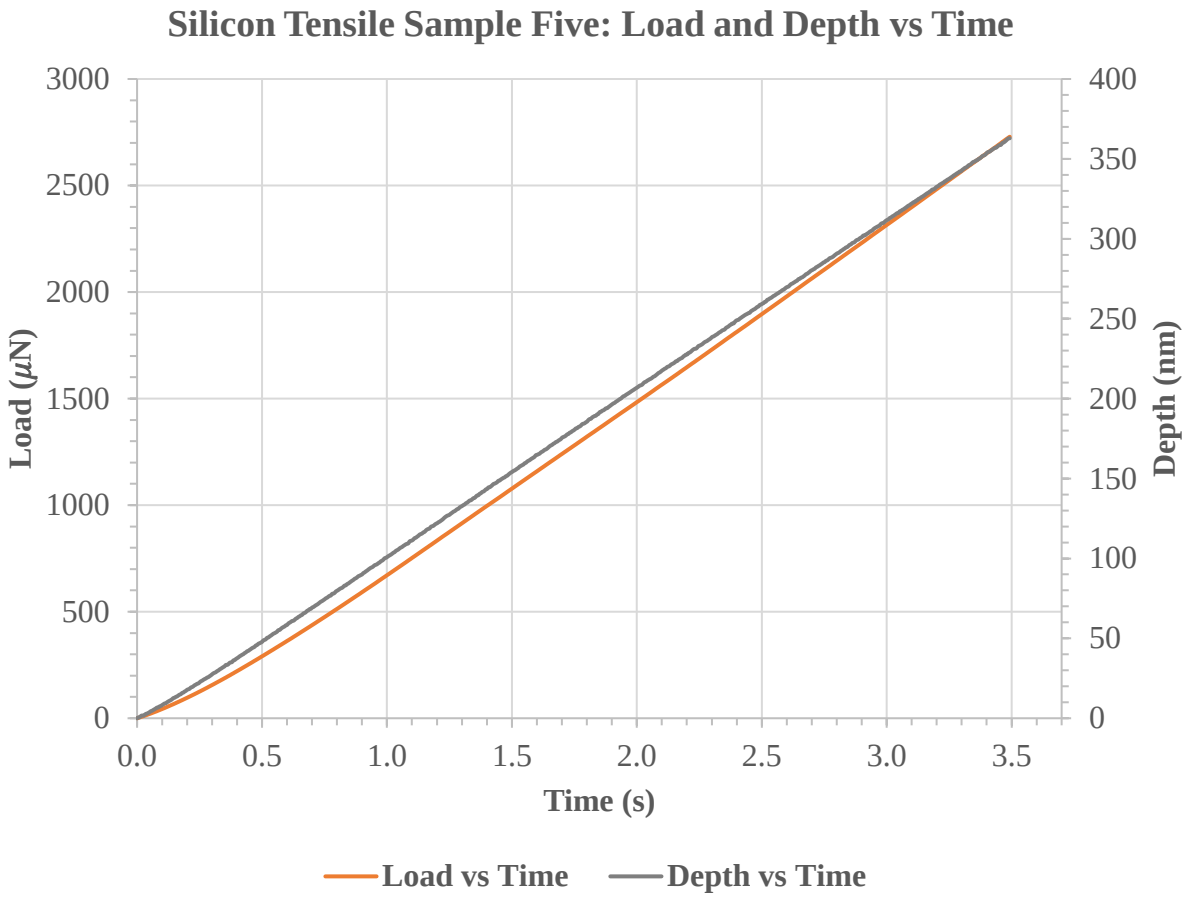

Figure 138. Silicon Tensile Sample Five: Load and Depth vs Time.

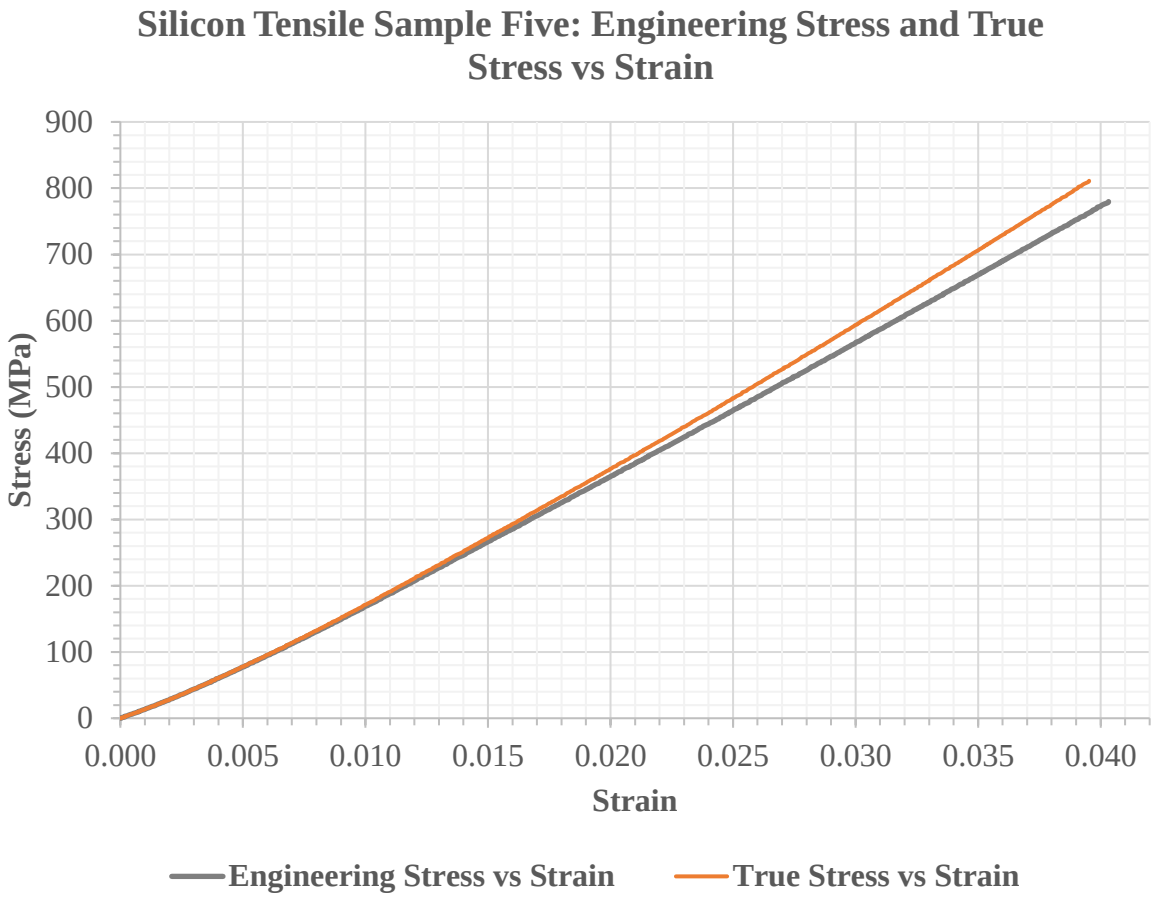

Figure 139. Silicon Tensile Sample Five: Engineering Stress and True Stress vs Strain.

Table 26. Silicon Tensile Sample Five: Mechanical Values.

Silicon Tensile Sample Five: Mechanical Values	
Engineering Fracture Strength (MPa)	779.682818
True Fracture Strength (MPa)	811.120409
Engineering Total Strain	0.040321
True Total Strain	0.039529
Modulus of Elasticity (GPa)	15.517465

7.9 Silicon Tensile Sample Seven

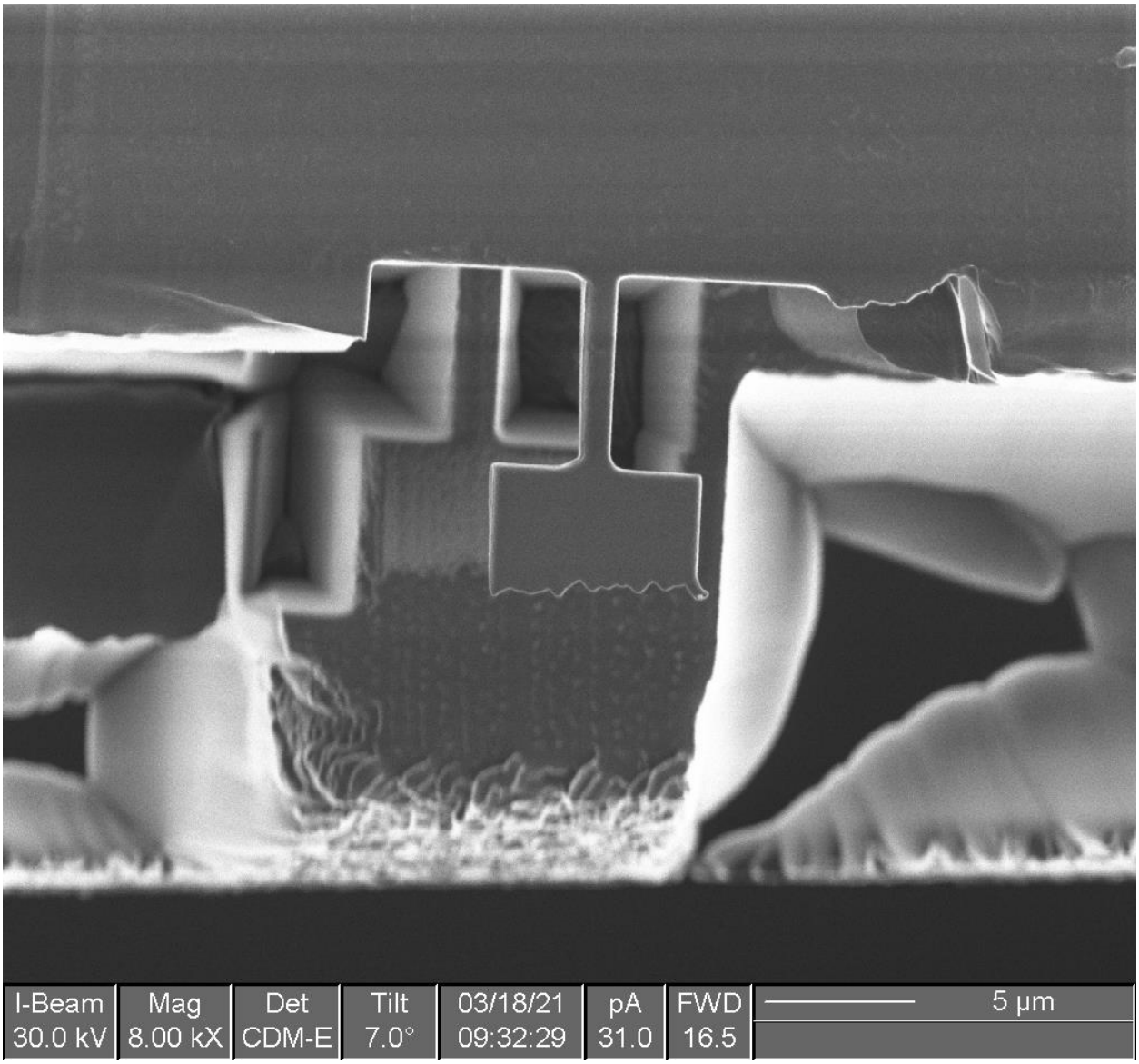

Figure 140. Silicon Tensile Sample Seven height by width cross section image.

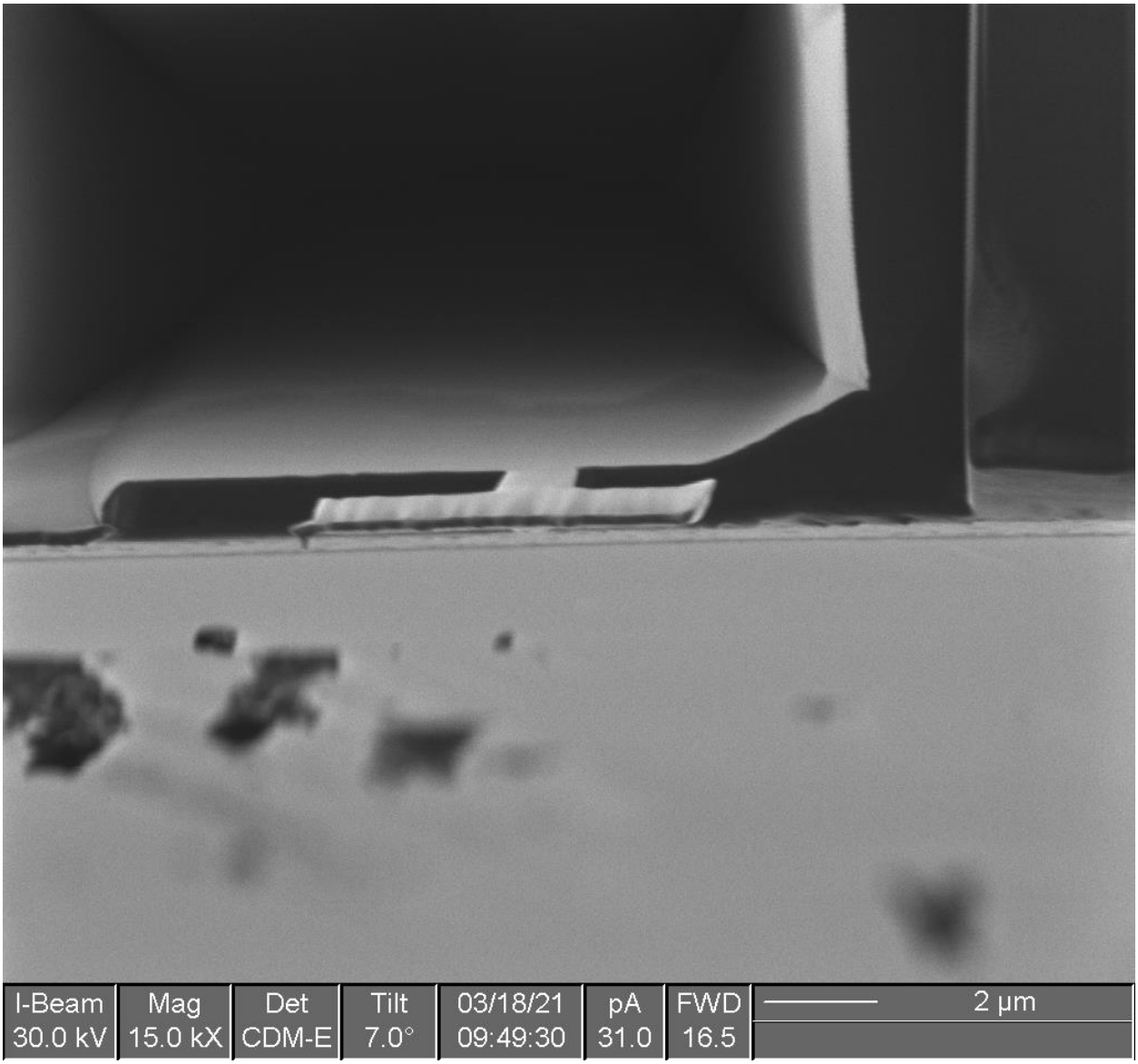

Figure 141. Silicon Tensile Sample Seven depth by width cross section image.

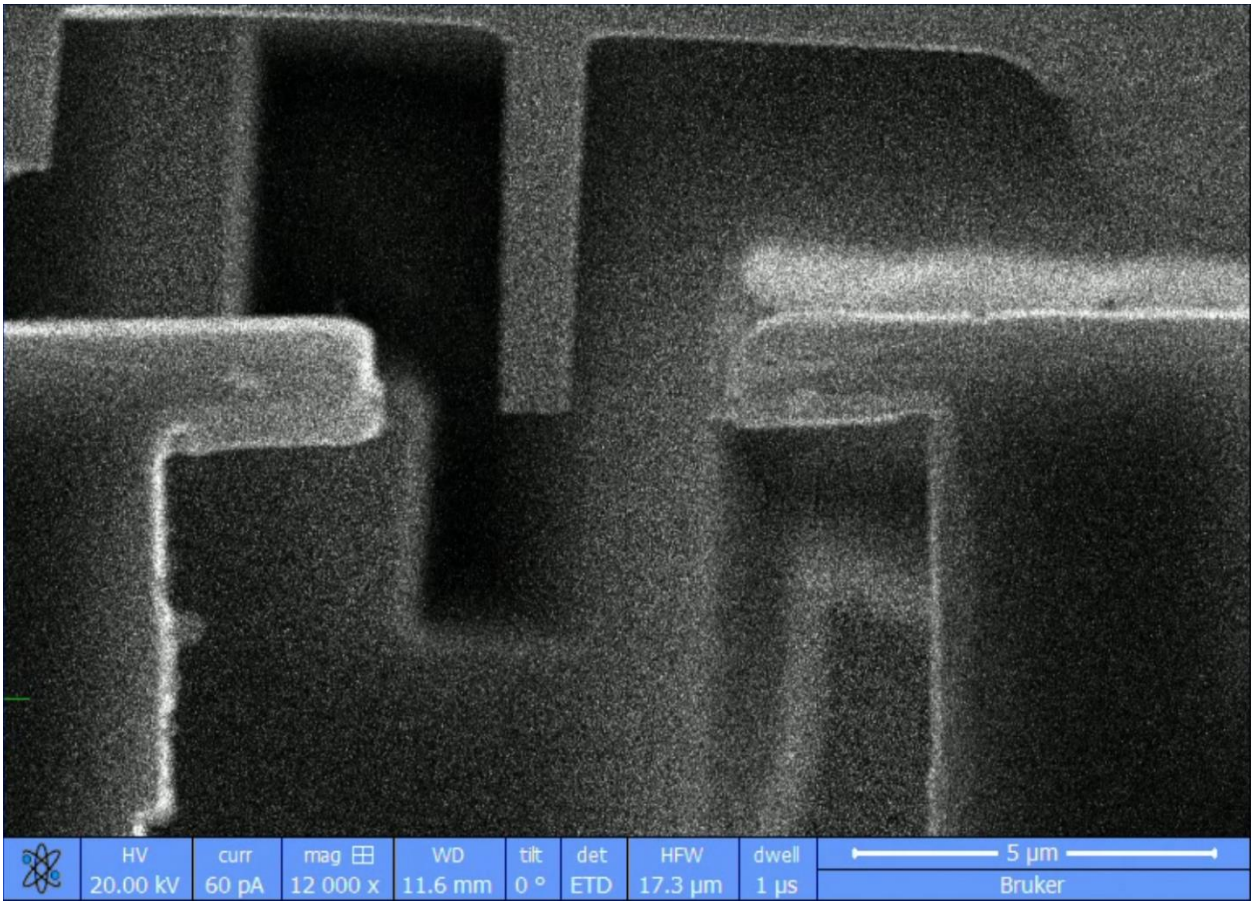

Figure 142. Silicon Tensile Sample Seven post failure image.

Table 27. Dimensions of Silicon Tensile Sample Seven, Gauge Section (μm).

Dimensions of Silicon Tensile Sample Seven, Gauge Section (μm)	
Height	**9.0**
Width	**1.1**
Depth	**0.7**

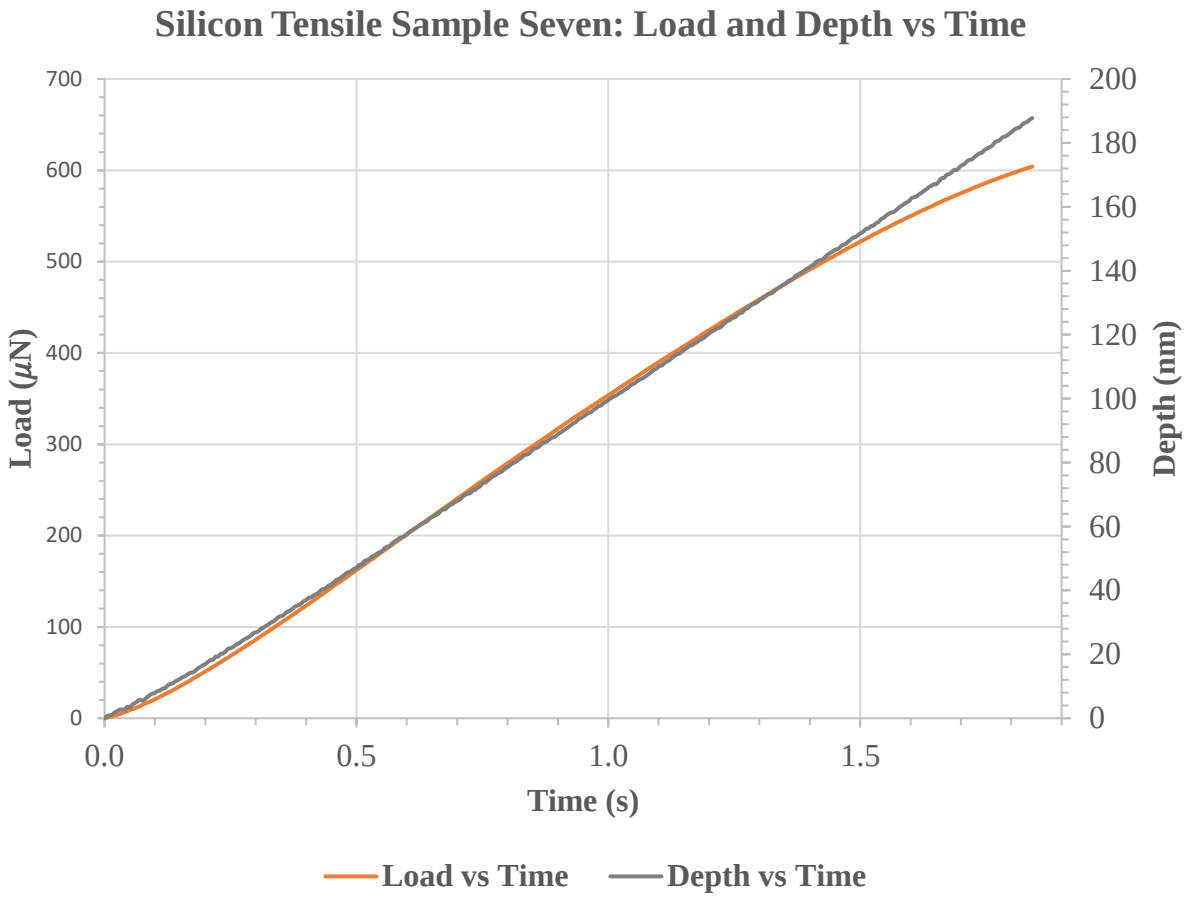

Figure 143. Silicon Tensile Sample Seven: Load and Depth vs Time.

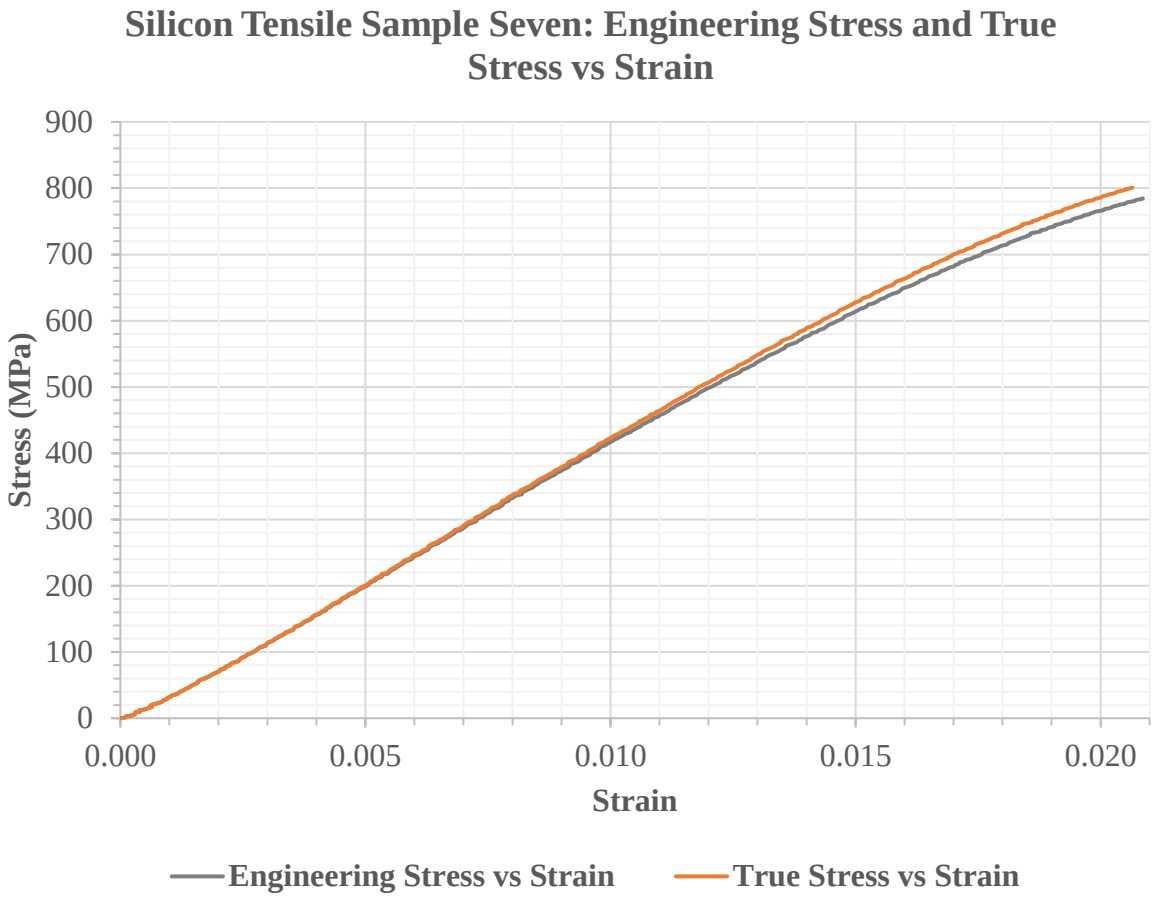

Figure 144. Silicon Tensile Sample Seven: Engineering Stress and True Stress vs Strain.

Table 28. Silicon Tensile Sample Seven: Mechanical Values.

Silicon Tensile Sample Seven: Mechanical Values	
Engineering Fracture Strength (MPa)	784.517116
True Fracture Strength (MPa)	800.883791
Engineering Total Strain	0.020862
True Total Strain	0.020647
Modulus of Elasticity (GPa)	38.573314

7.10 Silicon Tensile Sample Eight

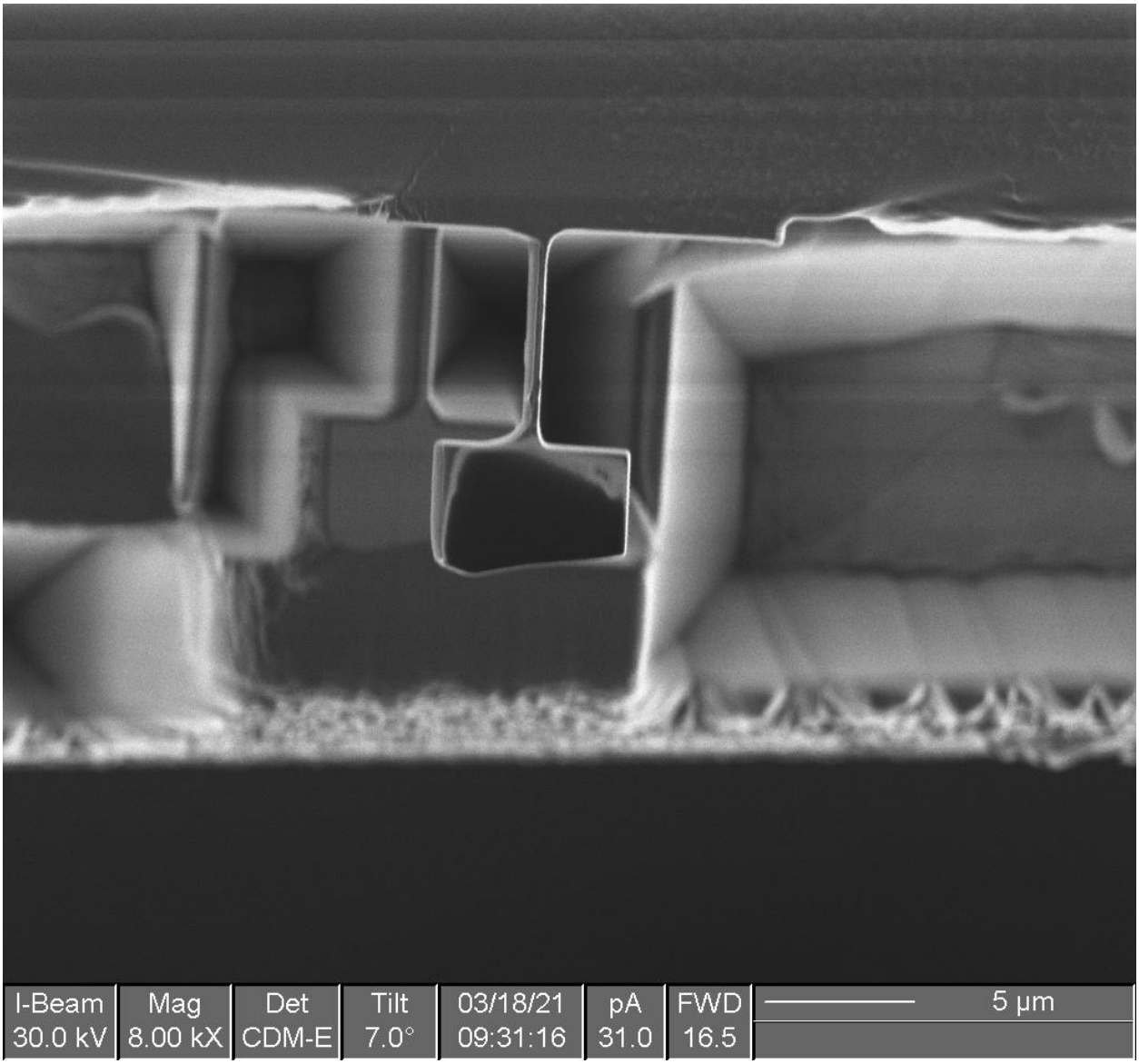

Figure 145. Silicon Tensile Sample Eight height by width cross section image.

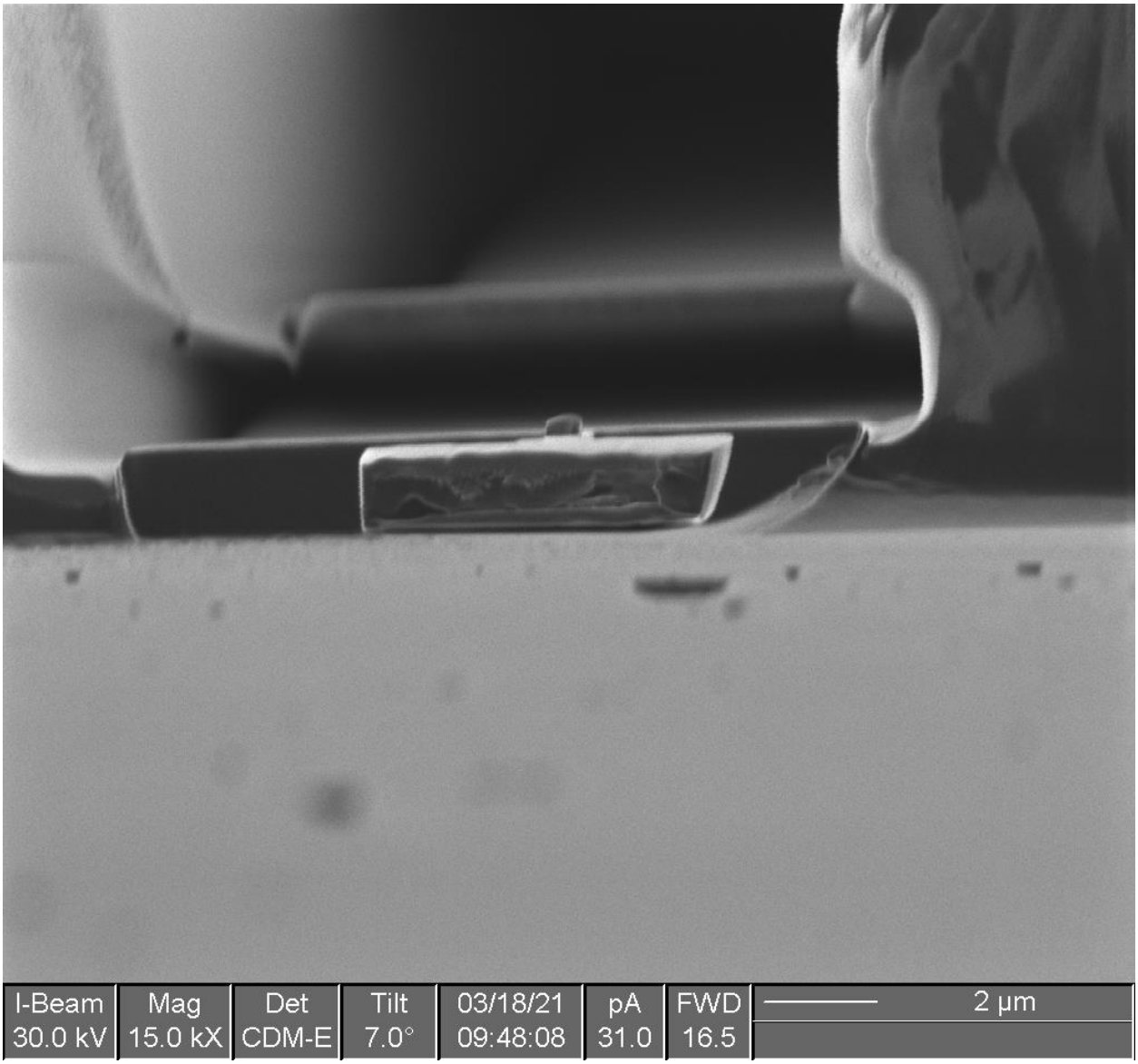

Figure 146. Silicon Tensile Sample Eight depth by width cross section image.

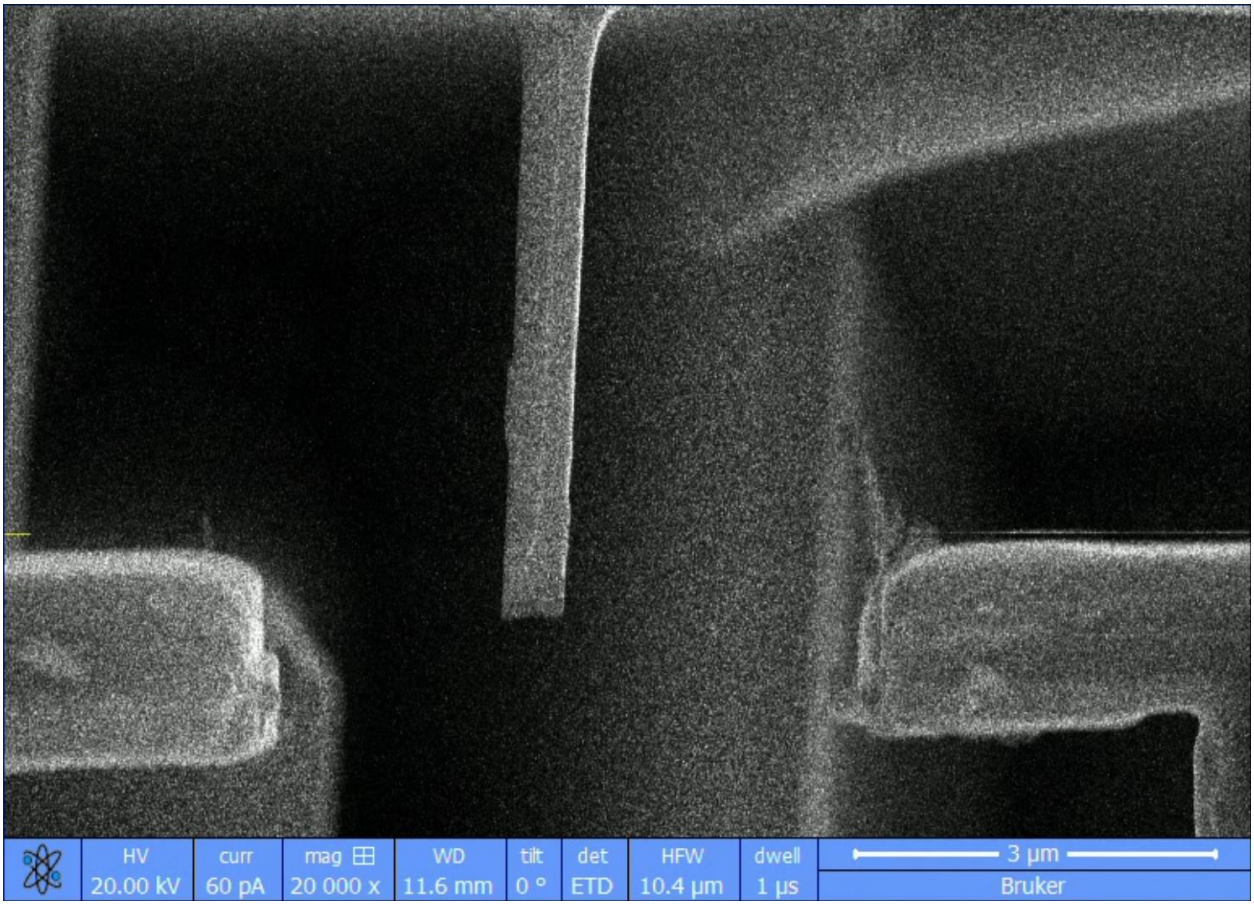

Figure 147. Silicon Tensile Sample Eight post failure image.

Table 29. Dimensions of Silicon Tensile Sample Eight, Gauge Section (μm).

Dimensions of Silicon Tensile Sample Eight, Gauge Section (μm)	
Height	**10.0**
Width	**0.6**
Depth	**2.0**

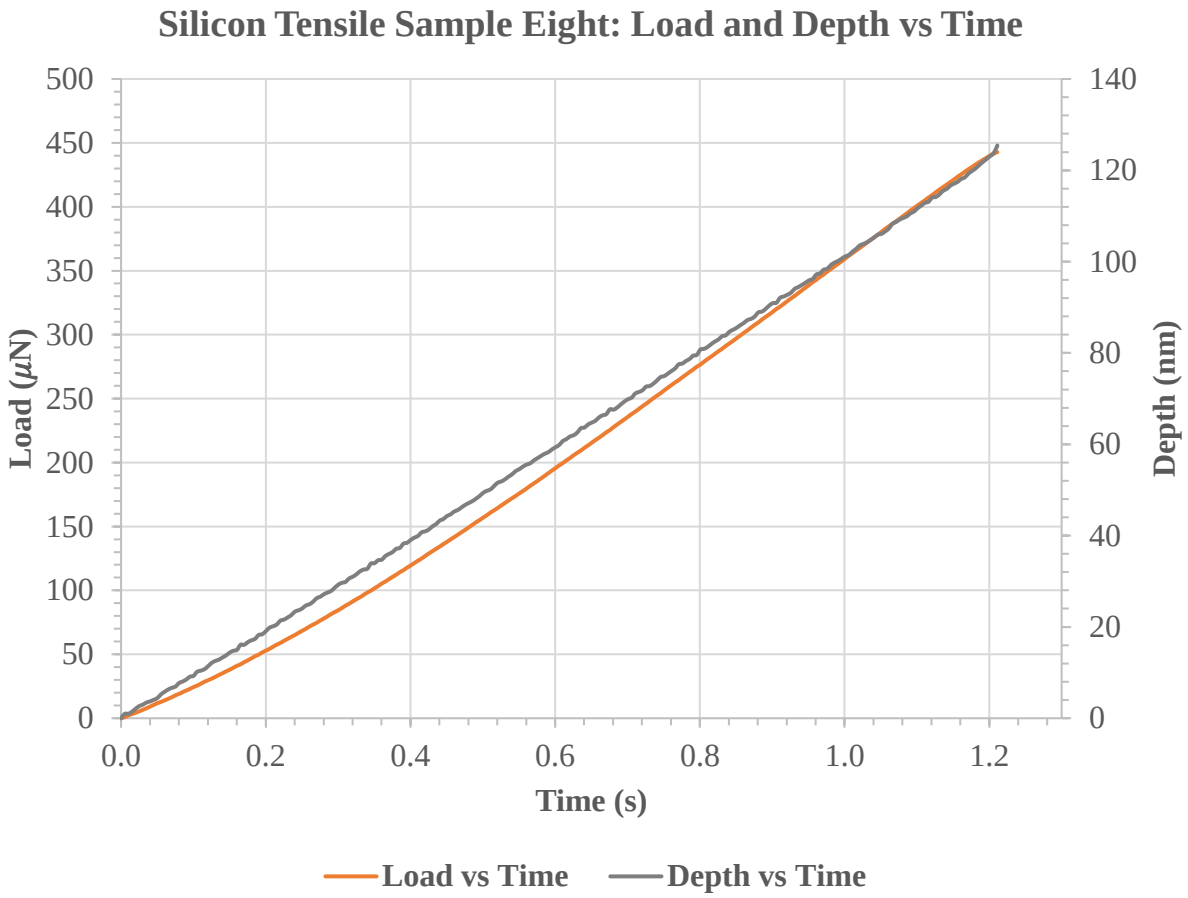

Figure 148. Silicon Tensile Sample Eight: Load and Depth vs Time.

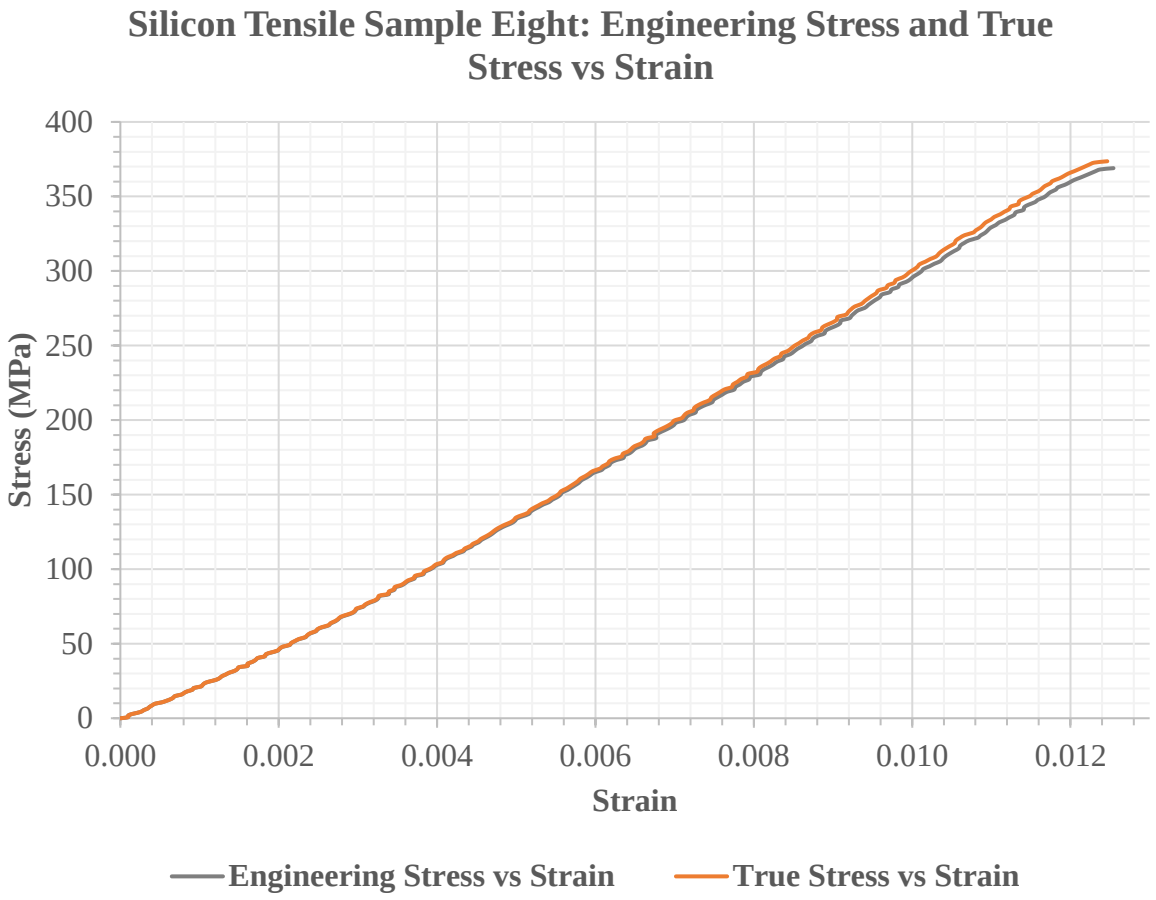

Figure 149. Silicon Tensile Sample Eight: Engineering Stress and True Stress vs Strain.

Table 30. Silicon Tensile Sample Eight: Mechanical Values.

Silicon Tensile Sample Eight: Mechanical Values	
Engineering Fracture Strength (MPa)	368.982236
True Fracture Strength (MPa)	373.610357
Engineering Total Strain	0.012543
True Total Strain	0.012465
Modulus of Elasticity (GPa)	26.654567